Springer Atmospheric Sciences

Tim Li
Pang-chi Hsu

Fundamentals of Tropical Climate Dynamics

EXTRAS ONLINE

Springer

Springer Atmospheric Sciences

More information about this series at http://www.springer.com/series/10176

Tim Li • Pang-chi Hsu

Fundamentals of Tropical Climate Dynamics

Springer

Tim Li
Department of Atmospheric Sciences
University of Hawaii
Honolulu, Hawaii, USA

College of Atmospheric Sciences
Nanjing University of Information Science
and Technology
Nanjing, China

Pang-chi Hsu
College of Atmospheric Sciences
Nanjing University of Information Science
and Technology
Nanjing, China

Additional material to this book can be downloaded from http://extras.springer.com.

Solution manual available at http://extra.springer.com.

ISSN 2194-5217 ISSN 2194-5225 (electronic)
Springer Atmospheric Sciences
ISBN 978-3-319-59595-5 ISBN 978-3-319-59597-9 (eBook)
DOI 10.1007/978-3-319-59597-9

Library of Congress Control Number: 2017942946

Printed on acid-free paper

This Springer imprint is published by Springer Nature
The registered company is Springer International Publishing AG
The registered company address is: Gewerbestrasse 11, 6330 Cham, Switzerland

Preface

This book is intended to be a textbook for an advanced graduate student course for master and PhD students in the major of atmospheric, oceanic, and climate sciences. It has been taught as a graduate course in the University of Hawaii at Manoa (UHM), National Taiwan University (NTU), and Nanjing University of Information Science and Technology (NUIST).

The objective of this book is to introduce (1) fundamental dynamics of tropical atmosphere and ocean, (2) simple and intermediate atmospheric and oceanic models, (3) observed phenomena associated with major climate models in the tropics, and (4) current understanding of theories and mechanisms associated with these modes.

A particular focus is on atmosphere–ocean interactions and physical processes relevant to (1) tropical mean climate such as the equatorial asymmetry of the intertropical convergence zone (ITCZ) and the annual cycles of sea surface temperature (SST) and wind at the equator, (2) formation of tropical cyclone (TC) and synoptic-scale variability in the western North Pacific (WNP), (3) propagation and initiation of atmospheric intraseasonal oscillations such as the Madden–Julian oscillation (MJO) and boreal summer intraseasonal oscillation (BSISO), (4) mechanisms for the El Niño–Southern Oscillation (ENSO) and the Indian Ocean Dipole (IOD), and (5) variability of the monsoon. Theories and conceptual ideas are introduced and discussed for better understanding of physical mechanisms behind the observational phenomena.

It was recalled that the first such course was taught in the Department of Atmospheric Sciences at NTU in 2005, when the lead author was in sabbatical. Due to unexpected large audience from NTU and other universities in Taiwan, a large department seminar room had to be assigned for this course for the first time. The following is a quote from a graduate student who at the moment was doing mesoscale meteorology as her PhD thesis topic: “I would select the climate dynamics as my PhD research topic if I could know earlier that such a topic is so fascinating and of fun.” In spring 2015, this course was offered at NUIST. About

150 graduate students and young faculty attended the course. Some had to arrive a half hour earlier to ensure they could have a front seat.

It is the authors' hope that through this book, graduate students are able not only to gain basic knowledge in climate dynamics but also to learn a way to conduct advanced research in atmospheric, oceanic, and climate sciences. Solutions to the questions are available at http://extras.springer.com.

Honolulu, Hawaii, USA — Tim Li
Nanjing, China — Pang-Chi Hsu

Acknowledgments

The lead author would like to express his sincere appreciation to Prof. Bin Wang for sharing equatorial wave dynamics notes and, along with Professors George Philander and C. P. Chang, for collaborations and long-term encouragement. This work was jointly supported by the China National 973 project 2015CB453200, NSFC grants 41,630,423/41475084, NSF AGS-1565653, the NRL grant N00173–16-1-G906, the Jiangsu NSF Key project (BK20150062), the Jiangsu Shuang-Chuang Team (R2014SCT001), and the Priority Academic Program Development (PAPD) of Jiangsu Higher Education Institutions. This is SOEST contribution number 10050, IPRC contribution number 1261, and ESMC number 164.

Contents

Chapter 1
Simple Dynamic Frameworks for Tropical Atmosphere and Ocean

Abstract In this chapter, free waves in a shallow water model system at the equatorial plane are first described, followed by a discussion of vertical mode separation. Then a number of simple or intermediate tropical atmospheric and oceanic models including the Gill model, the Lindzen–Nigam model, and the Cane–Zebiak model are introduced. These dynamic frameworks will be used in the subsequent chapters for theoretical and physical investigations.

1.1 Free Waves in an Equatorial Beta-Plane

In this section we discuss what free waves exist in a linear shallow water model at an equatorial beta-plane [for details, readers are referred to Matsuno (1966)]. The linear shallow water model governing equations may be written as

$$\frac{\partial u}{\partial t} - \beta y v = -\frac{\partial \phi}{\partial x} \tag{1.1a}$$

$$\frac{\partial v}{\partial t} + \beta y u = -\frac{\partial \phi}{\partial y} \tag{1.1b}$$

$$\frac{\partial \phi}{\partial t} + C_0^2 \left(\frac{\partial u}{\partial x} + \frac{\partial v}{\partial y} \right) = 0 \tag{1.1c}$$

where C_0 denotes gravity wave speed. The linear shallow water model equations fit for any vertical modes in a resting environment (see detailed derivation in Sect. 1.2), with only a difference in the value of C_0. For the first baroclinic mode atmosphere, $C_0 = 50$ m/s. For the first baroclinic mode ocean, $C_0 = 2.5$ m/s.

There are two parameters in Eq. (1.1), β and C_0, which form two intrinsic scales: a length scale $L = \sqrt{C_0/\beta}$ (equatorial Rossby radius of deformation) and a timescale $\tau = 1/\sqrt{\beta C_0}$. Let C_0 as velocity scale and C_0^2 as a scale for ϕ. Using these characteristic scales, Eq. (1.1) can be transferred into a set of nondimensional equations:

T. Li, P.-c. Hsu, *Fundamentals of Tropical Climate Dynamics*,
Springer Atmospheric Sciences, DOI 10.1007/978-3-319-59597-9_1

$$\frac{\partial u'}{\partial t'} - y'v' = -\frac{\partial \phi'}{\partial x'}, \tag{1.2a}$$

$$\frac{\partial v'}{\partial t'} + y'u' = -\frac{\partial \phi'}{\partial y'}, \tag{1.2b}$$

$$\frac{\partial \phi'}{\partial t'} + \frac{\partial u'}{\partial x'} + \frac{\partial v'}{\partial y'} = 0. \tag{1.2c}$$

A prime in Eq. (1.2) denotes nondimensional variables. Adequate side boundary conditions are that u', v', ϕ' are bounded (i.e., having finite values) as $y \to \pm\infty$.

1.1.1 Equatorial Kelvin Waves

We first examine a special solution of Eq. (1.2), in which the meridional velocity is always zero (i.e., $v' \equiv 0$). Then Eq. (1.2) becomes

$$\frac{\partial u'}{\partial t'} = -\frac{\partial \phi'}{\partial x'} \tag{1.3a}$$

$$y'u' = -\frac{\partial \phi'}{\partial y'} \tag{1.3b}$$

$$\frac{\partial \phi'}{\partial t'} + \frac{\partial u'}{\partial x'} = 0. \tag{1.3c}$$

Equation (1.3b) implies that zonal wind is always in geostrophic balance with meridional pressure gradient at and near the equator. The combination of (1.3a) and (1.3c) yields a wave equation:

$$\frac{\partial^2 u'}{\partial t'^2} - \frac{\partial^2 u'}{\partial x'^2} = 0.$$

The general solution of the wave equation above is

$$u' = F(x' \mp t')Y(y'),$$

where F is an arbitrary function. Substituting this into (1.3a), we have

$$\phi' = \pm u'.$$

Substituting the above solution into (1.3b), one may obtain

$$y'Y(y') \pm \frac{dY}{dy'} = 0.$$

The solution of the above equation is
$Y(y') = Y(0)\mathrm{e}^{\mp y'^2/2}$.

Note that only "-" sign in the above solution satisfies the "finite" side boundary condition. Thus the only physical solution of Eq. (1.3) is of the nondimensional form

$$u' = \phi' = F(x' - t')\mathrm{e}^{-y'^2/2},$$

or in a dimensional form

$$u = \frac{\phi}{C_0} = F(x - C_0 t)\mathrm{e}^{-\beta y^2/2C_0}, v \equiv 0. \tag{1.4}$$

The solution represented by Eq. (1.4) is called "equatorial Kelvin waves," because the governing Eq. (1.3) is identical to that of coastal Kelvin waves except the Coriolis force in this case is βy. The equatorial Kelvin waves have the following characteristics:

(A) The equatorial Kelvin waves move eastward at the phase speed of gravity waves, C_0.
(B) The Kelvin waves are trapped near the equator with an e-folding scale of $\sqrt{2C_0/\beta}$. For the first baroclinic mode atmosphere, $C_0 \approx 50$ ms^{-1} and $\sqrt{2C_0/\beta} \approx 2000$ km, while for the first baroclinic mode ocean, $C_0 \approx 2.5$ ms^{-1} and $\sqrt{2C_0/\beta} \approx 460$ km. Higher-order baroclinic modes are even more tightly trapped near the equator.
(C) $v = 0$, while u is exactly in geostrophic balance with ϕ. Facing the moving direction, high pressure is to the right (left) in the northern (southern) hemisphere.
(D) Kelvin waves are nondispersive because F represents an arbitrary wave packet that propagates without changing shape. This means that the group speed equals the phase speed, i.e., the energy is also propagated with a speed C_0.
(E) Physically, the equatorial Kelvin waves are just a gravity wave trapped to the equator because of Earth's rotation via geostrophic balance described in Eq. (1.3b). It reveals an important property of the equatorial zone: it acts as a wave guide.

Figure 1.1 shows the horizontal structure of zonal velocity and pressure characteristics of equatorial Kelvin waves.

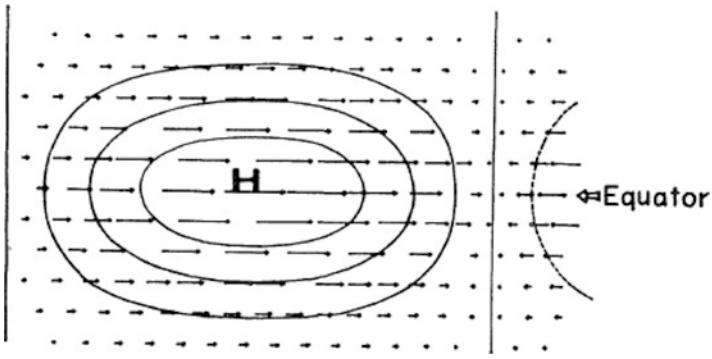

Fig. 1.1 Pressure and velocity distributions of eigensolution for $k = 0.5$. This wave behaves like as the Kelvin wave (From Matsuno (1966). © Copyright 1966, Meteorological Society of Japan (MSJ))

1.1.2 General Dispersion Relation

We now examine the general solutions in which meridional velocity does not vanish. Since the coefficients of Eqs. (1.2a, 1.2b, and 1.2c) are y-dependent only, the separation of y-dependent and x-dependent parts to the general wave solution is possible. Therefore, we search for a wave solution of the form

$$(u', v', \phi') = \mathrm{Re}(U(y), V(y), \Phi(y))\mathrm{e}^{i(kx-\omega t)}.$$

The side boundary conditions may be written as
$U(y), V(y), \Phi(y)$ are bounded, as $y \to \pm\infty$.
Substituting the above wave solution into Eq. (1.2) yields

$$-i\omega U - yV = -ik\Phi, \tag{1.5a}$$

$$-i\omega V + yU = -\frac{d\Phi}{dy}, \tag{1.5b}$$

$$-i\omega\Phi + ikU + \frac{dV}{dy} = 0. \tag{1.5c}$$

One may eliminate U and Φ to formulate a single equation for V. Solving for U and Φ from (1.5a) and (1.5c) leads to

$$U = \frac{1}{k^2 - \omega^2}\left(ik\frac{dV}{dy} - \boldsymbol{i\omega y V}\right), \tag{1.6a}$$

$$\Phi = \frac{1}{k^2 - \omega^2}\left(i\omega\frac{dV}{dy} - \boldsymbol{iky}\boldsymbol{V}\right). \tag{1.6b}$$

Applying (1.6a and 1.6b) into (1.5b), one can obtain

$$\frac{d^2V}{dy^2} + \left[\left(\omega^2 - k^2\right) - \frac{k}{\omega} - y^2\right]V = 0. \tag{1.7}$$

Note that in deriving Eqs. (1.6a and 1.6b), we have assumed $k^2 \neq \omega^2$.

Equation (1.7) is the Schrödinger equation for a simple harmonic oscillator. The side boundary conditions are only satisfied when the constant $k^2 - \omega^2 - k/\omega$ is equal to a positive odd integer, i.e.,

$$\omega^2 - k^2 - k/\omega = 2m + 1, \quad m = 0, 1, 2, \ldots \tag{1.8}$$

The solution of Eq. (1.7) is

$$V(y) = V_m(y) = \mathrm{e}^{-y^2/2}H_m(y), \quad m = 0, 1, 2, \ldots \tag{1.9}$$

where $H_m(y) \equiv \sum_{l=0}^{[m/2]} \frac{(-1)^l m!}{l!(m-2l)!}(2y)^{m-2l}$ satisfies the Hermite equation,

$$\frac{d^2H}{dy^2} - 2y\frac{dH}{dy} + 2mH = 0.$$

The first six orders $H_m(y)$ are listed below:

$$\begin{aligned}
H_0(y) &= 1.\\
H_1(y) &= 2y.\\
H_2(y) &= 4y^2 - 2.\\
H_3(y) &= 8y^3 - 12y.\\
H_4(y) &= 16y^4 - 48y^2 + 12.\\
H_5(y) &= 32y^5 - 160y^3 + 20y.
\end{aligned}$$

There is the following property for $H_m(y)$:

$$\int_{-\infty}^{\infty} H_m(y)H_n(y)\mathrm{e}^{-y^2}dy = \begin{cases} 0 & m \neq n \\ 2^m m!\sqrt{\pi} & m = n \end{cases}. \tag{1.10}$$

Let $V_m(y) \equiv \mathrm{e}^{-y^2/2}H_m(y)/\sqrt{2^m m!\sqrt{\pi}}$, we have

$$\int_{-\infty}^{\infty} V_m(y)V_n(y)dy = \begin{cases} 0, & m \neq n \\ 1, & m = n \end{cases}. \tag{1.11}$$

It is worth mentioning that $V_m(y)$ with an even (odd) m is symmetric (antisymmetric) about the equator. It has m nodal points in the domain $(-\infty, \infty)$. The values $y = \sqrt{2m+1}$ are turning latitudes: $V_m(y)$ is oscillatory at $|y| < \sqrt{2m+1}$ and exhibits a monotonic decay for $|y| > \sqrt{2m+1}$. Thus, the lower modes are more equatorially trapped.

1.1.3 Horizontal Structure

The meridional velocity $V(y)$ for the mth eigensolution $V_m(y)$ is described by Eq. (1.9). $U(y)$ and $\Phi(y)$ can be obtained from Eqs. (1.6a and 1.6b), with the use of the following recurrence relation for Hermite's polynomial:

$$\frac{dH_m(y)}{dy} = 2mH_{m-1}(y),$$
$$H_{m+1}(y) = 2yH_m(y) - 2mH_{m-1}(y).$$

For $m \geq 1$, the u', ϕ', and v' fields can be represented as:

$$v'_m = \mathrm{Re}V_m(y)\mathrm{e}^{i(kx-\omega t)}$$
$$u'_m = \mathrm{Re}\frac{i}{2}\left[\frac{V_{m+1}}{\omega - k} + \frac{2m}{\omega + k}V_{m-1}\right]\mathrm{e}^{i(kx-\omega t)}$$
$$\phi'_m = \mathrm{Re}\frac{i}{2}\left[\frac{V_{m+1}}{\omega - k} - \frac{2m}{\omega + k}V_{m-1}\right]\mathrm{e}^{i(kx-\omega t)}.$$

1.1.4 Dispersion Diagram

Equation (1.8) is the nondimensional dispersion equation, which describes the relationship between nondimensional wave number and frequency. For not losing generality, we specify ω to be always positively defined, while k can be either positive (corresponding eastward propagation) or negative (corresponding westward propagation). The frequency ω as a function of k is plotted in Fig. 1.2.

The dispersion equation (1.8) suggests that three different types of free waves exist near the equator.

We first examine the $m \geq 1$ cases. The dispersion equation can be written as

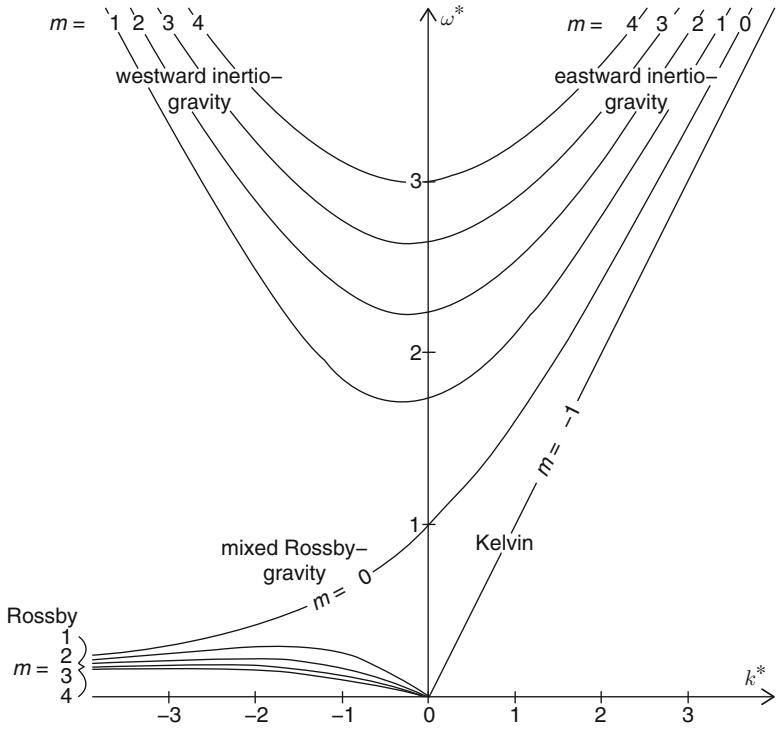

Fig. 1.2 Dispersion curves for equatorial waves (up to $m = 4$) as a function of the nondimensional frequency, ω, and nondimensional zonal wave number, k (From Kiladis et al. (2009). © Copyright 2009, American Geophysical Union (AGU))

$$k_m = -\frac{1}{2\omega} \pm \sqrt{\omega^2 + \frac{1}{4\omega^2} - (2m+1)}, \quad m = 1, 2, 3, \ldots$$

For free waves, a real zonal wave number is needed – an imaginary zonal wave number implies wave amplitude decaying or growing exponentially with x. To obtain a real k, one must require that

$$\omega^2 + \frac{1}{4\omega^2} - (2m+1) \geq 0,$$

which is equivalent to

$$\omega \geq \sqrt{\frac{m+1}{2}} + \sqrt{\frac{m}{2}} \geq 1 + \frac{1}{\sqrt{2}}, \quad m = 1, 2, \ldots \tag{1.12a}$$

or

$$\omega \le \sqrt{\frac{m+1}{2}} - \sqrt{\frac{m}{2}} \le 1 - \frac{1}{\sqrt{2}}, \quad m = 1, 2, \ldots \tag{1.12b}$$

Equations (1.12a and 1.12b) imply that there are two distinguished groups of waves, one with high frequency ($\omega \ge 1 + 1/\sqrt{2}$) and the other with low frequency ($\omega \le 1 - 1/\sqrt{2}$).

Differentiating with respect to k at both sides of the dispersion Eq. (1.8), one may derive the formula for zonal group velocity:

$$C_{gx} \equiv \frac{\partial \omega}{\partial k} = \frac{2k\omega + 1}{2\omega^2 + k/\omega},$$

which vanishes at

$$2k\omega = -1. \tag{1.13}$$

If one plots $2k\omega = -1$ in Fig. 1.2, this curve intercepts with frequency extrema at

$$\omega_{\text{extrema}} = \begin{cases} \sqrt{\dfrac{m+1}{2}} + \sqrt{\dfrac{m}{2}} & \text{for high frequency modes} \\ \sqrt{\dfrac{m+1}{2}} - \sqrt{\dfrac{m}{2}} & \text{for low frequency modes} \end{cases}$$

The interception point represents zero zonal group velocity for both the high-frequency and low-frequency wave groups.

1.1.5 *Low-Frequency Equatorial Rossby Waves*

For the low-frequency wave group, nondimensional frequency of these waves is smaller than $1 - 1/\sqrt{2} = 0.29$, which corresponds to a dimensional frequency $\omega_* \le 0.29\sqrt{\beta C_0}$. Taking $C_0 = 50\ \text{ms}^{-1}$ for the atmosphere, $\omega_* \le 10^{-5} s^{-1}$ or the period $T_* \ge 7.3$ days; taking $C_0 = 2.5\ \text{ms}^{-1}$ for the ocean, $\omega_* \le 2.15 \times 10^{-5} \text{s}^{-1}$ or the period $T_* \ge 34$ days.

For the low-frequency wave group, ω is small, thus $\omega^2 \ll 1/\omega^2$. The dispersion equation can then be approximated by

$$k_{m\pm} = -\frac{1}{2\omega} \pm \sqrt{\frac{1}{4\omega^2} - (2m+1)} < 0, \tag{1.14}$$

or

$$\omega = -\frac{k_m}{{k_m}^2 + (2m+1)}. \tag{1.15}$$

The dispersion Eq. (1.15) states that the higher the meridional mode index m, the lower the wave frequency ω.

Resuming the dimensional form, the phase speed is

$$\frac{\omega_*}{k_*} = -\frac{\beta}{k_*^2 + \frac{\beta}{C_0}(2m+1).} \tag{1.16}$$

Equation (1.16) resembles Rossby wave dispersion relation in a beta-plane channel except that the quantized y-wave number has a slightly different form due to the side boundary condition at $y = \pm\infty$. These low-frequency modes are, therefore, called equatorial Rossby waves. They occur because f varies with latitude.

For long Rossby waves with k_{m+} [i.e., taking "+" sign in (1.14)], the group velocity is westward (the slope is negative on the dispersion curve in Fig. 1.2), while for short Rossby waves with k_{m-} [i.e., taking "−" sign in (1.14)], the group velocity is eastward (the slope is positive).

For long Rossby waves, $k \to 0$, we have

$$\frac{\omega}{k} \approx -\frac{1}{2m+1}, \quad m = 1, 2, \ldots. \tag{1.17}$$

Equation (1.17) indicates that the long Rossby waves are approximately nondispersive. The dimensional westward phase speed is $(2m+1)^{-1}$ times gravity wave speed C_0. Thus, the long Rossby wave speed is at most one-third of the Kelvin wave speed. For example, if $C_0 = 2.5$ ms^{-1} for the first baroclinic mode in the equatorial Pacific Ocean, the $m = 1$ Rossby wave speed is approximately 0.8 ms^{-1}, which corresponds to a time of 6 months to cross the Pacific basin from east to west.

Figure 1.3 depicts geopotential and velocity distributions for $m = 1$ (left panel) and $m = 2$ (right panel) modes for equatorial Rossby waves.

The Rossby waves are characterized by a geostrophic relationship between pressure and wind fields. For the $m = 1$ mode, u and ϕ are symmetric about the equator, while v is antisymmetric. For the $m = 2$ mode, u and ϕ are antisymmetric about the equator, while v is symmetric.

1.1.6 High-Frequency Inertio-Gravity Waves

For the high-frequency wave group, nondimensional frequency of these waves exceeds $1 + 1/\sqrt{2} = 1.71$, or, dimensionally, $\omega_* > 1.71\sqrt{\beta C_0}$. Taking $C_0 = 50$ ms^{-1} for the atmosphere, $\omega_* \geq 5.77 \times 10^{-5}$s^{-1}, or the period $T_* \leq 1.26$ days. Taking

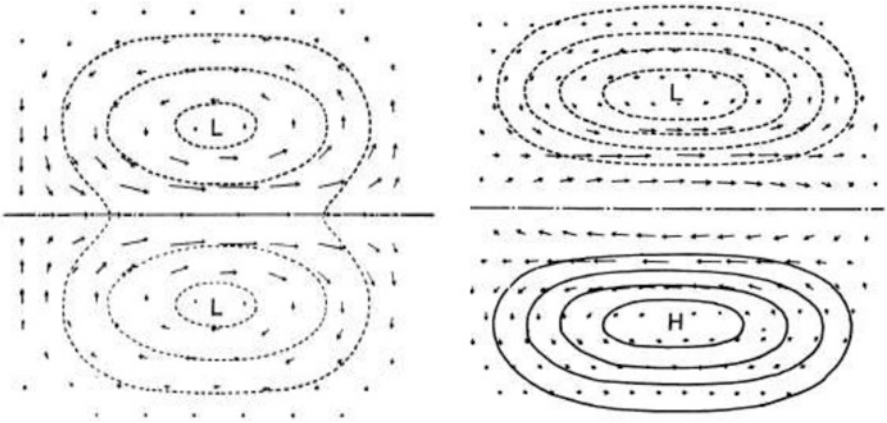

Fig. 1.3 Equatorial Rossby wave [$m = 1$ (left) and $m = 2$ (right)] (From Matsuno (1966). © Copyright 1966, Meteorological Society of Japan (MSJ))

$C_0 = 2.5\ \mathrm{ms}^{-1}$ for the ocean, $\omega_* \geq 1.29 \times 10^{-5}\mathrm{s}^{-1}$ or $T_* \leq 5.63$ days. The higher the meridional index m is, the shorter the period.

For high-frequency waves, $1/2\omega \ll 1$ and $\omega^2 \gg 1/\omega^2$. The dispersion relation may be approximated by

$$k_m = \pm\sqrt{\omega^2 - (2m+1)}$$

or

$$\omega^2 = k_m^2 + (2m+1). \tag{1.18}$$

In dimensional form, Eq. (1.18) becomes

$$\frac{\omega_*}{k_*} = \sqrt{C_0^2 + \frac{\beta C_0 (2m+1)}{k_{*m}^2}}$$

which resembles inertio-gravity wave speed in an f-plane:

$$\frac{\omega_*}{k_*} = \sqrt{C_0^2 + \frac{f^2}{k_*^2 + l_*^2}}$$

where C_0 is the gravity wave speed. Following Matsuno (1966), the high-frequency modes are called equatorial inertio-gravity waves.

Note that ω reaches minima at $\omega = \sqrt{\frac{m+1}{2}} + \sqrt{\frac{m}{2}}$.

For gravity waves with

$$k_{m+} = -\frac{1}{2\omega} + \sqrt{\omega^2 + \frac{1}{4\omega^2} - (2m+1)},$$

the zonal group velocity C_{gx} is eastward (i.e., a positive slope on dispersion curves in Fig. 1.2), whereas for gravity waves with

$$k_{m-} = -\frac{1}{2\omega} - \sqrt{\omega^2 + \frac{1}{4\omega^2} - (2m+1)},$$

the zonal group velocity is westward (i.e., a negative slope).

Figure 1.4 shows the eastward- and westward-propagating inertio-gravity waves for $m = 1$ and $m = 2$ modes. They are essentially ageostrophic and exhibit the nature of inertio-gravity waves. The $m = 1$ mode is trapped more tightly to the equator. The $m = 1$ mode has symmetric structures in ϕ and u but antisymmetric structure in v with respect to the equator. On the other hand, the $m = 2$ mode has an antisymmetric structure in ϕ and u, while v is symmetric about the equator.

1.1.7 Mixed Rossby–Gravity Waves

We now examine the $m = 0$ mode. This is a special mode, which has a distinguished nature from the $m \geq 1$ modes in many aspects.

For $m = 0$, the dispersion equation becomes $\omega^2 - k^2 - k/\omega = 1$, which yields two roots for k:

$$k = \omega - \frac{1}{\omega} \tag{1.19}$$

and

$$k = -\omega.$$

Recall that in deriving Eqs. (1.6a and 1.6b), we assume that $\omega^2 \neq k^2$. Hence, the second root should be rejected.

For the $m = 0$ mode, we have

$$V_0(y) = \mathrm{e}^{-y^2/2}, \quad \frac{dV_0}{dy} = \frac{1}{2}V_1, \quad yV_0 = \frac{1}{2}V_1;$$

thus Eqs. (1.6a and 1.6b) give

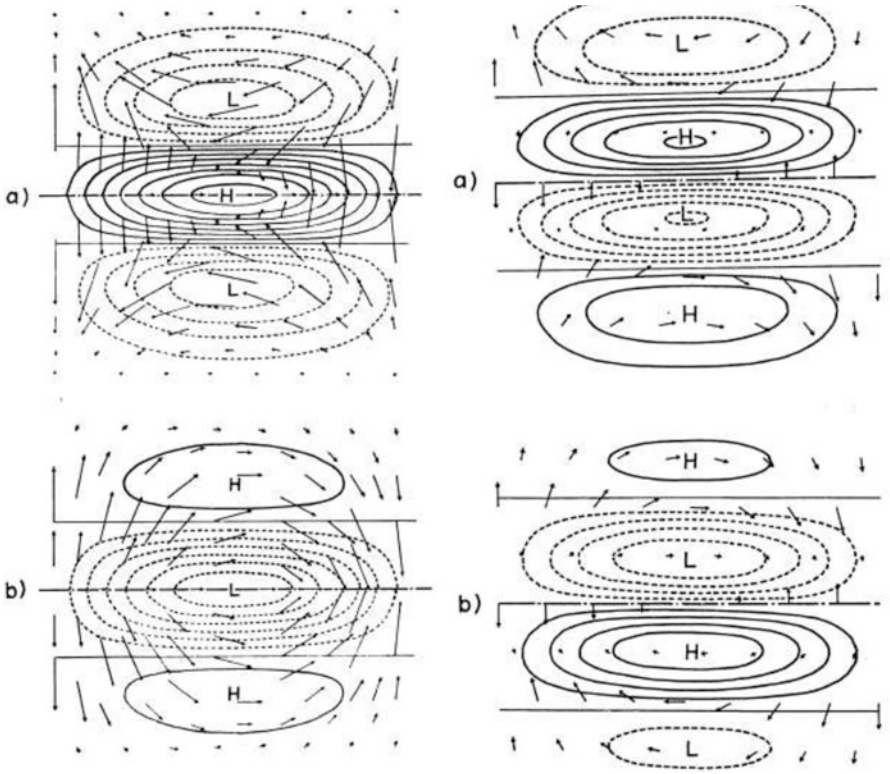

Fig. 1.4 Pressure and velocity distribution of inertio-gravity waves for $m = 1$ (*left panel*) and $m = 2$ (*right panel*). (**a**) Eastward propagating; (**b**) westward propagating (From Matsuno (1966). © Copyright 1966, Meteorological Society of Japan (MSJ))

$$U = \Phi = \frac{i\omega V_1}{2}.$$

Therefore,

$$v_0' = \mathrm{Re}\ \mathrm{e}^{-y^2/2}\mathrm{e}^{i(kx-\omega t)},$$
$$u_0' = \phi_0 = \mathrm{Re}\ i\omega V_1(y)\mathrm{e}^{i(kx-\omega t)}.$$

With $k = \omega - 1/\omega$, the solution becomes

$$v_0' = \mathrm{Re}\ \mathrm{e}^{-y^2/2}\mathrm{e}^{i[(\omega-1/\omega)x-\omega t]},$$
$$u_0' = \varphi_0' = \mathrm{Re}\ i\omega\mathrm{e}^{-y^2/2}y\mathrm{e}^{i[(\omega-1/\omega)x-\omega t]}.$$

The dispersion relation of Eq. (1.19) for mixed Rossby–gravity waves is described by the curve $m = 0$ in Fig. 1.2. Note that for large ω, one has $k = \omega$,

which is the asymptotic limit of high wave number gravity waves. On the other hand, for small ω, one has $k = -1/\omega$, which is the high wave number limit of the Rossby waves. For this reason, this particular $m = 0$ mode is called "mixed Rossby–gravity waves (MRG)" or "Yanai waves." This mixed mode is unique in the equatorial region.

The crossover point, $\omega = 1$, corresponds to a dimensional period $T^* = 2\pi/\sqrt{\beta C_0}$, which is about 9.6 days for $C_0 = 2.5$ ms^{-1} in the ocean and about 2.1 days for $C_0 = 50$ ms^{-1} in the atmosphere. The MRG waves with shorter periods ($k > 0$) propagate eastward, while the MRG waves with periods longer than T_* ($k < 0$) propagate westward.

The group velocity for the MRG waves, however, is always eastward, because

$$\frac{\partial \omega}{\partial k} = \frac{\omega^2}{\omega^2 + 1} > 0$$

for all ω.

Figure 1.5 shows the horizontal distribution of velocity and pressure characteristics of a westward- and an eastward-moving mixed Rossby–gravity wave (Matsuno, 1966). The westward-propagating MRG waves, characterized by clockwise or anticlockwise flow near the equator, may trigger the development of northwest-southeast-oriented synoptic-scale wave train and tropical cyclones in the WNP. For both the westward and eastward MRG waves, the pressure and zonal velocity are antisymmetric about the equator, while the meridional component v is symmetric.

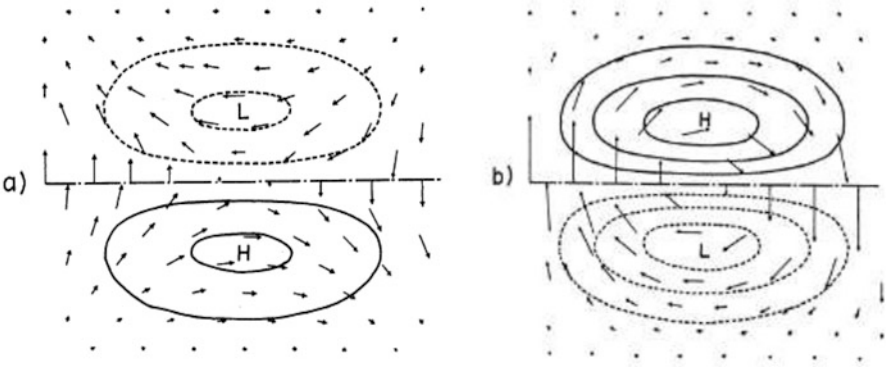

Fig. 1.5 Pressure and velocity distribution of mixed Rossby–gravity waves: (**a**) eastward moving ($k = 0.5$); (**b**) westward moving ($k = -0.5$) (From Matsuno (1966). © Copyright 1966, Meteorological Society of Japan (MSJ))

1.2 Vertical Mode Separation in a Stratified Atmosphere

The shallow water model discussed in Sect. 1.1 involves only independent variables of x, y, and t. What is the vertical structure of these free waves? In this section, it will be demonstrated that in a resting environment, all vertical modes have a similar set of shallow water model equations, with only difference in the gravity wave speed.

Linear primitive equations for adiabatic-stratified atmosphere in a p-coordinate may be written as:

$$\begin{cases} u_t{}' - fv' = -\phi_x{}' \\ v_t{}' + fu' = -\phi_y{}' \\ u_x{}' + u_y{}' + \omega_p{}' = 0 \\ \phi_{pt}{}' + \sigma\omega' = 0 \end{cases}, \tag{1.20}$$

where static stability parameter $\sigma \equiv \frac{R}{p}\frac{1}{\rho g}(\gamma_d - \gamma) = \frac{N^2}{\rho^2 g^2} = \frac{C_\alpha^2}{p^2}, C_\alpha^2 = \frac{R^2}{g}(\gamma_d - \gamma)\bar{T}$.

Consider a continuous atmosphere with vertical velocity vanishing at top and bottom of the troposphere. Assume $C_\alpha = $ const. Thus, static stability parameter, $\sigma = C_\alpha^2/p^2$, increases with height (or decreases with pressure).

Because statistic stability parameter σ changes with p only, Eq. (1.20) may have the following form of solutions:

$$\begin{cases} (u', v', \phi') = [u(x,y,t), v(x,y,t), \phi(x,y,t)]\dfrac{dw}{dp} \\ \omega' = \omega(x,y,t) \cdot w(p) \end{cases}.$$

In the above solution, w represents normalized vertical profile for vertical p-velocity. Substituting the above solutions into Eq. (1.20), one may derive two sets of equations:

$$\begin{cases} u_t - fv = -\phi_x \\ v_t + fu = -\phi_y \\ u_x + u_y = -\omega \end{cases}, \tag{1.21}$$

$$\phi_t \frac{d^2 w}{dp^2} + C_\alpha^2 \omega \frac{w}{p^2} = 0. \tag{1.22}$$

Equation (1.22) may be transformed to

$$\frac{\frac{d^2 w}{dp^2}}{\frac{w}{p^2}} = -\frac{C_\alpha^2 \omega}{\phi_t} = -\frac{C_\alpha^2}{C^2}, \tag{1.23}$$

where C is a constant.

From Eq. (1.23), we have

$$\begin{cases} \dfrac{d^2w}{dp^2} + \dfrac{C_\alpha^2 w}{C^2 p^2} = 0, & (1.24a) \\ \phi_t + C^2\omega = 0. & (1.24b) \end{cases}$$

Equation (1.24a) has the following solution:

$$w(p) = C_1 p^{\frac{1}{2}+b} + C_2 p^{\frac{1}{2}-b}, \quad \text{where} \quad b = \left(\frac{1}{4} - \frac{C_\alpha^2}{C^2}\right)^{\frac{1}{2}}.$$

Applying boundary conditions $\omega = 0$ at surface $p = p_s = 1000$ hPa and at the tropopause $p = p_u = 100$ hPa, we have

$$\begin{cases} C_1\, p_u^{\frac{1}{2}+b} = -C_2\, p_u^{\frac{1}{2}-b} \Rightarrow C_2 = -C_1 {p_u}^{2b} \\ C_1\, p_s^{\frac{1}{2}+b} = -C_2\, p_s^{\frac{1}{2}-b} \Rightarrow {p_s}^{2b} = {p_u}^{2b} \Rightarrow \left(\frac{p_u}{p_s}\right)^{2b} + = 1 \end{cases}$$

$$p^x = \mathrm{e}^{\ln p^x} = \mathrm{e}^{x \ln p} = 1$$

$$x \ln p = i2m\pi, m = 0, 1, 2, \ldots$$

$$\therefore b = i\frac{m\pi}{\ln\left(\dfrac{p_s}{p_u}\right)}, \quad m = \emptyset, 1, 2, \ldots \left(b \neq 0, \text{otherwise } w_{(p)} \equiv 0\right)$$

Therefore, we have

$$C_m = C_\alpha \left(\frac{1}{4} + \frac{m^2\pi^2}{\left(\ln \frac{p_s}{p_u}\right)^2}\right)^{-\frac{1}{2}}, \quad m = 1, 2, 3, \ldots$$

For a given realistic value of stratification in the atmosphere,

$$C_\alpha = \sqrt{\sigma_s p_s} = \sqrt{0.58 \times 10^{-2}\ \mathrm{m^2 s^{-2}\ mb^{-2}} \cdot 1000^2\ \mathrm{mb^2}} = 76\ \mathrm{m/s}.$$

Thus, the gravity wave speeds (C_m) of the first four vertical modes have the following values:

$$\begin{cases} C_1 = 50\ \mathrm{m/s} & \text{First baroclinic mode} \\ C_2 = 26.2\ \mathrm{m/s} & \text{Second baroclinic mode} \\ C_3 = 17.6\ \mathrm{m/s} & \text{Third baroclinic mode} \\ C_4 = 13.3\ \mathrm{m/s} & \text{Fourth baroclinic mode} \end{cases}$$

Substitute Eq. (1.24b) into Eq. (1.21). For each vertical mode, the zonal and meridional wind and geopotential fields satisfy the following shallow water model equations with C_m denoting the gravity wave speed for mth vertical mode:

$$\begin{cases} u_t - fv = -\phi_x \\ v_t + fu = -\phi_y \\ \phi_t + C_m^2(u_x + v_y) = 0. \end{cases}$$

1.3 The Gill Model

In the previous section, the free wave solutions in the tropics are derived. Now we examine how tropical waves and circulation respond to a specified heating. Gill (1980) considered a linear shallow water model system with the first baroclinic mode vertical structure. By considering a slightly different characteristic length scale $L = \sqrt{2C_0/\beta}$, nondimensional shallow water model equations may be written as:

$$\begin{cases} \dfrac{\partial u}{\partial t} - \dfrac{1}{2}yv = -\dfrac{\partial p}{\partial x} \\ \dfrac{\partial v}{\partial t} + \dfrac{1}{2}yu = -\dfrac{\partial p}{\partial y} \\ \dfrac{\partial p}{\partial t} + \dfrac{\partial u}{\partial x} + \dfrac{\partial v}{\partial y} = -Q \\ w = \dfrac{\partial p}{\partial t} + Q \end{cases},$$

where u, v, and p represent nondimensional low-level zonal wind, meridional wind, and geopotential height (or pressure) fields, and w and Q denote nondimensional mid-level vertical velocity and diabatic heating fields.

For seeking a steady state solution, one may substitute all time derivative terms with linear Rayleigh friction or Newtonian damping terms:

$$\begin{cases} \varepsilon u - \dfrac{1}{2}yv = -\dfrac{\partial p}{\partial x} \\ \varepsilon v + \dfrac{1}{2}yu = -\dfrac{\partial p}{\partial y} \\ \varepsilon p + \dfrac{\partial u}{\partial x} + \dfrac{\partial v}{\partial y} = -Q \\ w = \varepsilon p + Q \end{cases},$$

where ε is a constant damping coefficient.

Consider two special cases with a specified equatorially symmetric and anti-symmetric heating profile, respectively. In Case I, the heating is symmetric about the equator and has the form of

$$Q(x,y) = F(x)\exp\left(-\frac{1}{4}y^2\right).$$

In Case II, the heating is antisymmetric about the equator with the form of

$$Q(x,y) = F(x)y\exp\left(-\frac{1}{4}y^2\right).$$

The zonal extent of the forcing is assumed to be localized and have the form

$$F(x) = \begin{cases} \cos kx & |x| < L \\ 0 & |x| > L \end{cases},$$

where $k = \pi/2L$.

After some mathematical transformation, Gill (1980) derived the following analytical solutions for the linear system.

For Case I with specified symmetric forcing, there are two parts of the response. The first part has the form of

$$\left.\begin{array}{ll} (\varepsilon^2 + k^2)q_0 = 0 & \text{for } x < -L \\ (\varepsilon^2 + k^2)q_0 = -\varepsilon\cos kx - k[\sin\ kx + \exp\{-\varepsilon(L+x)\}] & \text{for } |x| < L \\ (\varepsilon^2 + k^2)q_0 = -k\{1 + \exp(-2\varepsilon L)\}\exp\{\varepsilon(L-x)\} & \text{for } x > L \end{array}\right\}$$

$$\left.\begin{array}{l} u = p = \dfrac{1}{2}q_0(x)\exp\left(-\dfrac{1}{4}y^2\right) \\ v = 0 \\ w = \dfrac{1}{2}\{\varepsilon q_0(x) + F(x)\}\exp\left(-\dfrac{1}{4}y^2\right) \end{array}\right\}.$$

This part of response is located at and to the east of the forcing, reflecting the atmospheric Kelvin wave nature.

The second part of the response has the form of

$$\left.\begin{array}{ll} \left\{(2n+1)^2\varepsilon^2 + k^2\right\}q_{n+1} = -k[1 + \exp\{-2(2n+1)\varepsilon L\}]\exp\{(2n+1)\varepsilon(x+L)\} & \text{for} x < -L \\ \left\{(2n+1)^2\varepsilon^2 + k^2\right\}q_{n+1} = -(2n+1)\varepsilon\cos kx + k[\sin kx - \exp\{(2n+1)\varepsilon(x-L)\}] & \text{for} |x| < L \\ \left\{(2n+1)^2\varepsilon^2 + k^2\right\}q_{n+1} = 0 & \text{for} x > L \end{array}\right\}$$

$$\left.\begin{aligned} p &= \frac{1}{2}q_2(x)\left(1+y^2\right)\exp\left(-\frac{1}{4}y^2\right) \\ u &= \frac{1}{2}q_2(x)\left(y^2-3\right)\exp\left(-\frac{1}{4}y^2\right) \\ v &= \{F(x)+4\varepsilon q_2(x)\}y\exp\left(-\frac{1}{4}y^2\right) \\ w &= \frac{1}{2}\left\{F(x)+\varepsilon q_2(x)\left(1+y^2\right)\right\}\exp\left(-\frac{1}{4}y^2\right) \end{aligned}\right\}$$

This second part of response is located at and to the west of the forcing, reflecting the atmospheric Rossby wave nature.

Figure 1.6 shows the zonal wind, meridional wind, and pressure fields in response to the equatorially symmetric heating. The following features are worth noting. Firstly, although the forcing is confined in a localized region, the response is far beyond the forcing region, as waves carry the forcing signal away from the region. Secondly, due to natural dissipation, maximum responses are confined near the forcing region, and the amplitude of the responses becomes weaker as waves move away from the forcing region. Thirdly, the horizontal length of the response to the east is about three times as large as that to the west, due to fact that the equatorial Kelvin wave speed is about three times as large as that of the equatorial Rossby waves. Fourthly, the meridional scale of the response is determined by a characteristic length scale, the equatorial Rossby radius of deformation.

For Case II with specified antisymmetric forcing, there is the following response solution:

$$\left.\begin{aligned} p &= \frac{1}{2}q_3(x)y^3\exp\left(-\frac{1}{4}y^2\right) \\ u &= \frac{1}{2}q_3(x)\left(y^3-6y\right)\exp\left(-\frac{1}{4}y^2\right) \\ v &= \left\{6\varepsilon q_3(x)(y^2-1)+F(x)y^2\right\}\exp\left(-\frac{1}{4}y^2\right) \\ w &= \left\{\frac{1}{2}\varepsilon q_3(x)y^3+F(x)y\right\}\exp\left(-\frac{1}{4}y^2\right) \end{aligned}\right\}$$

Figure 1.7 shows the zonal wind, meridional wind, and pressure fields in response to the equatorially antisymmetric heating. In contrast to Case I, there is no equatorially symmetric response to the antisymmetric forcing. For example, to the east of the forcing region, apparently there is no equatorial Kelvin wave response signal. A monsoonal type of circulation response is seen, with pronounced cross-equatorial flow and antisymmetric pressure fields.

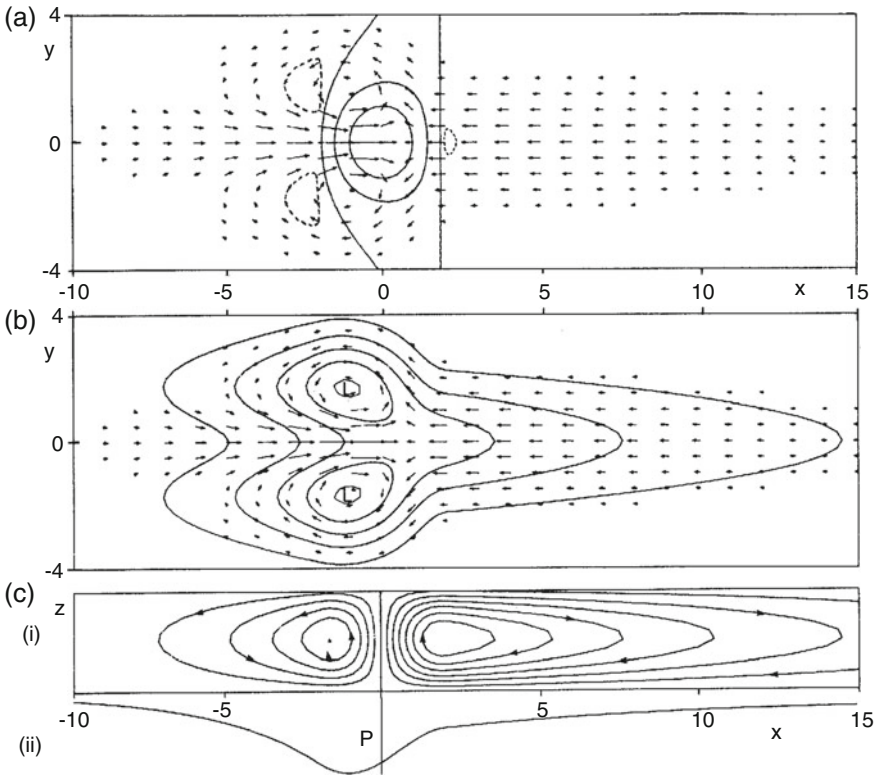

Fig. 1.6 Solutions for heating symmetric about the equator in the region $|x| < 2$ for decay factor $\varepsilon = 0.1$. (**a**) Contours of vertical velocity w (solid contours are 0, 0.3, and 0.6; broken contour is -0.1) superimposed on the velocity field for the lower layer. The field is dominated by the upward motion in the heating region where it has approximately the same shape as the heating function. Elsewhere, there is subsidence with the same pattern as the pressure field. (**b**) Contours of perturbation pressure p (contour interval 0.3) which is everywhere negative. There is a trough at the equator in the easterly regime to the east of the forcing region. On the other hand, the pressure in the westerlies to the west of the forcing region, though depressed, is high relative to its value off the equator. Two cyclones are found on the northwest and southwest flanks of the forcing region. (**c**) The meridionally integrated flow showing (*i*) stream function contours and (*ii*) perturbation pressure. Note the rising motion in the heating region (where there is a trough) and subsidence elsewhere. The circulation in the right-hand (Walker) cell is five times that in each of the Hadley cells shown in (**c**) (From Gill (1980). Copyright © 1980 Royal Meteorological Society)

A further solution with a combined symmetric and antisymmetric heating field is shown in Fig. 1.8. Due to the presence of both the symmetric and antisymmetric forcing fields, both the Kelvin wave response and the symmetric and antisymmetric Rossby wave responses occur. Such the combined forcing is often seen in observations.

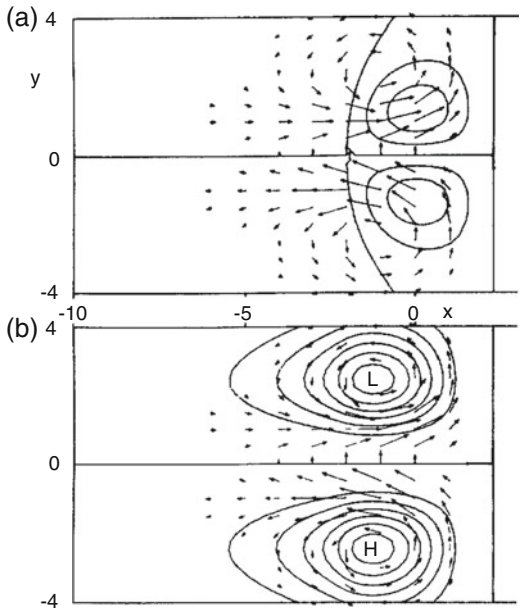

Fig. 1.7 Solutions for heating antisymmetric about the equator in the region $|x| < 2$ for decay factor $\varepsilon = 0.1$. (**a**) Contours of vertical velocity w (contour interval 0.3) superimposed on the velocity field for the lower layer. The field is dominated by the motion in the heating region where it is approximately the same shape as the heating function (positive in the northern hemisphere). Outside the forcing region, the pattern is the same as for the pressure field with subsidence in the northern hemisphere and weak upward motion in the southern hemisphere. There is no motion for $x > 2$. (**b**) Contours of perturbation pressure p (contour interval 0.3) which is positive in the south (where there is an anticyclone) and negative north of the equator (where there is a cyclone). The flow has the expected sense of rotation around the pressure centers and flows down the pressure gradient where it crosses the equator. All fields are zero for $x > 2$ (From Gill (1980). Copyright © 1980 Royal Meteorological Society)

1.4 The Lindzen–Nigam Model

In addition to being forced by heating in middle troposphere, low-level winds may be directly driven by pressure gradient in the planetary boundary layer (PBL) pressure gradient. Lindzen and Nigam (1987) related this PBL pressure gradient to sea surface temperature (SST) gradient.

Assume low-tropospheric temperature has a formula of

$$T(\lambda, \theta, z) = \bar{T}_s - \alpha z + T'_s \left(1 - \frac{\gamma Z}{H_0}\right),$$

where α is the lapse rate of zonal mean atmosphere in a given region, γ represents how fast the perturbation temperature decays with height, and such a vertical profile is based on the fact that the tropical perturbation temperature pattern in the lower

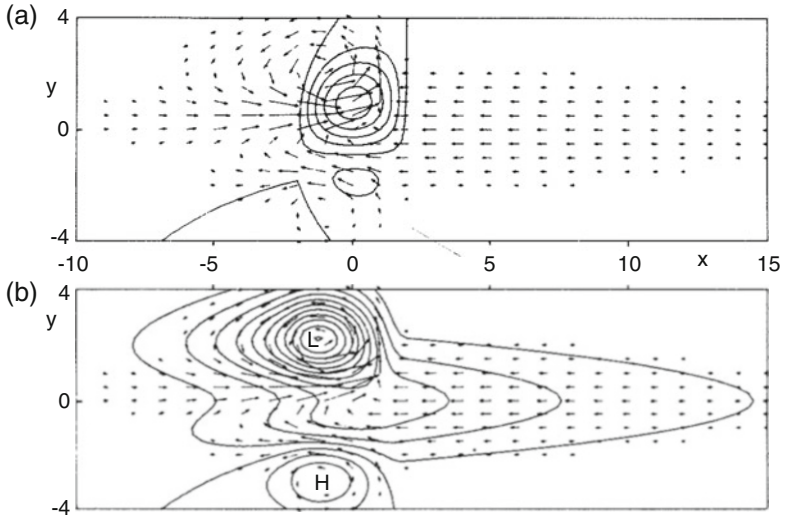

Fig. 1.8 Solution obtained by adding the solutions shown in the two previous figures, corresponding to heating which is confined to the region $|x| < 2$ and is mainly concentrated to the north of the equator. (**a**) Contours of vertical velocity w (contour interval 0.3) showing the dominance of the heating north of the equator. The flow to the east of the forcing region is the same as in Fig. 1.6, this being provided entirely by the symmetric part of the heating. West of the forcing, the westerly inflow is concentrated between the equator and $y = 2$. An easterly flow is found south of the equator. (**b**) Contours of perturbation pressure p (contour interval 0.3). The pattern is dominated by a low on the western flank of the heating region and by the equatorial trough. A high is found in the southern hemisphere (From Gill (1980). Copyright © 1980 Royal Meteorological Society)

troposphere resembles that of SST, with a decreased amplitude with height (Fig. 1.9).

Given the temperature field above, air density may be directly derived from the equation of state:

$$\rho = \rho_0[1 - n(T - T_0)],$$

where

$$\rho_0 = \rho(T_0) = 1.225 \text{ kg m}^{-3}, \quad T_0 = 288 \text{ K},$$
$$n = -\left[\frac{1}{\rho}\frac{\partial \rho}{\partial T}\right]_{T_0} = \frac{1}{T_0}.$$

Thus, we have

$$\rho = \rho_0[2 - nT].$$

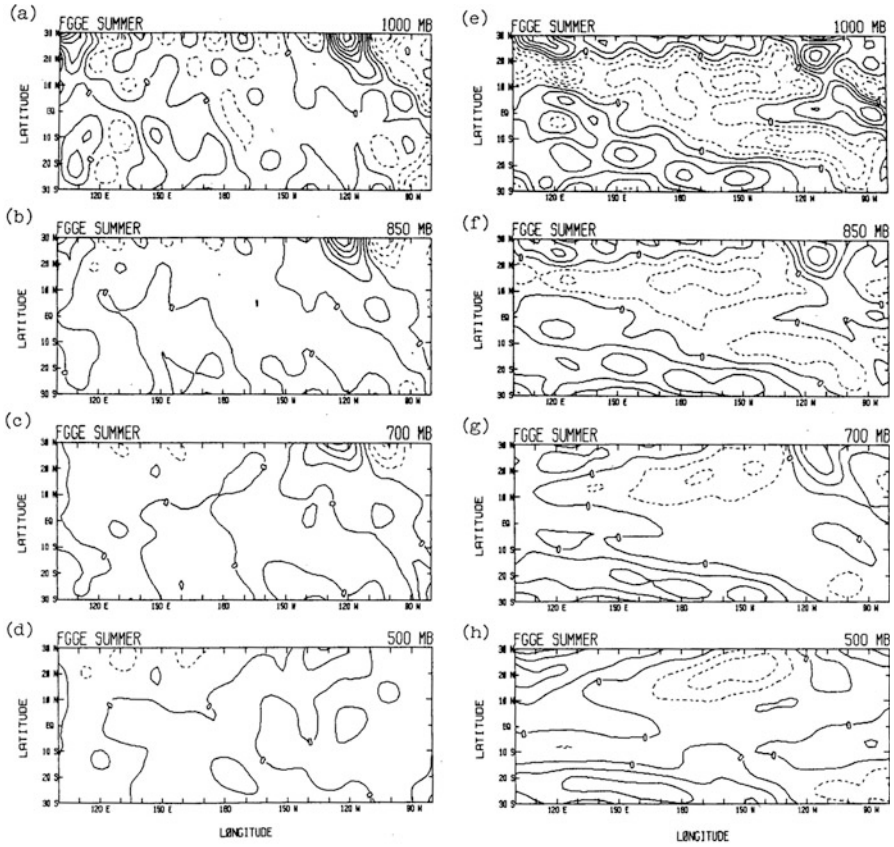

Fig. 1.9 The horizontal gradients in the ECMWF-analyzed eddy virtual temperature field are shown at four pressure levels over the Pacific basin during the FGGE summer zonal gradients in parts (**a**)–(**b**) and meridional gradients in parts (**e**)–(**h**), The contour interval is 10^{-6} K m^{-1}(or 1 K/1000 km), negative values are contoured using dashed lines, and the first solid contour is the zero contour (From Lindzen and Nigam (1987). © Copyright 1987 American Meteorological Society (AMS))

Integrating the hydrostatic equation from surface to the height at top of PBL, we have

$$p = (\lambda, \theta, Z) = p_T + g\rho_0(2 - nT_s)(Z_T - Z) + \frac{g\rho_0 n}{2}(\alpha + \gamma T_s')\left(Z_T^2 - Z^2\right),$$

where p_T denotes the pressure at top of PBL, $T_s = \overline{T_s} + T_s'$.

For a steady PBL flow, Coriolis force and pressure gradient force are approximately balanced by friction. Thus we have

$$\begin{cases} -fv = \dfrac{1}{\rho a \cos\,\theta}\dfrac{\partial p}{\partial \lambda} + \dfrac{1}{\rho}\dfrac{\partial \tau_x}{\partial z} \\ fu = -\dfrac{1}{\rho a}\dfrac{\partial p}{\partial \theta} + \dfrac{1}{\rho}\dfrac{\partial \tau_y}{\partial z} \end{cases},$$

where:

λ, θ the longitude and latitude, respectively
a ($=6.371 \times 10^6 m$) the radius of the earth
f ($2\Omega \sin\,\theta$) the variable Coriolis parameter
Ω ($=7.272 \times 10^{-5} s^{-1}$) the earth's angular velocity
u, v the zonal and meridional components of velocity, respectively
ρ [$=\rho(\lambda, \theta, z)$] the density
p [$=p(\lambda, \theta, z)$] the pressure
τ_x, τ_y the zonal and meridional and components, respectively, of the vertical turbulent stress

Integrating the above momentum equations from z = 0 to z = Z_T, we have

$$\begin{cases} -fV = -\dfrac{g}{a\cos\,\theta}\left[-Q\dfrac{dT_s{}'}{d\lambda}\right] + \dfrac{\tau_{x|z_T} - \tau_{y|0}}{\rho_0 Z_T} \\ fU = -\dfrac{g}{a}\left[-Q\dfrac{dT_s{}'}{d\theta} - \dfrac{nZ}{d\theta}\right] + \dfrac{\tau_{y|Z_T} - \tau_{y|0}}{\rho_0 Z_T} \end{cases},$$

where

$$Q = \left(\frac{nZ_T}{2}\right)\left[1 - \frac{2\gamma Z_T}{3H_0}\right],$$

$$(U, V) = \left[\frac{1}{\rho_0 Z_T}\right]\int_0^{Z_T} (u, v)\rho dz,$$

$$\left(\tau_x, {}^x\tau_y\right) |= -\rho_0 C_d \left(U^2 + V^2\right)^{1/2} (U, V).$$

By assuming a linear surface wind stress formula and a free surface at top of PBL that is used to adjust boundary layer divergence, Lindzen and Nigam (1987) derived the following PBL momentum equations in response to SST gradient-induced pressure gradient force:

$$\begin{cases} -fV' = -\dfrac{g}{a\cos\theta}\left[(2-n\bar{T}_s+n\alpha H_0)\dfrac{\partial h'}{\partial\lambda}-\dfrac{nH_0}{2}\left(1-\dfrac{2\gamma}{3}\right)\dfrac{\partial T_s{}'}{\partial\lambda}\right]-eU' \\ fV' = -\dfrac{g}{a}\left[(2-n\overline{T_s}+n\alpha H_0)\dfrac{\partial h'}{\partial\theta}-\dfrac{nH_0}{2}\left(1-\dfrac{2\gamma}{3}\right)\dfrac{\partial T_s{}'}{\partial\theta}-\dfrac{nh'}{2}\dfrac{\partial\overline{T_s{}'}}{\partial\theta}\right]-eV'. \\ h' = \tau_c\dfrac{H_0}{a\cos\theta}\left[\dfrac{\partial U'}{\partial\lambda}+\dfrac{\partial(V'\cos\theta)}{\partial\theta}\right] \end{cases}$$

Figure 1.10 shows the atmospheric PBL circulation response to a specified 1000 hPa virtual temperature forcing in boreal summer derived from the ECMWF FGGE analyses. The pronounced trade winds and the South Pacific convergence zone are well simulated. The overall low-level circulation features agree well with the observation. It is worth mentioning that the divergence field near the equator is very sensitive to the cumulus adjustment timescale, τ_c. Therefore, a proper value of τ_c (~30 min) is needed to simulate a realistic divergence field.

In a Cartesian coordinate, the Lindzen–Nigam model may be written as (see Wang and Li 1993):

$$\begin{cases} Eu - fv = -\left(\dfrac{\partial\phi}{\partial x}-A\dfrac{\partial T}{\partial x}\right) & (1.25a) \\ Ev + fu = -\left(\dfrac{\partial\phi}{\partial y}-A\dfrac{\partial T}{\partial y}\right) & (1.25b) \\ \phi + B\left(\dfrac{\partial u}{\partial x}+\dfrac{\partial v}{\partial y}\right) = 0 & (1.25c) \end{cases}$$

where u and v represent the zonal and meridional component of the surface wind, ϕ is the geopotential at the top of the boundary layer, T is the sea surface temperature (SST), and E is a damping coefficient. $A = gH_0/2T_0$ and $B = gH_0/\mu$ measure the strength of the pressure gradient force induced by the SST gradient and the strength of the "back pressure" effect; H_0 is the depth of the boundary layer; T_0 is a reference temperature; μ is an inverse relaxation time for the adjustment of the boundary layer height.

The linear equations of the Lindzen–Nigam model above (Eqs. 1.25a, 1.25b, and 1.25c) are mathematically identical to the Gill model, if one assumes that the heating in mid-troposphere is proportional to SST. Let $\Phi = \phi - AT, \varepsilon = E, \dot{Q} = \mu AT$, and $gH_0 = c_0^2$. Substituting these variables into Eqs. (1.20a–c), one may have

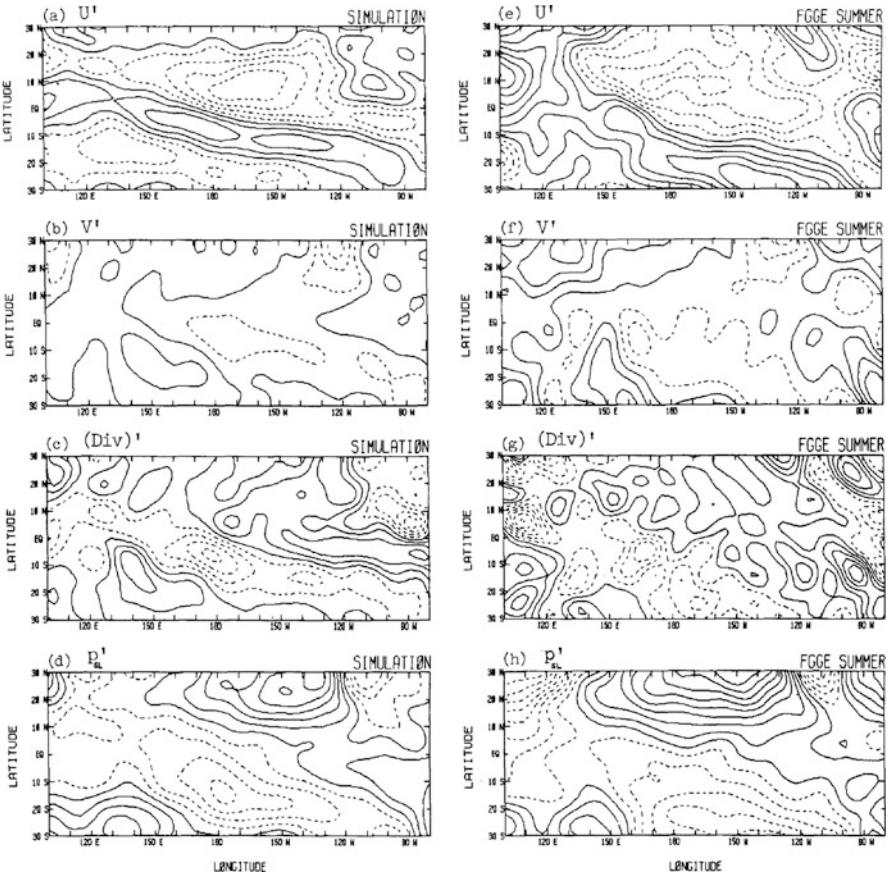

Fig. 1.10 The low-level summertime flow over the Pacific obtained from the linear model in which the boundary layer height is allowed to adjust to the horizontal convergence; $\varepsilon = (2.5 \text{ days})^{-1}$, $\tau_c =$ 30 min, and $H_0 = 3000$ m. The model solutions are shown in the left panel, whereas the corresponding fields from the ECMWF analysis are shown in the right panel. From top to bottom: Perturbations of zonal wind, meridional wind, divergence, and sea level pressure. The contour interval is as follows: U' and $V' = 1 \text{ ms}^{-1}$, $\text{div} = 4 \times 10^{-7} \text{ s}^{-1}$, and $P'_{SL} = 1\text{mb}$; negative values are contoured using dashed lines, and the first solid contour is the zero contour (From Lindzen and Nigam (1987). © Copyright 1987 American Meteorological Society (AMS))

$$\begin{cases} \varepsilon u - fv = -\dfrac{\partial \Phi}{\partial x} & (1.26a) \\ \varepsilon v + fu = -\dfrac{\partial \Phi}{\partial y} & (1.26b) \\ \mu \Phi + c_0^2 \left(\dfrac{\partial u}{\partial x} + \dfrac{\partial v}{\partial y} \right) = -\dot{Q} & (1.26c) \end{cases}$$

The equations above have the form of the Gill model, describing the low-level wind and geopotential height response to a prescribed mid-tropospheric heating.

1.5 The Cane–Zebiak Simple Coupled Atmosphere–Ocean Model

The first coupled atmosphere–ocean model that was able to simulate the ENSO-like variability is the Cane–Zebiak model (Cane et al. 1986; Zebiak and Cane 1987). The governing equations for the atmosphere are a Gill type model with a heating anomaly proportional to mean and perturbation SST (see Zebiak 1986):

$$\begin{cases} +\varepsilon u_a^n - \beta_0 y v_a^n = -(p^n/\rho_0)_x \\ \varepsilon v_a^n + \beta_0 y u_a^n = -(p^n/\rho_0)_y \\ \varepsilon(p^n/\rho_0) + c_a^2\left[(u_a^n)_x + (v_a^n)_y\right] = -\dot{Q}_s - \dot{Q}_1^{n-1} \end{cases}$$

where

$$\dot{Q}_S = (\alpha T)\exp[(\bar{T} - 30^\circ\mathrm{C})/16.7^\circ\mathrm{C}],$$
$$Q_1^n = \beta[M(\bar{c} + c^n) - M(\bar{c})],$$

and

$$M(x) = \begin{cases} 0, & x \le 0 \\ x, & x > 0 \end{cases}.$$

In the above equations, $\bar{T}$ is prescribed monthly mean SST, T is anomalous SST, $\bar{c}$ is prescribed monthly mean surface wind convergence, and c^n is the anomalous convergence at iteration n, defined by

$$c^n \equiv -(u_a^n)_x - (v_a^n)_y.$$

The governing equations for the ocean (see Cane 1984) include reduced gravity upper-ocean momentum equations and continuity equation for ocean thermocline depth (h):

$$u_t - \beta_0 y v = -g' h_x + \tau^{(x)}/\rho H - ru \tag{1.27a}$$
$$\beta_0 y u = -g' h_y + \tau^{(y)}/\rho H - rv \tag{1.27b}$$
$$h_t + H(u_x + v_y) = -rh \tag{1.27c}$$

where H denotes the mean thermocline depth, and

$$\mathbf{u} = H^{-1}(H_1\mathbf{u}_1 + H_2\mathbf{u}_2).$$

The subscripts 1 and 2 refer to the surface layer and underlying layer, respectively.

The equations governing the shear between layers 1 and 2 are

$$r_s u_s - \beta_0 y v_s = \tau^{(x)}/\rho H_1 \tag{1.27d}$$

$$r_s v_s + \beta_0 y u_s = \tau^{(y)}/\rho H_1 \tag{1.27e}$$

where $\mathbf{u}_s \equiv \mathbf{u}_1 - \mathbf{u}_2$.

Equations (1.27a), (1.27b), (1.27c), (1.27d) and (1.27e) allow the surface current $\mathbf{u}_1$ to be determined. For a given constant mixed-layer depth (H_1), the entrainment velocity is calculated:

$$w_s = H_1 \left[(u_1)_x + (v_1)_y \right].$$

The temperature equation for the surface layer is

$$\frac{\partial T}{\partial t} = -\mathbf{u}_1 . \nabla (\bar{T} + T) - \bar{\mathbf{u}}_1 . \nabla T - \left\{ M(\bar{w}_s + w_s) - M\left(\bar{w}\right) \right\} \times \bar{T}_z - M(\bar{w}_s + w_s) \frac{T - T_e}{H_1} - \alpha_s T.$$

where $\bar{\mathbf{u}}_1(x, y, t)$ and $\bar{w}_s(x, y, t)$ are the mean horizontal currents and upwelling, respectively, and $\bar{T}_z(x)$ is the prescribed mean vertical temperature gradient. The entrainment temperature anomaly T_e is defined by

$$T_e = \gamma T_{\text{sub}} + (1 - \gamma) T.$$

T_{sub} has the form

$$T_{\text{sub}} = \begin{cases} T_1 \left\{ \tan h[b_1(\bar{h} + h)] - \tan h\left(b_1 \bar{h}\right) \right\}, h > 0 \\ T_1 \left\{ \tan h[b_1(\bar{h} + h)] - \tan h\left(b_2 \bar{h}\right) \right\}, h < 0, \end{cases}$$

where $\bar{h}(x)$ is the prescribed mean upper layer depth.

Figure 1.11 shows the evolution of model-simulated Nino3 SST anomaly (SSTA). The simple coupled model reproduced an irregular interannual oscillation, with an average period of 3–5 years. Associated with the SST oscillation are the surface wind stress and the ocean thermocline depth anomalies. They all show coherent coupled patterns, indicative of air–sea interaction nature.

Figures 1.12 and 1.13 illustrate SST and surface wind anomaly patterns during a mature phase of an El Niño and a La Niña, respectively. In response to a positive SSTA in the eastern equatorial Pacific, anomalous westerlies appear to the west of the maximum SSTA center (Fig. 1.12). Two anomalous cyclonic gyres appear to the west of the maximum SSTA center, and they are a Rossby wave response to anomalous heating in the equatorial central Pacific. Anomalous easterlies associated with a Kelvin wave response appear to the east of the anomalous heat source. In contrast, divergent low-level flow anomaly occurs when a cold SSTA appears in the equatorial Pacific (Fig. 1.13).

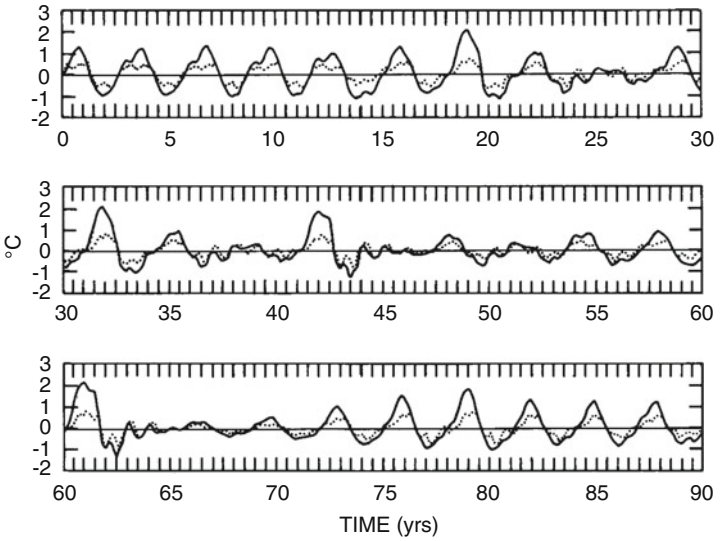

Fig. 1.11 Area-averaged SST anomalies for the 90-year model simulations. The *solid line* is Nino3 (5°N–5°S, 90°–150°W), and the *dotted line* is Nino4 (5°N–5°S, 150°W–160°E) (From Zebiak and Cane (1987). © Copyright 1987 American Meteorological Society (AMS))

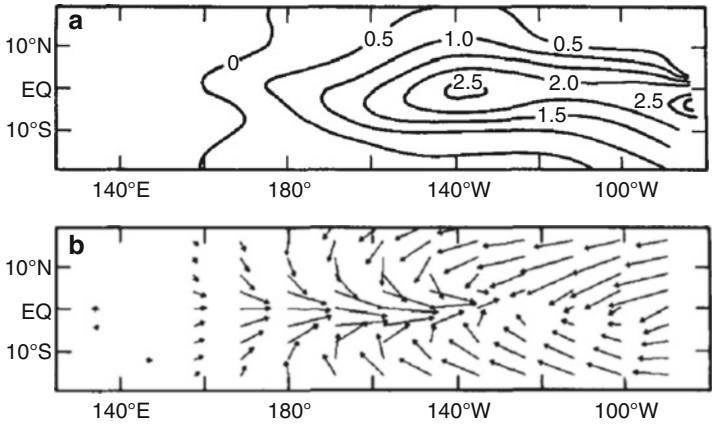

Fig. 1.12 Patterns of simulated SSTA and low-level wind anomaly during a mature phase of model El Niño in December of year 31 (From Zebiak and Cane (1987). © Copyright 1987 American Meteorological Society (AMS))

1.6 A 2.5-Layer Tropical Atmospheric Model

As discussed in the previous sections, the Gill model emphasizes the tropical atmospheric response to mid-tropospheric heating, whereas the Lindzen–Nigam model emphasizes the PBL atmospheric response to SST gradient-induced

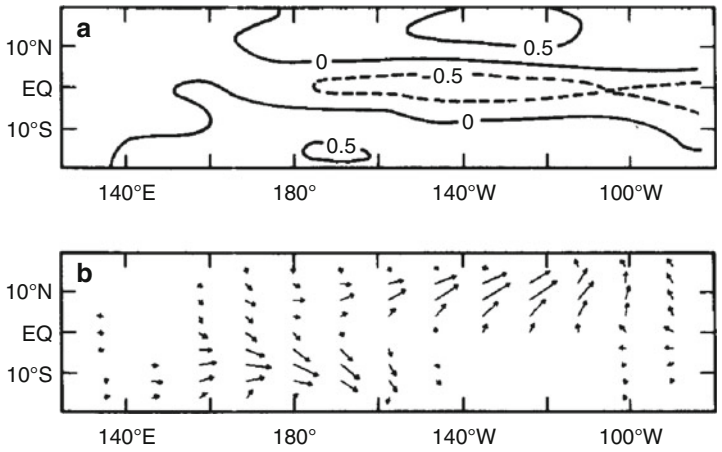

Fig. 1.13 As in Fig. 1.12, except for a La Niña phase in September of year 32 (From Zebiak and Cane (1987). © Copyright 1987 American Meteorological Society (AMS))

momentum forcing. Wang and Li (1993) combined the two models together and formed a 2.5-layer model that considers both the condensational heating in the free atmosphere and boundary layer SST forcing. Figure 1.14 illustrates the model vertical structure.

Considering a linear governing equations in an equatorial beta-plane, momentum, continuity, and thermodynamic equations in the free atmosphere can be written as

$$\frac{\partial \mathbf{V}}{\partial t} + \beta y k \times \mathbf{V} = -\nabla \phi + F_r,$$

$$\nabla \cdot \mathbf{V} + \frac{\partial \omega}{\partial p} = 0,$$

$$\frac{\partial}{\partial t}\left(\frac{\partial \phi}{\partial p}\right) + S(p)\omega = -\frac{R}{C_p p}\left(Q_p + Q_r\right),$$

where $\mathbf{V}$, ϕ, and ω represent horizontal wind vector, geopotential height, and vertical p-velocity, respectively, Q_p and Q_r denote the diabatic heating associated with precipitation and radiation, and S is a static stability parameter. Assume a portion (b) of column-integrated moisture convergence and evaporation is used for precipitation, we have

$$P_r = b\left[E_v - \frac{1}{g}\int_{p_u}^{p_s} \nabla \cdot (\bar{q}\mathbf{V})dp\right].$$

The precipitation is connected to Q_p through the following equation:

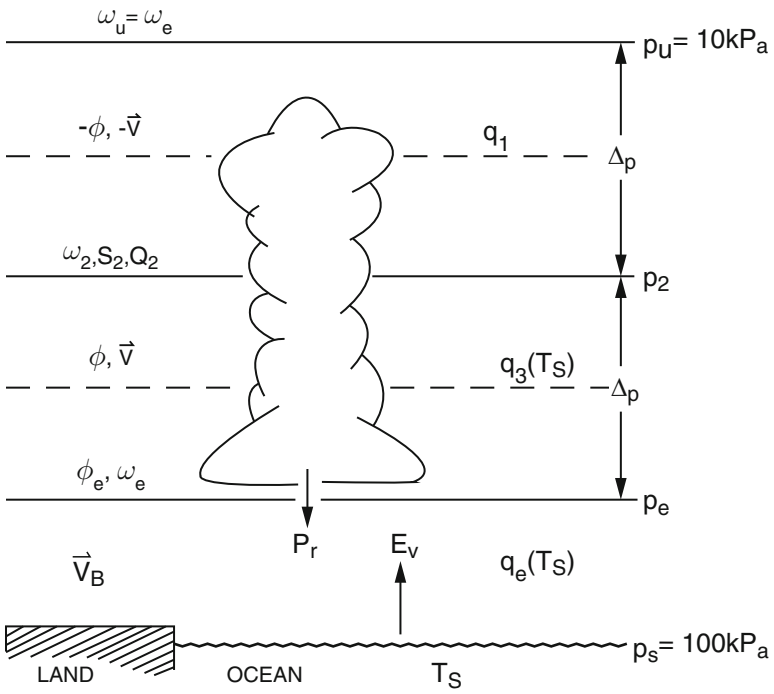

Fig. 1.14 Schematic diagram of the 2.5-layer atmospheric model (From Wang and Li (1993). © Copyright 1993 American Meteorological Society (AMS))

$$L_c P_r = \frac{1}{g}\int_{p_u}^{p_s} Q_p(p)dp.$$

Let vertical p-velocities at top of PBL (p_e) and at top of the troposphere (p_u) be

$$\omega = \omega_e \quad \text{at} \quad p = p_e$$
$$\omega = \omega_u \quad \text{at} \quad p = p_u.$$

Let free-atmospheric barotropic component be

$$\mathbf{V}_+ = \frac{1}{2}(\mathbf{V}_3 + \mathbf{V}_1), \quad \phi_+ = \frac{1}{2}(\phi_3 + \phi_1)$$

and free-atmospheric barotropic component be

$$\mathbf{V}_- = \frac{1}{2}(\mathbf{V}_3 - \mathbf{V}_1), \phi_- = \frac{1}{2}(\phi_3 - \phi_1).$$

Thus, the barotropic mode satisfies

$$\frac{\partial \mathbf{V}_+}{\partial t} + \beta y \widehat{k} \times \mathbf{V}_+ = -\nabla \phi_+ - \varepsilon_* \mathbf{V}_+,$$
$$\nabla \cdot \mathbf{V}_+ + \frac{1}{2\Delta p}(\omega_e - \omega_u) = 0,$$

and the baroclinic mode satisfies

$$\frac{\partial \mathbf{V}_-}{\partial t} + \beta y \widehat{k} \times \mathbf{V}_- = -\nabla \phi_- - \varepsilon_* \mathbf{V}_-,$$
$$\omega_2 = \omega_e + \Delta p \nabla \cdot \mathbf{V}_-,$$
$$\frac{\partial \phi_-}{\partial t} + \frac{s_2 \Delta p}{2}\omega_2 = -\frac{R\Delta p}{2C_p p_2}(Q_{p2} + Q_{r2}).$$

As the tropical tropospheric circulation has a dominant first baroclinic mode vertical structure, for simplicity, one may neglect free-atmospheric barotropic flow component by simply assuming that vertical p-velocity at top of the troposphere equals that at top of PBL (i.e., $\omega_u = \omega_e$). By doing so, the above barotropic and baroclinic component equations are decoupled.

Considering a well-mixed PBL, the boundary layer momentum equation satisfies

$$k \times \beta y \mathbf{V}_B = -\nabla \left[\frac{1}{p_s - p_e} \int_{p_e}^{p_s} \phi dp \right] - \frac{\rho_s g K_D}{p_s - p_e} \mathbf{V}_B, \tag{1.28a}$$
$$\omega_e = (p_s - p_e) \nabla \cdot \mathbf{V}_B, \tag{1.28b}$$

where

$$\mathbf{V}_B \equiv \frac{1}{(p_s - p_e)} \int_{p_e}^{p_s} \mathbf{V} dp.$$

Equation (1.28b) above states that vertical p-velocity at top of PBL is proportional to PBL convergence. Following Lindzen and Nigam (1987), temperature profile in PBL is proportional to SST. The PBL momentum equation above may be derived as

$$k \times \beta y \mathbf{V}_B = -\nabla \phi_e + \frac{R}{2} \frac{(p_s - p_e)}{p_e} \nabla T_s - \frac{\rho_s g K_D}{p_s - p_e} \mathbf{V}_B,$$

where ϕ_e is geopotential at top of PBL, T_s is SST, and K_D is a PBL friction coefficient.Combining the free-atmospheric baroclinic mode governing equations with the PBL momentum equation, one may derive a set of nondimensional governing equations below, with three dependent variables $\mathbf{V}$, ϕ_e, and $\mathbf{V}_B$, representing lower-tropospheric wind vector, lower-tropospheric geopotential height, and PBL wind vector, respectively:

Table 1.1 List of model parameters used in 2.5-layer atmospheric model

Parameter	Definition
$\varepsilon = \frac{\varepsilon^*}{\sqrt{\beta C_0}}$	Rayleigh friction coefficient
$N = \frac{\mu}{\sqrt{\beta C_0}}$	Newtonian cooling coefficient
$I = \frac{RL_c b}{C_p P_2 S_2 \Delta p}(\bar{q}_3 - \bar{q}_1)$	Heating coefficient due to free-troposphere moisture convergence
$B = \frac{RL_c b}{C_p P_2 S_2 \Delta p}\bar{q}_e$	Heating coefficient due to PBL moisture convergence
$G = \frac{\Delta p}{2p_2}\gamma$	Coefficient of longwave radiational forcing
$d = \frac{p_s - p_e}{\Delta p}$	Depth of the boundary layer
$F = \left(\frac{C_0}{\beta}\right)^{1/2} \frac{\rho_s g L_c b}{2C_p p_2} C_E K_q$	Coefficient of evaporation forcing
$A = \frac{p_s - p_e}{2p_e}$	Coefficient of SST gradient forcing
$E = \frac{\rho_s g K_D}{(p_s - p_e)\sqrt{\beta C_0}}$	Ekman number of the boundary layer

$$\frac{\partial}{\partial t}\mathbf{V} + yk \times \mathbf{V} = -\nabla\phi - \varepsilon\mathbf{V},$$

$$\frac{\partial}{\partial t}\phi + N\phi + (1 - \delta I)\nabla \cdot \mathbf{V} = -NG(T_s - \bar{T}_s) + d(\delta B - 1)\nabla \cdot \mathbf{V}_B - \delta F|\mathbf{V}_B|(T_s - T_*),$$

$$-yk \times \mathbf{V}_B = -\nabla\phi + A\nabla T_s - E\mathbf{V}_B,$$

where nondimensional parameters in the above equations have the following formula and physical meanings (see Table 1.1).

A nonlinear heating switch-on coefficient (δ) is specified in various scenarios. In the conditional heating scenario,

$$\delta = \begin{cases} 1, & P_r > 0, \\ 0 & \textbf{\textit{otherwise}} \end{cases}.$$

In the second scenario, the heating also depends on a threshold SST, that is,

$$\delta = \begin{cases} 1, & \text{if } T_s \geq 301\text{ K}, P_r > 0, \\ 0, & \text{otherwise} \end{cases}$$

In the third scenario, a SST-dependent heating coefficient is specified:

$$\delta = \begin{cases} 1, & \textbf{\textit{if}}\ T_s \geq 301.5K, P_r > 0, \\ (T_s - 298.5)/3, & \textbf{\textit{if}}\ 298.5K < T_s < 301.5K, P_r > 0 \\ 0, & \text{otherwise.} \end{cases}$$

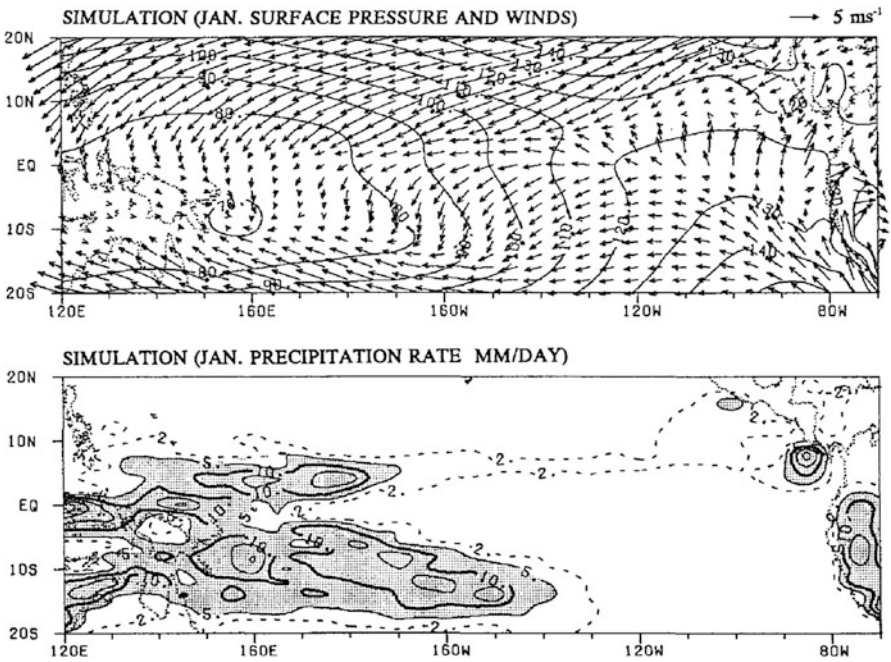

Fig. 1.15 (*Top*) Surface wind (vector) and pressure (unit: 0.1 hPa, a constant pressure of 1000 hPa has been removed) and (*bottom*) precipitation (unit: mm/day) fields simulated by the 2.5-layer atmospheric model with a SST-dependent nonlinear heating scheme (From Wang and Li (1993). © Copyright 1993 American Meteorological Society (AMS))

Given the January mean SST as a forcing field, the model is able to simulate January mean surface wind and precipitation fields, as illustrated in Fig. 1.15.

Schematic diagram Fig. 1.16 illustrates essential physical processes in the model through which SST affects tropical atmospheric circulation. Firstly, SST may directly affect mid-tropospheric diabatic heating processes through condensational heating (nonlinear switch-on heating coefficient), evaporational heating, and longwave radiative heating (Davey and Gill 1987) processes. Secondly, SST may modulate moisture distribution and thus the amplitude of column-integrated moisture convergence. Thirdly, SST can directly drive PBL flow through induced pressure gradient force. A key process in the 2.5-layer model is active interaction of free-atmospheric baroclinic flow and boundary layer flow. On one hand, lower-tropospheric geopotential influences PBL divergence. On the other hand, PBL moisture convergence further influences mid-tropospheric diabatic heating and thus lower-tropospheric wind and geopotential fields.

It is worth mentioning that the 2.5-layer model framework is intended to be used to study not only the mean atmospheric circulation response to SST but also the anomalous atmospheric response to ENSO-like SST forcing. It can be also used to study internal atmospheric modes such as the Madden–Julian Oscillation (MJO), as demonstrated in Chap. 3.

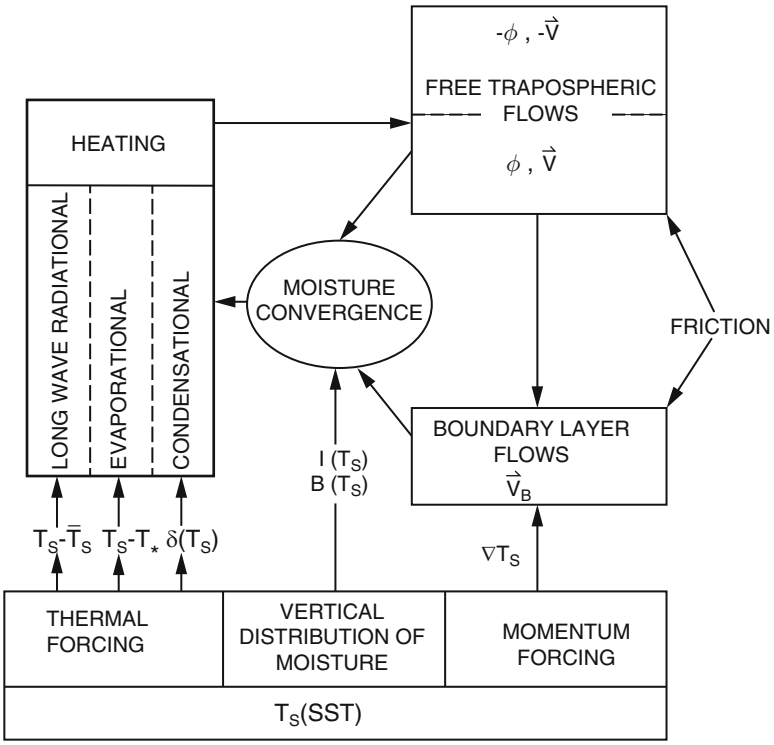

Fig. 1.16 Schematic diagram illustrating essential model physics (From Wang and Li (1993). © Copyright 1993 American Meteorological Society (AMS))

1.7 A 2.5-Layer Tropical Oceanic Model

An important feature of the Cane–Zebiak model is remarkable thermocline displacement in response to ENSO-related wind stress forcing at the equator. However, this model has a rather crude treatment in oceanic mixed-layer processes. To overcome this shortcoming, a 2.5-layer tropical oceanic model was developed by Wang et al. (1995), in which the upper-ocean wave dynamics of the Cane–Zebiak model was coupled with Kraus–Turner (1967) mixed-layer process. Figure 1.17 illustrates the vertical structure of this 2.5-layer ocean model.

The hydrostatic motion in the upper active ocean can be described by reduced gravity, primitive equations for Boussinesq fluid in z coordinates (Schopf and Cane 1983):

$$\frac{\partial P}{\partial z} = b \equiv \alpha g(T - T_r), \tag{1.29a}$$

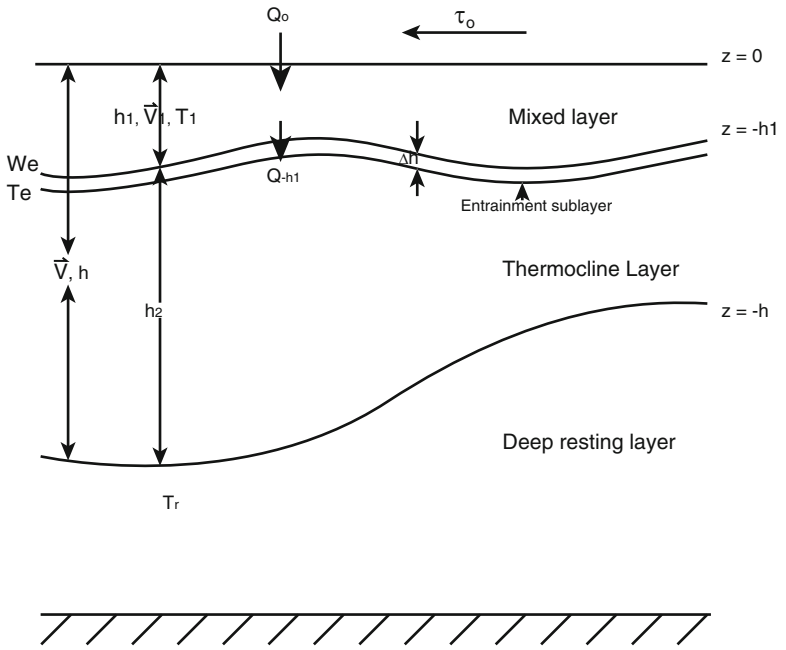

Fig. 1.17 Schematic diagram of the vertical structure of the model ocean. The surface $z = -h_1$ and $z = -h$ represent mixed-layer base and thermocline depth, respectively. Both vary with time and space (From Wang et al. (1995). © Copyright 1995 American Meteorological Society (AMS))

$$\frac{\partial V}{\partial t} + V \cdot \nabla V + w\frac{\partial V}{\partial z} + fk \times V = -\nabla_z P + \frac{1}{\rho_r}\frac{\partial \tau}{\partial z} + \mu \nabla^2 V, \tag{1.29b}$$

$$\nabla_z \cdot V + \frac{\partial w}{\partial z} = 0, \tag{1.29c}$$

$$\frac{\partial T}{\partial t} + V \cdot \nabla T + w\frac{\partial T}{\partial z} = \frac{1}{\rho_r c_w}\frac{\partial Q}{\partial z} + \mu \nabla^2 T, \tag{1.29d}$$

where b is the buoyancy, $\alpha = 2.5 \times 10^{-4\text{o}}\text{C}^{-1}$ is the thermal expansion coefficient of sea water, g is the gravity, f is the Coriolis parameter, $\rho_r = 10^3$ kg m^{-3} is the reference density in the inert layer, $c_w = 4.2 \times 10^7$ J g^{-1} K^{-1} is the heat capacity of water, $\mu = 10^4$ m^2 s^{-1} is the horizontal turbulent momentum mixing or heat diffusion coefficient, Q is the downward heat flux, τ is the vertical Reynolds stress, P is the perturbation pressure associated with motion divided by ρ_r, and V and w are the horizontal and vertical components of the velocity. For brevity, the curvature terms have been neglected in Eq. (1.29).

To describe the entrainment process, it is convenient to transform the z coordinates into generalized s coordinates (Kasahara 1974) using a single-value, monotonic function of z:

$$s = s(x, y, z, t),$$

which can transform a variable surface $z = g(x, y, t)$ into a constant surface in the s coordinates. The corresponding equations of motion in the s coordinates can be derived as follows:

$$\frac{\partial \tilde{h}}{\partial t} + \nabla_s \cdot \left(\tilde{h}V\right) + \frac{\partial w_e}{\partial s} = 0, \tag{1.30a}$$

$$\frac{\partial V}{\partial t} + V \cdot \nabla_s V + \frac{w_e}{\tilde{h}}\frac{\partial V}{\partial s} + fk \times V = -(\nabla_s P - b\nabla_s z) + \frac{1}{\rho_r \tilde{h}}\frac{\partial \tau}{\partial s} + \mu\nabla^2 V, \tag{1.30b}$$

$$\frac{\partial T}{\partial t} + V \cdot \nabla_s T + \frac{w_e}{\tilde{h}}\frac{\partial T}{\partial s} = \frac{1}{\rho_r c_w \tilde{h}}\frac{\partial Q}{\partial s} + \mu\nabla^2 T, \tag{1.30c}$$

where

$$\tilde{h} \equiv \frac{\partial z}{\partial s} = \left(\frac{\partial s}{\partial z}\right)^{-1}, \tag{1.30d}$$

$$w_e \equiv \tilde{h}\frac{ds}{dt} = w - \left(\frac{\partial z}{\partial t}\right)_s - V \cdot \nabla_s z, \tag{1.30e}$$

$$P \equiv \int_{sh}^{s} b\tilde{h}\, ds, \tag{1.30f}$$

where $s_h \equiv s(x, y, -h, t)$ represents the thermocline layer base in the s coordinates, where the perturbation pressure vanishes.

Applying the governing equations to the mixed layer and the entire upper ocean, respectively, one may derive two sets of governing equations for the mixed-layer and the mean upper-ocean currents.

1.7.1 Mixed-Layer Equations

Horizontal velocity and temperature are assumed to be independent of depth within the mixed layer (ML), ($z \leq -h_1$). To transform the variable ML base in the z coordinates into a constant surface ($s = -1$), it suffices to use

$$s = \frac{z}{h_1}, 0 \geq z \geq -h_1,$$

so that $\tilde{h} = h_1$. Integrating (1.30a–c) with respect to s from -1 to 0 yields

$$\frac{\partial h_t}{\partial t} + \nabla \cdot (h_1 \mathbf{V}_1) = W_e, \tag{1.31a}$$

$$\begin{aligned} &\frac{\partial \mathbf{V}_1}{\partial t} + \mathbf{V}_1 \cdot \nabla \mathbf{V}_1 + fk \times \mathbf{V}_1 = -\frac{1}{2}[\nabla(b_1 h) + b_1 \nabla h_1] \\ &-\frac{W_e}{h_1} \wp(W_e) \mathbf{V}_s + \frac{\tau_0 - \tau_{-h_1}}{\rho_r h_1} + \mu \nabla^2 \mathbf{V}_1, \end{aligned} \tag{1.31b}$$

$$\frac{\partial T_1}{\partial t} + \mathbf{V}_1 \cdot \nabla T_1 = -\frac{W_e}{h_1} \wp(W_e)(T_1 - T_e) + \frac{Q_0 - Q_{-h_1}}{\rho_r c_w h_1} + \mu \nabla^2 T, \tag{1.31c}$$

where $\mathbf{V}_1$ is the vertically mean current in the ML, $W_e = w_e$ $(s = -1)$ is the entrainment velocity at the ML base (Schopf and Cane 1983), $b_1 = \alpha g(T_1 - T_r)$ is the buoyancy in the ML, $\mathbf{V}_s$ is the vertical shear across the ML base, $\wp(W_e)$ is a Heaviside step function of W_e, and Q_0 and Q_{-h1} are downward fluxes at the surface and the ML base, respectively. In derivation of (1.31b), it was assumed that the temperature in the thermocline layer decreases linearly from T_1 to T_r.

To predict $\mathbf{V}_1$, h_1, and T_1, the following variables must be determined: (1) thermocline depth h and the vertical shear $\mathbf{V}_s$, (2) entrainment velocity W_e and entrained water temperature T_e, and (3) Reynolds stress at ocean surface τ_0 and at the ML base τ_{-h1} and downward heat fluxes Q_0 and Q_{-h1}.

A Kraus–Turner type of oceanic mixed layer was used to estimate entrainment rate (W_e):

$$\begin{aligned} W_e \wp(W_e) h_1 \alpha g(T_1 - T_e) &= 2 m_s u_*^3 - \frac{h_1}{2}[(1 + m_b) B_0 - (1 - m_b)|B_0|] \\ &-\frac{\alpha g}{\rho_r c_w}\left(h_1 - \frac{2}{\gamma}\right) I_0 \end{aligned}$$

where u_* is frictional velocity and B_0 and I_0 denote the net surface heat flux and downward shortwave radiation.

1.7.2 Determination of the Thermocline Depth and Shear Flow

To determine thermocline depth, one may consider equations of motion governing the entire upper active ocean. To derive these equations, we use transformation

$$s = \frac{z}{h}, 0 \geq z \geq -h, \tag{1.32a}$$

so that the base of the thermocline becomes $s = -1$ in the s coordinates defined by Eq. (1.32a) and $\tilde{h} \equiv \partial z / \partial s = h$. The perturbation pressure is

$$P = \int_{-1}^{s} \boldsymbol{bhds} \approx h\bar{b}(s+1), \tag{1.32b}$$

where $\bar{b}$ is the vertically averaged buoyancy. When the temperature in the thermocline layer decreases linearly from T_1 to T_r, $\bar{b}$ is related to b_1 by

$$\bar{b} = \frac{b_1}{2}\left(1 + \frac{h_1}{h}\right). \tag{1.32c}$$

Vertical integration of Eqs. (1.30a, 1.30b) and use of Eqs. (1.32a, 1.32b, 1.32c) yield

$$\frac{\partial h}{\partial t} + \nabla \cdot (h\mathbf{V}) = 0,$$

$$\frac{\partial \mathbf{V}}{\partial t} + \mathbf{V} \cdot \nabla \mathbf{V} + fk \times \mathbf{V} = -\nabla(\bar{b}h) + \frac{h}{2}\nabla\bar{b} + \frac{\tau_0}{\rho_r h} + \mu\nabla^2\mathbf{V},$$

where $\mathbf{V}$ is vertically averaged currents above the thermocline depth. The interfacial stress and the entrainment at $z = -h$ were neglected.

To estimate the vertical shear $\mathbf{V}_s$, we use the following approximation:

$$h\mathbf{V} = h_1\mathbf{V}_1 + h_2\mathbf{V}_2,$$

where $\mathbf{V}_2$ and h_2 are the vertically mean currents and thickness of the thermocline layer, respectively. In terms of $\mathbf{V}$ and $\mathbf{V}_1$, the shear

$$\mathbf{V}_s = \frac{h}{h - h_1}(\mathbf{V}_1 - \mathbf{V}).$$

The subsurface entrainment temperature was determined based on the following formula:

$$T_1 - T_e = \Delta h_e \frac{T_1 - T_r}{h - h_1}.$$

Table 1.2 below lists the main parameters and their values used in the model.

Forced by the climatological monthly wind stress, cloudiness, and solar radiation at top of the atmosphere, the model is able to reproduce observed SST, mixed-layer and upper-ocean mean currents, vertical entrainment velocity, and mixed-layer and thermocline depth fields. When forced by observed wind stress and heat flux forcing, the model is able to capture the interannual SST anomaly patterns associated with ENSO. For details of the model simulations, readers are referred to Wang et al. (1995).

Table 1.2 List of the model parameters and the standard values in the control experiment

T_r	Reference temperature of the inert layer	10 °C
R	Solar radiation penetration coefficient	0.55
G	Solar radiation attenuation coefficient	0.04 m^{-1}
C_D	Drag coefficient	1.3×10^{-3}
C_E	Moisture transfer coefficient	1.5×10^{-3}
h_0	Depth of constant-shear layer	10 m
m_s	Turbulent mixing coefficient due to wind stirring	1.25–0.4
m_b	Turbulent mixing coefficient due to convection	0.2
Δh_e	Thickness of the entrainment layer	5 m
μ	Horizontal turbulent momentum and heat diffusion coefficient	10^4 m^2 s^{-1}
r_h	Rayleigh damping coefficient for the thermocline depth equation	0
r	Rayleigh damping coefficient for the horizontal momentum equation	0

Questions

1. The linear shallow water equations on the equatorial beta-plane are:

$$\frac{\partial u}{\partial t} - \beta y v = -\frac{\partial \phi}{\partial x}$$
$$\frac{\partial v}{\partial t} + \beta y u = -\frac{\partial \phi}{\partial y}$$
$$\frac{\partial \phi}{\partial t} + c^2\left(\frac{\partial u}{\partial x} + \frac{\partial v}{\partial y}\right) = 0$$

   Assume this set of equations describe the lowest baroclinic mode in the atmosphere. How are dependent variables u, v, and ϕ interpreted? What is the physical meaning of c, and what determines its value? What is the typical value of c?

2. For Problem 1, derive the nondimensional form of the equations.
3. Following Problem 2, derive the dispersion equation with proper meridional boundary conditions.
4. What types of free waves exist in the above shallow water model system?
5. What are phase and energy propagation characteristics of the waves in the above shallow water model system?
6. Write the shallow water model governing equations for the equatorial Kelvin wave.
7. What are the vertical and horizontal structures of the Kelvin waves described in Problem 6?
8. Explain based on physical principles in both an atmospheric barotropic model and an atmospheric baroclinic 2-level model why the equatorial Kelvin waves propagate eastward along the equator.
9. What are major features of the equatorial Kelvin waves?

10. Prove that a first baroclinic Gill model with mid-tropospheric diabatic heating proportional to SST has the same mathematic formula as the Lindzen–Nigam boundary layer model.

References

Cane MA (1984) Modeling sea level during El Niño. J Phys Oceanogr 15:213–221
Cane M, Zebiak SE, Dolan SC (1986) Experimental forecasts of El Nino. Nature 321: 827–832
Davey MK, Gill AE (1987) Experiments on tropical circulation with a simple moist mode. Q J R Meteorol Soc 113:1237–1269
Gill AE (1980) Some simple solutions for heat-induced tropical circulation. Q J R Meteorol Soc 106:447–462
Kasahara A (1974) Various vertical coordinate systems used for numerical weather prediction. Mon Weather Rev 102:509–522
Kiladis GN, Wheeler MC, Haertel PT, Straub KH, Roundy PE (2009) Convectively coupled equatorial waves. Rev Geophys 47:RG2003
Kraus EB, Turner JS (1967) A one-dimensional model of the seasonal thermocline. Part II: The general theory and its consequences. Tellus 19:98–105
Lindzen RS, Nigam S (1987) On the role of sea surface temperature gradients in forcing low level winds and convergence in the tropics. J Atmos Sci 44:2418–2436
Matsuno T (1966) Quasigeostrophic motions in the equatorial area. J Meteorol Soc Jpn 44:25–43
Schopf PS, Cane MA (1983) On equatorial dynamics, mixed layer physics and sea surface temperature. J Phys Oceanogr 13:917–935
Wang B, Li T (1993) A simple tropical atmospheric model of relevance to short-term climate variation. J Atmos Sci 50:260–284
Wang B, Li T, Chang P (1995) An intermediate model of the tropical Pacific Ocean. J Phys Oceanogr 25:1599–1616
Zebiak SE (1986) Atmospheric convergence feedback in a simple model for el Niño. Mon Weather Rev 114:1263–1271
Zebiak SE, Cane MA (1987) A model el Niño–southern oscillation. Mon Weather Rev 115:2262–2278

Chapter 2
Roles of Air–Sea Interaction in Shaping Tropical Mean Climate

Abstract In this chapter, the observed characteristics of the mean climate such as the equatorial asymmetry of the intertropical convergence zone (ITCZ) and the equatorial annual cycle in the tropical Pacific are first described. Next the physical mechanisms responsible for the ITCZ asymmetry and the annual cycle are discussed, from theoretical analysis and idealized modeling perspectives.

2.1 ITCZ Asymmetry

The tropical time–mean climate in the eastern Pacific and Atlantic exhibits a remarkable asymmetry relative to the equator, with abundant rainfall and the intertropical convergence zone (ITCZ) residing north of the equator, and cold SST tongue at and south of the equator (Fig. 2.1). From a pure meteorological point of view, the ITCZ asymmetry is attributed to the north–south SST asymmetry. From a pure oceanographic point of view, the asymmetry in SST is caused by the asymmetry in the atmospheric forcing field. The circular argument suggests that air–sea interaction may play a role.

If one regards the coupled atmosphere–ocean system as a whole, then only external forcing is solar radiation at top of the atmosphere, which, for long-term mean, is perfectly symmetric about the equator. Then a natural question is, given such a symmetric forcing, why is the response of the coupled system asymmetric? What are the fundamental physical processes that cause the asymmetry? Why does such an asymmetry appear only in the eastern Pacific and the eastern Atlantic, not in the western Pacific and Indian Ocean?

Another fascinating feature of the mean state is the annual cycle of SST and wind fields in the equatorial eastern Pacific and eastern Atlantic. Observations show that both the SST and surface wind in the regions exhibit a marked 12-month period (Fig. 2.2), but the solar radiation at the top of the atmosphere is dominated by a semiannual (6 months) period, as the sun crosses the equator twice a year. Again such an annual frequency could be easily interpreted from a pure meteorological or a pure oceanographic point of view. However, considering the Earth climate is a coupled atmosphere–ocean system, one has to explain why the annual frequency is of atmospheric and oceanic variables and is observed while the forcing is semiannual.

T. Li, P.-c. Hsu, *Fundamentals of Tropical Climate Dynamics*,
Springer Atmospheric Sciences, DOI 10.1007/978-3-319-59597-9_2

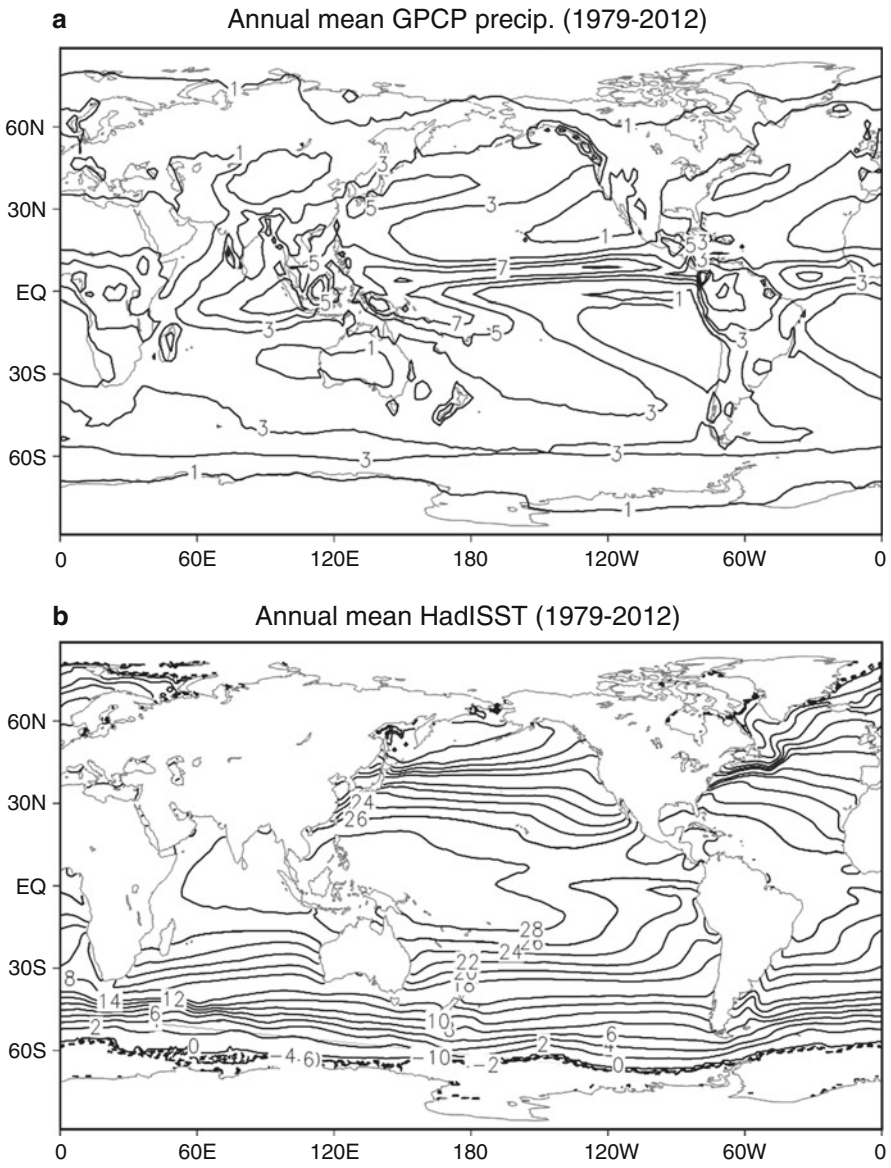

Fig. 2.1 Patterns of global annual mean precipitation (*top*, unit: mm/day) and SST (*bottom*, unit: °C) averaged during 1979–2012 (Source: Global Precipitation Climatology Project (GPCP) monthly precipitation and Hadley Centre Sea Ice and Sea Surface Temperature data (HadISST), respectively)

To address the science questions above, one needs first to examine the observed evolution features of OLR, wind, and SST in the tropical eastern Pacific domain from March (when the Pacific cold tongue is weakest) forward. Figure 2.3 shows

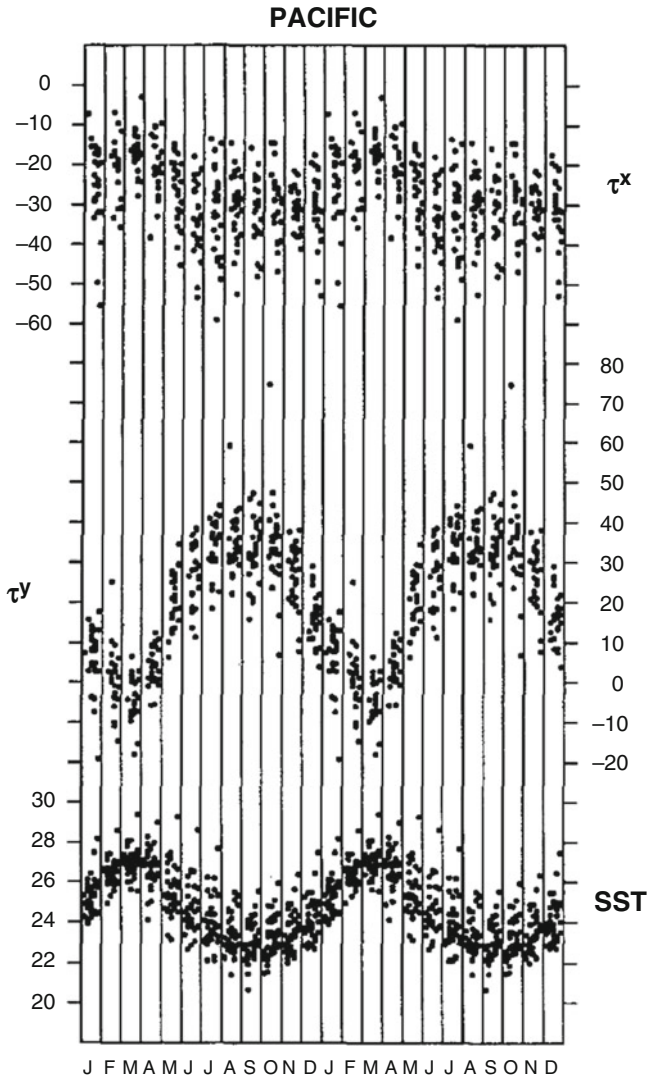

Fig. 2.2 Time evolution of zonal wind stress to the west (4°S–4°N, 130°–110°W) and meridional wind stress to the north (0°–8°N, 120°–100°W) of the Pacific cold tongue and SST at the cold tongue (4°S–4°N, 104°–86°W) (From Mitchell and Wallace (1992). © Copyright 1992 American Meteorological Society (AMS))

the difference fields from March to May (May minus March) and from May to August (August minus May). As time progresses, north–south SST gradients increase and so do the cross-equatorial flows and the antisymmetric components of SLP and OLR fields. Therefore, the observational analysis implies that the cold tongue development experiences a positive feedback loop between the atmospheric

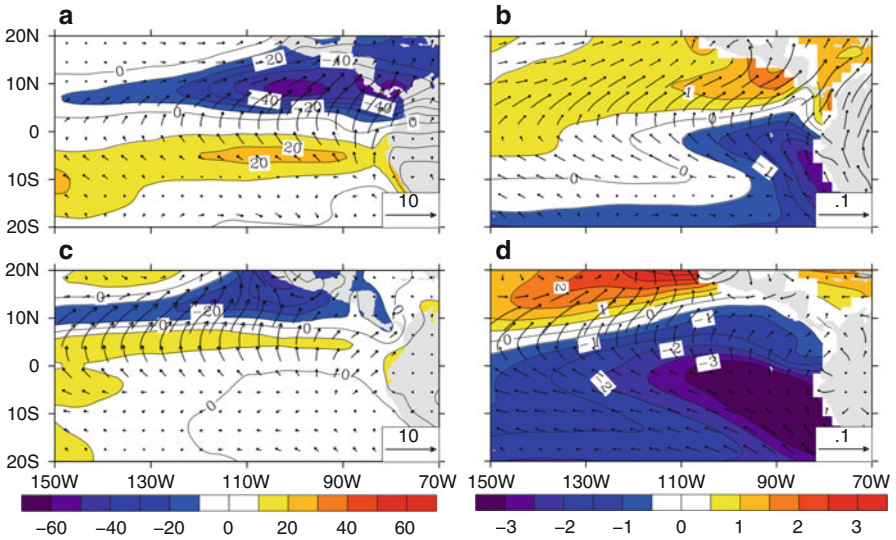

Fig. 2.3 The difference fields of observed (*left*) climatological OLR (contour interval, 10 W m^{-2}) and surface wind (m s^{-1}) and (*right*) SST (contour interval, 0.5 °C) and wind stress (Nt m). The *top panel* shows the difference between March and May (May minus March), and the *bottom panel* shows the difference between May and August (August minus May) (After Mitchell and Wallace (1992). © Copyright 1992 American Meteorological Society (AMS))

and oceanic antisymmetric modes, that is, an antisymmetric SST pattern induces cross-equatorial winds, which may further strengthen the north–south SST gradient.

2.2 Theories

Motivated by the observed evolution patterns, several theories have been proposed to understand the ITCZ asymmetry. The main idea behind the theories is that air–sea interaction may favor most unstable growth of an antisymmetric mode. The first theory, proposed by Chang and Philander (1994), focused on a positive dynamic air–sea feedback among meridional wind, ocean upwelling, and SST. They considered a simple coupled air–sea model listed below. The atmospheric component is the Lindzen–Nigam model, and the ocean component is a simplified Cane–Zebiak model:

$$E\tau^x - f\tau^y = -\alpha\left(\frac{\partial \phi}{\partial x} - A\frac{\partial T}{\partial x}\right) \tag{2.1}$$

$$E\tau^y + f\tau^x = -\alpha\left(\frac{\partial \phi}{\partial y} - A\frac{\partial T}{\partial y}\right) \tag{2.2}$$

$$\phi + B\left(\frac{\partial \tau^x}{\partial x} + \frac{\partial \tau^y}{\partial y}\right) = 0 \tag{2.3}$$

where τ^x and τ^y are the zonal and meridional component of the surface wind stress, ϕ is the geopotential at the top of the boundary layer, T is the sea surface temperature, and E is a mechanical damping due to the vertical diffusion of momentum and surface drag. $A = gH_0/2T_0$ and $B = gH_0/\mu\alpha$ measure the strength of the pressure force induced by the SST gradients and the strength of the "back pressure" effect; H_0 is the depth of the boundary layer; T_0 is a reference temperature; μ is an inverse relaxation time for the adjustment of the boundary layer height; and α converts the wind speeds into surface wind stresses.

It was shown that thermocline variation on the annual timescale is negligible. Neglecting the upper-ocean wave and thermocline variation, the Cane–Zebiak model may be simplified as

$$T_t + \bar{u}_1 T_x + \bar{v}_1 T_y + \frac{\bar{w}}{H_1}(T - \gamma h) + \bar{u}_1 T_x + v_1 \bar{T}_y + w\bar{T}_z + \varepsilon T - \kappa \nabla^2 T = 0 \tag{2.4}$$

$$\begin{bmatrix} u_1 \\ v_1 \end{bmatrix} = \frac{H_2}{H}\begin{bmatrix} u_e \\ v_e \end{bmatrix}, \quad w = \frac{H_1 H_2}{H}\nabla \cdot V_e \tag{2.5}$$

$$\begin{bmatrix} u_e \\ v_e \end{bmatrix} = \frac{1}{\Delta_0}\begin{bmatrix} r_s\tau^x + f\tau^y \\ r_s\tau^y - f\tau^x \end{bmatrix}, \quad \Delta_0 = H_1\left(r_s^2 + f^2\right), \tag{2.6}$$

where H_1 and H denote the depth of a constant mixed layer and the mean depth of thermocline; H_2 is the difference between H and H_1; $(\bar{u}_1, \bar{v}_1)$ and (u_1, v_1) represent the mean and perturbation zonal and meridional currents; h denotes the thermocline depth anomaly, which is assumed to be zero.

An eigenvalue analysis of the simple coupled model above indicates that there are two unstable modes (Fig. 2.4). The first mode has an antisymmetric structure relative to the equator. The second mode has an equatorially symmetric structure. The former has a greater growth rate than the latter, indicating that atmosphere–ocean interaction favors mostly the equatorially antisymmetric mode. Note that the most unstable mode has a zero wave number, implying that this mode supports a zonally uniform structure.

The schematic diagram of Fig. 2.5a illustrates what air–sea interaction processes are involved in leading to unstable development of an antisymmetric mode. Consider a perfectly symmetric background mean state. Initially, we introduce a weak antisymmetric SST perturbation, with a positive (negative) SSTA north (south) of the equator. If the symmetric mean state is stable, the initial perturbation would dissipate with time, due to natural dissipation process. If the system is unstable, the

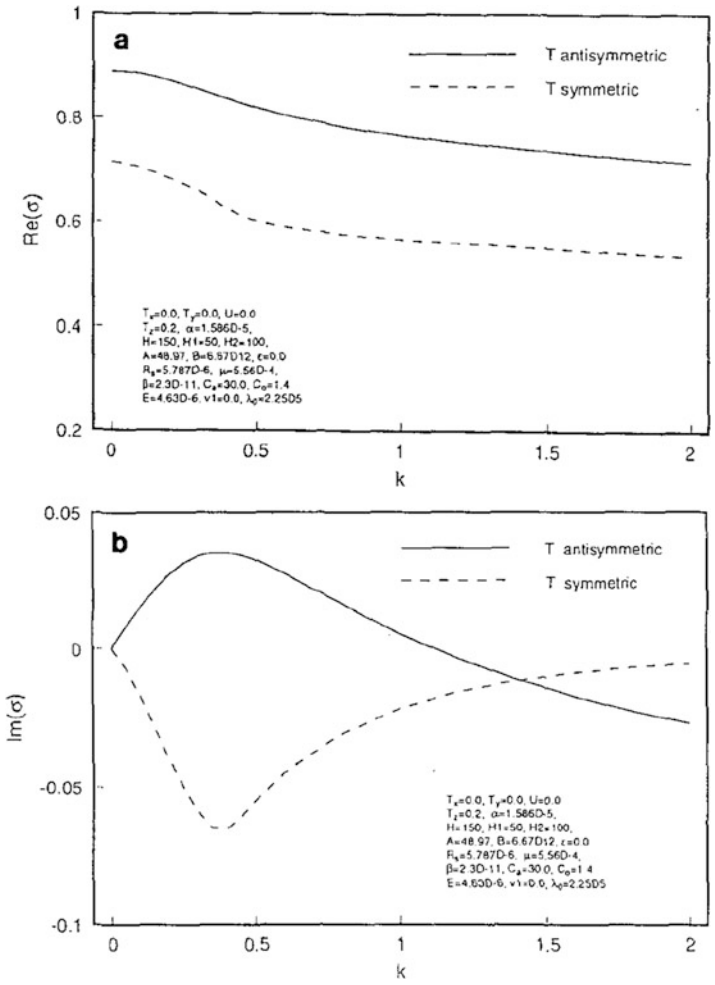

Fig. 2.4 (**a**) Growth rate and (**b**) frequency of the coupled model of Chang and Philander (1994) as a function of zonal wave number. *Solid* and *dashed lines* represent the antisymmetric and symmetric SST modes, respectively (From Chang and Philander (1994). © Copyright 1994 American Meteorological Society (AMS))

antisymmetric mode would grow exponentially with time. As a result, an antisymmetric mean state will be established.

In response to the initial weak antisymmetric SSTA forcing, a southerly wind anomaly is induced. The southerly wind converges onto the anomalous warm water, over which convection occurs, and drives the oceanic Ekman currents. The ocean Ekman current has a maximum northward component at the equator where the Coriolis force vanishes. Far away from the equator, the oceanic Ekman currents have a smaller northward component because the Coriolis force deflects the wind-driven ocean currents to the left (right) in the southern (northern) hemisphere. As a

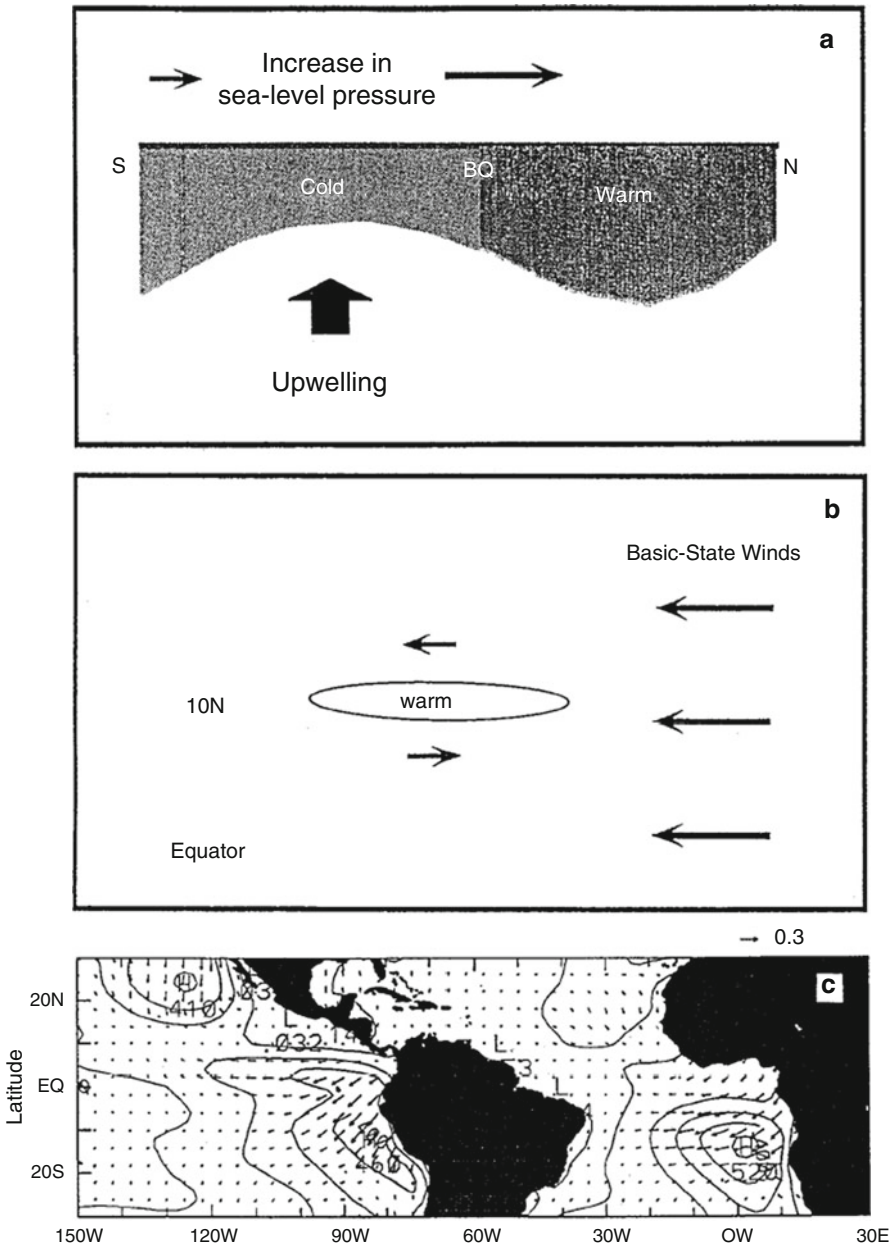

Fig. 2.5 Schematic diagrams illustrating key processes involved in the meridional wind–upwelling–SST feedback (**a**) and the wind–evaporation–SST feedback (**b**). Contours and vectors in (**c**) show the annual mean stratus cloud amount and the amplitude/phase of annual cycle of the stratus cloud (with downward/westward indicating July/October maximum) (From Li (1997). © Copyright 1997 American Meteorological Society (AMS))

result, the northward component of the oceanic Ekman current leads to surface divergence (convergence) south (north) of the equator. This promotes an asymmetry anomalous vertical velocity at bottom of the oceanic surface (or mixed) layer. An upwelling (downwelling) appears at south (north) of the equator. The asymmetric vertical velocity further strengthens the initial antisymmetric SST perturbation. As a result, there is a positive feedback loop among the anomalous SST, meridional wind, and SST. Through this positive feedback cycle, the asymmetric SST perturbation grows.

The coupled air–sea instability mentioned above was referred to as the "meridional wind–upwelling–SST" feedback (Li 1997). In addition to this dynamic air–sea feedback, there are two types of thermodynamic air–sea feedbacks, with one involving the "wind–evaporation–SST" feedback (Xie and Philander 1994) and another involving the "stratus cloud–radiation–SST" feedback (Li and Philander 1996; Philander et al. 1996).

The "wind–evaporation–SST" feedback was originally proposed by Neelin et al. (1987) and Emmanuel (1987), in studying a prominent atmospheric low-frequency oscillation, the Madden–Julian oscillation (MJO). It was further applied by Xie and Philander (1994) in studying the ITCZ asymmetry problem. The key to this mechanism lies in a background wind distribution, depicted in Fig. 2.5b. Suppose initially there is a positive SST perturbation located at 10°N. In response to this SST forcing, westerly (easterly) wind anomalies are generated to the south (north) of the SST perturbation. The westerly anomalies to the south tend to reduce the surface evaporation because the basic-state winds are easterlies. This leads to a positive time change rate for SST. As a result, the SST anomaly intensifies and propagates equatorward. Near the equator, strong oceanic upwelling induced by mean easterlies causes an extremely cold SST tongue, which suppresses the atmospheric convection and prevents further equatorward movement of the ITCZ. As a result, the positive SST perturbation and associated anomalous convection have to stay a few degrees in latitude away from the equator. It has been shown that without the equatorial cold tongue, a case in the western Pacific, the maximum SST center would move to the equator.

The third type of air–sea interaction involves the positive feedback between the low-level marine stratus clouds and SST (Li and Philander 1996; Philander et al. 1996). Whereas the convective clouds favor the warm waters in the western Pacific, the low-level stratus clouds form over colder water in the eastern Pacific (Fig. 2.5c). These stratus clouds vary seasonally and have maximum values in September when the SST is lowest. The low-level stratus clouds are particularly important in a coupled ocean–atmosphere system because they are involved in a positive feedback cycle: the lower the SST, the larger the static stability of the lower troposphere, the stronger the atmospheric inversion, and the thicker the deck of low-level stratus clouds; the increase in the clouds further shields the ocean from shortwave radiation and causes even lower SST. An observational data analysis revealed that there is a negative correlation between the low-level stratus cloud amount and SST in the eastern tropical Pacific and Atlantic. With a decrease in SST, the low-level stratus

clouds increase dramatically, which further reduces the shortwave radiation into the ocean and results in a colder SST.

The discovery of the positive ocean–atmosphere interaction processes provides a theoretical basis in understanding the fundamental cause of the climate asymmetry. But what is the relative importance of the aforementioned three air–sea feedbacks in shaping the climate asymmetry? Li (1997) attempted to address the question by considering the three air–sea feedback processes in a unified framework. In a realistic parameter regime, the aforementioned three air–sea feedback processes are of equal importance in contributing to the observed asymmetry in the eastern Pacific.

Positive air–sea feedbacks favor the development of an antisymmetric mode with ITCZ being located in either hemisphere depending on the sign of the initial perturbation. Why does the nature select northern hemisphere (NH) as a preferred location of ITCZ? Furthermore, in reality the ITCZ asymmetry happens only in the eastern tropical Pacific and eastern Atlantic, not in the western Pacific and Indian Ocean. What determines the preferred longitudinal location? These questions will be addressed in the next section.

2.3 Effects of Asymmetric Land Mass and Coastal Geometry

One possible cause of the preferred NH location of ITCZ is greater land mass in NH. An atmospheric GCM (GFDL R30 model) was used to address this hypothesis (Philander et al. 1996; Li 1997). To understand the sole effect of the asymmetric land mass, a symmetric SST relative to the equator is specified as the model lower-boundary condition; the annual mean insolation is specified at the top of the atmosphere, and it is symmetric about the equator. In spite of greater land mass in NH, the mean wind simulated by the model remains symmetric about the equator in the tropical Pacific. The result is quite different in the tropical Atlantic, where there are northward cross-equatorial winds. The cause of this wind asymmetry is attributed to a thermal contrast between the heated northwestern Africa and the cooler ocean to its south.

Two important features of the surface wind field in the tropical Pacific (Fig. 2.6b) are worth noting. Firstly, there are strong easterlies at the equator even though the SST does not vary zonally. Such winds, when allowed to influence the ocean, can drive warm surface waters westward and upwell cold water from below to the surface in the east, resulting in a strong east–west asymmetry in SST (the warm-pool–cold-tongue thermal contrast). This type of air–sea interaction along the zonal direction is responsible for determining the strength of the Walker circulation. Secondly, because of the tilt of the American coast, the trade winds to the south (north) of the equator are essentially parallel (perpendicular) to the coast. As we know, the parallel-to-coast winds may induce strong upwelling along

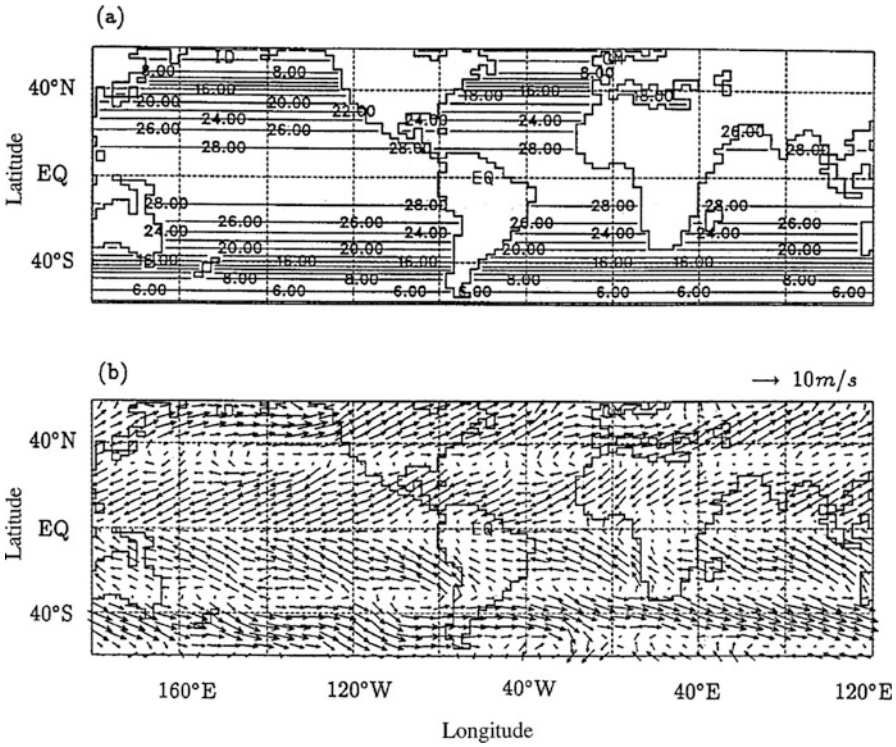

Fig. 2.6 (**a**) A prescribed zonal-mean symmetric SST (°C) field derived from the climatological monthly mean COADS dataset (averaged between 140°E and 180°). (**b**) The R30-model simulated surface wind field forced by the above prescribed symmetric SST and annual mean solar radiation (From Li (1997). © Copyright 1997 American Meteorological Society (AMS))

the coast and cool SST there. Therefore, when coupled to the ocean, the winds can help set up a north–south asymmetry in SST by inducing anomalous cooling (warming) off the coast of Peru (Panama). Once this initial weak SST asymmetry is set up, the ocean–atmosphere feedbacks mentioned in the previous section could further amplify the equatorial asymmetry, to finally reach the observed strength.

To test this hypothesis and to understand the relative role of various air–sea feedbacks, a set of coupled sensitivity experiments were conducted. In the first set, a focus was on the dynamic air–sea coupling, that is, the atmosphere influences the ocean solely through wind stresses, while the surface heat fluxes in the model were specified as a Newtonian damping term that restores the model SST toward a prescribed symmetric SST field shown in Fig. 2.6a. The ocean model starts from a symmetric SST condition (as shown in Fig. 2.6a). Because of the quick development of equatorial easterlies, an east–west asymmetry, characterized by a warm pool in the western Pacific and a cold tongue in the eastern Pacific (Fig. 2.7a), is established. Because of the tilt of the western coasts of the Americas, a north–south asymmetric SST pattern develops (Fig. 2.7a). Accompanied with the development

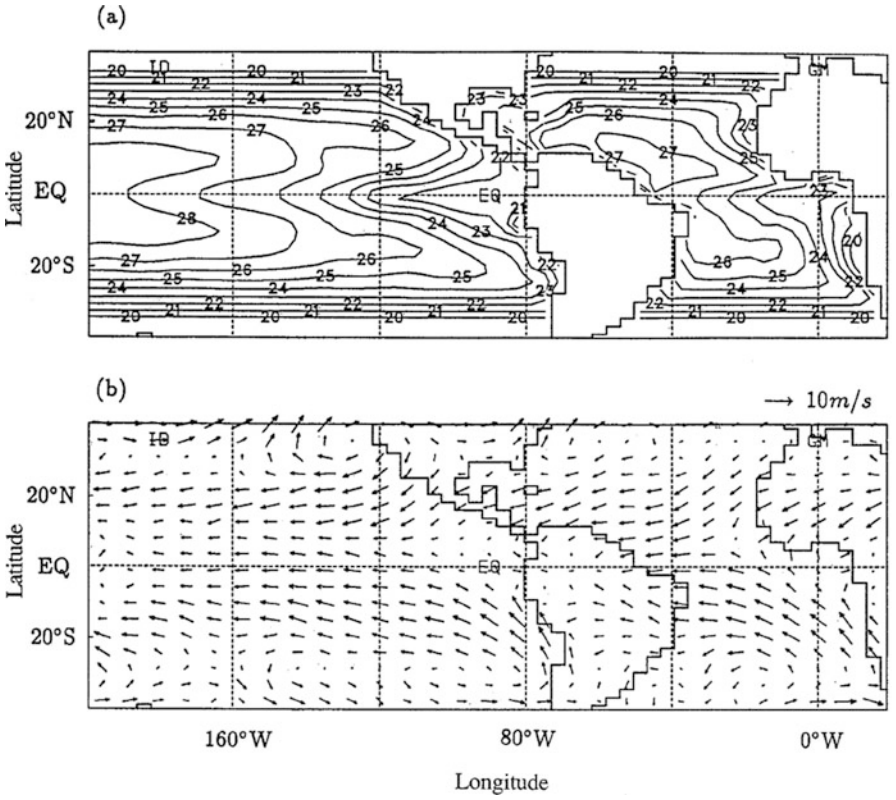

Fig. 2.7 The simulated (**a**) SST (°C) and (**b**) surface wind fields from a hybrid coupled GCM. Only the dynamic coupling is considered in this case. The thermodynamic coupling, such as the surface evaporation and cloud effects, is intentionally suppressed. The model starts from a symmetric SST condition as shown in Fig. 2.6a (From Li (1997). © Copyright 1997 American Meteorological Society (AMS))

of the asymmetric SST pattern is northward cross-equatorial flow in the eastern tropical Pacific (Fig. 2.7b).

The dynamic coupling in this model setting contains two important, distinctive processes: (1) a coastal wind-upwelling mechanism that perturbs SST in the vicinity of the coastal regions and is responsible for the initiation of an equatorial asymmetry and (2) the meridional wind–SST feedback that further amplifies the asymmetry through a positive feedback loop. The former is a coastal mode that primarily involves air–sea interactions in the vicinity of the coast, and the latter is an equatorially trapped mode whose meridional extent is determined by the Rossby radius of deformation.

The importance of the tilted coast in initiating the climate asymmetry in the Pacific was further demonstrated by Philander et al. (1996), who specified an idealized western coast of the Americas that is parallel to a longitude. The idealized

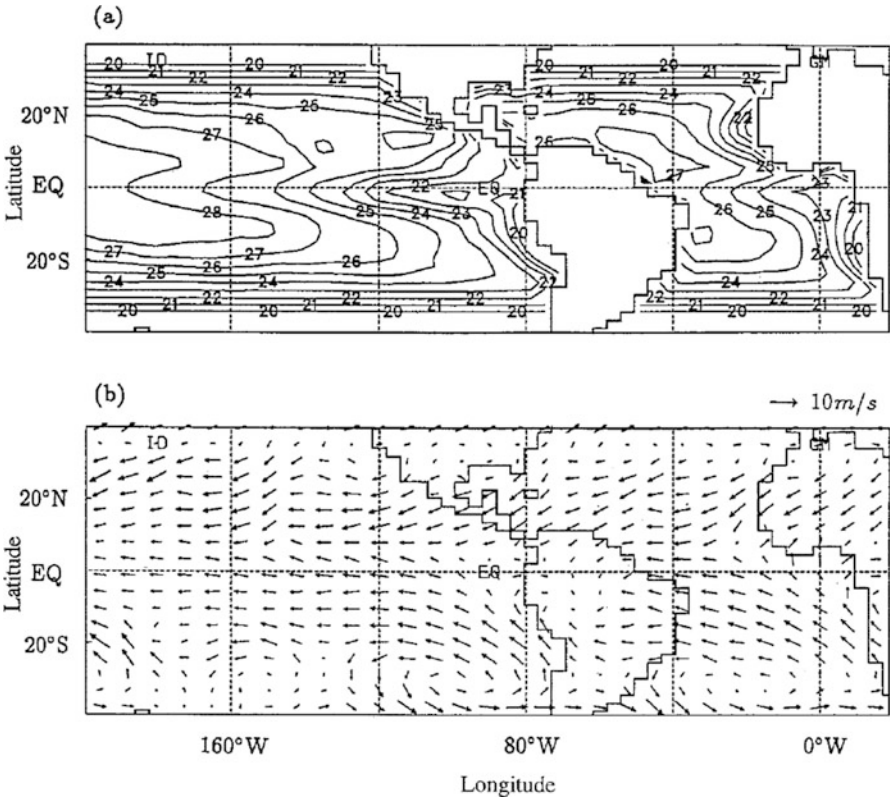

Fig. 2.8 The simulated (**a**) SST (°C) and (**b**) surface wind fields from the hybrid coupled GCM in the presence of the dynamic coupling, the evaporation–wind feedback, and the low-level stratus cloud–SST feedback (From Li (1997). © Copyright 1997 American Meteorological Society (AMS))

numerical model experiment showed that in the absence of the coast asymmetry, no equatorial asymmetric SST patterns are generated in the eastern Pacific.

The intensity of the equatorial asymmetry is further strengthened when the "wind–evaporation–SST" feedback and the "stratus cloud–radiation–SST" feedback are turned on in the coupled experiments, in addition to the dynamic air–sea feedback, as shown in Fig. 2.8.

To sum up, the coupled atmosphere–ocean GCM experiments demonstrated that the essential cause of the preferred NH ITCZ location differs in the tropical Pacific and Atlantic. In the Atlantic, it is primarily attributed to a thermal contrast between the heated northwestern Africa and the cooler ocean to its south. In the Pacific, it is due to the coastal asymmetry of America. The specific coastal and land asymmetries favor a warmer SST and enhanced convection north of the equator and northward cross-equatorial flow. The atmosphere–ocean feedbacks further magnify the coast- and land-induced asymmetry.

While the preferred NH location for ITCZ is attributed to the aforementioned coastal and land asymmetry, the preferred longitudinal location of the ITCZ asymmetry is mainly determined by the depth of climatological mean thermocline at the equator. This is because air–sea interactions are most active in the region where mean thermocline is shallow. The contrasting mean conditions between west and east of the ocean basins are ultimately caused by the dominance of trade winds in both the tropical Pacific and Atlantic. The wind in the tropical Indian Ocean, on the other hand, is unique as it is dominated by north–south monsoonal flows. Thus the ultimate cause of longitudinal ITCZ location is the global distribution of land and ocean that determines where the monsoonal flow and trades prevail and thus determines the east–west tilting of equatorial ocean thermocline.

2.4 Annual Cycle at the Equator

Various factors may contribute to the annual periodicity of SST and wind fields at the equator. Firstly, the solar radiation at the top of the atmosphere has an annual harmonic, with both a symmetric and an antisymmetric component. The former is associated with the elliptic orbit of the Earth – the Sun is closer to the Earth in January and further from the Earth in July. The latter is associated with the tilting of the Earth's axis, which causes the season. But this antisymmetric component has a zero amplitude right on the equator. Which of the above solar radiation components is critical?

Secondly, the SST and wind annual cycles occur only in the equatorial eastern Pacific and Atlantic, where the mean climate is asymmetrically relative to the equator. What is the role of the asymmetric mean state in causing the annual variation of atmospheric and oceanic variables?

To address these questions, Li and Philander (1996) constructed a simple atmosphere–ocean coupled model in which the annual mean state is prescribed and the model is forced by time-dependent solar radiation at the top of the atmosphere.

The atmospheric component of this coupled model is the Lindzen-Nigam model:

$$EV + \beta yU = \frac{\partial \phi}{\partial y} + A\frac{\partial T}{\partial y}, \tag{2.7}$$

$$EU - \beta yV = \frac{\partial \phi}{\partial x} + A\frac{\partial T}{\partial x}, \tag{2.8}$$

$$\varepsilon \phi = -C_0^2\left(\frac{\partial U}{\partial x} + \frac{\partial V}{\partial y}\right), \tag{2.9}$$

where U and V are zonal and meridional wind components; φ is the geopotential at the top of the atmospheric boundary; E is a boundary-layer frictional coefficient; ε is an inverse timescale for cumulus convection adjustment; $A = gH_0/2T_0$ and

$C_0^2 = gH_0$, respectively, measure the strength of the pressure gradient force induced by SST gradients and a barotropic gravity wave speed in the boundary layer; H_0 is the depth of the boundary layer; and T_0 is a reference temperature. In the present study, we set $E = 1/2.5$ day^{-1}, $\varepsilon = 1/30$ min^{-1}, $H_0 = 3000$ m, and $T_0 = 288$ K.

The ocean component of the coupled model is similar to that of Zebiak and Cane (1987) with slight modification in the shear current equation and the SST equation:

$$\frac{\partial \mathbf{v}}{\partial t} + f\mathbf{k} \times \mathbf{v} = -g'\nabla h + \frac{\tau}{\rho H} - r\mathbf{v} + \upsilon\nabla^2\mathbf{v}, \tag{2.10}$$

$$\frac{\partial h}{\partial t} + H\nabla \cdot \mathbf{v} = -rh + \kappa\nabla^2 h, \tag{2.11}$$

$$\frac{\partial \tilde{\mathbf{v}}}{\partial t} + f\mathbf{k} \times \tilde{\mathbf{v}} = \frac{\tau}{\rho H_1} - r_s\tilde{\mathbf{v}} + \upsilon\nabla^2\tilde{\mathbf{v}}, \tag{2.12}$$

$$\begin{aligned}\frac{\partial T}{\partial t} &+ \mathbf{v_1} \cdot \nabla(\bar{T} + T) + \bar{\mathbf{v}}_\mathbf{1} \cdot \nabla T \\ &= -[M(\bar{w} + w) - M(\bar{w})]\bar{T}_z - M(\bar{w} + w)T_z + \frac{Q}{\rho C_w H^w 1} - \alpha T + \kappa\nabla^2 T,\end{aligned} \tag{2.13}$$

where $\mathbf{v}$ and $\tilde{\mathbf{v}}$ denote the mean upper-ocean current and the shear current between the mixed layer and the layer below;

$$\mathbf{v_1} = \mathbf{v} + \frac{H_2}{H}\tilde{\mathbf{v}}$$

represents the surface current; $H_1 = 25$ m and $H = 150$ m are mean mixed layer, thermocline depths, and $H_2 = H - H_1$; $w = H_1$ is the vertical entrainment velocity at the base of the mixed layer; $M(x) = x$, if $x > 0$, and $M(x) = 0$, otherwise, is the Heaviside function; h denotes the varying thermocline; T is sea surface temperature; T_z is the vertical temperature gradient between surface and subsurface; Q denotes surface heat fluxes associated with solar radiation and latent heat fluxes; g' and ρ represent reduced gravity and the density of the upper ocean; r, r_s, and α represent damping coefficients for momentum and heat and have the values $r = 1/150\,\text{day}^{-1}$, $r_s = 1$ day^{-1}; and $\alpha = 1/60\,\text{day}^{-1}$ and υ and κ stand for diffusion coefficients ($3 \times 10^3 \text{m}^2\text{s}^{-1}$). All quantities with a bar denote the annual mean fields, and the others denote departures from the mean.

The model was forced by seasonally varying solar radiation forcing at the top of the atmosphere, which contains three components: (1) a semiannual harmonic component associated with the meridional movement of the sun that crosses the equator twice a year, (2) an annual harmonic symmetric component that is associated with elliptic orbit, and (3) an annual harmonic antisymmetric component that is associated with tilting of Earth's axis. In the presence of all the solar forcing and the realistic mean state, the model is able to reproduce the observed annual cycles of SST in the tropical Pacific. The simulated SST in the equatorial western Pacific is

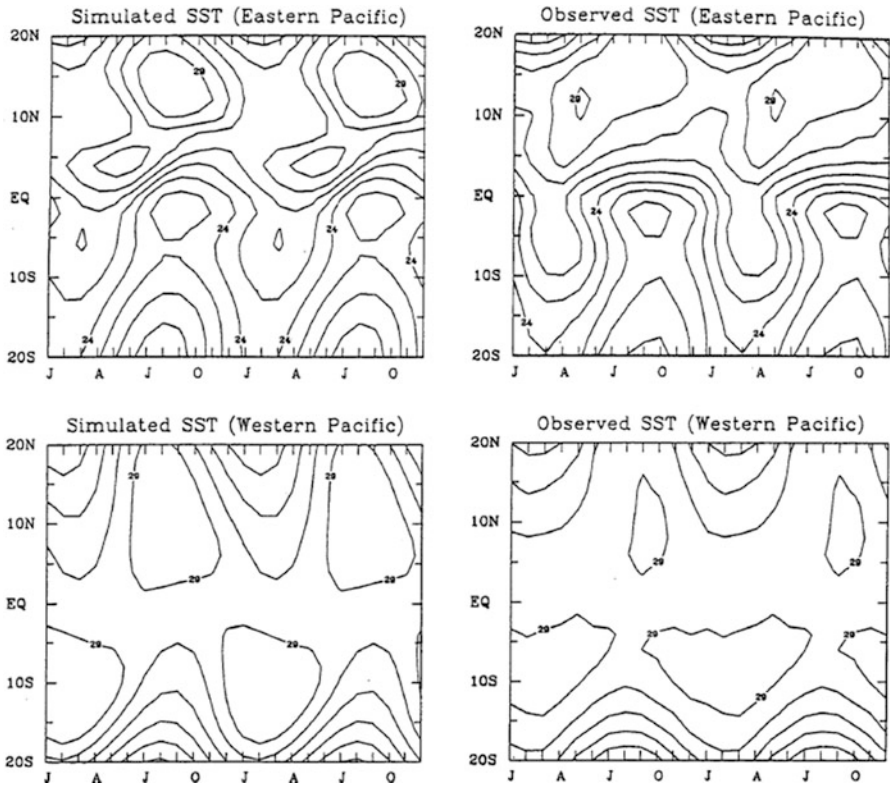

Fig. 2.9 The annual cycles of sea surface temperatures, simulated and observed, in the eastern Pacific (90°–110°W; *upper panels*) and in the western Pacific (160°E–180; *lower panels*). The model results are from the reference case in which the model is forced with the complete seasonal solar radiation; a realistic, asymmetric annual mean basic state is specified and the western coast of the Americas coincides with a meridian (From Li and Philander (1996). © Copyright 1996 American Meteorological Society (AMS))

characterized by a 6-month period, while the SST in the equatorial eastern Pacific is characterized by a 12-month period (Fig. 2.9), consistent with the observation.

Given that the model control experiment is able to reproduce the observed annual cycle in the eastern equatorial Pacific, sensitivity experiments are further carried out to understand the effect of the asymmetric mean state and the relative roles of various components of solar forcing. When a symmetric mean state is specified, no annual cycle is found in the eastern equatorial Pacific. This confirms the important role of the mean state asymmetry in causing the annual cycle. The specific roles through which the mean state impacts the annual cycle will be discussed below. As to the various components of solar forcing, it is found that the symmetric annual harmonic (related to Earth's elliptic orbit) is not important so is the semiannual harmonic. The most important forcing is the one related to the tilt of Earth's axis. Although being zero at the equator, it is critical to cause the annual

SST cycle right on the equator. This is because this antisymmetric annual-harmonic solar forcing results in an antisymmetric SST anomaly, which further drives cross-equatorial winds, leading to the SST change at the equator through anomalous temperature advection and heat fluxes.

The top panel of Fig. 2.10 shows the time–latitude section of the simulated SST field when one considers only dynamic air–sea coupling (i.e., heat flux effects including surface latent heat flux and cloud shortwave radiation variations are intentionally suppressed). There is an annual cycle in SST at the equator. The key process to cause the annual SST variation at the equator in this case is anomalous meridional temperature advection as shown in the bottom panel of Fig. 2.10. Note that the mean meridional temperature gradient $\bar{T}_y$ is positive in the eastern equatorial Pacific. Thus, the anomalous ocean current, v', which changes direction seasonally, cools the equator during the northern summer and warms it during the northern winter. In other words, the term $-v'\bar{T}_y$ leads to an annual SST cycle at the equator. The term $-\bar{v}T'_y$ also contributes to an annual SST cycle because the mean ocean current $\bar{v}$ is northward (in response to the mean northward cross-equatorial wind) and because anomalous meridional temperature gradient T'_y changes sign with the seasons in response to the seasonal change of anomalous cross-equatorial wind according to the meridional wind–upwelling–SST feedback mechanism (Chang and Philander 1994). The above anomalous meridional advection processes become important only when the asymmetric mean state is presented. In the case when the mean state is symmetric about the equator, both $\bar{T}_y$ and $\bar{v}$ vanish at the equator.

The results in Fig. 2.10 show the seasonal cycle that involves the strictly dynamical response of the ocean to the winds. There will be an annual cycle at the equator even if the winds generate no currents but merely cause evaporation, provided the time–mean state has northward winds at the equator. This is possible because the intensification of those winds during the northern summer and their weakening during the northern winter will cause an annual variation in surface evaporation and hence in SST. The dotted line in Fig. 2.11 depicts that variation on the equator at 100° W. It is modest in amplitude but is magnified if we take into account the combined effects of the surface evaporation and the dynamical response discussed in Fig. 2.10. The solid line of Fig. 2.11 shows this combined effect. The further amplification of the annual harmonic is possible because of the low-level cloud–radiation–SST feedback mentioned previously. The lower the sea surface temperatures, the thicker the cloud layer and the smaller the shortwave radiation into the ocean. The dashed line in Fig. 2.11 shows how SST varies when the dynamical response, the surface evaporation, and the stratus cloud feedbacks are all included. This case almost recovers the seasonal SST variation in the control experiment, which is close to the observed amplitude.

To sum up, the eastern equatorial Pacific has a pronounced annual cycle in fields such as SST, both components of the surface winds, and cloudiness. The challenge is to explain how the seasonal variations in solar radiation force such a response. The results described above indicate that the annual cycle is forced by the

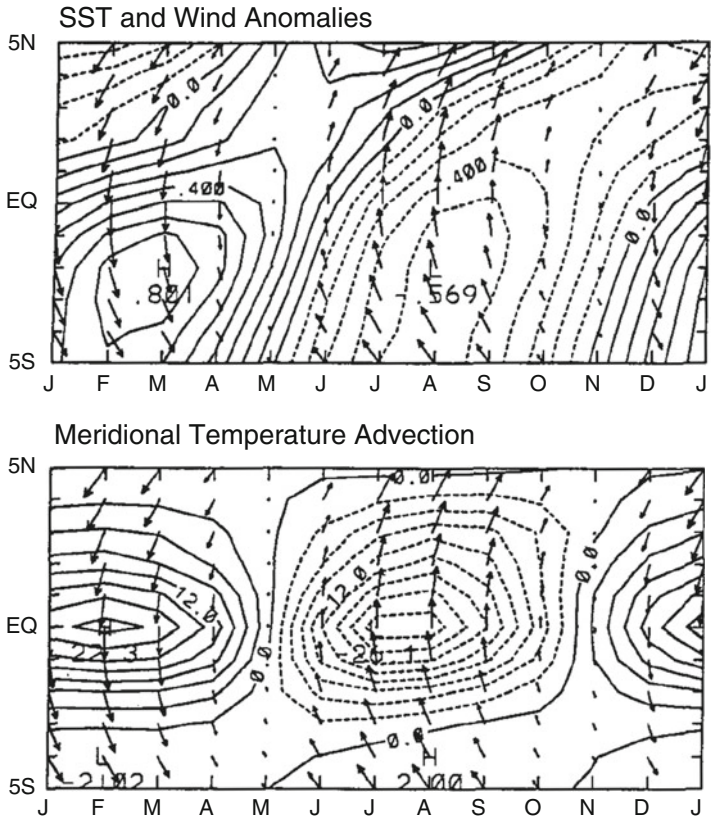

Fig. 2.10 Time–latitude section of the simulated SST field (*top*, interval, 0.1 °C) and anomalous meridional advection (bottom, interval, $3e^{-8}$ K/s) at 100°W in the presence of dynamic air–sea coupling only (From Li and Philander (1996). © Copyright 1996 American Meteorological Society (AMS))

antisymmetric component of the seasonally varying solar radiation. This is possible because of the mean state asymmetry, an asymmetry that is prominent in the eastern tropical Pacific but not the Indian Ocean or western tropical Pacific. That asymmetry permits an annual cycle on the equator even in a model that couples the atmosphere to a one-dimensional mixed-layer ocean. In such a coupled model, the northward winds at the equator will be intense toward the end of the northern summer and relaxed toward the end of the southern summer. Surface evaporation associated with these winds will cause SST near the equator to be low in August and September and high in March and April. In other words, the model will have an annual cycle in SST at the equator. The amplitude will be modest but can be augmented by next taking into account the dynamical response of the ocean to the winds: intense northward winds induce upwelling and low SST at and to the south of the equator. Further amplification is possible by including the effects of low-level stratus clouds. They form when cold surface waters lead to an

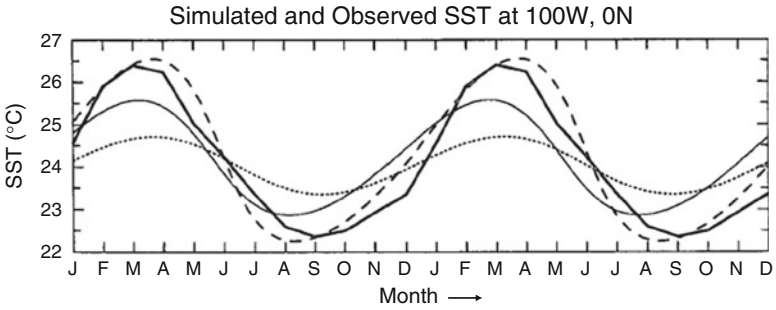

Fig. 2.11 Seasonal variations of SST at 0°, 100°W in three cases. The SST is determined strictly by evaporation in the case of the *dotted line*, by evaporation and oceanic upwelling in the case of the *solid line*, and by evaporation, upwelling, and the presence of low-level stratus clouds in the case of the dashed line. The heavy *black line* corresponds to the observed variations. In all three cases, a realistic time–mean state that is asymmetric about the equator is specified; the model is forced by part of annually varying solar radiation that is strictly antisymmetric about the equator; and the western coast of the Americas coincides with a meridian (From Li and Philander (1996).)

atmospheric inversion and strengthen that inversion by further cooling the surface waters.

In addition to the asymmetric mean state, there are several other factors that contribute to the annual cycle at the equator. They include the annual cycle in solar radiation associated with the ellipticity of the Earth's orbit and the asymmetry, relative to the equator, of the western coast line of the Americas. Their contributions are modest and remain so even when ocean–atmosphere interactions and feedbacks associated with low-level clouds are taken into account.

Questions

1. Describe what unstable positive air–sea feedback processes are involved in the antisymmetric mode development in Chang and Philander (1994).
2. Under what conditions do the positive feedback processes mentioned in Problem 1 work?
3. Describe what unstable positive air–sea feedback processes are involved in the symmetric mode development in Chang and Philander (1994).
4. Under what conditions do the positive feedback processes mentioned in Problem 3 work?
5. In addition to dynamic air–sea feedback mentioned in Problem 1, what types of thermodynamic air–sea feedback processes are involved in the development of the antisymmetric mode (relative to the equator)?
6. Why do unstable dynamic and thermodynamic air–sea feedback processes mentioned above occur only in the tropical eastern Pacific and the tropical eastern Atlantic?
7. Air–sea feedback processes mentioned above favor the occurrence of ITCZ in either hemisphere. Why does the observed ITCZ always stay north of the

equator? What control the preferred ITCZ location north of the equator in the tropical Pacific and Atlantic?

8. Why do the annual variations of observed SST and wind move westward along the equator? What air–sea interaction processes are involved in the westward propagation?
9. Why do observed SST and wind fields have a dominant annual (12-month) period in the equatorial eastern Pacific while the sun crosses the equator twice a year? What physical processes are involved in generating the annual cycle?
10. In Problem 9, what happens if the time–mean climate state is symmetric about the equator in the tropical eastern Pacific?

References

Chang P, Philander SGH (1994) A coupled ocean-atmosphere instability of relevance to the seasonal cycle. J Atmos Sci 51:3627–3648

Emanuel KA (1987) An air-sea interaction model of intraseasonal oscillation in the tropics. J Atmos Sci 44:2324–2340

Li T (1997) Air-sea interactions of relevance to the ITCZ: the analysis of coupled instabilities and experiments in a hybrid coupled GCM. J Atmos Sci 54:134–147

Li T, Philander SGH (1996) On the annual cycle of the equatorial eastern Pacific. J Clim 9:2986–2998

Mitchell TP, Wallace JM (1992) The annual cycle in equatorial convection and sea surface temperature. J Clim 5:1140–1156

Neelin JD, Held IM, Cook KH (1987) Evaporation–wind feedback and low-frequency variability in the tropical atmosphere. J Atmos Sci 44:2341–2348

Philander SGH, Gu D, Lambert G, Li T, Halpern D, Lau N-C, Pacanowski RC (1996) Why the ITCZ is mostly north of the equator. J Clim 9:2958–2972

Xie SP, Philander SGH (1994) A coupled ocean-atmosphere model of relevance to the ITCZ in the eastern Pacific. Tellus 46:340–350

Zebiak SE, Cane MA (1987) A model el Niño–southern oscillation. Mon Weather Rev 115:2262–2278

Chapter 3
Madden-Julian Oscillation: Observations and Mechanisms

Abstract In this chapter, the observed features of the Madden–Julian Oscillation (MJO) are first introduced, followed by the discussions of physical mechanisms responsible for the eastward propagation and initiation of MJO. Next the boreal summer intraseasonal oscillation (BSISO) is described, with a special emphasis on the mechanisms responsible for its northward propagation over the monsoon regions. Finally the interaction of MJO or BSISO with higher-frequency motions is discussed.

3.1 Introduction

The Madden–Julian Oscillation (MJO) is the most prominent mode of intraseasonal variability in the tropics. It was firstly discovered by Madden and Julian (1971), who found that winds in Canton Island (located in the central equatorial Pacific) had a characteristic period of 40–50 days. It was further found that this intraseasonal mode has a planetary zonal scale, coupled with convection, propagating slowly eastward along the equator (Fig. 3.1, Madden and Julian 1972). Later analyses with modern observational data confirmed the planetary zonal scale characteristic and showed that the oscillation is more broadband than the original 40–50-day period and can span a range of 10–90 days.

MJO is a primary predictability source for extended-range (10–30-day) forecast. Accurate prediction of MJO and atmospheric intraseasonal variability is crucial for bridging the gap between short-range weather and long-range (monthly or seasonally) climate prediction. Most of current operational models, however, have low skills in predicting MJO (Jiang et al. 2015). Understanding MJO propagation and initiation mechanisms is important for improving the model representation of MJO.

3.2 Observed Structure and Evolution Features

Figure 3.2 shows the composite wind and divergence fields at 1000 hPa, 850 hPa, and 200 hPa in association with MJO where its major convective center appears over the equatorial eastern Indian Ocean. The horizontal pattern of MJO low-level

T. Li, P.-c. Hsu, *Fundamentals of Tropical Climate Dynamics*,
Springer Atmospheric Sciences, DOI 10.1007/978-3-319-59597-9_3

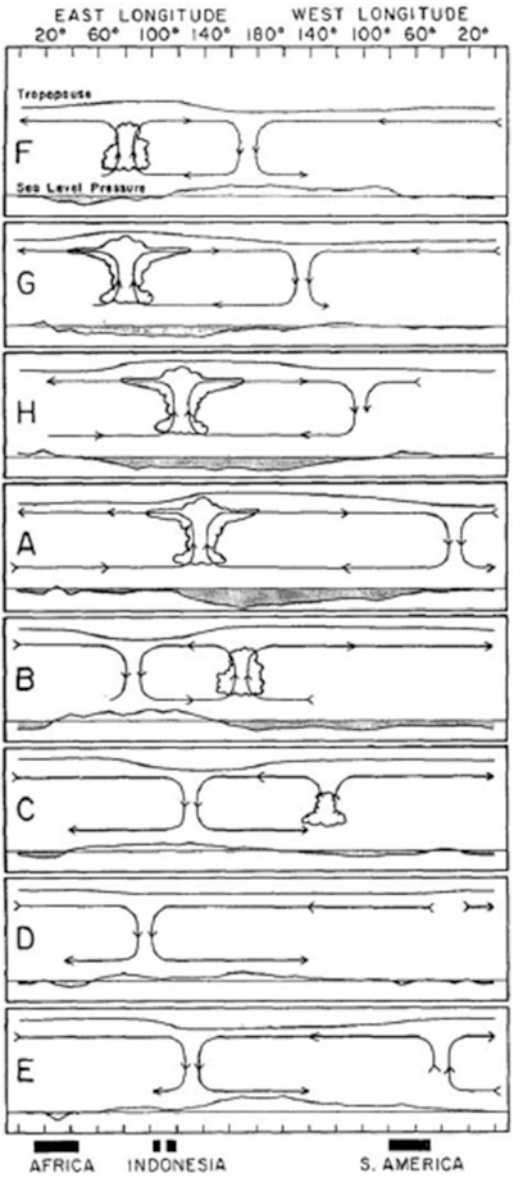

Fig. 3.1 Schematic diagram illustrating the circulation structure and phase propagation of MJO (From Madden and Julian (1972). © Copyright 1972 American Meteorological Society (AMS))

circulation exhibits a Kelvin–Rossby wave couplet, with two cyclonic gyres residing at both sides of the equator to the west of the MJO convective center and pronounced easterlies to the east of the convective center. The upper-level circulation is in general opposite to that at the low level. Thus, MJO exhibits, to a large extent, the first baroclinic mode vertical structure in the free atmosphere.

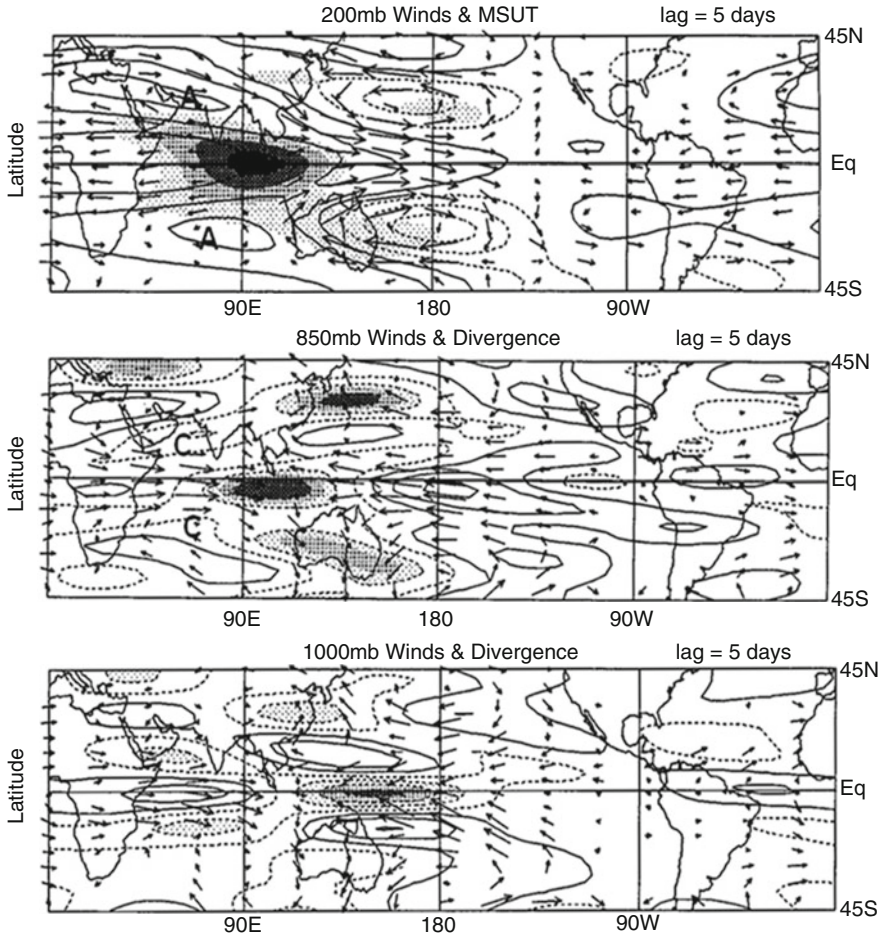

Fig. 3.2 Horizontal patterns of wind (vector) and geopotential height (contour) fields at 200 hPa and brightness temperature (as a proxy of convection, dark shaded) (*top*), wind (vector), and divergence (contour) fields at 850 hPa (*middle*) and 1000 hPa (*bottom*) regressed onto a MJO convection index at the eastern equatorial Indian Ocean (From Hendon and Salby (1994). © Copyright 1994 American Meteorological Society (AMS))

While the wind convergence at 850 hPa is out of phase with that at 200 hPa, convergence at 1000 hPa leads that at 850 hPa. Such a distinctive planetary boundary layer (PBL) feature may be better viewed in the vertical–longitude sections of MJO-scale divergence, specific humidity, vertical p-velocity, and zonal wind fields (Fig. 3.3). Over the maximum convective center, low-level convergence and upper-level divergence are clearly seen in the free atmosphere above 850 hPa. In association with the divergence, profile is maximum ascending motion at 300–400 hPa. Below 850 hPa, there is a clear zonal asymmetry (relative to the convective center) in the divergence field, with convergence (divergence)

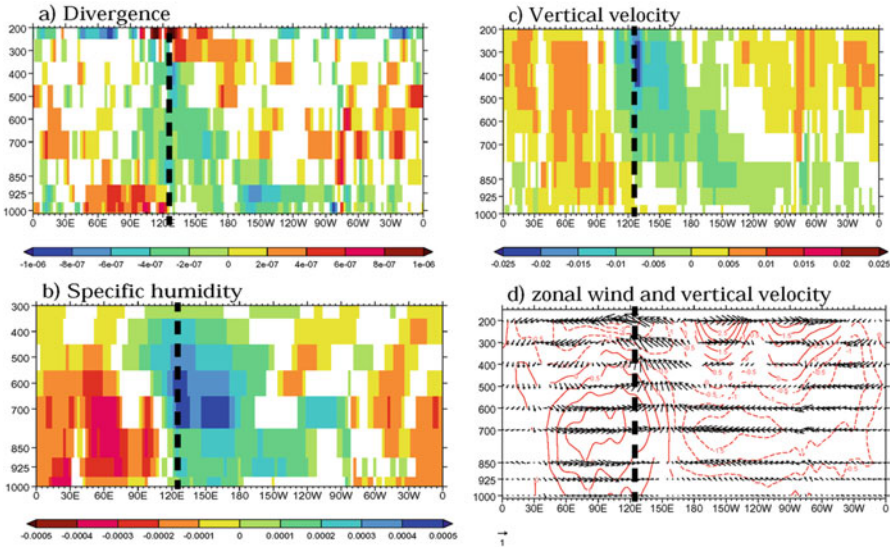

Fig. 3.3 Longitude-vertical sections of composite (**a**) divergence, (**b**) specific humidity, (**c**) vertical p-velocity, and (**d**) zonal wind fields in reference of MJO convection at 120°E (From Sperber (2003). © Copyright 2003 American Meteorological Society (AMS))

appearing to the east (west) of the MJO convection. As a result, the ascending motion tilts eastward with decreased height. The specific humidity profile follows well the vertical velocity profile, that is, a maximum humidity center appears in phase with the convection in middle-lower troposphere (600–800 hPa), while positive moisture anomalies lead the convection below 800 hPa. Low-level westerlies appear at and to the west of the convective center, while low-level easterlies, with longer horizontal extent, appear to the east of the convective center.

3.3 Mechanisms for Eastward Propagation

Various theories have been proposed to understand the eastward propagation of MJO. The first theory considered MJO as a convectively coupled Kelvin wave, but the so-derived MJO modes prefer a short wavelength for most unstable mode (Wang 1988a), and the eastward phase speed is too fast. The second theory emphasized wind-induced surface heat exchange (WISHE) feedback (Emanuel 1987; Neelin et al. 1987). However, this mechanism requires the presence of the mean easterly in the tropical Indian Ocean–western Pacific warm pool, which is not true (Wang 1988b). The third theory considered MJO as a Kelvin–Rossby wave couplet that couples with convection and PBL frictional effect (Wang and Li 1994; Li and Wang 1994a). Such a free-atmospheric wave – nonlinear diabatic heating – PBL interaction results in a horizontal and vertical structure similar to the observed

MJO (Hendon and Salby 1994; Jones and Weare 1996; Maloney and Hartmann 1998; Chao and Chen 1999; Moskowitz and Bretherton 2000; Sperber 2003). More recent theories emphasized the role of air–sea interaction (e.g., Flatau et al. 1997; Lau and Sui 1997; Hendon and Glick 1997; Shinoda and Hendon 1998; Wang and Xie 1998), interaction with synoptic-scale eddies (e.g., Majda and Biello 2004; Biello and Majda 2005; Khouider and Majda 2006, 2007; Biello et al. 2007), and moisture perturbation (Maloney 2009; Hsu and Li 2012; Sobel and Maloney 2013).

In the following we focus on the discussion of the wave–convection–frictional convergence feedback mechanism (Wang and Li 1994) and the moisture feedback mechanism (Hsu and Li 2012).

The model framework of Wang and Li (1994) is essentially same as the 2.5-layer model discussed in Sect. 1.6 (Wang and Li 1993) except that an interactive nonlinear heating is applied. It consists of the first baroclinic mode free atmosphere and a well-mixed PBL. The atmospheric low-frequency motion in free troposphere satisfies the linearized primitive equations in a pressure vertical coordinate at an equatorial beta-plane:

$$\begin{aligned}
\frac{\partial u'}{\partial t} &= -\beta y v' - \frac{\partial \phi'}{\partial x} - \varepsilon u' + K\nabla^2 u' \\
\frac{\partial v'}{\partial t} &= -\beta y u' - \frac{\partial \phi'}{\partial y} - \varepsilon v' + K\nabla^2 v' \\
\frac{\partial T'}{\partial t} &= \frac{p}{R}\bar{S}\omega' + \frac{Q'}{C_p} - \mu T' + K\nabla^2 T' \\
\frac{\partial u'}{\partial x} &+ \frac{\partial v'}{\partial y} + \frac{\partial \omega'}{\partial p} = 0 \\
\frac{\partial \phi'}{\partial p} &= -\frac{RT'}{p}
\end{aligned} \tag{3.1}$$

where u', v', ω', ϕ', and T' denote perturbation zonal and meridional wind, vertical pressure velocity, geopotential, and temperature, respectively; ε and μ, the Rayleigh friction and Newtonian cooling coefficients; K, a diffusion coefficient; and $\bar{S}$, background dry static stability parameter.

The perturbation precipitation is proportional to column-integrated moisture convergence on the basis of the moisture equation by assuming that the moisture tendency vanishes. The precipitation rate P may be written as

$$P = -\frac{\delta b}{g}\left[\omega_m'(\bar{q}_2 - \bar{q}_1) - \omega_e'(\bar{q}_e - \bar{q}_2)\right]. \tag{3.2}$$

Thus, perturbation condensational heating in middle troposphere is proportional to vertically integrated moisture convergence:

$$Q'_m = \frac{\delta b L_c}{\Delta p}\left[-\omega'_m(\bar{q}_2 - \bar{q}_1) - \omega'_e(\bar{q}_e - \bar{q}_2)\right], \tag{3.3}$$

where δ is a nonlinear switch-on coefficient, and it equals to one (zero) when there is column-integrated moisture convergence (divergence); b is a constant heating efficiency coefficient, L_c is the latent heat; Δp is the half-depth of the free atmosphere; ω'_e represents vertical p-velocity at the top of the PBL; and $\bar{q}_e$, $\bar{q}_2$, and $\bar{q}_1$ denote the background mean-specific humidity in the boundary layer, lower, and upper troposphere, respectively.

The PBL momentum equation satisfies three-force balance among the pressure gradient force, the Coriolis force, and the Rayleigh friction. The PBL momentum equations take the form of

$$\beta y v'_B - \frac{\partial \phi'_e}{\partial x} - E_x u'_B = 0, \tag{3.4a}$$

$$-\beta y u'_B - \frac{\partial \phi'_e}{\partial y} - E_y v'_B = 0, \tag{3.4b}$$

$$\omega'_e = (p_s - p_e)\left(\frac{\partial u'_B}{\partial x} + \frac{\partial v'_B}{\partial y}\right), \tag{3.4c}$$

where p_s is pressure at the model surface; ϕ'_e represents perturbation geopotential at top of PBL (p_e); u'_B and v'_B are vertically averaged zonal and meridional winds in the boundary layer; and E_x and E_y are Rayleigh friction coefficients in the zonal and meridional directions, respectively. The reason for the use of different zonal and meridional Rayleigh friction coefficients was discussed in Li and Wang (1994b).

The equations above form a closed set of equations with the approximation that the perturbation geopotential ϕ'_e equals to lower-troposphere ϕ'. The model was solved numerically with a tropical channel from 40°S to 40°N and a spatial grid box of 5° longitude by 2° latitude. The perturbation moisture was neglected, while the mean moisture is determined by an empirical formula relating to SST (Li and Wang 1994b). A constant SST of 29 °C was specified in Wang and Li (1994). A realistic SST distribution was specified in an accompanying paper (Li and Wang 1994a).

Figure 3.4 shows the evolution of the model-simulated MJO. The phase propagation speed is about 10–15 m/s, which is faster than the observed. When a longitudinally dependent SST is specified, the model is able to capture slower (faster) propagation in the warm pool (cold tongue) (Li and Wang 1994a).

A special feature of simulated MJO in the 2.5-layer model is that PBL convergence leads the convection, similar to the observation. The fundamental cause of eastward propagation in the model is attributed to the heating parameterization. On the one hand, mid-tropospheric heating associated with MJO convection forces a baroclinic Rossby wave response to the west and a baroclinic Kelvin wave response to the east, forming a horizontal pattern of the Kelvin–Rossby wave couplet. On the other hand, PBL convergence induced by a low-pressure anomaly at top of PBL

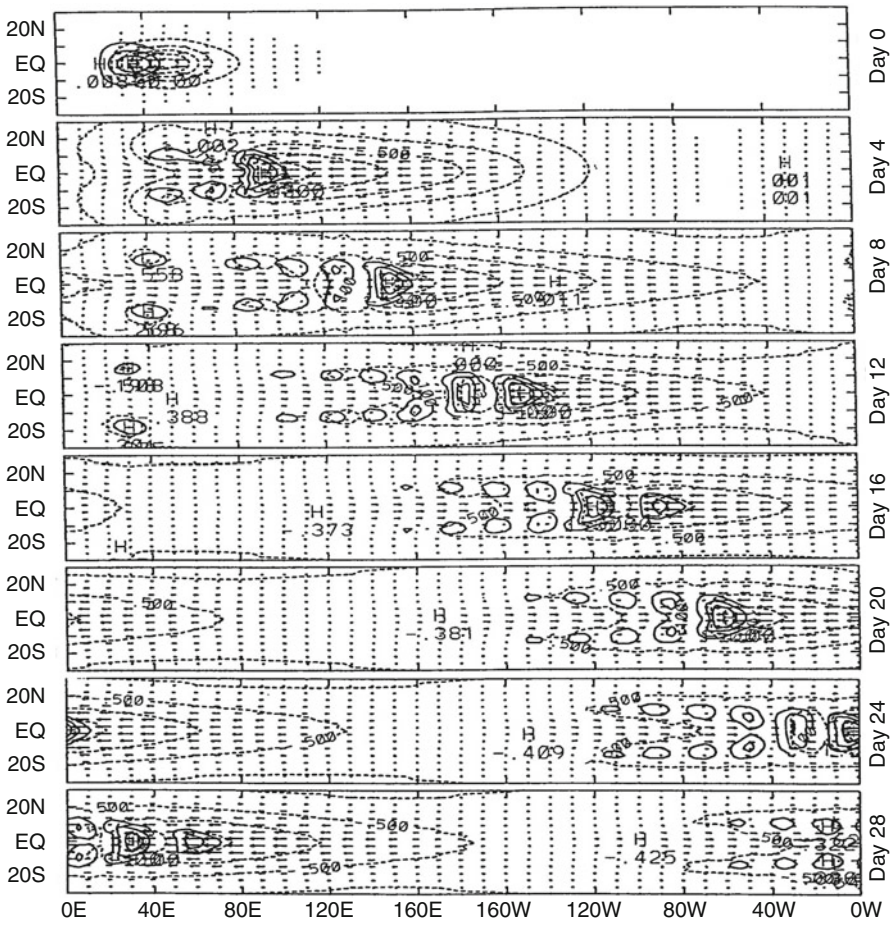

Fig. 3.4 Evolution patterns of rainfall (contour), low-level wind (vector), and low-level geopotential height (contour) fields simulated by Wang and Li (1994) (© Copyright 1994 American Meteorological Society (AMS))

associated with the free-atmospheric Kelvin wave response shifts the heating to the east of the MJO convection, leading to an eastward heating tendency. As a result of the free-atmospheric wave–PBL–convection interaction, the MJO envelope moves eastward.

In Wang and Li (1994), the MJO-scale moisture perturbation was intentionally neglected. By doing so, one may simultaneously link mid-tropospheric condensational heating to PBL convergence. However, in reality, there is a gradual upward moistening process. New convection occurs east of the MJO center only when the local atmosphere becomes convectively unstable.

The observed moisture distribution in Fig. 3.3 shows that the mid-tropospheric moisture anomaly is approximately in phase with the MJO convection, while the

specific humidity anomaly in PBL leads the convection. To demonstrate how this PBL moisture asymmetry affects the MJO propagation via atmospheric destabilization, the vertical profile of the intraseasonal equivalent potential temperature (θ_e) was examined. The equivalent potential temperature depends on both the specific humidity and temperature profiles of actual atmosphere. If a layer of air mass is initially moist but unsaturated and within the layer $\partial\theta_e/\partial z < 0$, then we call the layer potentially (or convectively) unstable. If such a layer is brought to saturation by sufficient lifting, the whole layer becomes unstable (Holton 1992; Emanuel 1994).

Figure 3.5 shows an obvious increase of low-level equivalent potential temperature to the east of MJO convection. Defining a convective instability parameter as the difference of equivalent potential temperature between 850–1000 hPa and 400–500 hPa; one may find that the atmosphere becomes more (less) potentially unstable to the east (west) of the MJO convection. Therefore, the low-level moistening is an important precursory signal for setting up of an unstable stratification and for triggering of new convection east of the existing MJO convection.

For an observer at a fixed location, the westward tilting of moisture with height implies that the observer would witness an upward moistening process, that is, the near saturated moist layer develops from near surface and expands gradually toward the middle and upper troposphere (Fig. 3.6). This scenario is consistent with the fact that shallow and congestus clouds appear prior to deep convection (Johnson et al. 1999; Kikuchi and Takayabu 2004; Benedict and Randall 2007). The shallow convection helps transport moisture upward, leading to the continuous development of large-scale convective envelope.

The discussion above suggests that the zonal asymmetry of PBL moisture holds a key for MJO eastward propagation. A natural question is what causes the moisture asymmetry. To address this question, Hsu and Li (2012) diagnosed vertically (1000–700-hPa) integrated moisture budgets. The intraseasonal moisture tendency is determined by the sum of horizontal and vertical moisture advections and the atmospheric apparent moisture sink, Q_2 (Yanai et al. 1973).

$$\frac{\partial q'}{\partial t} = -(\mathbf{V}\cdot\nabla q)' - \left(\omega\frac{\partial q}{\partial p}\right)' - \left(\frac{Q_2}{L}\right)' \tag{3.5}$$

where q is the specific humidity, t is the time, $\mathbf{V}$ is the horizontal wind vector, ∇ is the horizontal gradient operator, p is the pressure, ω is the vertical pressure velocity, Q_2 is the atmospheric apparent moisture sink, and L is the latent heat of condensation. Each term in the left- and right-hand side of Eq. (3.5) is applied with a 20–90-day-filtered operator, integrated from 1000 to 700 hPa.

Figure 3.7 shows the contribution from each of the moisture budget terms in Eq. (3.5). The largest contribution arises from the vertical moisture advection term. In addition, the horizontal moisture advection also contributes to the moistening, although its magnitude is about five times smaller than the vertical advection. The

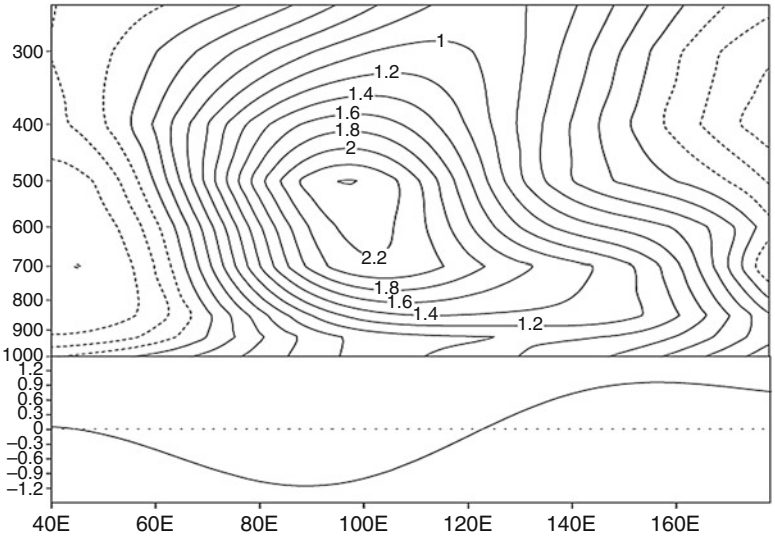

Fig. 3.5 Zonal–vertical distributions of 0°–10°S averaged MJO-scale equivalent potential temperature (θ_e', *upper panel*) and a convective instability index (bottom panel) defined as the difference of θ_e' at the PBL and the middle troposphere. The MJO convective center is located at the central-eastern Indian Ocean at 95°E. Unit: K (From Hsu and Li (2012). © Copyright 2012 American Meteorological Society (AMS))

Q_2 term tends to reduce the moistening in the lower troposphere, due to both precipitation process and reduced surface evaporation east of the convection.

A further decomposition of the vertical moisture advection indicates that the PBL moistening east of the MJO convection is primarily attributed to the vertical advection of the background mean moisture by anomalous ascending motion. Since the anomalous ascending motion is caused by PBL convergence (due to mass continuity), a key question becomes what causes the PBL convergence east of the MJO convection?

Schematic diagram in Fig. 3.8 illustrates key processes that contribute to the zonal asymmetry of PBL convergence. Firstly, mid-tropospheric heating associated with MJO convection induces a baroclinic free-atmospheric response, with a Kelvin (Rossby) wave response to the east (west). The anomalous low pressure at top of the PBL associated with the Kelvin wave response may induce a convergent flow in the PBL. Meanwhile, a PBL divergence occurs at the equator between two Rossby cyclonic gyres west of the convective center. Thus, the heating-induced free-atmospheric wave effect alone can induce an east-west asymmetry in the PBL divergence field. The second process is associated with air–sea interaction. A warm (cold) SSTA is generated to the east (west) of the MJO convection due to reduced (enhanced) surface evaporation. The asymmetric SSTA may induce PBL convergence (divergence) east (west) of the MJO convection, through the Lindzen and Nigam (1987) mechanism discussed in Sect. 1.4. Therefore, the asymmetric PBL

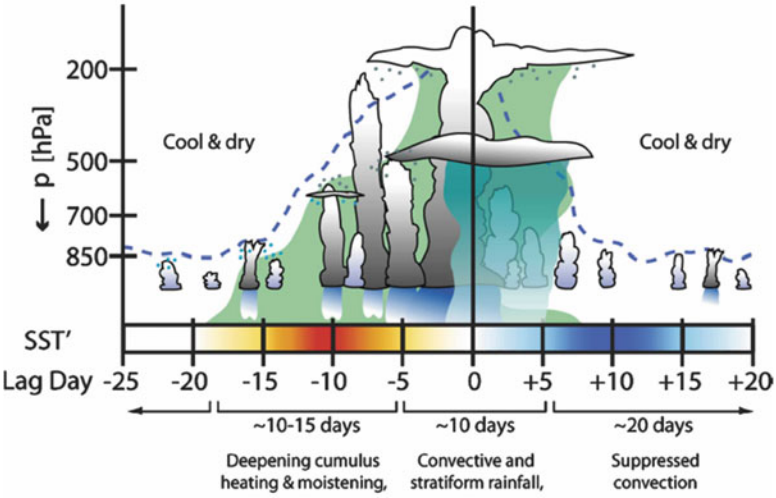

Fig. 3.6 Schematic diagram illustrating temporal phase relationships among anomalous moisture, shallow convection, and deep convection associated with MJO. The horizontal axis denotes lagged days relative to the day of maximum rainfall (day 0). The vertical axis is the pressure. The approximate cloud top is indicated by the *dashed blue line*, while *green* shading represents the general area of positive moisture anomalies. *Light blue dots* above shallower convective clouds represent moistening via detrainment, while *gray dots* below stratiform cloud types represent ice crystal fallout and moistening (From Benedict and Randall (2007). © Copyright 2007 American Meteorological Society (AMS))

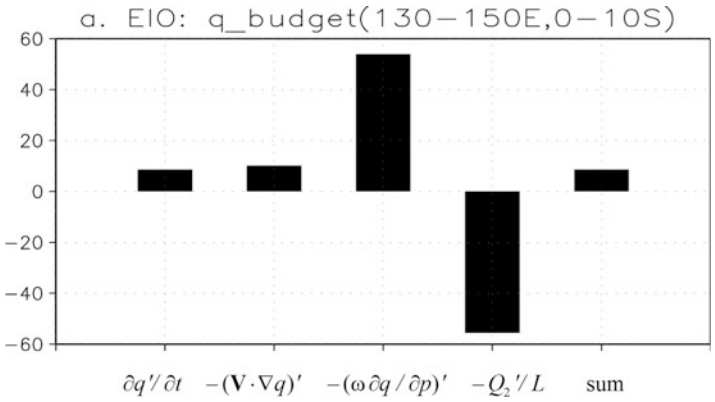

Fig. 3.7 Vertically (1000–700-hPa) integrated intraseasonal moisture budget terms over region (130°–150°E, 0°–10°S) to the east of MJO convective center at 95°E. From left to right: observed specific humidity tendency, horizontal moisture advection, vertical moisture advection, latent heating, and sum of these budget terms. Unit is 10^{-7} kg m^{-2} s^{-1}. ERA-40 data are used (From Hsu and Li (2012). © Copyright 2012 American Meteorological Society (AMS))

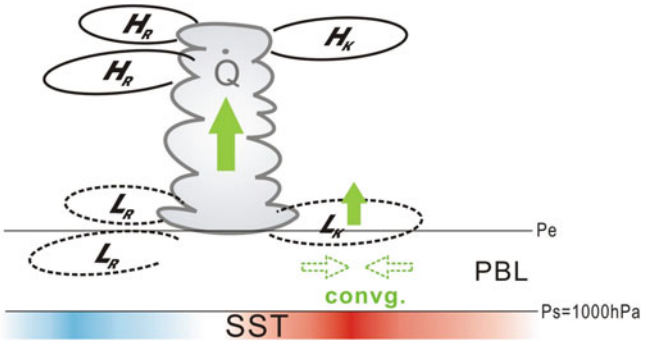

Fig. 3.8 Schematic diagram illustrating boundary layer convergence induced by free-atmospheric wave dynamic and SSTA gradient effect. Cloud stands for the main MJO convective center; solid (*dashed*) curves with H_K (L_K) and H_R (L_R) indicate a high (low)-pressure anomaly associated with Kelvin and Rossby wave response to convective heating; *red* and *blue* shadings denote positive and negative SST anomalies, respectively; *solid green arrows* indicate the anomalous ascending motion; *dashed green arrows* represent the boundary layer convergence; and Ps and Pe are pressure levels at *bottom* and *top* of the PBL, respectively (From Hsu and Li (2012). © Copyright 2012 American Meteorological Society (AMS))

convergence may be induced by both the underlying SSTA and free-atmospheric wave effects.

To examine the relative roles of the SSTA forcing and the heating-induced free-atmospheric wave effects, Hsu and Li (2012) diagnosed the boundary layer momentum budget equation:

$$f\mathbf{k} \times \mathbf{V}'_{\mathbf{B}} + E\mathbf{V}'_{\mathbf{B}} = -\nabla\phi'_e + \frac{R}{2}\frac{(p_s - p_e)}{p_e}\nabla T_s' \tag{3.6}$$

where a prime denotes the MJO-scale variable; f is the Coriolis parameter; $\mathbf{k}$ is the unit vector in the vertical direction; $\mathbf{V_B}$ denotes the vertically averaged horizontal wind in the boundary layer; ∇ is the horizontal gradient operator; ϕ_e denotes the geopotential at the top of the boundary layer; R is the gas constant of air; p_s and p_e are pressures at the bottom and top of the PBL, respectively; T_s is the surface temperature; and E is the friction coefficient and is equal to 10^{-5} s^{-1}.

The first term in the right-hand side of Eq. (3.6) represents the free-atmospheric wave effect, whereas the second term in the right-hand side of Eq. (3.6) represents the SSTA forcing effect. To test the sensitivity of the diagnosis result to the boundary layer depth, two different PBL depths, 1000–850 hPa and 1000–700 hPa, were applied.

The diagnosis of each term in Eq. (3.6) using the ERA40 reanalysis data shows that the free-atmospheric wave effect in response to the MJO heating plays a major role in determining the PBL convergence. It accounts for 90% and 75% of the total boundary layer convergence in the case of $p_e = 850$ and $p_e = 700$, respectively. The warm SST anomaly ahead of MJO convection, on the other hand, also plays a role.

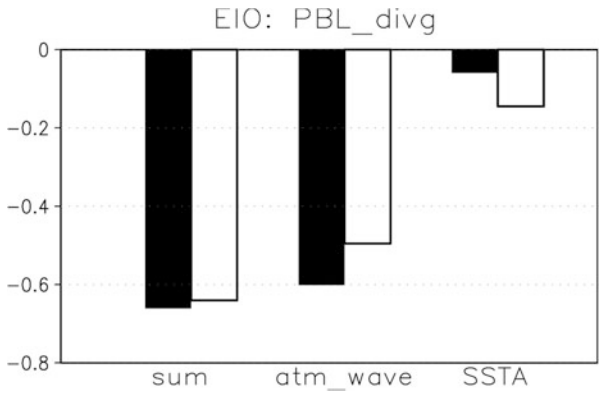

Fig. 3.9 (From *left* to *right*) Total boundary layer convergence averaged over (130°–150°E, 0°–10°S) induced by both the free-atmospheric wave dynamic and SST anomaly and relative contributions of wave dynamic and SSTA effect in the case of $P_e = 850$ hPa (*filled bars*) and $P_e = 700$ hPa (*hollow bars*). Unit is 10^{-6} s^{-1} (From Hsu and Li (2012). © Copyright 2012 American Meteorological Society (AMS))

It contributes about 10–25% to the observed PBL convergence. Because PBL convergence-induced vertical advection is a major factor affecting the low-level moisture asymmetry, the result presented above suggests that both the heating-induced free-atmospheric waves and air–sea interaction contribute to the eastward propagation (Fig. 3.9).

3.4 Initiation Mechanisms

Another fundamental question of MJO dynamics is how it is initiated over the western equatorial Indian Ocean (WIO). A conventional theory is that MJO initiation arises from the circumnavigation of a preceding MJO event that travels around the global tropics (e.g., Lau and Peng 1987; Wang and Li 1994). The premise behind this circumnavigating hypothesis is that the upper-level divergent signal, after decoupled with convection over the Pacific cold tongue, continues moving eastward and triggers new convection after it moves into warmer and moister Indian Ocean. In this scenario, the upper-tropospheric forcing from the upstream (i.e., from west of the initiation region) holds a key in triggering new convection over the WIO. However, as demonstrated later, this circumnavigating process is not crucial for MJO initiation.

In addition to tropical processes, MJO may be triggered by extratropical or mid-latitude processes. For example, a case study by Hsu et al. (1990) suggested that the mid-latitude perturbations may propagate into the tropics and trigger MJO over the WIO. However, specific processes through which mid-latitude waves

induce MJO convection is still unclear. Large samples are needed to derive statistically significant results.

3.4.1 MJO Initiation Processes Revealed from a 20-Year Composite Analysis

Using 20-year (1982–2001) observed OLR and ERA40 reanalysis data, Zhao et al. (2013) examined precursor signals associated with MJO initiation over the WIO. Figure 3.10 illustrates the composite evolution of OLR from day −9 to day 0 at a 3-day interval. Day 0 is referred to a time when MJO convection appears in the central equatorial IO. The OLR evolution maps reveal that the MJO convection was firstly initiated in the southwestern IO, and then it propagates eastward. During its eastward journey, the convection is strengthened and shifts toward the equator.

Based on the composite OLR evolution maps, the region of (20°S–0°N, 50°E–70°E) was defined as the MJO convection initiation region. To reveal precursor signals associated with the convection initiation, Zhao et al. (2013) examined the time evolution of several key variables averaged over the region. Figure 3.11a presents the time evolution of the intraseasonal (20–90-day) OLR anomaly averaged over the initiation region. Note that the OLR anomaly transitions from a positive to a negative value at day −15. Consistent with the OLR transition is the switch of sign of the mid-tropospheric vertical motion, from an anomalous descending motion to an anomalous ascending motion (Fig. 3.11b). Thus day −15 was regarded as the initiation date.

Seven days prior to the initiation date, a marked sign change of the specific humidity and temperature fields appear in the lower troposphere (Fig. 3.11c and d), that is, the lower-tropospheric specific humidity and temperature anomalies transition from a negative value to a positive value 1 week prior to the initiation date. The specific humidity perturbation is initially confined at low level and gradually penetrates into the middle troposphere. At day −15, the positive moisture anomaly has extended up to 500 hPa. The temperature perturbation, on the other hand, is primarily confined below 700 hPa till day −8.

The marked increase of both the lower-tropospheric specific humidity and temperature leads to an increase of equivalent potential temperature (θ_e) and moist static energy (MSE) in the lower troposphere, as shown in Figs. 3.11e, f. The vertical time cross section of θ_e shows that about 1 week prior to the initiation date, a positive θ_e perturbation appears in the lower troposphere. This positive perturbation intensifies rapidly while extending upward, closely following the specific humidity evolution.

The observational analysis above indicates that lower-tropospheric moistening and prior to the convection initiation are crucial for the establishment of a convectively unstable stratification. What processes contribute to the lower-

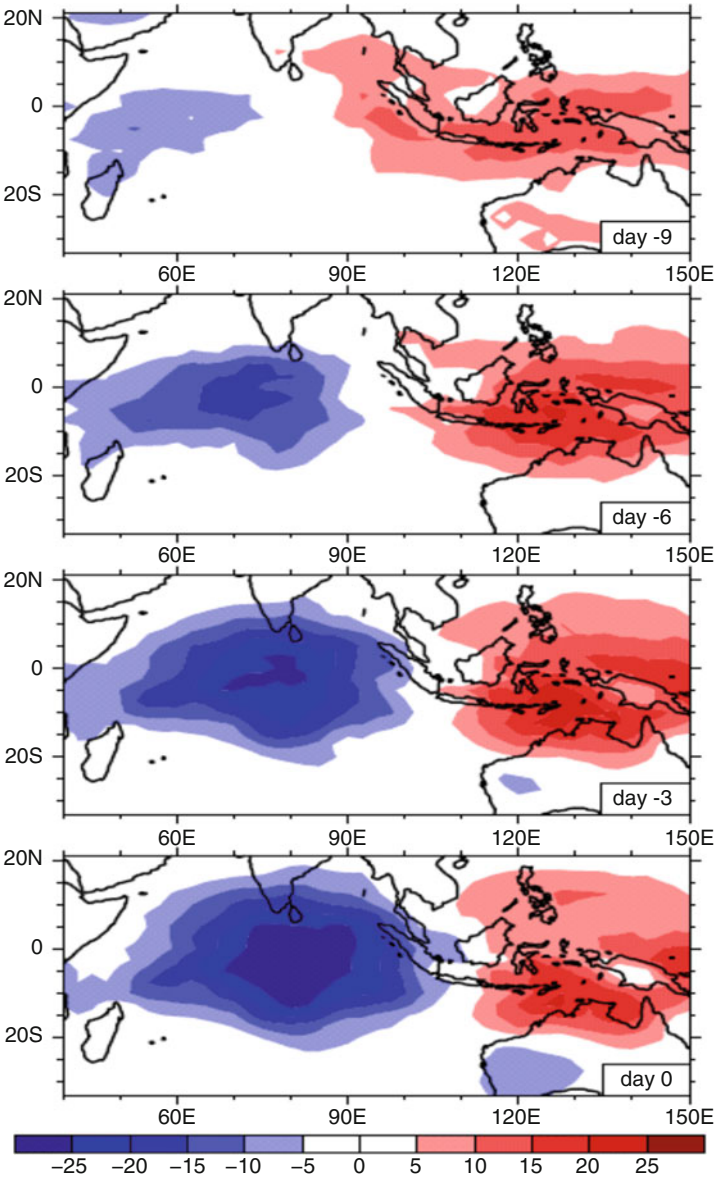

Fig. 3.10 Evolution of the observed composite OLR (unit: W m^{-2}) pattern from day −9 to day 0 at a 3-day interval. The negative OLR represents enhanced MJO convection. Day 0 corresponds to a time when maximum MJO convection is located in the eastern equatorial IO (From Zhao et al. (2013). © Copyright 2013 American Meteorological Society (AMS))

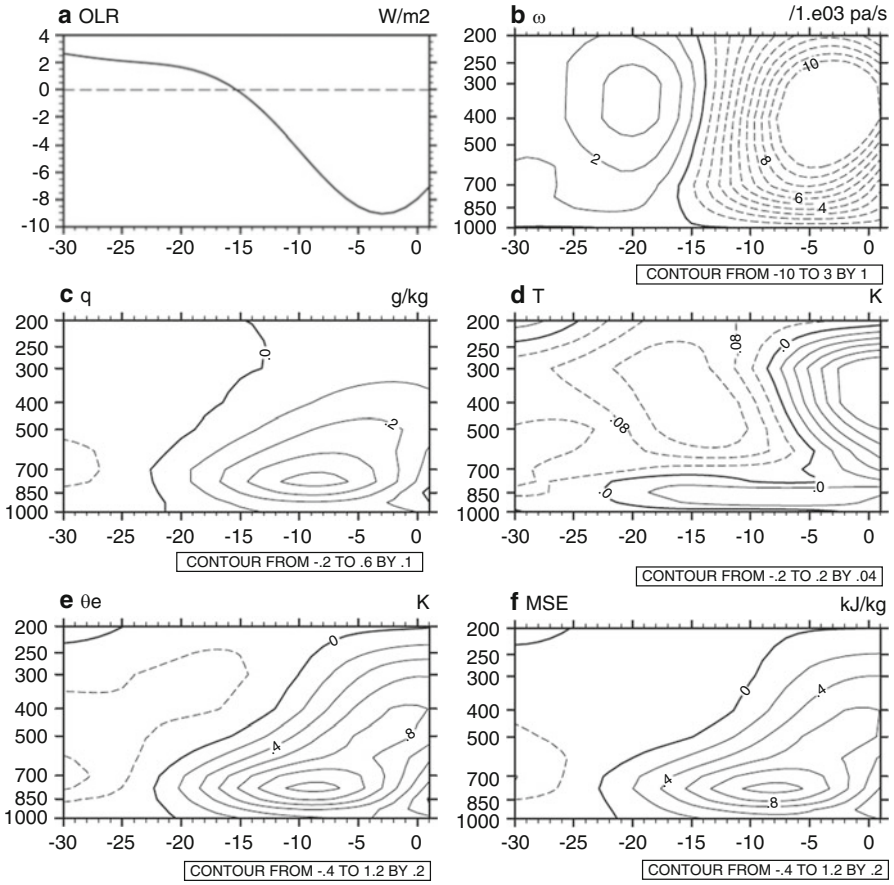

Fig. 3.11 Evolutions of (**a**) the composite intraseasonal OLR anomaly and (**b**–**f**) vertical profiles of intraseasonal vertical velocity, specific humidity, temperature, equivalent potential temperature (θ_e), and moist static energy (MSE) fields averaged over the MJO initiation region (50°–70°E, 20°S–0°N) (From Zhao et al. (2013). © Copyright 2013 American Meteorological Society (AMS))

tropospheric moistening? To address this question, a vertically integrated (from 1000 hPa to 700 hPa) intraseasonal moisture budget was diagnosed.

Figure 3.12 shows the moisture budget diagnosis result. It is clear that the positive moisture tendency during the initiation period (from day −25 to −15) is mainly attributed to the horizontal advection, while the vertical advection (due to subsidence and associated divergence) is against the lower-tropospheric moistening. The result indicates that the lower-tropospheric moistening process during the MJO initiation is very different from that during its eastward propagation. In the latter case, the lower-tropospheric moistening is primarily attributed to the vertical advection associated with PBL convergence (Hsu and Li 2012).

The apparent moisture source term ($-Q_2/L$) plays a minor but positive role in the low-tropospheric moistening. This is because anomalous descending motion

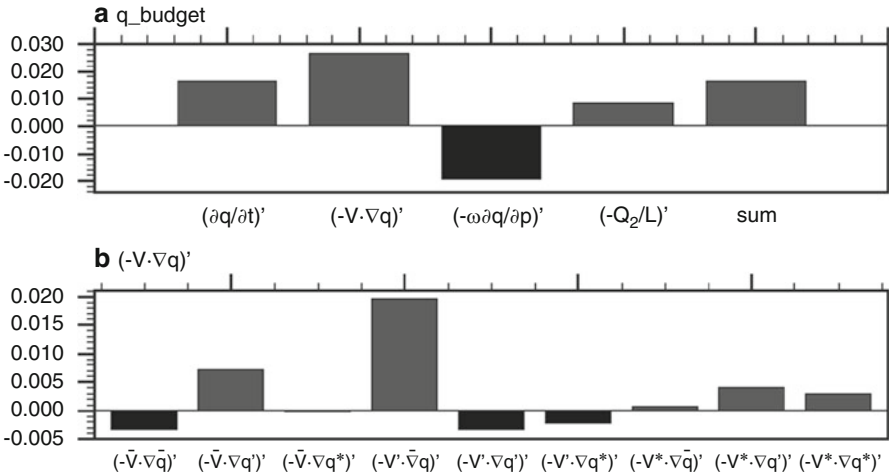

Fig. 3.12 (**a**) 1000 hPa–700 hPa integrated intraseasonal moisture budget terms averaged during the period of day −25 to day −15 over 50°–70°E, 20°S–0°N. From left to right: observed specific humidity tendency, horizontal moisture advection, vertical moisture advection, apparent moisture source, and sum of the last three terms. (**b**) Individual components of the horizontal moisture advection term (From Zhao et al. (2013). © Copyright 2013 American Meteorological Society (AMS))

during the initiation period reduces the mean precipitation, leading to less condensational heating and thus more moisture retained in the atmosphere. The surface latent heat flux anomaly, on the other hand, does not contribute to the moistening during the initiation period (figure not shown).

To examine specific advection processes that contribute to the lower-tropospheric moistening, both the specific humidity and wind fields are decomposed into three components, the low-frequency background state (LFBS, with a period longer than 90 days), the intraseasonal (20–90-day) component, and the high-frequency (with a period less than 20 days) component. Figure 3.12b shows the contributions from each of nine horizontal advection terms. The largest term comes from the advection of the mean moisture by the MJO flow. The second largest term is the advection of anomalous moisture by the LFBS flow.

Figure 3.13 presents the horizontal patterns of the LFBS specific humidity field and the MJO wind perturbation field. Both the background specific humidity and anomalous wind fields were derived based on the time average from day −25 to day −15 and vertical integration from 1000 hPa to 700 hPa. The maximum LFBS specific humidity is located along 10°S, where the seasonal mean convection is also strongest. Note that the MJO flow during the initiation period is dominated by anomalous easterlies and two anticyclonic Rossby gyres over the tropical Indian Ocean. Such a wind anomaly resembles the Gill (1980) pattern and is typically observed when the suppressed MJO convection is located in the eastern Indian Ocean (EIO). A further examination of the intraseasonal OLR field confirms that a maximum positive OLR center associated with MJO is indeed located over the EIO

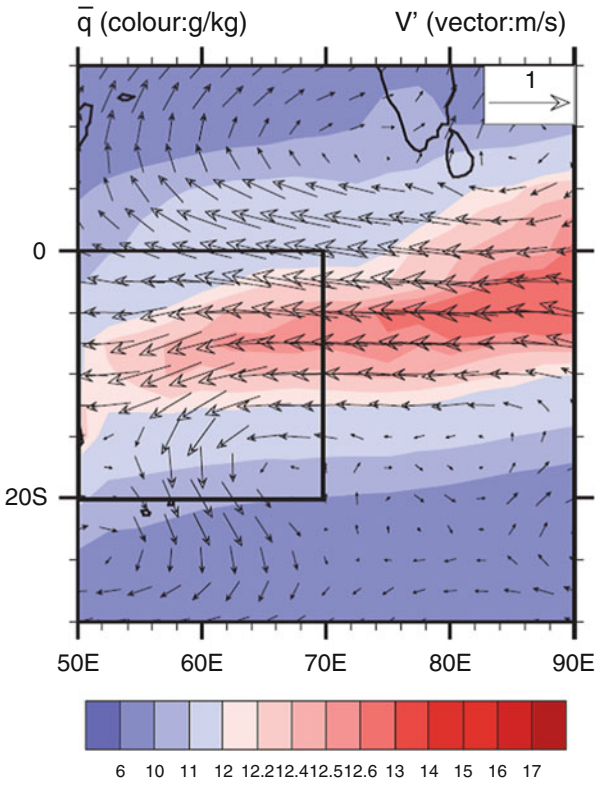

Fig. 3.13 Vertically integrated (from 1000 hPa to 700 hPa) intraseasonal wind and LFBS specific humidity fields averaged during the initiation period (day −25 to day −15) (From Zhao et al. (2013). © Copyright 2013 American Meteorological Society (AMS))

during the period. The anomalous winds advect the background high moisture in such a way that they increase the lower-tropospheric moisture over the initiation region (20°S–0°N, 50°E–70°E).

The moisture budget analysis above reveals that the low-tropospheric moistening prior to the MJO initiation is primarily attributed to the anomalous easterly over the equatorial IO. What causes the anomalous easterly? There are two possible sources in generating the anomalous wind. Firstly, the anomalous easterlies may be a direct Kelvin wave response to a positive MJO heating over western Pacific (Fig. 3.14a). This is possible as the preceding MJO convection travels eastward along the equator after initiated over the WIO. This represents an upstream forcing of the circumnavigating MJO mode. Secondly, the anomalous wind may be a direct Rossby wave response to a negative MJO heating over the EIO (Fig. 3.14b). This is possible because a suppressed-phase MJO, after initiated in the WIO, moves eastward. This scenario represents a downstream forcing of an opposite-phase MJO in the EIO.

By examining the composite OLR and wind evolution maps during the initiation period, Zhao et al. (2013) noted that the anomalous easterlies over the equatorial IO from day −25 to day −15 were primarily driven by the negative heating anomaly

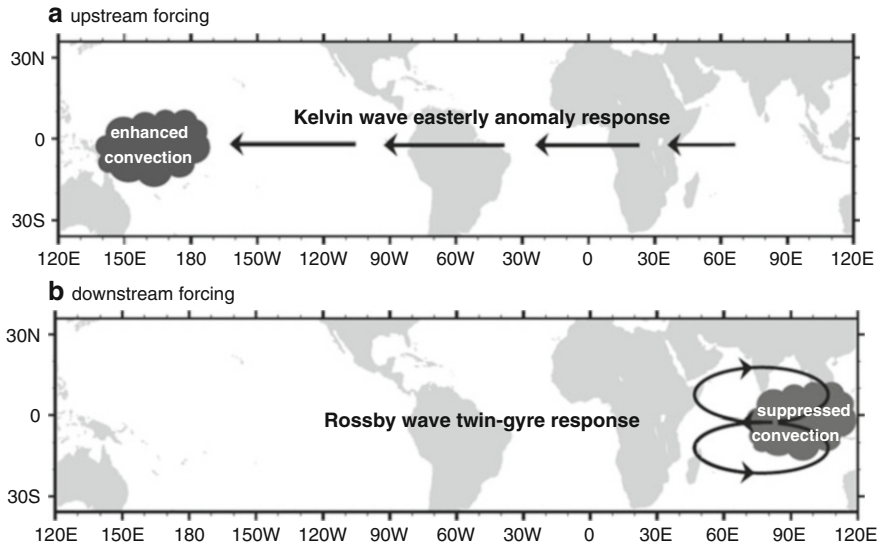

Fig. 3.14 Schematic diagrams illustrating (**a**) an upstream forcing scenario in which a positive MJO heating in the western Pacific may induce an anomalous easterly over the western Indian Ocean (WIO) through Kelvin wave response and (**b**) a downstream forcing scenario in which a negative heating anomaly associated with suppressed-phase MJO may induce twin-gyre circulation in the tropical Indian Ocean through Rossby wave response (From Zhao et al. (2013). © Copyright 2013 American Meteorological Society (AMS))

over the EIO, not the preceding convective MJO phase in the western equatorial Pacific. Thus, the initiation of new convection over WIO is a direct Rossby wave response to the preceding suppressed MJO heating over the EIO.

To obtain the statistically robust signal of the mid-latitude impact, Zhao et al. (2013) examined the upper-tropospheric (200 hPa) geopotential height anomaly pattern and associated wave activity flux during the initiation period for all cases (Fig. 3.15). Note that the geopotential height anomaly displays a wave train pattern, with high-pressure centers located southeast of South America and southeast of Africa and low-pressure centers in between and to the east of Madagascar.

To illustrate wave energy dispersion characteristics, a phase-independent wave activity flux was calculated following Takaya and Nakamura (2001):

$$\mathrm{W} = \frac{1}{2|\bar{\mathrm{u}}|}\begin{pmatrix} \bar{u}\left(\psi'^{2}{}_{x} - \psi'\psi'_{xx}\right) + \bar{v}\left(\psi'_{x}\psi'_{y} - \psi'\psi'_{xy}\right) \\ \bar{u}\left(\psi'_{x}\psi'_{y} - \psi'\psi'_{xy}\right) + \bar{v}\left(\psi'^{2}{}_{y} - \psi'\psi'_{yy}\right) \end{pmatrix} \tag{3.7}$$

where a bar and a prime denote the LFBS and the intraseasonal anomaly, W represents the horizontal wave activity flux, u and v are zonal and meridional wind velocity, and ψ denotes the stream function.

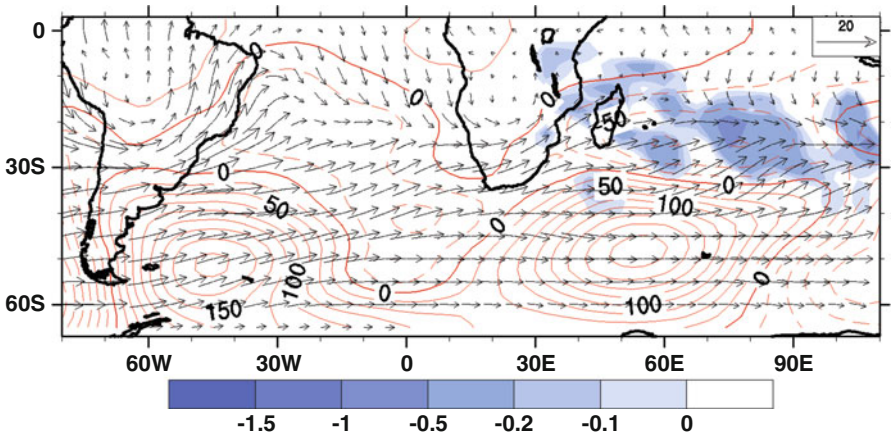

Fig. 3.15 20–90-day filtered observed geopotential height anomaly (contour, unit: $m^2\ s^{-2}$), Rossby wave activity flux (vector, unit: $m^2\ s^{-2}$), and wave flux divergence (color, unit: 10^{-5} ms^{-2}, only negative values are shaded over the Indian Ocean) at 200 hPa during the initiation period from day −25 to day −15 (From Zhao et al. (2013). © Copyright 2013 American Meteorological Society (AMS))

Figure 3.15 shows that there are pronounced eastward wave activity fluxes over mid-latitude southern hemisphere, indicating that the Rossby wave energy propagates eastward. The eastward wave activity fluxes turn northward and converge onto the tropical Indian Ocean between 10°S and 30°S. The wave flux convergence implies that the wave energy is accumulated over the region. A similar wave activity flux feature is also found in the lower-tropospheric geopotential height anomaly field (figure not shown), indicating that the Rossby wave train has an equivalent barotropic structure. Thus, the southern hemisphere mid-latitude Rossby wave perturbations may trigger MJO initiation in the tropical Indian Ocean through wave energy accumulation.

The observational analysis above suggests that the circumnavigating signal around the globe is not critical for MJO initiation in WIO. To further support this claim, idealized numerical experiments with ECHAM4 were conducted. In a control experiment, the model was integrated for 20 years with specified climatologic monthly SST. In a sensitivity experiment (named EXP_TA), the eastward-propagating intraseasonal signal was suppressed over the tropical Atlantic region (20°S–20°N, 60°W–20°E). For detailed model experiment designs, readers are referred to Zhao et al. (2013). Figure 3.16 shows the power spectrum of simulated intraseasonal OLR fields from both the control experiment and the EXP_TA run based on a wavenumber–frequency analysis. The magnitudes of averaged 20–90-day OLR spectrum for zonal wavenumber 1 in both the experiments are quite similar. This points out that the overall eastward-propagating MJO variance has little change even though the circumnavigating mode is greatly suppressed.

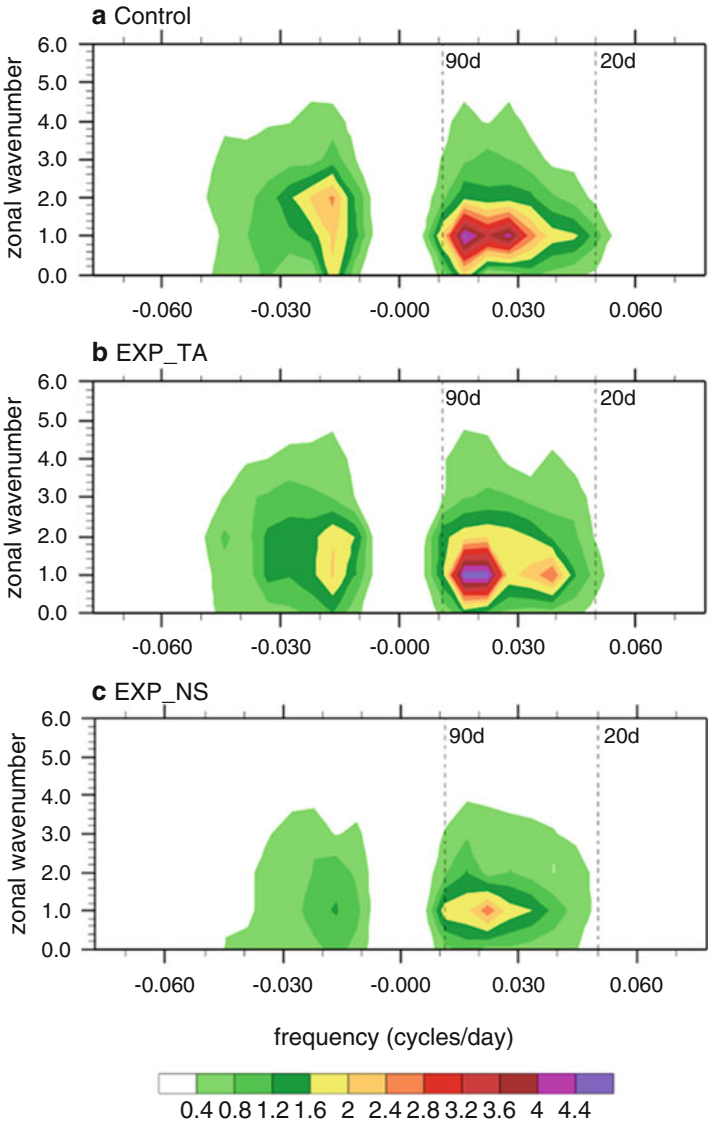

Fig. 3.16 Wavenumber–frequency spectra (unit: $W^2\ m^{-4}$) of the intraseasonal OLR anomaly derived from the 20-year simulation of the Control (*top*), EXP_TA (*middle*), and EXP_NS (*bottom*) experiments. The spectrum analysis was done for a limited domain over (40°E–180°E, 20°N–20°S) (From Zhao et al. (2013). © Copyright 2013 American Meteorological Society (AMS))

The role of the mid-latitude forcing effect was examined through additional sensitivity experiments. In EXP_NS, a Newtonian damping was applied over two latitudinal zones, 20°S–30°S and 20°N–30°N, to force the model prognostic

variables toward the controlled climatologic annual cycle in the two zones. By doing so, the intraseasonal and higher-frequency variability over the zones was greatly suppressed, and tropics–mid-latitude connection was broken. As a result, the mid-latitude influence on the tropical MJO variability was intentionally suppressed. By comparing the intraseasonal OLR spectrum in the control run and the EXP_NS run (bottom panel of Fig. 3.16), one can see that the MJO variability in the tropics weakens significantly. The averaged spectrum for zonal wavenumber 1 and 20–90-day period was reduced by 45%. Thus, the numerical result confirms that the remote forcing from mid-latitudes is important in affecting the overall MJO variance in the tropics.

To further understand the relative role of southern hemisphere (SH) and northern hemisphere (NH) mid-latitude forcing effect, two additional sensitivity experiments named as "EXP_SH" and "EXP_NH" were conducted. In EXP_SH (EXP_NH) run, the equatorward propagation of SH (NH) mid-latitude waves was blocked. Compared to the control run, the averaged spectrum for zonal wavenumber 1 and 20–90-day period in the EXP_SH (EXP_NH) was reduced by 42% (7%). Thus, the sensitivity experiments indicate that most of the spectrum reduction in EXP_NS was attributed to the SH wave effect. Therefore, the remote forcing from mid-latitude SH is crucial for triggering MJO convection in boreal winter.

3.4.2 MJO Initiation Processes Revealed from DYNAMO Case Study

A multination joint field campaign named DYNAMO/CINDY2011 (Dynamics of MJO/ Cooperative Indian Ocean Experiment on Intraseasonal Variability in Year 2011) took place in the equatorial IO in late 2011. During the campaign period, two strong MJO events occurred from middle of October to middle of December (referred to as MJO I and MJO II, respectively; see Fig. 3.17). Based on the rainfall Hovmöller diagram, the two MJO events were initiated over the western equatorial Indian Ocean (WIO) around 50°–60°E. Using multiple observational data products (ERA-Interim, ECMWF final analysis, and NASA MERRA), specific processes that triggered the MJO convection were examined.

It was found that MJO initiation processes are quite different for the two events. Ten days prior to MJO I initiation, a marked large-scale ascending motion anomaly appeared in the lower troposphere over the WIO. Initially near the surface, the ascending motion anomaly gradually deepened into the upper troposphere. A positive specific humidity anomaly also appeared in the lower troposphere prior to the initiation date, but it lagged the anomalous ascending motion by 5 days (Fig. 3.18c). A low-level moisture budget diagnosis indicates that the moistening during Oct. 9–13 was attributed to anomalous vertical advection. A key question

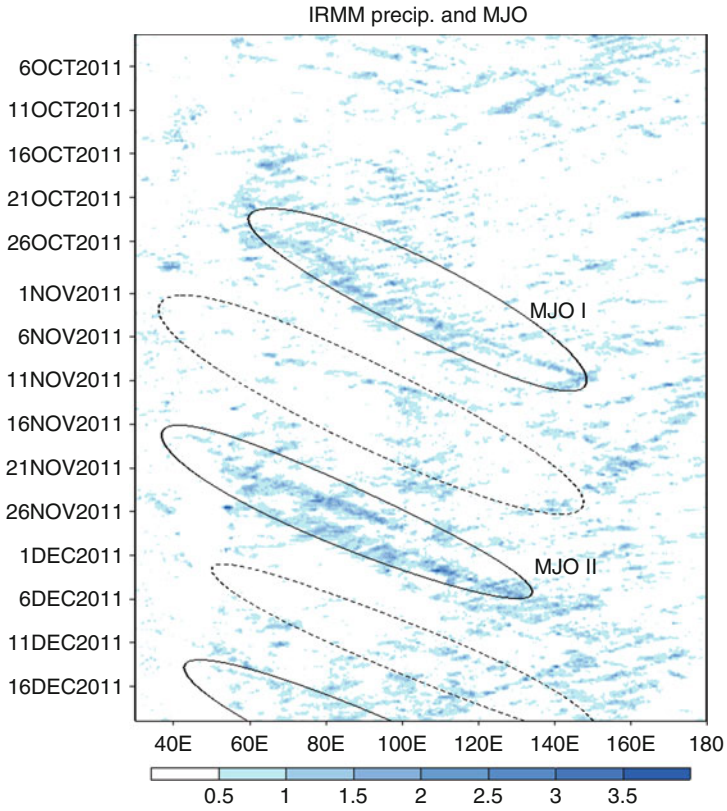

Fig. 3.17 Time–longitude section of observed rainfall (unit: mm/day) averaged along 10°S–10°N using the TRMM precipitation data. Contours denote the MJO-filtered rainfall based on the Wheeler–Kiladis wavenumber–frequency filtering

then is what caused the anomalous ascending motion during the earlier initiation stage (Oct. 5–8)?

The diagnosis of vertically integrated (1000–700 hPa) temperature budget reveals that the ascending motion is triggered by anomalous warm horizontal advection (Fig. 3.19a). The warm horizontal advection was balanced approximately by the adiabatic cooling term, while local temperature tendency is relatively small (Fig. 3.19a). This warm advection – adiabatic – cooling feature is robust among the three different reanalysis datasets. This warm advective effect acts in a similar way as that discussed in the traditional omega equation for a quasi-geostrophic system (Holton 1992).

A further decomposition of the horizontal temperature advection reveals that the warm advection was primarily caused by advection of mean high temperature by a large-scale cyclonic gyre anomaly over the northern IO (Fig. 3.19b). This large-scale cyclonic gyre was a Rossby wave response to positive heating anomalies over the off-equatorial western Pacific and South China Sea (SCS). The anomalous

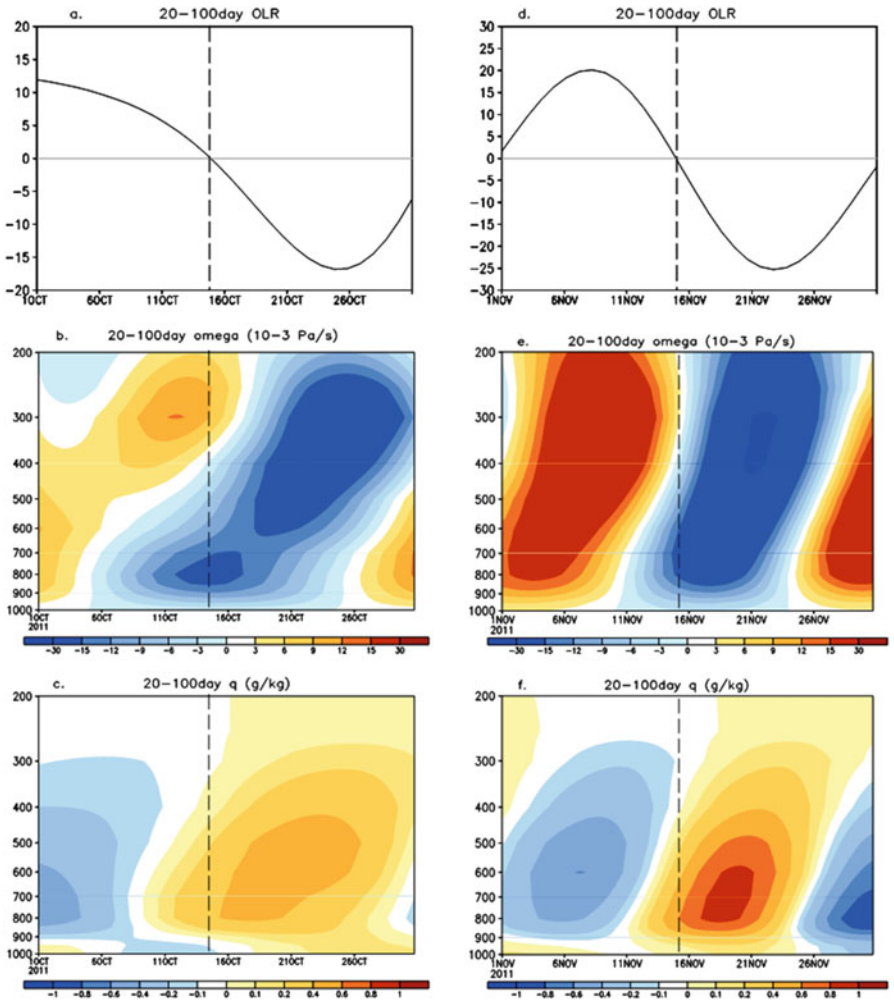

Fig. 3.18 Evolutions of (**a**) 20–100-day filtered OLR anomaly and (**b–c**) vertical profiles of intraseasonal vertical velocity and specific humidity anomalies during Oct. 2011 averaged over the MJO I initiation regions. The vertical velocity and specific humidity fields are the ensemble average of ERA-interim, ECMWF FNL, and MERRA datasets for both the initiation domains (50°–60°E, 5°S–5°N) and (45°–65°E, 10°S–10°N). (**d–f**) as in (**a–c**) but during Nov. 2011 (From Li et al. (2015). © Copyright 2015 American Meteorological Society (AMS))

cyclonic gyre and the western Pacific heat source persisted from October 1 to October 8.

Different from MJO I, precursor signals associated with MJO II were characterized by the occurrence of positive specific humidity and ascending motion anomalies (Figs. 3.18e–f), 4 days prior to the initiation date (which was defined at Nov. 14 according to the anomalous OLR evolution, Fig. 3.18d). To quantitatively

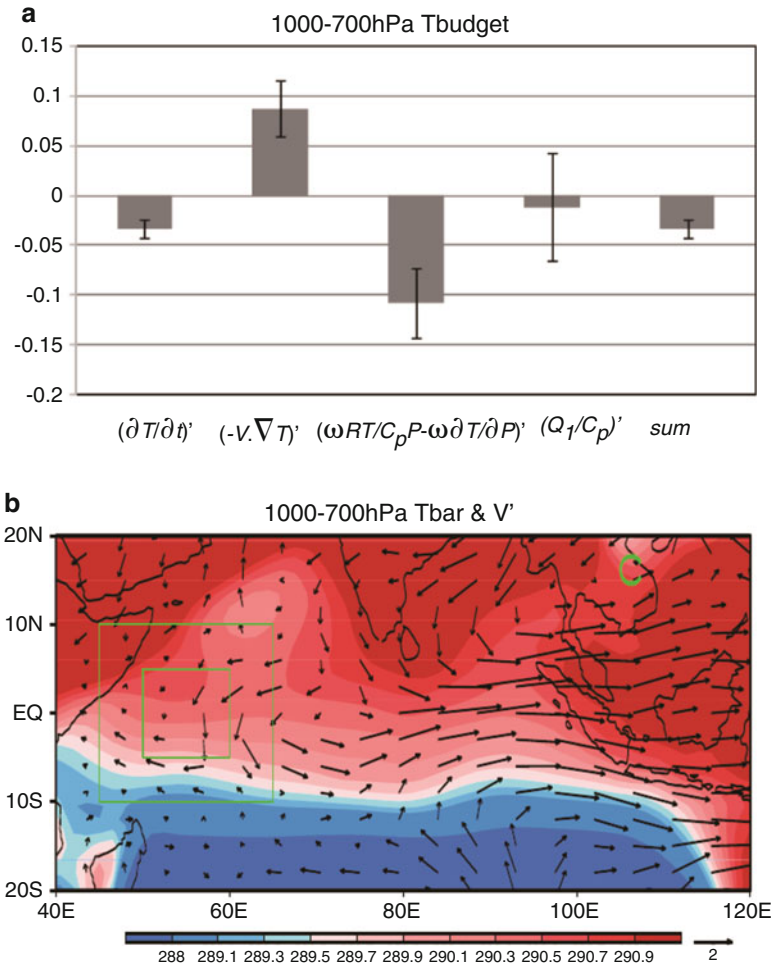

Fig. 3.19 Vertically integrated (1000–700 hPa) (**a**) temperature budget terms (unit: K day^{-1}) averaged during Oct. 5–8. The result is based on the ensemble average of ERA-Interim, ECMWF FNL, and MERRA with two initiation domains (50°–60°E, 5°S–5°N) and (45°–65°E, 10°S–10°N) shown in *green boxes* in **b**. Bars with whiskers indicate a standard deviation of six ensemble members. (**b**) Anomalous wind (vector; unit, m/s) and mean temperature (*shading*; unit, K) fields at 850 hPa. Symbol "C" denotes the center of the anomalous cyclonic gyre (From Li et al. (2015). © Copyright 2015 American Meteorological Society (AMS))

examine the cause of low-level moistening, a vertically (1000–700 hPa) integrated moisture budget analysis was performed, and the result shows that the moistening during the initiation period (Nov. 10–13) is attributed to both the horizontal and vertical advections.

To sum up, the MJO II initiation process resembles that of the 20-year composite analysis (Zhao et al. 2013), that is, lower-tropospheric moistening was attributed to the moisture advection by anomalous easterlies over the equatorial IO. It was a

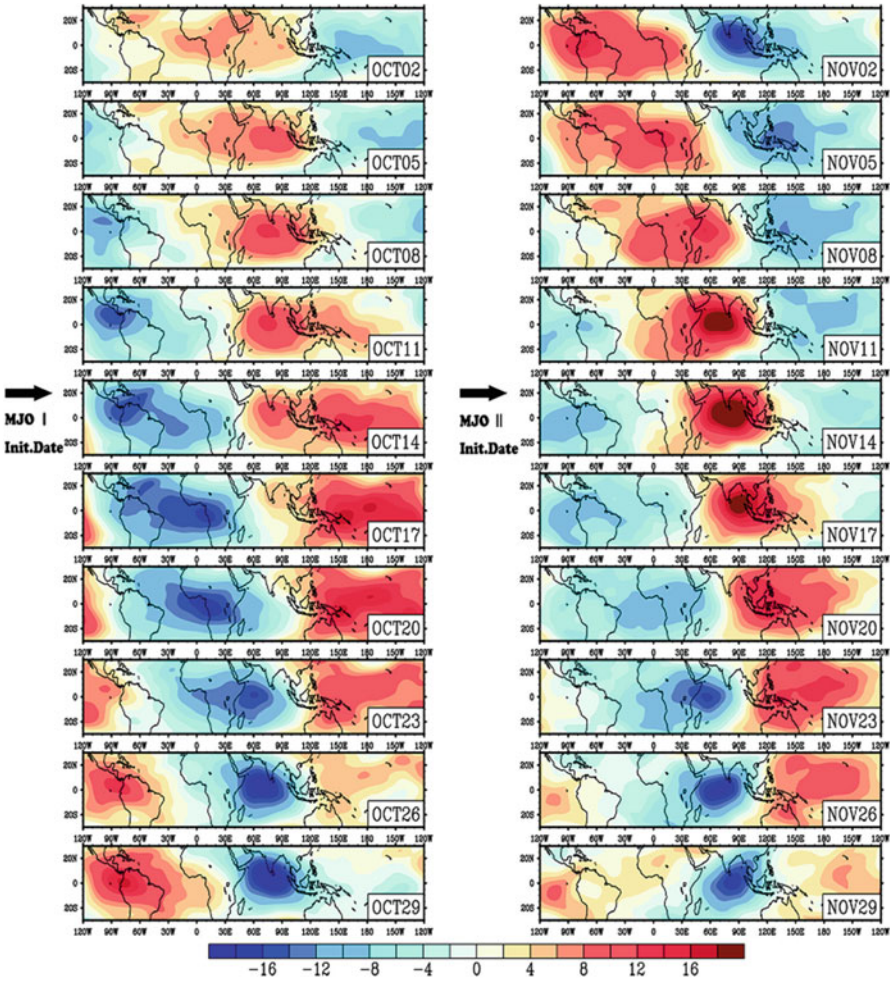

Fig. 3.20 Evolution of the 20–100-day filtered velocity potential field at 200 hPa (color; unit, 10^6 m^2 s^{-1}) in October (*left*) and November (*right*) 2011 based on the three dataset ensemble. *Red* (*blue*) denotes upper-level convergence (divergence). *Black arrows* indicate the initiation dates for MJO I and II, respectively (From Li et al. (2015). © Copyright 2015 American Meteorological Society (AMS))

successive event. MJO I, on the other hand, is a primary event, forced by low-frequency heat source in SCS/western Pacific. The contrast of anomalous precursor winds at the equator (westerly vs. easterly) implies different triggering mechanisms for the MJO I and II events.

An important issue related to MJO initiation is what is the role of global circumnavigation of upper-tropospheric divergent signals associated with a preceding MJO? From the evolution maps of the 20–100-day filtered upper-tropospheric velocity potential field (Fig. 3.20), one can see that on both the initiation dates (Oct.

14 and Nov. 14), anomalous upper-tropospheric divergence centers appeared over the South America/Atlantic sector, far away from the WIO. The upper-tropospheric divergence centers arrived over the WIO around Oct. 23 and Nov. 23, 9 days after the MJO initiation. This indicates that the upper-tropospheric forcing did not contribute to the occurrence of precursor low-level ascending motion and moisture signals over the WIO for both the events.

3.4.3 *Understanding MJO Initiation from an Air–Sea Interaction Point of View*

TRMM microwave imager (TMI) measurements reveal a season-dependent feature of intraseasonal SST variability in the tropical Indian Ocean. The amplitude of intraseasonal SST variability is strongest in boreal winter along 5–10°S and become much weaker in boreal summer. The cause of this seasonal dependence was studied using a 2.5-layer ocean model forced by ERA40 reanalysis products during 1987–2001 (Li et al. 2008). It is found that the seasonal change of background zonal wind is critical in allowing anomalous shortwave radiation and latent heat flux/ocean entrainment being in phase during boreal winter but being out of phase during boreal summer.

The strong intraseasonal SST variability in boreal winter poses an interesting question, namely, does a SST anomaly induced by a preceding eastward-propagating MJO exert a delayed effect to the initiation of subsequent opposite-phase MJO?

Figure 3.21 shows the SSTA pattern and evolution associated with eastward propagation of intraseasonal OLR and wind stress anomalies. In pentad −1, westerly wind stress and negative OLR signals associated with an active phase of MJO appear in the tropical Indian Ocean. Since the background wind is westerly in the vicinity of this latitude in boreal winter, a positive zonal wind stress anomaly increases the evaporative cooling in the region. This gives rise to the in-phase relationship between the anomalous surface shortwave radiation and the latent heat flux, and together they act with the ocean entrainment to strongly cool the SST. As a result, in pentad 0 and +1, a cold SSTA develops over the western to central Indian Ocean along ~10°S. In pentad +2, as the active MJO phase almost passes the entire Indian Ocean domain, the SSTA remains negative over the entire tropical Indian Ocean. At this time, a weak suppressed convective phase appears at about 55–60°E, collocated with the cold SSTA center. The positive OLR anomaly subsequently expands eastward and grows.

It is noteworthy that suppressed convection tends to develop over the location where cold SSTA is already present for 5–10 days, as inferred from the sequence of charts from pentad +1 to +3. This phase relationship between the SST and convection implies a delayed two-way air–sea interaction scenario for the MJO, this is, on the one hand, an ocean cooling induced by the active (westerly) phase of the MJO

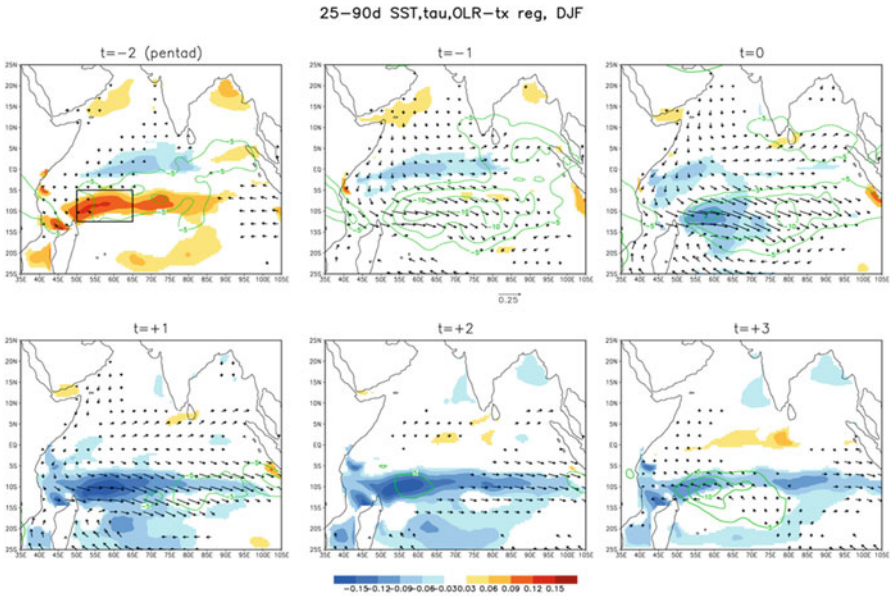

Fig. 3.21 Evolutions of regressed SSTA (*shading*), surface wind stress (*arrow*), and OLR (*red contours* for positive and *green contours* for negative values, starting from $+5\text{Wm}^{-2}$; interval, 2.5Wm^{-2}) anomalies from pentad -2 to $+3$, regressed against the SSTA over the southwestern Indian Ocean box (shown in *top right panel*) in DJF. Wind stress and SST (OLR) anomalies exceeding a 95% (90%) significance level were plotted

through combined cloud radiative forcing and surface evaporation/ocean vertical mixing, and, on the other hand, the so-induced western Indian Ocean cold SSTA in turn initiates a subsequent inactive (easterly) phase of the MJO. Thus, air–sea interactions may play a role in the initiation of the successive MJO events over the western Indian Ocean during boreal winter.

To summarize, two initiation processes are identified for successive MJO events. They are low-level moisture accumulation due to horizontal advection of anomalous easterlies induced by Rossby wave downstream effect of a preceding inactive phase of MJO and a forcing of warm SSTA in WIO induced by preceding suppressed-phase MJO. For primary events, MJO may be triggered by either warm advection-induced anomalous ascending motion or convergence of wave activity flux from extratropics.

3.5 Boreal Summer Intraseasonal Oscillation (BSISO)

Tropical intraseasonal oscillations (ISOs) exhibit pronounced seasonality in its intensity, frequency (Hartmann et al. 1992), and movement (Wang and Rui 1990; Wu et al. 2005). In boreal winter, it is dominated by the eastward propagation MJO

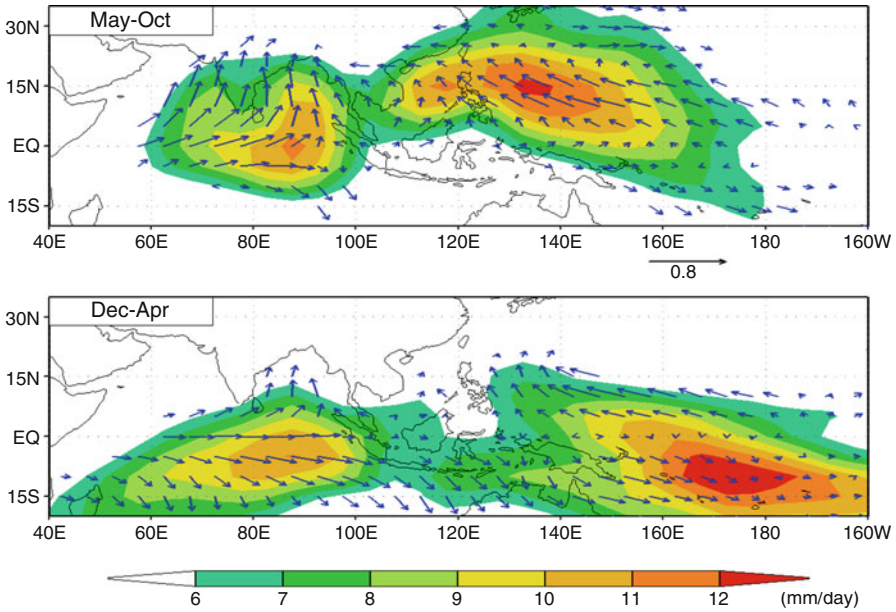

Fig. 3.22 Standard deviation of 20–80-day filtered precipitation anomalies (shaded; unit, mm/day) and the precipitation propagation vector during northern summer in May to October (*upper*) and northern winter in December to April (*bottom*). The data used for this analysis are CMAP rainfall during 1979–1998

mode, but in boreal summer the eastward-propagating mode substantially weakens, whereas northward propagation prevails in the Indian monsoon region (Yasunari 1979, 1980; Hartmann and Michelsen 1989; Gadgil and Srinivasan 1990; Gautier and Di Julio 1990; Wang and Rui 1990) and the northwestward propagation prevails over the western North Pacific (WNP) (Murakami 1980; Lau and Chan 1986; Knutson and Weickmann 1987; Nitta 1987; Chen and Murakami 1988; Hsu and Weng 2001). Due to distinctive characteristics in winter and summer, in this book we refer boreal winter ISO as MJO and boreal summer ISO as BSISO.

Figure 3.22 shows the standard deviation of 20–80-day filtered rainfall anomalies and MJO propagation vectors in boreal winter and summer. Here the propagation vectors were calculated based on the lead–lag correlation maps of localized intraseasonal rainfall centers. Focusing on strong MJO variance regions, one can see that major convective branches associated with MJO in northern winter are confined south of the equator and propagate eastward, whereas major convective activity associated with MJO in northern summer is confined north of the equator and propagate northward in northern IO and northwestward in WNP.

Figure 3.23 illustrates the temporal evolution patterns of OLR anomalies associated with the northward propagation of BSISO. A negative sign has multiplied to the original OLR anomalies so that a positive value denotes an enhanced

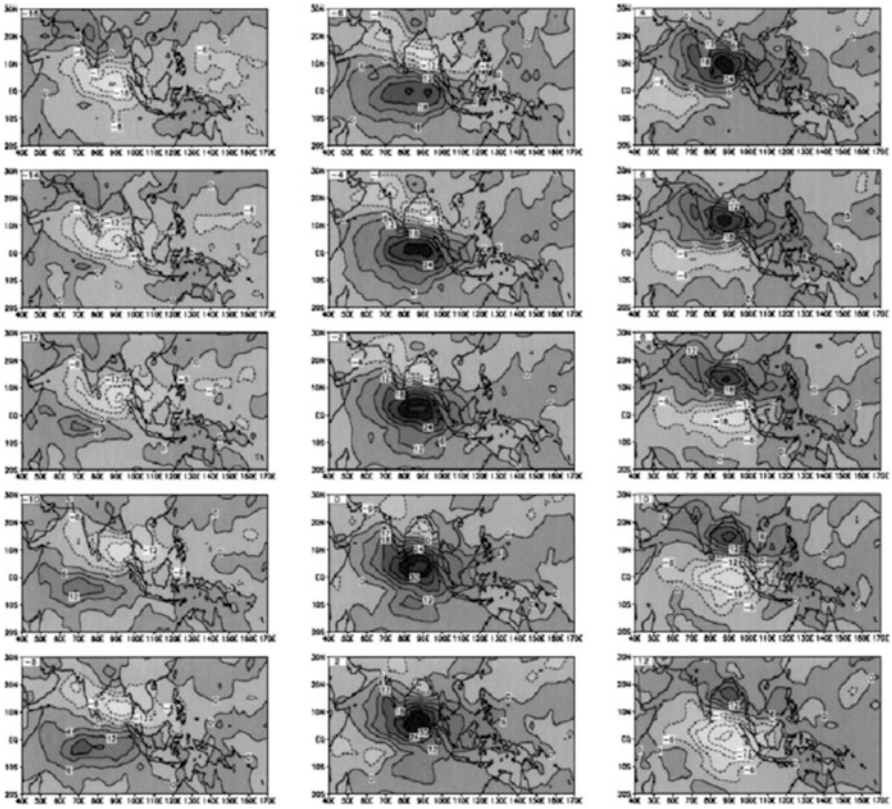

Fig. 3.23 Two-day sequence of the OLR anomaly in boreal summer associated with 20–80-day filtered OLR time series at 5°N, 90°E. A negative sign has multiplied to the OLR field (From Jiang et al. (2004). © Copyright 2004 American Meteorological Society (AMS))

convection anomaly. Note that after the convection initiates in the western IO, it grows as it moves eastward along the equator. After arriving over the eastern IO, major convective branch associated with BSISO moves northward over the Bay of Bengal (BoB). The average speed of the northward propagation is about one degree per day (or 1 m/s). At day 0 or 2, a northwest–southeast-oriented rainband structure, expanding from India/northern Arabian Sea to Maritime Continent, is clearly seen.

To reveal mechanisms that give rise to the northward propagation of the BSISO, Jiang et al. (2004) analyzed both the observations (NCEP reanalysis) and atmospheric general circulation model (ECHAM4) simulations. Daily NCEP–NCAR reanalysis dataset for a period from 1980 to 2001 is used. The horizontal resolution of the reanalysis data is 2.5° longitude by 2.5° latitude, and vertically there are 12 pressure levels. Time filtering is applied to each meteorological field for both the model output and the NCEP–NCAR reanalysis.

Figure 3.24 shows the meridional–vertical structure of the composite BSISO mode from NCEP reanalysis. To clearly illustrate the meridional phase relationship,

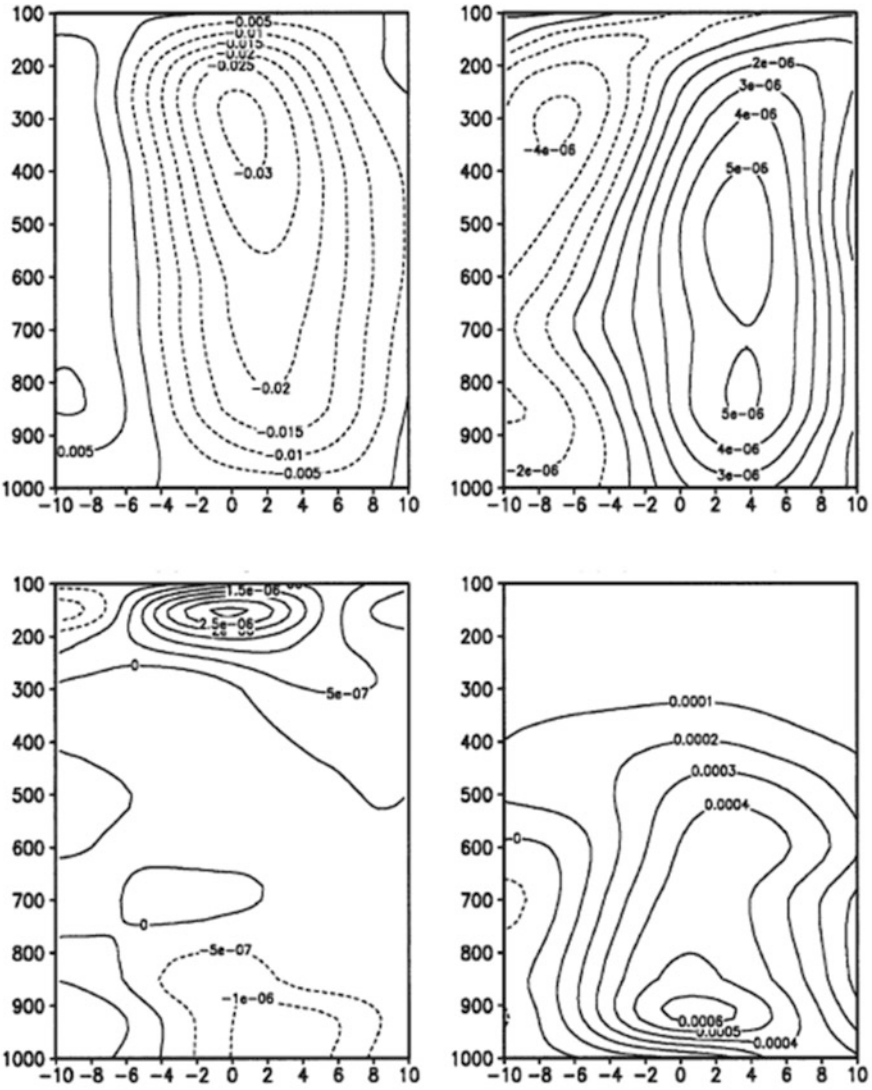

Fig. 3.24 The composite meridional–vertical structure of the 20–80-day filtered p-vertical motion (*top left*), divergence (*bottom left*), vorticity (*top right*), and specific humidity (*bottom right*) fields of the northward-propagating BSISO mode derived from NCEP reanalysis fields during 1980–2001. Positive (negative) values in the x-axis represent the latitude (unit, degree) to the north (south) of the BSISO convective center at 0 (From Jiang et al. (2004). © Copyright 2004 American Meteorological Society (AMS))

a cubic spline interpolation was applied to each field in the meridional direction. From Fig. 3.24, one can see that maximum vertical motion occurs in the middle troposphere (about 400mb) and coincides well with the convection center.

Associated with this maximum ascending motion are the low-level convergence and the upper-tropospheric divergence.

The most striking asymmetric structure (with respect to the convection center) appears in the vorticity field. A positive vorticity center with an equivalent barotropic structure is located 400 km north of the convection center, while a negative vorticity with the same equivalent barotropic structure appears to the south of the convection center. Another striking asymmetry appears in the specific humidity field. A maximum specific humidity center shifts about 150 km to the north of the convection center in the lower troposphere. The temperature and geopotential height fields also show a significant phase difference relative to the convection.

The asymmetric feature of vorticity and humidity with respect to the BSISO convection is well reproduced by the model (not shown). The resemblance of the model and observed BSISO structure and propagation characteristics suggests that to the first order of approximation, it is the internal atmospheric dynamics that are essential to cause the northward propagation. Based on the meridional and vertical structures illustrated above, the two mechanisms were unveiled to explain the northward propagation:

3.5.1 The Vertical Shear Mechanism

This mechanism is motivated by the observed BSISO structure that an equivalent barotropic vorticity field appears to the north of the convection center. In the following, a 2.5-layer atmospheric model was used to demonstrate how the vertical shear of the summer mean flow causes the coupling of free-atmospheric barotropic and baroclinic modes, which leads to the development of a meridionally asymmetric barotropic vorticity field.

For simplicity, consider a 2D case with vanished zonal gradients for all variables. The governing equation for a linear motion in an f-plane under a constant vertical shear of the mean zonal flow can be written as

$$\frac{\partial \zeta_-}{\partial t} + f_0 D_- = -\bar{u}_T \frac{\partial D_+}{\partial y} + K \cdot \nabla^2 \zeta_-, \tag{3.8}$$

$$\frac{\partial D_-}{\partial t} - f_0 \zeta_- + \nabla^2 \varphi_- = K \cdot \nabla^2 D_-, \tag{3.9}$$

$$\frac{\partial \zeta_+}{\partial t} + f_0 D_+ = 2\bar{u}_T \frac{\partial}{\partial y}(2D_+ + D_-) + K \cdot \nabla^2 \zeta_+, \tag{3.10}$$

$$\frac{\partial D_+}{\partial t} - f_0 \zeta_+ + \nabla^2 \varphi_+ = K \cdot \nabla^2 D_+, \tag{3.11}$$

$$\frac{\partial \varphi_-}{\partial t} - f_0 \bar{u}_T v_+ + {c_0}^2 (1 - I) D_- = {c_0}^2 (B - 1) D_+ + K \cdot \nabla^2 \varphi_-, \tag{3.12}$$

where $\bar{u}_T = \bar{u}_1 - \bar{u}_3/2$ denotes the constant vertical shear of the mean flow and f_0 is the Coriolis parameter at a reference latitude (12°N). Variables with a subscript "+" ("−") represent a barotropic (baroclinic) mode. For the detailed derivation of the governing equations and the description of major parameters and their values in the equations, readers are referred to Jiang et al. (2004).

The motion in the PBL is controlled by the geopotential height at the top of the boundary layer, which is assumed to be same as the geopotential height in the lower troposphere (Wang and Li 1993). Thus, we have

$$E u_B - f_0 v_B = 0, \tag{3.13}$$

$$E v_B + f_0 u_B = -\frac{\partial (\varphi_+ - \varphi_-)}{\partial y}. \tag{3.14}$$

Equations (3.13 and 3.14) lead to

$$\frac{-E}{E^2 + {f_0}^2} \frac{\partial^2 (\varphi_+ - \varphi_-)}{\partial y^2} = \frac{\partial v_B}{\partial y} = \frac{w_B}{p_s - p_e} = -\frac{2\Delta p}{p_s - p_e} D_+, \tag{3.15}$$

where E is the Ekman coefficient.

Consider initially there is a purely baroclinic structure perturbation (i.e., initially the barotropic mode is zero). Based on Eq. (3.10), the generation of the barotropic mode in the free atmosphere can only be realized through the vertical shear of the mean flow in the form of meridional advection of the baroclinic divergence, that is,

$$\frac{\partial \zeta_+}{\partial t} \propto 2\bar{u}_T \frac{\partial D_-}{\partial y}. \tag{3.16}$$

Equation (3.16) may be transformed into another formula:

$$\frac{\partial \zeta_+}{\partial t} \propto \frac{\partial \bar{u}}{\partial z} \frac{\partial w'}{\partial y}. \tag{3.16a}$$

where w' denotes the ISO perturbation vertical velocity in the middle troposphere and $\partial \bar{u}/\partial z$ represents the vertical shear of the basic-state zonal flow.

The generation of the barotropic vorticity may further lead to the development of the barotropic divergence in the free atmosphere:

$$\frac{\partial D_+}{\partial t} \propto f_0 \zeta_+. \tag{3.17}$$

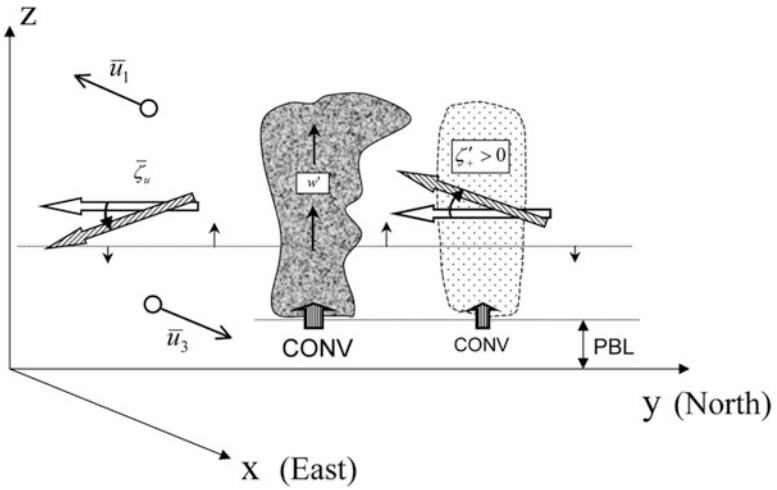

Fig. 3.25 Schematic diagram for the generation of the barotropic vorticity due to the twisting of the background southward vorticity (*hollow double arrow*) associated with the easterly shear by BSISO perturbation vertical motion (From Wang (2006). Copyright © 2006, Praxis. Springer Berlin Heidelberg)

Equations (3.16) and (3.16a) imply that the baroclinic and barotropic modes are closely coupled in the presence of the vertical shear of the mean flow. In reality, the vertical structure of the atmospheric mean flow in boreal summer is characterized by a strong easterly shear in the monsoon region.

Schematic diagram in Fig. 3.25 illustrates how the BSISO perturbation interacts with the mean easterly shear, leading to the generation of an equivalent barotropic vorticity north of the BSISO convection. In the monsoon region, the background lower-level (upper-level) westerly (easterly) leads to a southward mean vorticity (as indicated by open double arrows). To the north (south) of the BSISO convection center, upward motion decreases (increases) with y. Thus the vorticity twisting term leads to an upward or positive (downward or negative) vorticity to the north (south). The positive barotropic vorticity may induce a barotropic divergence in situ in the northern hemisphere ($f_0 > 0$, according to Eq. 3.17). The free atmosphere divergence, along with the Ekman pumping effect, further leads to a boundary layer convergence (to satisfy the continuity equation). The boundary layer moisture convergence favors the development of convective heating to the north of the MJO convective center, promoting northward propagation.

3.5.2 The Moisture–Convection Feedback Mechanism

The observed BSISO structures show clearly a phase leading of specific humidity to convection. It is argued that this meridional asymmetry of perturbation moisture

may cause the northward shift of the convective heating, leading to the northward propagation. A key question is what causes the meridional asymmetry of the low-level specific humidity anomaly. It is argued that both the anomalous moisture advection by the mean flow and the anomalous advection of the mean moisture by perturbation wind contribute to this asymmetric humidity distribution (Jiang et al. 2004).

As we know, the observed summer mean flow over the eastern Indian Ocean sector has a prevailing northward component in the PBL. The moisture advection by this northward summer mean flow in the boundary layer, together with the advection of the mean specific humidity by perturbation vertical motion in the PBL, may be, at least partially, responsible for the asymmetry of the specific humidity with respect to the convection. Mathematically, this process may be expressed as

$$\frac{\partial q}{\partial t} \propto -\bar{v}_B \frac{\partial q}{\partial y} - w_B \frac{\partial \bar{q}}{\partial p}.$$

Physically, it is interpreted as follows. Consider strong BSISO convection with anomalous low-level convergence and upper-level divergence. The low-level convergence would induce upward motion, which advects mean moisture upward to a certain height. The advection by the mean meridional wind may further shift the anomalous specific humidity center to the north of the convection. The shifted moisture anomaly would favor subsequent development of new convection to the north.

Another possible process is through the anomalous advection of the mean moisture by the ISO meridional wind in the presence of the mean meridional specific humidity gradient. The meridional distribution of JJA surface specific humidity averaged over the Indian subcontinent sector shows that the maximum moisture is located around 20°N over the northern Indian Ocean. To the south of 20°N, the meridional gradient of the mean specific humidity is positive. Considering the advection by the perturbation meridional wind, the anomalous moisture equation may be written as

$$\frac{\partial q}{\partial t} \propto -v_B \frac{\partial \bar{q}}{\partial y}.$$

In response to the BSISO heating, the perturbation wind has a southward (northward) component to the north (south) of the convection center. As a result of this advective process, the perturbation moisture attains a meridionally asymmetric structure, with a positive anomaly (negative) center to the north (south) of the convection center. This moisture-convection feedback mechanism works provides a valuable addition to the vertical shear mechanism, and they work together to explain the observed northward propagation feature.

3.6 Interactions with High-Frequency Eddies

MJO exhibits a multi-scale characteristic. Nakazawa (1988) showed that within the MJO convective envelope, there are multi-scale clouds ranged from individual cumulus and mesoscale convective systems (MCS) to super star clusters (SSC). The latter is often referred to as convectively coupled Kelvin waves. Within the MJO large-scale convective envelope, there are higher-frequency westward-propagating transient waves, including tropical depression (TD)–mixed Rossby-gravity wave (MRG)-type perturbations (Takayabu and Nitta 1993; Dickinson and Molinari 2002; Aiyyer and Molinari 2003; Frank and Roundy 2006). As MJO propagates eastward from the Indian Ocean to the western Pacific, it interacts with higher-frequency weather systems such as TCs and lower-frequency modes such as ENSO (Liebmann et al. 1994; Maloney and Hartmann 2000a, b; Vecchi and Harrison 2002; Straub and Kiladis 2003; Jones et al. 2004a, b; Batstone et al. 2005).

The tropical IO and WNP are regions of enhanced MJO variability in boreal summer. These regions, not by coincidence, are also regions with most active synoptic-scale variability (SSV) including synoptic wave train and TC activity (Lau and Lau 1990; Liebmann et al. 1994; Hartmann and Maloney 2001; Maloney and Dickinson 2003; Straub and Kiladis 2003; Batstone et al. 2005).

It is well known that MJO/BSISO exerts a large-scale control on SSV (Hendon and Liebmann 1994; Maloney and Hartmann 1998, 2000a, b; Straub and Kiladis 2003). Some diagnostic studies suggested that barotropic energy conversion between the MJO flow field and higher-frequency eddies was responsible for latter's growth (Sobel and Maloney 2000; Maloney and Hartmann 2001; Hartmann and Maloney 2001; Maloney and Dickinson 2003). Maloney and Hartmann (1998, 2000a, b) suggested that MJO westerlies may set up favorable conditions for TC development by inducing cyclonic low-level vorticity and near-zero vertical wind shear. Using wave accumulation as a precondition for TC genesis, Sobel and Maloney (2000) found a relationship between TC genesis and MJO. They concluded that the wave activity convergence associated with tropical depression-type disturbances is stronger during the active phase of MJO.

Compared with the MJO impact on SSV, the synoptic-scale feedback to MJO has received less attention (Batstone et al. 2005). While MJO exerts a large-scale control on SSV, it is not clear how and to what extent the integrated effect of synoptic-scale (including TC) activity may further feedback to MJO. Krishnamurti et al. (2003) speculated that about 30–50% of the total surface heat flux on the MJO timescale might come from the interaction of MJO with other timescales. Biello and Majda (2005), Biello et al. (2007), and Majda and Stechmann (2009) suggested that the synoptic-scale momentum and temperature flux convergences may modulate the large-scale MJO circulation.

Following Majda and Stechmann (2009), Wang and Liu (2011) constructed a scale interaction model in which there are two-way interactions between MJO and high-frequency eddies [including SCC and westward-propagating inertial–gravity waves (WIG) or two-day waves]. They assumed that the westward-tilted super

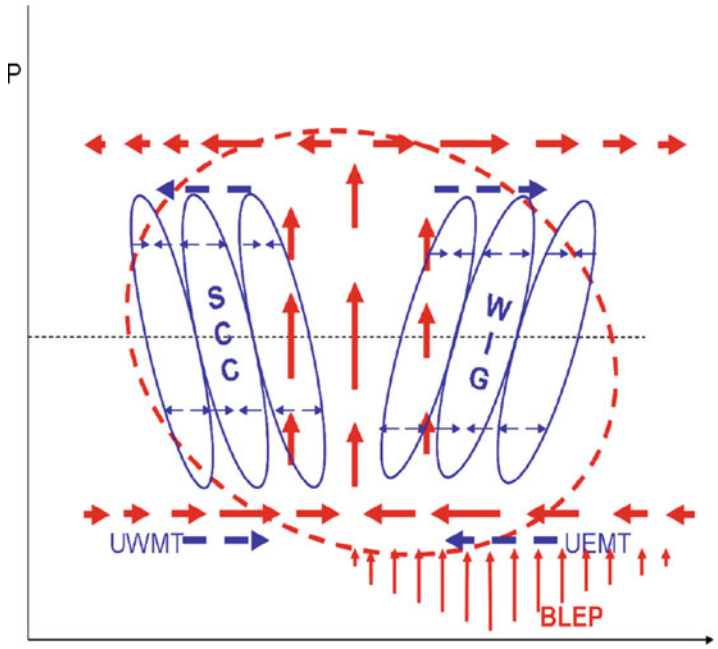

Fig. 3.26 Schematic diagram describing multi-scale structure associated with MJO. The *red ellipse* and *thick arrows* represent, respectively, the convective complex and planetary-scale zonal circulations associated with MJO. The *blue ellipse* and *thin arrows* denote vertically tilted meso-synoptic disturbances (SCCs and WIG waves) and associated convergence/divergence, respectively. The *thick blue arrows* represent eddy-induced upscale easterly/westerly momentum transfer (UEMT/UWMT). The *red thin arrows* represent the boundary layer Ekman pumping (BLEP) (From Wang and Liu (2011). © Copyright 2011 American Meteorological Society (AMS))

cloud clusters are located in the west part of the convection center of the MJO, while the enhanced eastward-tilted 2-day waves occur to the east of the MJO convective center. Their numerical experiment showed that in such a scenario the eddy momentum transport would enhance the lower-troposphere westerly (easterly) in the rear (front) of the MJO, respectively, which presents a positive feedback for the MJO. Figure 3.26 illustrates a schematic diagram for such positive feedback processes.

It is worth mentioning that this scale interaction process is SCC/WIG location dependent. A negative feedback can be obtained when SCC (WIG) prevail in the front (back) of the MJO (Liu and Wang 2012a). The eastward-tilted WIG or 2-day waves also have positive eddy moisture transfer, which will moisten the middle troposphere and enhance the MJO (Liu and Wang 2012b).

To examine the two-way interaction between the tropical ISO and SSV, Zhou and Li (2010) conducted an observational analysis. A 3–10-day band-pass filter was applied to extract the synoptic-scale signal at different phases of MJO. Figure 3.27 shows that the strength of atmospheric synoptic-scale variability (SSV) differs

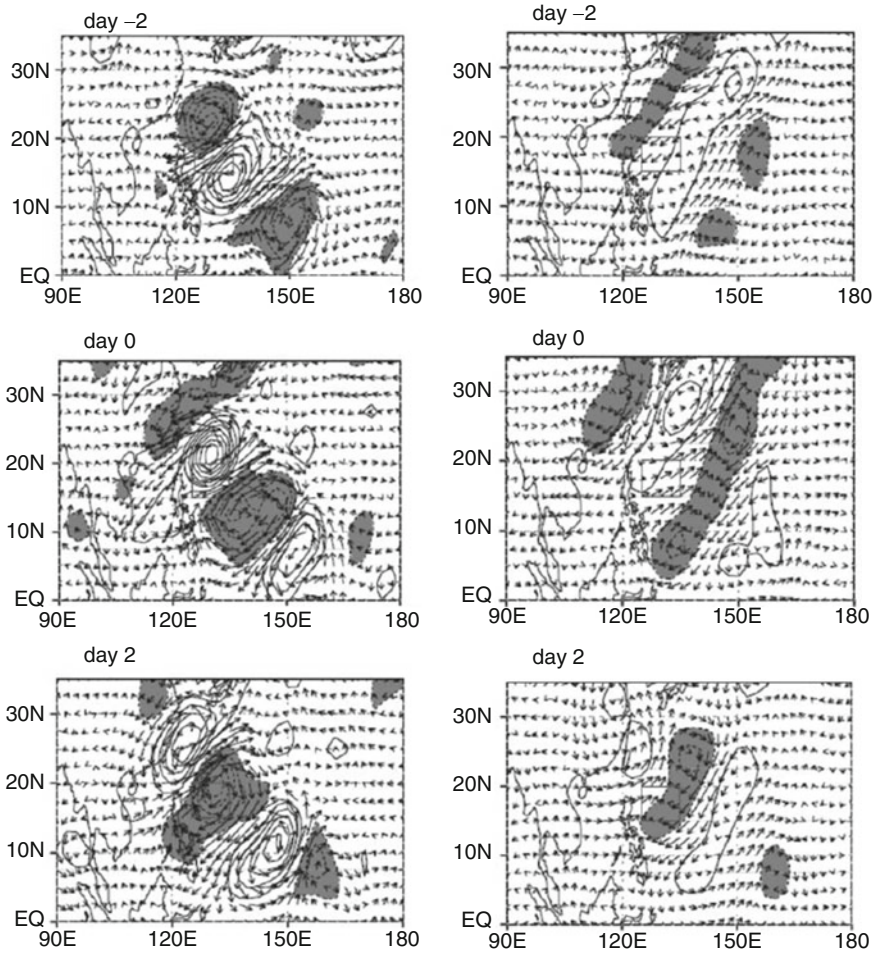

Fig. 3.27 Time evolution of the 3–10-day-filtered QuikSCAT surface wind (vector; unit, $m \cdot s^{-1}$) and vorticity (contour; interval, $0.3 \times 10^{-5} s^{-1}$) fields from day −2 to day 2 during the ISO active (*left*) and suppressed (*right*) phases. Day 0 corresponds to a time when the maximum synoptic disturbance appears in the reference box (From Zhou and Li (2010). © Copyright 2010 American Meteorological Society (AMS))

markedly between MJO active and suppressed phases in the WNP (Zhou and Li 2010). During the active phase, a well-organized synoptic-scale wave train with alternative cyclonic and anticyclonic flows occurs, consistent with the observed (Lau and Lau 1990). In contrast, during the MJO suppressed phase, the wave train is much weaker and loosely organized.

Zhou and Li (2010) developed a method to quantitatively examine high-frequency feedback to low-frequency motion. In this work, they focused on

examining the upscale feedback of SSV to MJO through nonlinear rectification of surface latent heat flux (LHF). The surface LHF may be written as

$$\mathrm{LHF} = L\rho C_E \mid \mathbf{V} \mid (q_s - q_a), \tag{3.18}$$

where $L = 2.5 \times 10^6 \mathrm{J} \cdot \mathrm{kg}^{-1}$ is the latent heat of condensation, $\rho = 1.225\ \mathrm{kg} \cdot \mathrm{m}^{-3}$ is the air density at the standard sea level, C_E is an exchange coefficient, $|\mathbf{V}|$is the 10-m wind speed (derived from 6-hourly ECMWF data), q_s is the sea surface-specific humidity (derived from 6-hourly interpolated TMI SST and 6-hourly sea-level pressure from the ECMWF TOGA analysis), and q_a is the specific humidity at 10 m (derived from 6-hourly sea-level pressure and dew point temperature from the ECMWF TOGA analysis).

To examine to what extent SSV contributes to the intraseasonal surface LHF, zonal and meridional wind components (u, v) and air–sea humidity difference (Δq) fields are separated into three components, a low-frequency (greater than 90 days) background mean state (LFBS), a synoptic-scale component, and an intraseasonal (20–90-day) component.

Firstly, the LHF is calculated based on the sum of all the three components (which is approximately equal to the total field). The so-calculated LHF is then subject to a 20–90-day band-pass filtering. Secondly, the LHF is calculated based on the sum of the LFBS and the synoptic-scale component only (without involving the ISO component). The same 20–90-day filter is then applied to this LHF field.

By comparing the standard deviation of both the intraseasonal LHF fields, one may reveal what percentage of the intraseasonal LHF comes from the SSV–mean flow interaction. Figure 3.28 shows the ratio of the standard deviation of the two intraseasonal LHF fields. Note that the ratio exceeds 30% over most of the tropical Indian Ocean, western Pacific, and eastern North Pacific, indicating a great upscale feedback of SSV to the intraseasonal surface LHF in the region. Maximum SSV feedback may exceed 50% in some regions of the western and northeastern Pacific. In general, the strong upscale feedback occurs in the region where both the MJO and synoptic-scale variabilities are large.

SSV may also feedback to MJO through nonlinear rectification of atmospheric apparent heating (Hsu and Li 2011). According to Yanai et al. (1973), the atmospheric apparent heat source (Q_1) and apparent moisture sink (Q_2) may be computed as residuals of the thermodynamic and moisture equations, respectively:

$$Q_1 = c_p \frac{\partial T}{\partial t} - c_p(\omega\sigma - V \cdot \nabla T), \tag{3.19a}$$

$$Q_2 = -L\frac{\partial q}{\partial t} - LV \cdot \nabla q - L\omega\frac{\partial q}{\partial p}, \tag{3.19b}$$

where c_p denotes the specific heat at constant pressure, T temperature, t time, ω vertical p-velocity, $\sigma = (\mathrm{RT}/c_p p) - (\partial \mathrm{T}/\partial \mathrm{p})$ the static stability, R gas constant, p pressure, V horizontal velocity, ∇ the horizontal gradient operator, L the latent

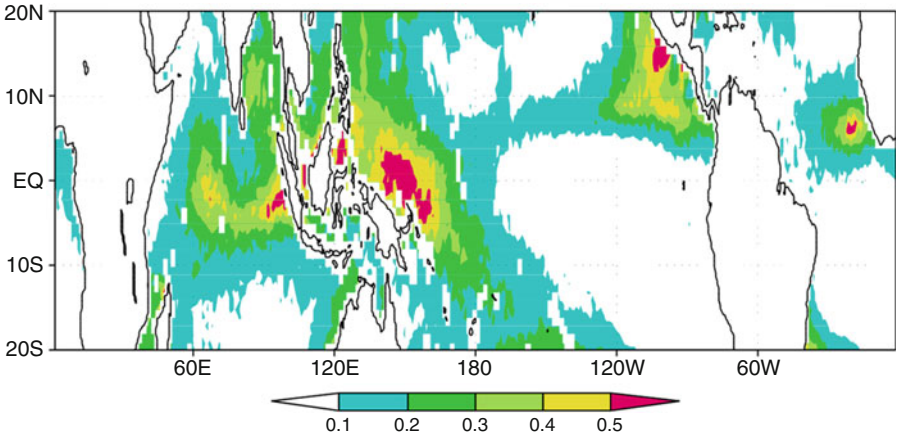

Fig. 3.28 The ratio of the standard deviations of the nonlinearly rectified intraseasonal latent heat flux (calculated based on synoptic-scale and LFBS fields) and the total intraseasonal latent heat flux (calculated based on synoptic-scale, MJO, and LFBS fields) (From Zhou and Li (2010). © Copyright 2010 American Meteorological Society (AMS))

heat of condensation, and q specific humidity. Q_1 represents the total diabatic heating including radiation, latent heating, surface heat flux, and sub-grid scale heat flux convergences. Q_2 represents the latent heating due to condensation or evaporation processes and sub-grid scale moisture flux convergences (Yanai et al. 1973).

The feedback of SSV to intraseasonal apparent heat and moisture sources was estimated through the following methods. Firstly, all the variables (u, v, ω, T, q) are partitioned into the LFBS, intraseasonal, and synoptic-scale components. Then Q_1 and Q_2 fields are calculated based on the sum of the LFBS, intraseasonal (10–90-day), and synoptic-scale (3–10-day) components. The so-calculated Q_1 and Q_2 fields are then subjected to a 10–90-day band-pass filter to reveal the overall strength of the intraseasonal Q_1 and Q_2 variabilities. Figure 3.29 shows the standard deviation of 1000–100 hPa averaged 10–90-day heating rate (Q_1/c_p) calculated based on the total fields above. Note that three maximum variability centers are identified, and they are located in the Indian monsoon region (70°–100°E, 10°–20°N), the Philippine Sea–WNP sector (120°–150°E, 10°–20°N), and the tropical eastern Pacific (90°–120°W, 5–15°N), as shown in Fig. 3.29a. The spatial pattern of the 10–90-day diabatic heating corresponds well to the gross features of the intraseasonal precipitation shown in Li and Wang (2005), reflecting the diabatic heating source for the summer ISO. The vertical profiles of the apparent heat sources averaged over the tropical Indian Ocean and western and eastern North Pacific show a maximum value near 400–500 hPa, with a heating rate of 2–2.5 K day^{-1} (Fig. 3.29d).

Secondly, the effects of eddy–eddy and eddy–mean flow interactions on the intraseasonal apparent heat source were estimated. Two methods were developed for this purpose. One is to calculate the Q_1 and Q_2 fields based on the sum of the

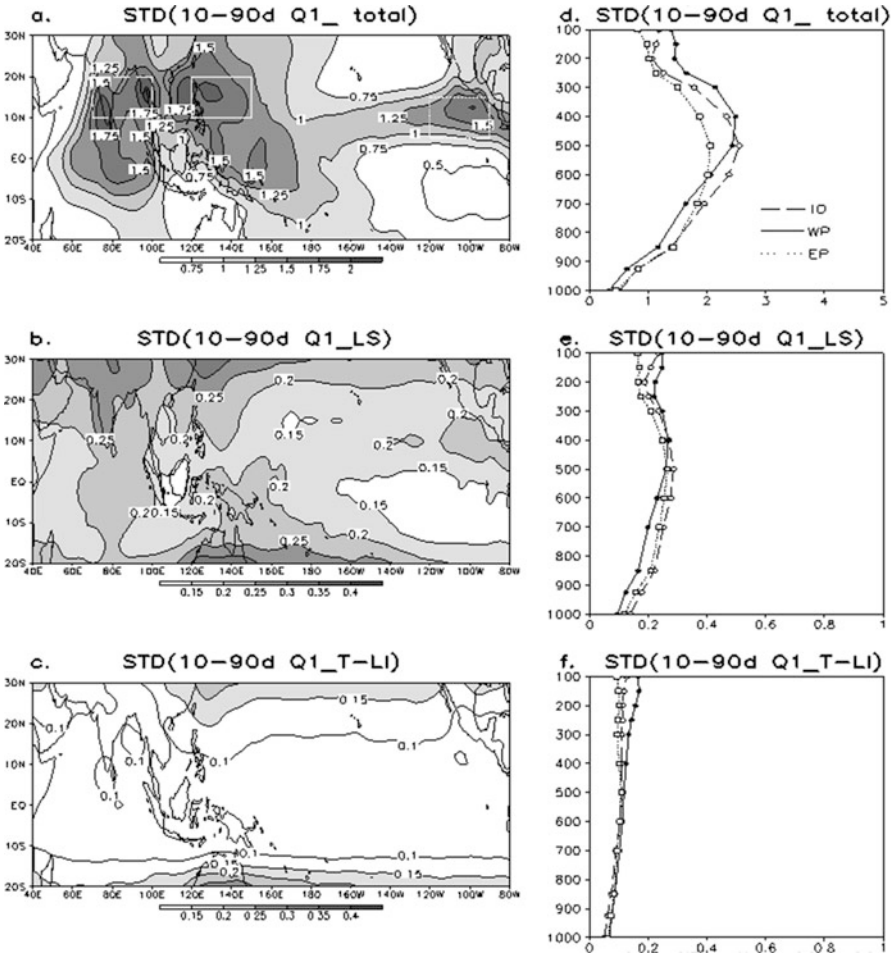

Fig. 3.29 Standard deviations of 10–90-day vertically averaged heating rates (Q_1/c_p; unit, Kday^{-1}) calculated based on (**a**) the total fields, (**b**) the LS components, and (**c**) the T-LI method. (**d**–**f**) show the vertical profiles of (**a**)–(**c**) averaged over the Indian monsoon region (70°–100°E, 10°–20°N, *dashed line*), the WNP sector (120°–150°E, 10°–20°N, *solid line*), and the tropical eastern Pacific (90°–120°W, 5°–15°N, *dotted line*) (From Hsu and Li (2011). © Copyright 2011 American Meteorological Society (AMS))

LFBS and synoptic (hereafter LS) components (without the involving of the MJO flow). The so-calculated Q_1 and Q_2 fields are then subjected to a 10–90-day band-pass filter. This calculation, however, does not include the effect of the eddy–MJO interaction. The standard deviation of vertically averaged 10–90-day heating rate (Q_1/c_p) calculated based on the LS components is displayed in Fig. 3.29b. The amplitude of the nonlinearly rectified heating over the tropical Indian Ocean and western Pacific regions is 0.2–0.25 K day^{-1} (Fig. 3.29b). The vertical profiles of the

nonlinearly rectified heating fields averaged over the three active ISO regions show a maximum in the mid-troposphere (Fig. 3.29e).

The second method has the following procedure: (1) calculating Q_1 and Q_2 with the sum of the LFBS and ISO (hereafter LI) components, (2) applying a 10–90-day band-pass filter to the resulting Q_1 and Q_2 fields, and (3) subtracting the time series of the Q_1 and Q_2 fields above from the time series of the Q_1 and Q_2 fields calculated based on the total components. The so-calculated intraseasonal Q_1 and Q_2 fields reflect the interactions of SSV with both the LFBS and ISO flows. The second method is called the T-LI method.

The amplitude of the nonlinearly rectified Q_1 field derived by the T-LI method is a little weaker (Fig. 3.29c), compared with that derived based on the LS components (Fig. 3.29b), even though their spatial distributions are similar. The same methods are applied to the Q_2 field. The overall horizontal patterns of the calculated intraseasonal Q_2 fields (figure not shown) are quite similar to the corresponding Q_1 fields. The major difference lies in the vertical profiles. The maximum amplitudes of the total and nonlinearly rectified intraseasonal Q_2 fields all appear in the lower troposphere (between 700 and 850 hPa).

Figure 3.30 shows the ratios of standard deviations of the nonlinearly rectified Q_1 and Q_2 fields calculated based on the two methods to standard deviations of the total intraseasonal Q_1 and Q_2 fields. The nonlinearly rectified Q_1 and Q_2 based on both the methods account for 10–30% of the total intraseasonal Q_1 and Q_2 variabilities, indicating that high-frequency eddies can significantly modulate the intraseasonal diabatic heating in the active MJO and SSV regions.

The role of scale interactions in the maintenance of eddy kinetic energy (EKE) during the ISO wet and dry phases was examined through the development of a new EKE diagnostic tool that separates the effect of ISO and LFBS (Hsu et al. 2011). As the summer mean state always contributes positively to EKE, synoptic eddies extract energy from ISO during its active phase. This positive barotropic energy conversion occurs when the synoptic eddies interact with low-level cyclonic and convergent ISO flows. This contrasts to the ISO dry phase during which synoptic eddies lose energy to the ISO flow. The anticyclonic and divergent ISO flow during the dry phase is responsible for the negative barotropic energy conversion.

In addition, SSV may exert an upscale feedback to MJO through eddy momentum transport (Majda and Stechmann 2009; Hsu and Li 2011) and the modulation of intraseasonal SST variations (Li et al. 2008). For more detailed discussions, readers are referred to a MJO review paper by Li (2014).

Questions

1. What is the horizontal and vertical structure of MJO?
2. Why does MJO propagate eastward along the equator? What theories have been proposed in an attempt to explain the eastward propagation?
3. What causes the preferred planetary zonal scale selection for MJO?
4. What hypotheses have been proposed to explain the initiation of MJO convection in the western Indian Ocean?

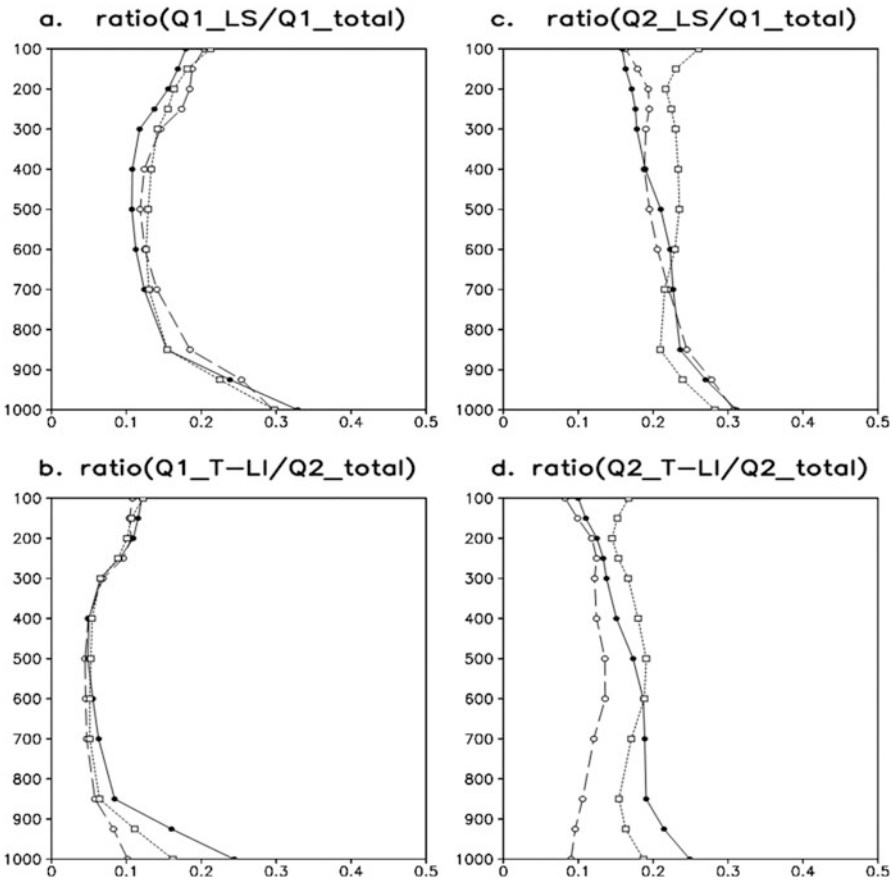

Fig. 3.30 Vertical distributions of ratios of standard deviations of the nonlinear rectified 10–90-day Q_1 field calculated based on (**a**) the LS components and (**b**) the T-LI method and standard deviations of the total intraseasonal Q_1 over the three box regions (shown in Fig. 29a). (**c**) and (**d**) are the same as (**a**) and (**b**) except for Q_2 (From Hsu and Li (2011).)

5. Describe specific processes through which a preceding suppressed-phase MJO may help trigger a new convective phase MJO?
6. What is the fundamental difference in variance and propagation characteristics between boreal winter and boreal summer intraseasonal oscillation (ISO) in the tropics?
7. Describe possible physical processes that cause the bifurcation of ISO propagation after it approaches the Maritime Continent between boreal summer and boreal winter.
8. Describe mechanisms through which the ISO propagates northward over tropical Indian Ocean in boreal summer.

9. What is the role of air–sea interaction in affecting MJO propagation and structure?
10. Describe specific processes through which higher-frequency variability may feedback to MJO.

References

Aiyyer AR, Molinari J (2003) Evolution of mixed Rossby-gravity waves in idealized MJO environments. J Atmos Sci 60:2837–2855

Batstone CP, Matthews AJ, Stevens DP (2005) Coupled ocean-atmosphere interactions between the Madden-Julian oscillation and synoptic-scale variability over the warm pool. J Clim 18:2004–2020

Benedict J, Randall DA (2007) Observed characteristics of the MJO relative to maximum rainfall. J Atmos Sci 64:2332–2354

Biello JA, Majda AJ (2005) A new multi-scale model for the Madden-Julian oscillation. J Atmos Sci 62:1694–1721

Biello JA, Majda AJ, Moncrieff MW (2007) Meridional momentum flux and super-rotation in the multi-scale IPESD MJO model. J Atmos Sci 64:1636–1651

Chao WC, Chen B (1999) On the role of surface friction in tropical intraseasonal oscillation. In: Preprints, 23-d conference on Hurricanes and Tropical Meteorology, vol II. American Meteorological Society, Dallas, TX, pp 815–818

Chen T-C, Murakami M (1988) The 30–50-day variation of convective activity over the western Pacific Ocean with the emphasis on the northwestern region. Mon Weather Rev 116:892–906

Dickinson M, Molinari J (2002) Mixed Rossby-gravity waves and western Pacific tropical cyclogenesis. Part I: Synoptic evolution. J Atmos Sci 59:2183–2195

Emanuel KA (1987) An air–sea interaction model of intraseasonal oscillations in the tropics. J Atmos Sci 44:2324–2340

Emanuel KA (1994) Atmospheric convection. Oxford University Press, New York, 580 pp

Flatau MK, Flatau P, Phoebus P et al (1997) The feedback between equatorial convection and local radiative and evaporative processes: the implications for intraseasonal oscillations. J Atmos Sci 54:2373–2386

Frank WM, Roundy PE (2006) The role of tropical waves in tropical cyclogenesis. Mon Weather Rev 134:2397–2417

Gadgil S, Srinivasan J (1990) Low frequency variation of tropical convergence zones. Meteorol Atmos Phys 44:119–132

Gautier C, DiJuli B (1990) Cloud effect on air-sea interactions during the 1979 Indian summer monsoon as studied from satellite observations. Meteorol Atmos Phys 44:119–132

Gill AE (1980) Some simple solutions for heat-induced tropical circulation. Q J R Meteorol Soc 106:447–462

Hartmann DL, Maloney ED (2001) The Madden-Julian oscillation, barotropic dynamics, and North Pacific tropical cyclone formation. Part II: Stochastic barotropic modeling. J Atmos Sci 58:2559–2570

Hartmann DL, Michelsen ML (1989) Intraseasonal periodicities in Indian rainfall. J Atmos Sci 46:2838–2862

Hartmann DL, Michelsen ML, Kelein SA (1992) Seasonal variations of tropical intraseasonal oscillations: a 20–25-day oscillation in the western Pacific. J Atmos Sci 49:1277–1289

Hendon HH, Glick J (1997) Intraseasonal air-sea interaction in the tropical Indian and Pacific oceans. J Clim 10:647–661

Hendon HH, Liebmann B (1994) Organization of convection within the Madden-Julian oscillation. J Geophys Res 99:8073–8083

Hendon HH, Salby ML (1994) The life cycle of Madden-Julian oscillation. J Atmos Sci 51:2207–2219
Holton JR (1992) An introduction to dynamic meteorology, Third edn. Academic Press, San Diego, p 511
Hsu P-C, Li T (2011) Interactions between boreal summer intraseasonal oscillations and synoptic-scale disturbances over the western North Pacific. Part II: Apparent heat and moisture sources and eddy momentum transport. J Clim 24:942–961
Hsu P-C, Li T (2012) Role of the boundary layer moisture asymmetry in causing the eastward propagation of the Madden-Julian oscillation. J Clim 25:4914–4931
Hsu H-H, Weng C-H (2001) Northwestward propagation of the intraseasonal oscillation in the western North Pacific during the boreal summer: structure and mechanism. J Clim 14:3834–3850
Hsu H-H, Hoskins BJ, Jin F-F (1990) The 1985/86 intraseasonal oscillation and the role of the extratropics. J Atmos Sci 47:823–839
Hsu P-C, Li T, Tsou C-H (2011) Interactions between boreal summer intraseasonal oscillations and synoptic-scale disturbances over the western North Pacific. Part I: Energetics diagnosis. J Clim 24:927–941
Jiang X, Li T, Wang B (2004) Structures and mechanisms of the northward propagating boreal summer intraseasonal oscillation. J Clim 17:1022–1039
Jiang X et al (2015) Vertical structure and physical processes of the Madden-Julian oscillation: Exploring key model physics in climate simulations. J Geophys Res Atmos 120:4718–4748
Johnson RH, Rickenbach TM, Rutledge SA, Ciesielski PE, Schubert WH (1999) Trimodal characteristics of tropical convection. J Clim 12:2397–2418
Jones C, Weare BC (1996) The role of low-level moisture convergence and ocean latent heat fluxes in the Madden-Julian oscillation: an observational analysis using ISCCP data and ECMWF analyses. J Clim 9:3086–3140
Jones C, Waliser DE, Lau KM, Stern W (2004a) The Madden- Julian oscillation and its impact on northern hemisphere weather predictability. Mon Weather Rev 132:1462–1471
Jones C, Waliser DE, Lau KM, Stern W (2004b) Global occurrences of extreme precipitation and the Madden-Julian oscillation: observations and predictability. J Clim 17:4575–4589
Khouider B, Majda AJ (2006) A simple multicloud parameterization for convectively coupled tropical waves. Part I: Linear analysis. J Atmos Sci 63:1308–1323
Kikuchi K, Takayabu YN (2004) The development of organized convection associated with the MJO during TOGA COARE IOP: trimodal characteristics. Geoph Res Lett 31:L10101
Khouider B, Majda AJ (2007) A simple multicloud parameterization for convectively coupled tropical waves. Part II: Nonlinear simulations. J Atmos Sci 64:381–400
Knutson TR, Weickmann KM (1987) 30–60 day atmospheric oscillations: composite life cycles of convection and circulation anomalies. Mon Weather Rev 115:1407–1436
Krishnamurti TN, Chakraborty DR, Cubukcu N et al (2003) A mechanism of the MJO based on interactions in the frequency domain. Q J R Meteorol Soc 129:2559–2590
Lau K-M, Chan PH (1986) Aspects of the 40–50-day oscillation during the northern summer as inferred from outgoing longwave radiation. Mon Weather Rev 114:1354–1367
Lau K-H, Lau N-C (1990) Observed structure and propagation characteristics of tropical summertime synoptic-scale disturbances. Mon Weather Rev 118:1888–1993
Lau K-M, Peng L (1987) Origin of low frequency (intraseasonal) oscillations in the tropical atmosphere. Part I: The basic theory. J Atmos Sci 44:950–972
Lau K-M, Sui C-H (1997) Mechanisms of short-term sea surface temperature regulation: observations during TOGA-COARE. J Clim 10:465–472
Li T (2014) Recent advance in understanding the dynamics of the Madden-Julian oscillation. J Meteorol Res 28:1–33
Li T, Wang B (1994a) The influence of sea surface temperature on the tropical intraseasonal oscillation: a numerical study. Mon Weather Rev 122:2349–2362

Li T, Wang B (1994b) A thermodynamic equilibrium climate model for monthly mean surface winds and precipitation over the tropical Pacific. J Atmos Sci 51:1372–1385
Li T, Wang B (2005) A review on the western North Pacific monsoon: synoptic-to-interannual variability. Terr Atmos Ocean Sci 16:285–314
Li T, Tam F, Fu X, Zhou T, Zhu W (2008) Causes of the intraseasonal SST variability in the tropical Indian Ocean. Atmos Ocean Sci Lett 1:18–23
Li T, Zhao C, Hsu P-C, Nasuno T (2015) MJO initiation processes over the tropical Indian Ocean during DYNAMO/CINDY2011. J Clim 28:2121–2135
Liebmann B, Hendon HH, Glick JD (1994) The relationship between tropical cyclones of the western Pacific and Indian oceans and the Madden-Julian oscillation. J Meteorol Soc Jpn 72:401–412
Lindzen RS, Nigam S (1987) On the role of sea surface temperature gradients in forcing low-level winds and convergence in the tropics. J Atmos Sci 44:2418–2436
Liu F, Wang B (2012a) A model for the interaction between the 2-day waves and moist Kelvin waves. J Atmos Sci 69:611–625
Liu F, Wang B (2012b) Impacts of upscale heat and momentum transfer by moist Kelvin waves on the Madden-Julian oscillation: a theoretical model study. Clim Dyn. doi:10.1007/s00382-011-1281-0
Madden RA, Julian PR (1971) Detection of a 40-50 day oscillation in the zonal wind in the tropical Pacific. J Atmos Sci 28:702–708
Madden RA, Julian PR (1972) Description of global scale circulation cells in the tropics with a 40–50 day period. J Atmos Sci 29:1109–1123
Majda AJ, Biello JA (2004) A multiscale model for tropical intraseasonal oscillations. Proc Natl Acad Sci 10:4736–4741
Majda AJ, Stechmann SN (2009) A simple dynamical model with features of convective momentum transport. J Atmos Sci 66:373–392
Maloney ED (2009) The moist static energy budget of a composite tropical intraseasonal oscillation in a climate model. J Clim 22:711–729
Maloney ED, Dickinson MJ (2003) The intraseasonal oscillation and the energetics of summertime tropical western North Pacific synoptic-scale disturbances. J Atmos Sci 60:2153–2168
Maloney ED, Hartmann DL (1998) Frictional moisture convergence in a composite life cycle of the Madden-Julian oscillation. J Clim 11:2387–2403
Maloney ED, Hartmann DL (2000a) Modulation of eastern North Pacific hurricanes by the Madden-Julian oscillation. J Clim 13:1451–1460
Maloney ED, Hartmann DL (2000b) Modulation of hurricane activity in the Gulf of Mexico by the Madden-Julian oscillation. Science 287:2002–2004
Maloney ED, Hartmann DL (2001) The Madden-Julian oscillation, barotropic dynamics, and North Pacific tropical cyclone formation. Part I: Observations. J Atmos Sci 58:2545–2558
Moskowitz BM, Bretherton CS (2000) An analysis of frictional feedback on a moist equatorial Kelvin mode. J Atmos Sci 57:2188–2206
Murakami T (1980) Empirical orthogonal function analysis of satellite-observed outgoing longwave radiation during summer. Mon Weather Rev 108:205–222
Nakazawa T (1988) Tropical super clusters within intraseasonal variations over the western Pacific. J Meteorol Soc Jpn 66:823–839
Neelin JD, Held IM, Cook KH (1987) Evaporation–wind feedback and low-frequency variability in the tropical atmosphere. J Atmos Sci 44:2341–2348
Nitta T (1987) Convective activities in the tropical western pacific and their impact on the northern-hemisphere summer circulation. J Meteorol Soc Jpn 65:373–390
Shinoda T, Hendon HH (1998) Mixed layer modeling of intraseasonal variability in the tropical western Pacific and Indian oceans. J Clim 11:2668–2685
Sobel AH, Maloney ED (2000) Effect of ENSO and the MJO on western North Pacific tropical cyclones. Geophys Res Lett 27:1739–1742

Sobel AH, Maloney ED (2013) Moisture modes and the eastward propagation of the MJO. J Atmos Sci 70:187–192
Sperber KR (2003) Propagation and the vertical structure of the Madden-Julian oscillation. Mon Weather Rev 131:3018–3037
Straub KH, Kiladis GN (2003) Interactions between the boreal summer intraseasonal oscillation and higher-frequency tropical wave activity. Mon Weather Rev 131:945–960
Takaya K, Nakamura H (2001) A formulation of a phase independent wave-activity flux for stationary and migratory quasigeostrophic eddies on a zonally varying basic flow. J Atmos Sci 58:608–627
Takayabu YN, Nitta T (1993) 3–5 day period disturbances coupled with convection over the tropical Pacific Ocean. J Meteorol Soc Jpn 71:221–246
Vecchi GA, Harrison DE (2002) Monsoon breaks and subseasonal sea surface temperature variability in the Bay of Bengal. J Clim 15:1485–1493
Wang B (1988a) Dynamics of tropical low frequency waves: an analysis of moist Kelvin waves. J Atmos Sci 45:2051–2065
Wang B (1988b) Comments on "An air-sea interaction model of intraseasonal oscillation in the tropics". J Atmos Sci 45:3521–3525
Wang B (2006) Theory, chapter 10 in tropical intraseasonal oscillation in the atmosphere and ocean, Lau WK-M, Waliser DE (eds). Praxis Publishing.
Wang B, Li T (1993) A simple tropical atmospheric model of relevance to short-term climate variation. J Atmos Sci 50:260–284
Wang B, Li T (1994) Convective interaction with boundary-layer dynamics in the development of a tropical intraseasonal system. J Atmos Sci 51:1386–1400
Wang B, Liu F (2011) A model for scale interaction in the Madden-Julian oscillation. J Atmos Sci 68:2524–2536
Wang B, Rui H (1990) Dynamics of the coupled moist Kelvin-Rossby wave on an equatorial β-plane. J Atmos Sci 47:397–413
Wang B, Xie X (1998) Coupled modes of the warm pool climate system part I: The role of Air-Sea interaction in maintaining Madden-Julian oscillation. J Clim 11:2116–2135
Wu MLC, Schubert SD, Suarez MJ et al (2005) Seasonality and meridional propagation of the MJO. J Clim 19:1901–1921
Yanai M, Esbensen S, Chu J-H (1973) Determination of bulk properties of tropical cloud clusters from large-scale heat and moisture budgets. J Atmos Sci 30:611–627
Yasunari T (1979) Cloudiness fluctuation associated with the northern hemisphere summer monsoon. J Meteorol Soc Jpn 57:227–242
Yasunari T (1980) A quasi-stationary appearance of 30–40 day period in the cloudiness fluctuation during summer monsoon over India. J Meteorol Soc Jpn 58:225–229
Zhao C-B, Li T, Zhou T (2013) Precursor signals and processes associated with MJO initiation over the tropical Indian Ocean. J Clim 26:291–307
Zhou C, Li T (2010) Upscale feedback of tropical synoptic variability to intraseasonal oscillations through the nonlinear rectification of the surface latent heat flux. J Clim 23:5738–5754

Chapter 4
Tropical Cyclone Formation

Abstract In this chapter, precursor synoptic signals prior to tropical cyclone (TC) genesis in the western North Pacific (WNP) is first described, followed by the discussion of origin of the summertime synoptic-scale wave train in the WNP and the energy source and dispersion characteristics of Pacific easterly waves. Next numerical simulations of TC formation are described, with a particular focus on cyclogenesis in the wake of a preexisting TC due to its energy dispersion and the genesis efficiency of an initial mid-level vortex versus an initial bottom vortex. The climatologic aspect of the tropical cyclogenesis is further discussed, with a focus on the large-scale control of the atmospheric intraseasonal oscillation (ISO) and El Niño-Southern Oscillation (ENSO). A methodology is developed to rank key cyclogenesis parameters at tropical Pacific and Atlantic basins. Finally the robust signals of future TC projection in the North Pacific from high-resolution global model simulations are discussed.

4.1 Introduction

Tropical cyclone (TC) genesis is a process through which random cumulus-scale cloud systems are organized and developed into a warm-core, cyclonic system with sustainable winds. Due to the lack of reliable data over open oceans and complicated scale interactions involved, understanding of TC genesis remains limited.

The western North Pacific (WNP) is the most frequent TC genesis region. The summer mean circulation in the WNP has some unique features. For example, the WNP is the region of the greatest warm pool in boreal summer, with averaged SST greater than 29°C. The low-level circulation is characterized by a confluence zone between the monsoon westerly and the trade easterly and a meridional shear line that separates westerlies to the south and easterlies to the north. The low-level convergence and cyclonic vorticity overlap with intense convection, forming the WNP monsoon trough. Such a mean flow characteristic differs greatly from that in the North Atlantic (NATL).

While the summer mean circulation provides a favorable environmental condition for cyclogenesis, it is synoptic-scale disturbances that actually trigger individual cyclogenesis events. Recent advances in satellite observations make it possible to reveal detailed synoptic-scale precursor signals associated with tropical

T. Li, P.-c. Hsu, *Fundamentals of Tropical Climate Dynamics*,
Springer Atmospheric Sciences, DOI 10.1007/978-3-319-59597-9_4

cyclogenesis. In Sect. 2, synoptic-scale disturbances prior to the formation of TC in the WNP are described based on the observational analysis. Different from the NATL basin where the major perturbation source is Africa easterly waves, precursor perturbations in the WNP include TC energy dispersion (TCED)-induced Rossby wave train, northwest–southeast oriented synoptic wave train (SWT), and Pacific easterly wave (PEW).

The origins of the synoptic wave train and the Pacific easterly wave are discussed in Sect. 3. This is followed by the modeling of TC genesis in Sect. 4. The process through which TCED-induced Rossby wave train interacting with a monsoon gyre leads to the formation of a new TC is discussed first. Next, given an environmental mid-level or bottom vortex initially, how the TC-scale vortex is developed and organized from random cumulus-scale clouds is further diagnosed with cloud-resolving model simulations. The genesis efficiency under the environmental mid-level and bottom vortex is compared.

From a climatologic aspect, what determines the TC genesis frequency in WNP and NATL? In Sect. 5 the large-scale control of TC genesis by the ISO and ENSO is discussed. A methodology that quantitatively measures the relative importance of genesis parameters in the NATL and WNP is then introduced.

How TC frequency changes under global warming is addressed in Sect. 6 through the diagnosis of high-resolution global atmospheric general circulations models (AGCMs), forced with specified future SST warming patterns. The models projected a zonal shift in the North Pacific, with a large decrease (increase) of TC genesis number in the western (central) Pacific. The mechanism responsible for the distinctive regional TC changes is further discussed.

4.2 Precursor Synoptic Signals

The structure and evolution characteristics of tropical perturbations prior to TC formation in the WNP were investigated through the analysis of QuikSCAT, TMI, and other observational data (Fu et al. 2007). Thirty-four TC genesis events were identified in the boreal summers of 2000 and 2001. Among 34 TCs, six (20%) are associated with TCED, eleven cases (30%) are associated with SWT (including those originated from equatorial mixed Rossby-gravity waves), and seven cases (20%) are associated with PEW. In the following these genesis scenarios are discussed.

4.2.1 Cyclogenesis in the Wake of a Preexisting TC Due to TCED

The first type synoptic-scale disturbance associated with TC genesis in the WNP is Rossby wave energy dispersion from a preexisting TC (TCED). A vortex is subject to Rossby wave energy dispersion even in a simple barotropic framework. While a vortex moves northwestward due to the mean flow steering and the planetary vorticity gradient, Rossby waves emit energy southeastward (Anthes 1982; Flierl 1984; Flierl and Haines 1994; McDonald 1998). As a result, a Rossby wave train with alternating anticyclonic and cyclonic vorticity perturbations forms in its wake (Carr and Elsberry 1994, 1995). A study of three-dimensional (3D) Rossby wave energy dispersion showed that TCED-induced Rossby wave train has a baroclinic structure and that the upper-level wave train develops rapidly and triggers downward energy propagation that enhances the lower-level Rossby wave train (Ge et al. 2008).

Cyclogenesis due to TCED was suggested previously (Frank 1982; Davidson and Hendon 1989; Briegel and Frank 1997; Ritchie and Holland 1997) without a detailed description of the wave train structure and evolution. Using the satellite data, Li et al. (2003) showed the Rossby wave train pattern and its connection with cyclogenesis. Among the 34 cases identified in the summers of 2000–2001, six cyclogenesis cases are associated with TCED. Figure 4.1 illustrates an example. It shows the evolution of the 3–8-day filtered QuikSCAT wind fields from 1 August to 9 August 2000. Letter "A" in Fig. 4.1 represents the location of Typhoon Jelawat that formed on August 1. During the first 2–3 days, due to its weak intensity, Jelawat did not generate a visible Rossby wave train in its wake. During its northwestward journey, the intensity of Jelawat increased. With its steady intensification, the Rossby wave train became more and more evident in its wake. On 6 August, a clear wave train was observed. This Rossby wave train has a zonal wavelength of about 2500 km, oriented in a northwest–southeast direction.

The most remarkable characteristic of this wave train is that it had a large meridional wavelength. A half meridional wavelength was about 4000 km on 6 August. The meridional wavelength of the wave train was greatly reduced in subsequent days, leading to generation of a new TC on 9 August. Note that this new TC Ewiniar (represented by letter "B" in Fig. 4.1) formed in the cyclonic vorticity center of the Rossby wave train.

The vertical profile of the Rossby wave train produced by TCED was examined with 3–8-day filtered NCEP–NCAR reanalysis data at different levels (Fu et al. 2007). There was no clear wave pattern at 200 hPa, but the wave train was evident at middle and lower troposphere with little vertical tilt. The cyclonic circulation region of the wave train coincided well with the region of concentrated cloud liquid water, whereas the anticyclonic circulation region of the wave train was cloud-free.

It was noted that some TCs did not reproduce a Rossby wave train in their wakes. Whether or not a TC generates a Rossby wave train depends on TC size or intensity (Flierl et al. 1983; Li and Fu 2006), its radial wind profile (Shapiro and Ooyama

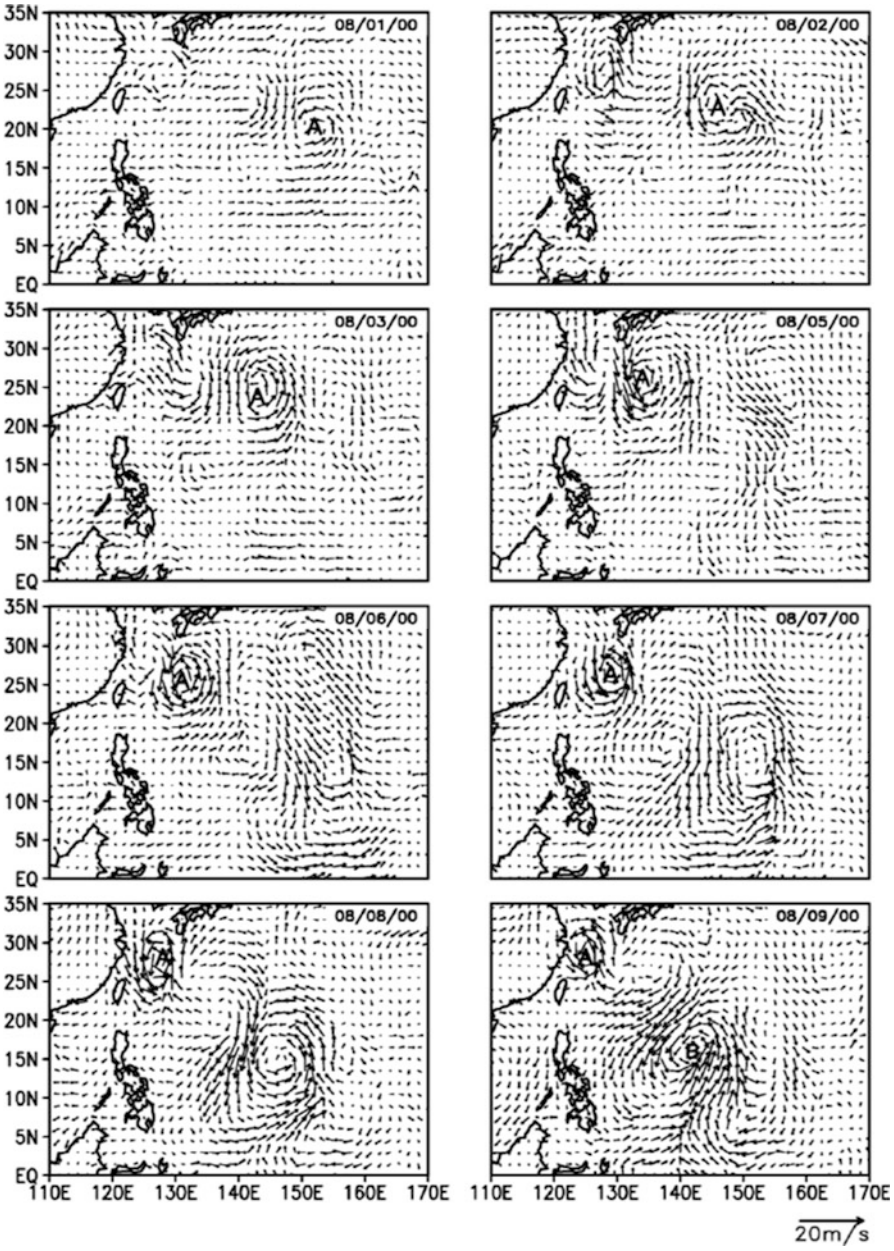

Fig. 4.1 Time sequences of synoptic-scale surface wind patterns associated with the Rossby wave energy dispersion of Typhoon Jelawat. "A" represents the *center* location of Jelawat that formed on 1 August 2000. "B" represents the *center* location of a new TC named Ewiniar that formed on 9 August 2000 in the wake of the Rossby wave train of Jelawat (From Fu et al. (2007). © Copyright 2007 American Meteorological Society (AMS))

1990), and its environmental flow such as vertical shear (Ge et al. 2007). Whether or not a new TC can form in the Rossby wave train depends on the background flow the wave train is embedded in. A larger environmental low-level cyclonic vorticity and/or a larger environmental low-level convergence may favor cyclogenesis in the Rossby wave train (Li and Fu 2006; Li et al. 2006).

4.2.2 TC Genesis Associated with SWT

The second type of TC genesis happens within a synoptic wave train (SWT) that does not involve a preexisting TC. An observational study by Lau and Lau (1990) showed that the dominant synoptic-scale mode in the summertime WNP is a northwest–southeast oriented wave train, which has a typical wavelength of ~2500 km and propagates northwestward. The intensity of the SWT increases as they move northwestward from the lower latitudes to the WNP.

During 2000 and 2001 summers, there were eleven TCs that formed in the SWT. An example is illustrated here for the formation of Typhoon Man-yi, formed on 2 August 2001 (Fig. 4.2). Three days prior to its genesis, a northwest–southeast-oriented wave train developed in the WNP. This wave train had well-defined cyclonic and anticyclonic circulations and covered a region between 130°E–160°E and 0°N–25°N. The wave train moved slowly northwestward. On 2 August, Man-yi developed in the cyclonic vorticity region of the wave train.

Among the eleven SWT-induced cyclogenesis cases, four were associated with equatorial MRG waves. The MRG wave has an equatorially antisymmetric structure with pronounced clockwise cross-equatorial flow. An example is given for Typhoon Sepat [see Fig. 7 of Fu et al. (2007)]. An equatorial MRG wave appeared on 24 August 2001 near the dateline. As its phase propagates westward, the group velocity of the MRG wave was eastward. This led to the development of the second MRG wave to its east, which had counter-clockwise flow. Meanwhile, the original MRG wave deviated to the north of the equator. This led to the development of a northwest–southeast-oriented wave train in the WNP. The wave train was clearly seen in the 3–8-day filtered wind field on 26 August. As the wave train continued to develop, a new TC named Sepat formed in the cyclonic vorticity region of the wave train on 27 August. Such a transition process from an equatorial MRG wave to off-equator tropical depression (TD)-type disturbances is consistent with previous studies (Takayabu and Nitta 1993; Dickinson and Molinari 2002).

4.2.3 TC Genesis Associated with Easterly Waves

The third type of cyclogenesis in the WNP is associated with the development of Pacific easterly waves (PEW). Different from African easterly waves, the energy source of the PEW comes from mid-latitude Jet (a specific discussion of this subject

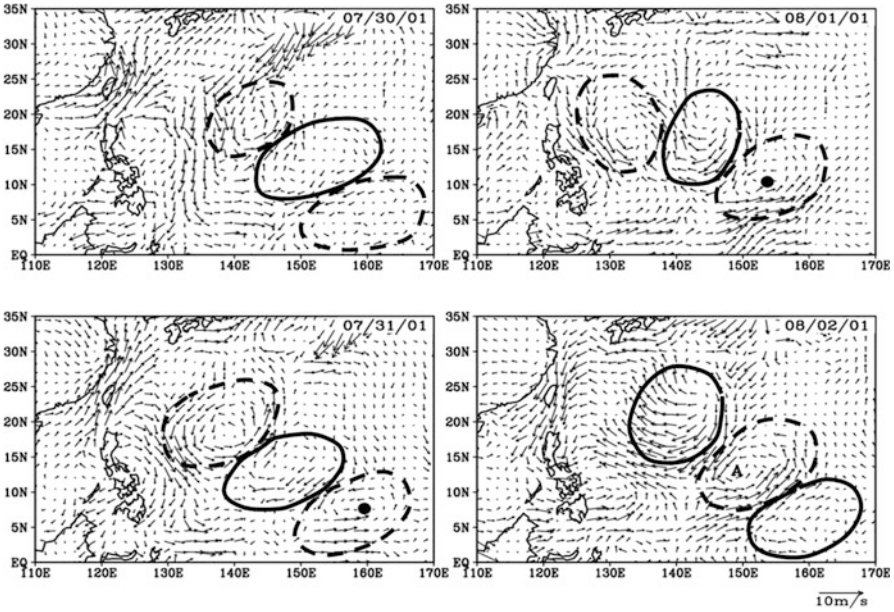

Fig. 4.2 Time evolution of 3–8-day filtered QuikSCAT surface wind patterns associated with synoptic wave train. The *dots* indicate the center location of cyclonic circulation prior to genesis of Typhoon "Man-yi"; "A" indicates the center location of Typhoon "Man-yi" on the day of genesis. Cyclonic/anticyclonic circulation is marked with *dashed*/*solid circle* (From Fu et al. (2007). © Copyright 2007 American Meteorological Society (AMS))

will be given in Sect. 3). During 2000–2001 summers, seven PEW-induced cyclogenesis cases were identified. Only cyclogenesis cases that were associated with clear westward propagation signals in both the perturbation kinetic energy and rainfall fields derived from the TMI data were considered as PEW-induced cyclogenesis cases.

An example of PEW-induced TC genesis is given for Typhoon Kong-rey, which formed on 22 July 2001. Figure 4.3 shows the time–longitude cross section of the perturbation kinetic energy and the precipitation rate along the latitude 25°N where Kong-rey formed. Both the precipitation and the perturbation energy showed clear westward propagation prior to the genesis of Kong-rey. The wave signals could be traced back 4–5 days prior to Kong-rey's formation. The phase speed of the easterly wave was estimated around 4–5 longitude degrees per day.

The vertical cross section of the easterly wave derived from 3–8-day filtered NCEP–NCAR reanalysis data showed that this easterly wave was quite deep and had an equivalent barotropic structure (Fu et al. 2007). The wave amplitude had two maxima at 600–700 hPa and 200–300 hPa, respectively. This vertical profile was consistent with previous observational studies of easterly wave structures (Reed and Recker 1971).

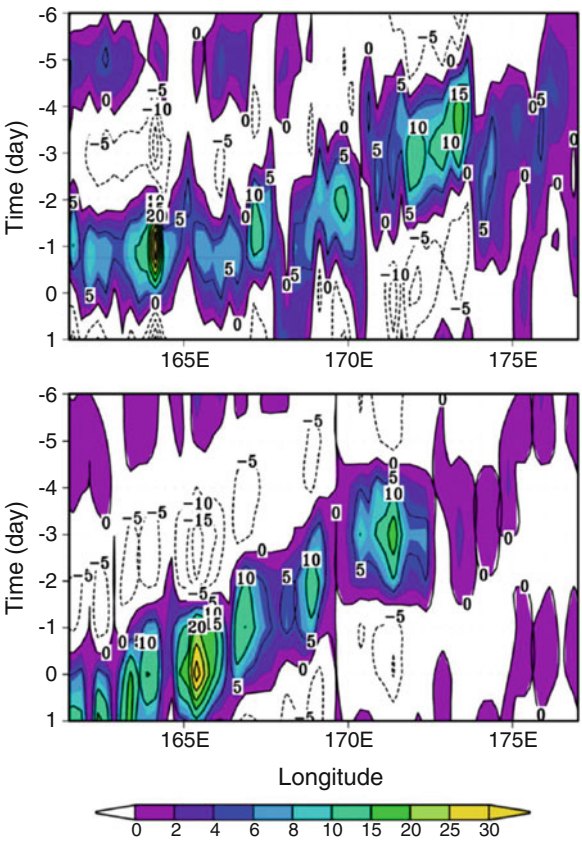

Fig. 4.3 Time–longitude profiles of the surface kinetic energy $(u^2 + v^2)'/2$ (*upper panel*, units: m^2s^{-2}) and precipitation rate (*lower panel*, units: mm day^{-1}) along 25°N. The horizontal axis is longitude and the vertical axis is time in days. Typhoon Kong-rey formed at 150.2°E, 25°N on 22 July 2001 (corresponding to day 0). Both panels show clear westward-propagating signals prior to the birth of Kong-rey (From Fu et al. (2007). © Copyright 2007 American Meteorological Society (AMS))

4.2.4 Precursor Signals in the Middle or Upper Troposphere

The previous three types of genesis scenarios have primarily low-level precursor signals. It was found that some TCs did not have significant surface precursor signals; rather, they had precursor signals in the middle or upper troposphere.

One such example is Typhoon Usagi, which formed on 9 August 2001. Figure 4.4 shows that this cyclogenesis event was associated with preexisting cloud activity. Three days prior to the genesis of Usagi, clouds represented by TMI cloud liquid water content had already appeared over the region where Usagi formed. However, from the 3–8-day filtered QuikSCAT wind fields, there was no clear cyclonic wind perturbation at the surface.

A further analysis of the NCEP final analysis product showed that 2–3 days prior to the TC genesis, a mid-level cyclonic vortex had already set up. The mid-level vortex was accompanied with a weak warm core above and a cold core below and eventually led to the cyclone development near the surface. This mid-level vortex triggering process has been suggested by Simpson et al. (1997), although specific

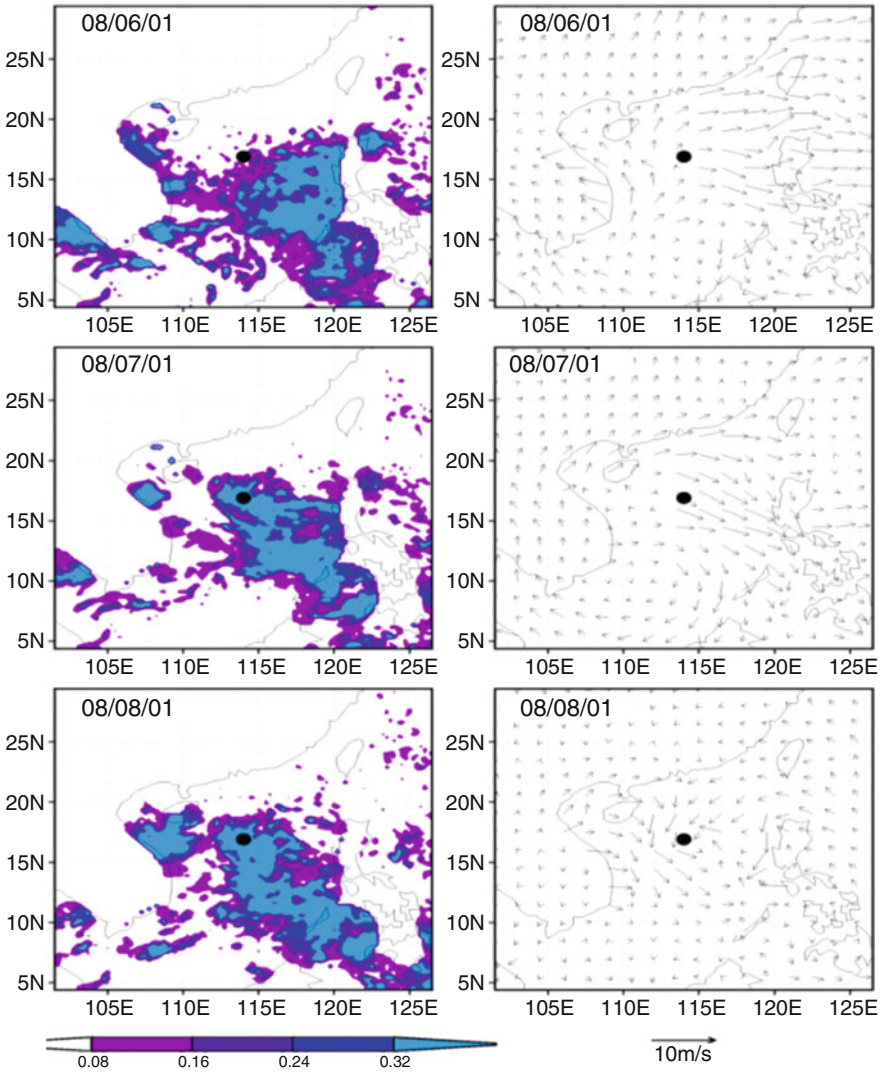

Fig. 4.4 Time evolution of TMI cloud liquid water (*left*) and 3–8-day filtered QuikSCAT surface wind (*right*) prior to the genesis of TC Usagi. Usagi formed on 9 Aug 2001. The *dots* indicate the position where Usagi formed (From Fu et al. (2007). © Copyright 2007 American Meteorological Society (AMS))

processes that lead to the downward development of cyclonic vorticity are not clear. Numerical simulations in Sect. 4 will further explore this cyclogenesis process.

Some TC genesis events in the WNP were related to upper tropospheric forcing. Colon and Nightingale (1963) examined the evolution of 200 hPa flows and found that a poleward flow aloft, such as those in the eastern side of troughs in the westerlies or those in the western side of anticyclones, is a favorable environmental

condition for the development of low-level perturbations. Sadler (1976) developed a synoptic model to describe the role of the tropical upper tropospheric trough (TUTT). He suggested that TUTT might have three effects on TC development. Firstly, the accompanying sub-equatorial ridge on the south side of TUTT lies over the low-level low that may decrease the vertical shear; secondly, a divergent flow on the south and east side of the cyclonic circulation in TUTT may increase the ventilation aloft to help the development of a low-level low; thirdly, a channel to large-scale westerlies may be established for efficient outflow of the heat released by increased convection in the developing depression.

During 2000–2001 summers, three genesis events were associated with the upper tropospheric forcing (Fu et al. 2007). An example is Typhoon Nari, which formed on 6 September 2001. Two days prior to its formation, an upper-level trough is located approximately 20 degrees west of the genesis location. One day later, this trough moved eastward 10 longitude degrees. In the meantime, this upper-level trough deepened, and the southwesterly flow on the east side of the trough became stronger. On the genesis date, this trough was within 5 degrees to the northwest of Nari's genesis position. As a result, strong southwesterlies dominated in this area, and an outflow channel was set up in upper levels north of Nari. This led to the enhancement of low-level disturbances and was possibly responsible for Nari's genesis.

4.3 Origin of Synoptic-Scale Wave Trains and Easterly Waves in WNP

Dominant synoptic-scale variability in the WNP is a northwest–southeast oriented synoptic-scale wave train (Lau and Lau 1990). The wave train extends toward the southeast with a wave-like pattern that consists of alternating regions of cyclonic and anticyclonic circulations, propagating northwestward. The wave train has a typical wavelength of ~2500 km and a timescale of 6–10 days.

What causes the genesis of SWT in the WNP? Li (2006) hypothesized that the SWT is an unstable mode of the summer mean flow in the presence of the convection–circulation–moisture (CCM) feedback. To test this hypothesis, an anomaly atmospheric general circulation model (AGCM) was employed. The model was modified from the original version of Princeton global spectrum atmospheric model (Held and Suarez 1994). It was linearized by a specified 3D basic state [see the appendix of Li (2006) for the detailed derivation of the model and the treatment of circulation-dependent perturbation heating]. This anomaly model was used in studying an asymmetric atmospheric response to equatorially symmetric forcing (Wang et al. 2003) and MJO initiation in the western Indian Ocean (Jiang and Li 2005).

The model used sigma ($\sigma = p/p_s$) as its vertical coordinate, and vertically there were five evenly distributed sigma levels, with a top level at $\sigma = 0$ and a bottom

level at $\sigma = 1$. The horizontal resolution was T42. Rayleigh friction was applied to the momentum equations, with the damping rate of 1 day^{-1} taken in the lowest model level ($\sigma = 0.9$) to mimic the planetary boundary layer, linearly decaying to 0.1 day^{-1} at the level of $\sigma = 0.7$. Newtonian cooling with an e-folding timescale of 10 days was applied to the temperature equation at all the model levels. Because the focus of the study was on tropical perturbations, a strong damping of 1 day^{-1} was applied in the perturbation momentum and temperature equations over higher-latitude regions (beyond 40°N and 40°S). A realistic summer (JJA) mean state of $\bar{u}, \bar{v}, \bar{T}, \bar{P}_s$ was prescribed as the basic state, taken from the long-time mean of the NCEP–NCAR reanalysis.

Initially a small perturbation with a zonal wavenumber 9 structure was introduced. In the presence of both the summer mean flow and the convection–moisture–circulation feedback, the model captured the growth of the most unstable mode in WNP. The fastest growing mode in the model had a typical observed synoptic-scale wave train structure in WNP (see Fig. 4.5a). The wave train, oriented in the northwest–southeast direction, had alternative cyclonic and anticyclonic circulation regions and a zonal wavelength of 2500 km. The preferred geographic location for the perturbation growth appeared in the WNP, primarily due to high moist static energy (MSE) in the region. This is because the background MSE condition would lead to the strongest CCM feedback, given the same perturbation vorticity. The unstable mode, with an eastward tilting vertical structure, propagated northwestward.

In the absence of the CCM feedback, the initial perturbation did not grow; rather, it decayed. This indicated that the climatologic summer mean flow alone (without involving of the CCM feedback) was unable to destabilize tropical perturbations. Thus, the summer mean flow only supported a weakly damped mode in the tropics. This differs fundamentally from mid-latitude baroclinic instability waves, which gain energy directly from the mean westerly jet. The numerical result was consistent with the observational study by Lau and Lau (1992), who pointed out that the primary heat source for the SWT was the latent heating associated with deep convection.

Although the summer mean flow alone was unable to cause the perturbation growth, it did play a role in determining a preferred length scale, wave train structure, and propagation characteristics. Figure 4.5b illustrates the meridional wind structure of the least damped mode in the absence of the CCM feedback. A northwest–southeast-oriented wave train pattern emerged. The wave train had alternative cyclonic and anticyclonic circulation regions, with a wavelength of about 2500 km. The weakly damped mode propagated toward the west and northwest.

Further sensitivity experiments with different initial conditions indicated that the final structure of the unstable mode was not sensitive to the initial conditions. In all cases the model reproduced the most unstable modes that had a synoptic wave train structure similar to that shown in Fig. 4.5a. This supported the hypothesis that the summertime synoptic wave train in the WNP was a result of instability of the summer mean flow in the presence of the CCM feedback. Any types of

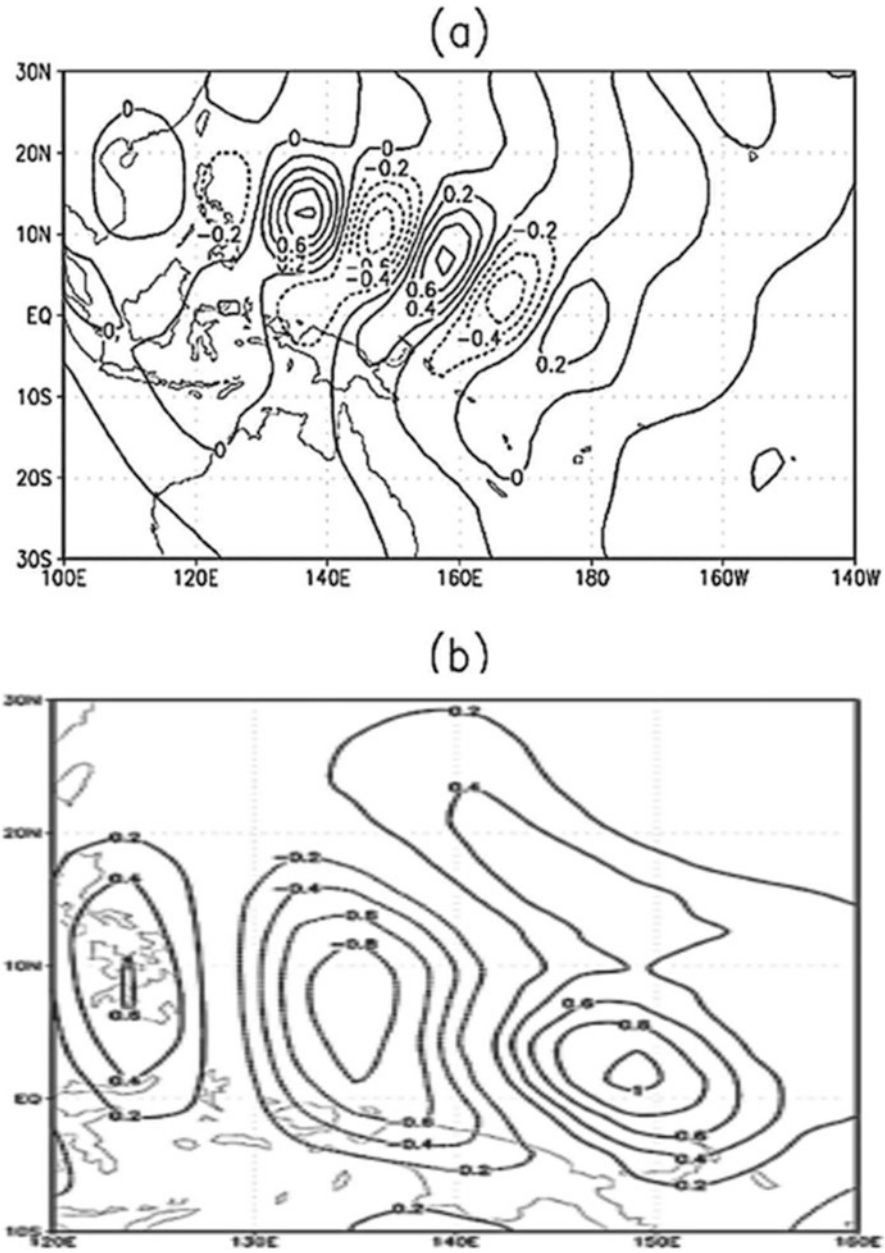

Fig. 4.5 Horizontal patterns of normalized meridional wind fields at $\sigma = 0.7$ (contour interval: 0.2) associated with (**a**) the most unstable mode in the presence of the CMC feedback and (**b**) the least damped mode in the lack of the CMC feedback (From Li (2006). © Copyright 2006 American Meteorological Society (AMS))

perturbations under such a background condition could grow and develop into the wave train pattern.

To reveal the energy accumulation mechanism and dispersion characteristics of Pacific easterly waves, Tam and Li (2006) conducted an observational analysis using NCEP–NCAR reanalysis data. A phase-independent wave-activity flux of Takaya and Nakamura (2001) was applied to examine the wave-activity and energy accumulation associated with PEW. The convergence of the wave-activity flux was found in the region of 135°–160°E, 10°–25°N. Such convergence could lead to the amplification of Rossby waves, and its pattern was in agreement with the region of positive growth of the observed perturbations.

Negative zonal group velocity associated with the PEW was found everywhere in the WNP, indicative of Rossby wave energy moving to the west at low level. The zonal wavelength of the PEW was estimated. It was found that the zonal wavenumber, k, increased as the wave moves westward. The zonal scale contraction led to the convergence of the group velocity (hence wave activity). There was accumulation of wave activity in the low levels associated with a wave packet of the PEW. The largest contribution to the wave-activity accumulation came from the convergence of intrinsic group velocity, which was attributed to the contraction of wavelength toward the west and the change of the horizontal tilt of waves. By comparison, convergence of the mean flow contributed less to the wave-activity accumulation.

It was found that the phase relationship between convection and vorticity depended on longitudinal positions. Signals of enhanced convection were in phase with positive low-level vorticity anomalies west of about 150°E, but to the east the vorticity led the convection by one quarter of a wavelength. This indicated that there were two different dynamical regimes along the "storm tracks" of synoptic-scale activity. In the eastern portion or at the entrance of the storm tracks, heat flux associated with synoptic-scale eddies was found to be equatorward (i.e., $v'T' < 0$) in the mid-troposphere. This could be seen in composite maps of circulation as well as eddy covariance statistics.

Associated with the negative heat flux signals was downward injection of wave activity from the upper levels. In the upper troposphere, southward wave activity from the extratropics was able to penetrate into the tropics near the dateline. Figure 4.6 is a schematic diagram illustrating 3D energy propagation characteristics associated with PEW. The result suggested that the energy source of Pacific easterly waves originated from mid-latitude Pacific jet. This hypothesis was supported by a case study in which upper-level activity was able to initiate a synoptic-scale wave train with strong surface circulation features. Potential vorticity anomalies intruded into the Tropics due to wave breaking were seen to cause downward development, leading to low-level disturbances which subsequently moved westward and grew.

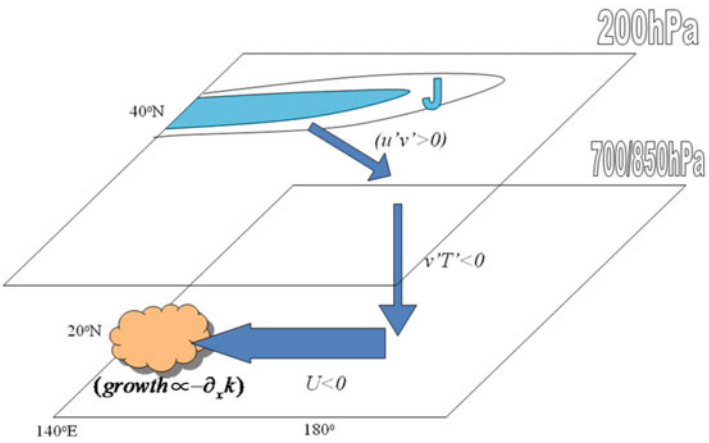

Fig. 4.6 A schematic diagram illustrating the southward wave energy propagation from the mid-latitude Pacific jet to tropical central Pacific, downward energy propagation in the tropical central Pacific, and westward wave-activity flux in the lower troposphere over the western North Pacific. Both wave scale contraction and confluent mean flows contribute to the energy accumulation of easterly waves in the maximum perturbation growth region (135°E–160°E, 10°–25°N)

4.4 Numerical Simulations of TC Genesis

4.4.1 Cyclogenesis Due to TCED

The cyclogenesis associated with TC energy dispersion was simulated in a 3D model. The atmospheric model used in the study was the triply nested movable mesh primitive equation model (TCM3). A detailed description of the model and experiment design can be found in Li et al. (2006). An initial vortex was spun up on a beta-plane for 10 days. The environmental temperature and moisture profiles were the same as those in Wang (2001) and represented the mean summertime conditions over the western Pacific. At the end of the 10-day integration, a 3D Rossby wave train pattern developed. To study the mean flow effect, an idealized monsoon gyre (MG) pattern was specified. This MG had a size of 3000 km and a central minimum pressure 2–3 hPa lower than the surrounding environment. The maximum wind of the MG was about 5 m s^{-1} at a radius of 300 km from the center. Both the pattern and amplitude of the specified MG were quite close to the observed composite (Ritchie and Holland 1999).

The following three experiments were conducted. In the first experiment (Exp1), the model was initialized with the Rossby wave train only. This experiment was designed to examine whether the wave train alone can develop into a TC in a resting environment. In the second experiment (Exp2), how the background MG evolved with time was examined, without the involvement of the TCED-induced Rossby wave train. In the third experiment (Exp3), the Rossby wave train was superposed

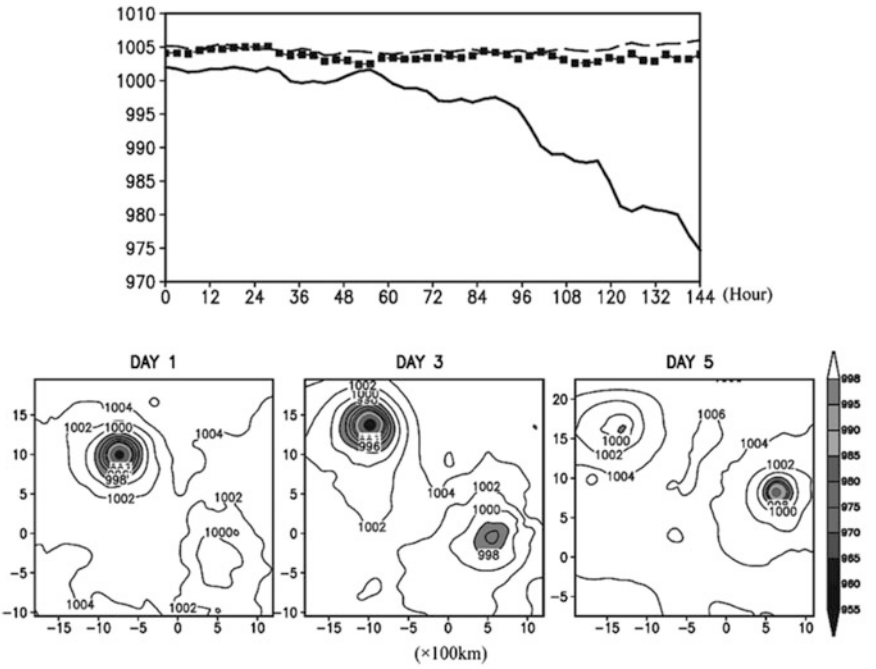

Fig. 4.7 Time evolution of minimum sea-level pressure fields (*upper panel*) for Exp1 (*dashed line*), Exp2 (*dotted line*), and Exp3 (*solid line*). The *lower panels* show the surface pressure (unit, hPa) patterns at day 1, 3, and 5 in Exp3 (From Li et al. (2006). © Copyright 2006 American Meteorological Society (AMS))

on the MG as the initial condition; it was designed to examine whether the wave train–MG interaction could lead to cyclogenesis.

The simulation results (Fig. 4.7) showed that while the wave train alone or the MG alone did not cause cyclogenesis, the superposition of wave train and MG led to the generation of a new TC. This result suggested that a proper mean flow pattern was essential for the TCED-induced wave train to develop into a TC. The simulated new vortex exhibited realistic TC characteristics, including a tilted eyewall, a warm core, and a vigorous in–up–and–out mean secondary circulation with mean subsidence in the eye region.

Figure 4.8 shows the evolution of simulated vorticity, relative humidity, vertical velocity, and rainfall rate (averaged over a 120 km by 120-km domain centered at the maximum low-level vorticity) in Exp3. Two important features in the vorticity field were worth noting. First, maximum vorticity generation occurred in the PBL, and with the TC development the cyclonic vorticity gradually penetrated from the PBL into the upper troposphere. Secondly, during the initial development stage, the PBL vorticity experienced an oscillatory growth. For instance, the vorticity grew rapidly between hours 60 and 64, slowed down or even decayed afterward, and re-intensified at hours 72–78. The averaged rain rate also exhibited a clear

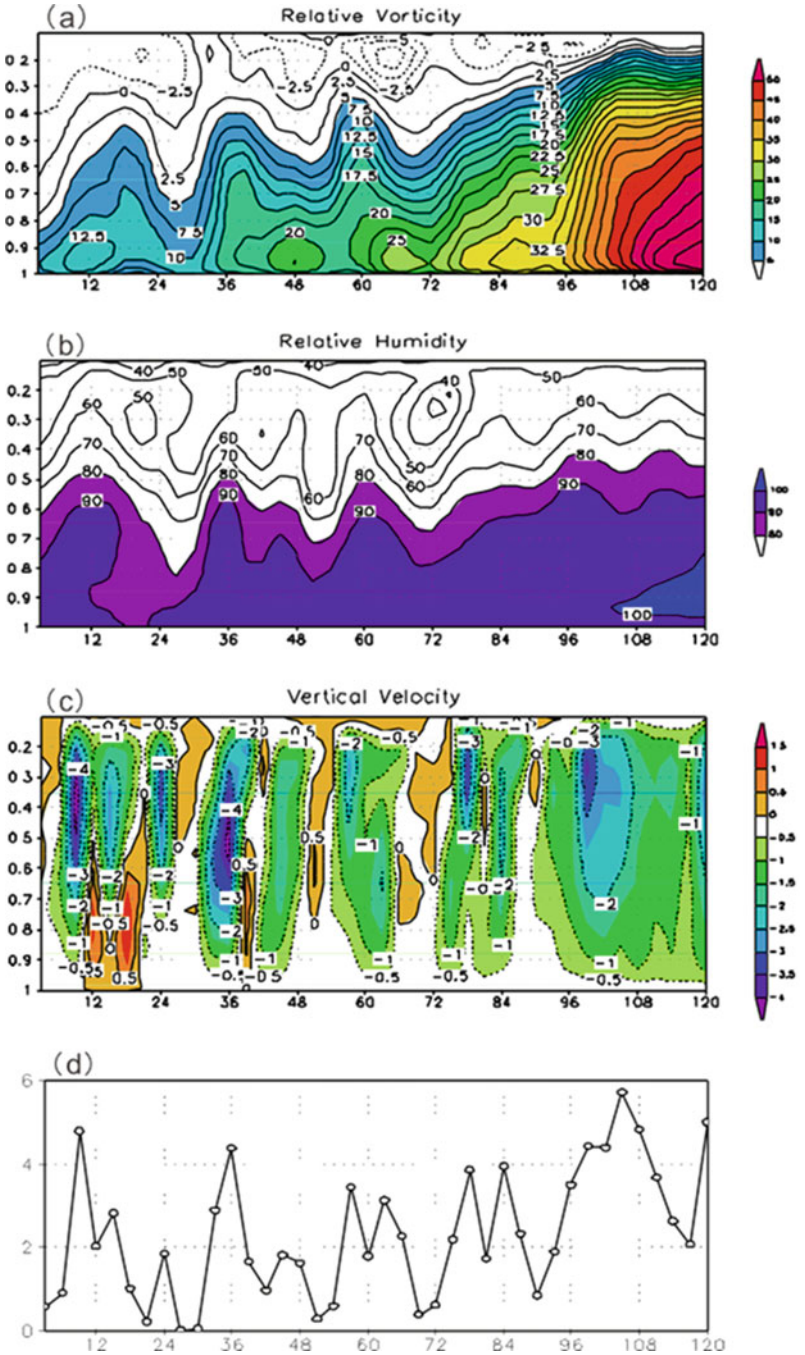

Fig. 4.8 Time evolution of (**a**) vorticity (unit, 10^{-5} s^{-1}), (**b**) relative humidity (unit, %), (**c**) vertical motion (unit, 10^{-5} s^{-1}), and (**d**) rainfall rate (unit, mm/hr) averaged over a 120 km by 120-km domain centered at the low-level maximum vorticity in Exp3. The horizontal axis is time (unit, hours) and the vertical axis in (**a**–**c**) is the sigma level (From Li et al. (2006). © Copyright 2006 American Meteorological Society (AMS))

oscillatory evolution with periods ranged from 9 to 15 h. This oscillation feature was clearly seen in the vorticity or rainfall field averaged even over a larger domain (e.g., 240 km by 240 km).

The oscillatory vorticity development was closely related to the evolution of vertical motion and relative humidity fields. It can be seen from Fig. 4.8 that there are alternations of updraft and downdraft, corresponding well to convectively "active" and "break" phases. While the ascending motion associated with penetrated convection led to PBL convergence and thus a positive vorticity tendency, the downdraft led to PBL divergence and thus a negative vorticity tendency. A vorticity budget analysis indicated that the generation of the PBL vorticity in the model was primarily attributed to the divergence term. The vertical motion regulated the moisture profile through vertical moisture transport, leading to the alternative change of relative humidity in mid-troposphere.

The oscillatory development found in the model was validated by observed rainfall and cloud-top temperature evolutions (Li et al. 2006). The diagnosis of the model output showed that the oscillatory development was attributed to the discharge and recharge of the PBL moisture and its interaction with convection and circulation. The moisture–convection feedback regulated the TC development through controlling the atmospheric stratification, raindrop-induced evaporative cooling and downdraft, PBL divergence, and vorticity generation. On one hand, ascending motion associated with deep convection transported moisture upward and led to the discharge of PBL moisture and a convectively stable stratification. On the other hand, the convection-induced raindrops evaporated, leading to mid-level cooling and downdraft. The downdraft further led to dryness and a reduction of equivalent potential temperature. This reduction along with the recharge of PBL moisture due to surface evaporation led to re-establishment of a convectively unstable stratification and thus new convection.

4.4.2 *Cyclogenesis Efficiency: Mid-level Versus Bottom Vortex*

TC genesis may occur either in an environment with a near bottom vortex (EBV) or an environment with a mid-level vortex (EMV). Which scenario leads to greater genesis efficiency? A cloud-resolving WRF model was used to address this question. The model was quadruply nested. The mesh sizes in all four domains were 181×181 with horizontal grid sizes of 54, 18, 6, and 2 km, respectively. There were 27 levels in the vertical. The Kain–Fritsch convective scheme (Kain and Fritsch 1990) was applied in the two outer meshes, and an explicit microphysics scheme (Lin et al. 1983) was used in the finer meshes. Initial water vapor mixing ratio and other thermodynamic variables were assumed horizontally homogeneous and had the vertical profiles of typical January mean observations at Willis Island, northeast of Australia (Holland 1997). The model was set on an *f*-plane centered at 15°N, and

a quiescent environment with a constant sea surface temperature (SST) of 29 °C was specified. For more detailed model description, readers are referred to Ge et al. (2013).

Four experiments were designed. The first experiment (MID_VORTEX) mimicked a mid-level precursor condition, in which initial vortex had a maximum vorticity at 600 hPa, with a maximum wind speed of 8 m s^{-1} at a radius of 100 km and a size of 500-km radius where the wind vanished. The vorticity gradually decreased both upward and downward and vanished at the surface. In the second experiment (BTM_VORTEX), an initial maximum precursor perturbation with a maximum wind speed of 8 ms^{-1} was located at the surface. Figures 4.9a, b show the vertical–radial cross section of the tangential wind of these initial vortexes. The third and the fourth experiment contained a shallow mid-level vortex (SHAL_MID) and a shallow bottom vortex (SHAL_BTM), respectively, to identify the PBL effects and to better separate the mid-level and the bottom vortices. Their vertical wind profiles are shown in Figs. 4.9c, d.

In all the four experiments, after integration of several days, a TC with realistic dynamic and thermodynamic structures formed. The simulated TC characteristics included a tilted eyewall, a vigorous in–up–and–out secondary circulation, and subsidence within the eyewall. The maximum tangential wind speed reached to 60 ms^{-1} at a radius of about 20 km. Strong inflow appeared in the PBL, with maximum inflow just outside the radius of the maximum tangential wind. A broad outflow layer appeared in the upper troposphere outside the eyewall.

A marked difference among these experiments was the timing of a rapid pressure drop, suggesting that each event possessed distinct genesis efficiency. Here the genesis time was defined as time when the maximum surface wind reached 17.5 ms^{-1} – a criterion for the tropical storm strength. Figure 4.10 shows the time evolutions of the corresponding maximum surface wind speed from the four experiments. Based on the definition above, the genesis time occurred at hour 33 for BTM_VORTEX, hour 66 for MID_VORTEX, hour 78 for SHAL_BTM, and hour 114 for SHAL_MID, respectively.

Figure 4.11 presents the vertical cross section of relative vorticity and temperature anomaly fields averaged over a 100 km × 100 km domain centered at the minimum sea level pressure (MSLP) from the four experiments. In MID_VORTEX, the initial mid-level vorticity maximum coincided well with a cold (warm) core below (above) 600 hPa (top-left panel of Fig. 4.11), due to the thermal wind balance relationship. During the first 30 h, the mid-level cyclonic vorticity gradually weakened and the "cold core" structure became less distinct. The mid-level vortex re-intensified and created a maximum vorticity center at 500 hPa at hour 48. Associated with this re-establishment of the mid-level vortex was the development of a cold-warm-core couplet and the mid-level convergence. The temperature anomaly (defined as the departure from the mean temperature over the innermost domain) showed a clear cold (warm) anomaly below (aloft) 600 hPa. A weak divergence appeared around 800 hPa before hour 60, implying descending motions and a relative dry layer between 600 and 800 hPa. The thermodynamic structure at hours 48–60 bore the characteristics of stratiform precipitation regime (Yuter and Houze 1995), indicating that stratiform cloud was dominated at this time.

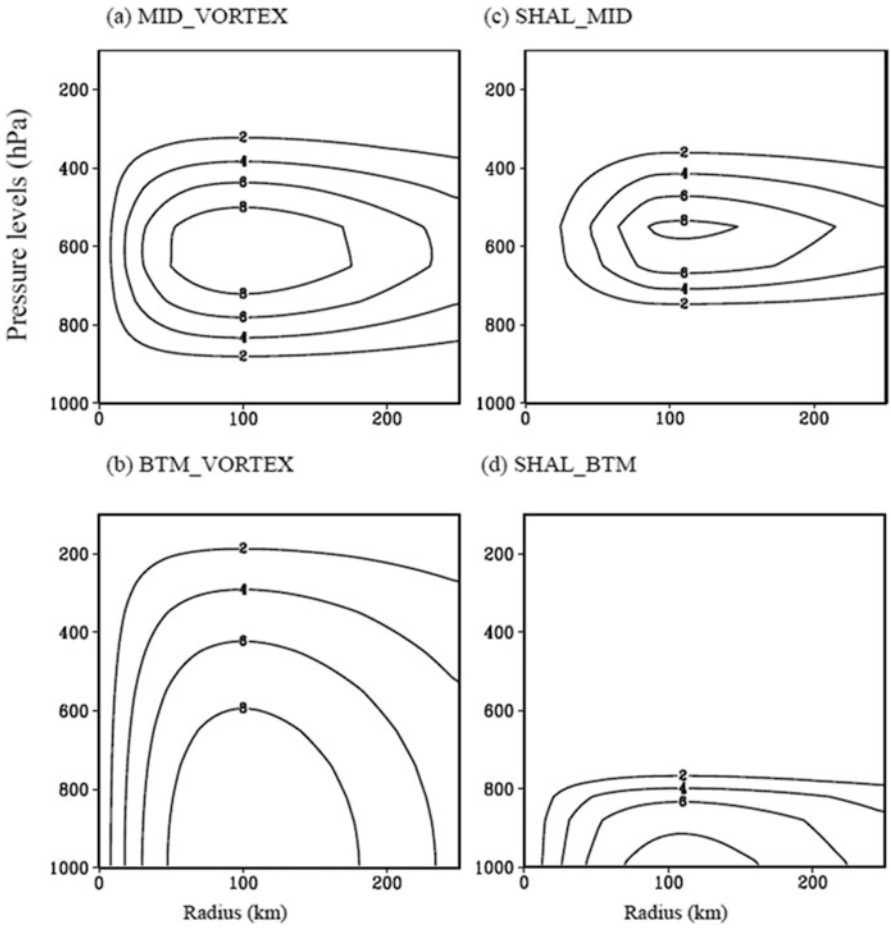

Fig. 4.9 The vertical–radial cross section of tangential velocity (ms^{-1}) of the initial vortex in (**a**) MID_VORTEX, (**b**) BTM_VORTEX, (**c**) SHAL_MID, and (**d**) SHAL_BTM (From Ge et al. (2013). © Copyright 2013 Journal of Tropical Meteorology office)

The similar plots for BTM_VORTEX were depicted in the bottom-left panel of Fig. 4.11. In this case, a rapid pressure drop occurred after hour 33, indicating faster TC development compared to MID_VORTEX. Although initially the maximum vorticity appeared at the low level, a mid-level vorticity enhancement was observed at hour 30. Associated with this mid-level vorticity enhancement was a cold-warm-core couplet (i.e., a cold core at lower level and a warm core above, bottom-left panel of Fig. 4.11). The temperature and vorticity profiles at that time were associated with a mid-level convergence and downdrafts below, reflecting stratiform cloud regime. Although the TC genesis was slower in the two shallow vortex cases, the vorticity and temperature evolution characteristics in SHAL_MID and

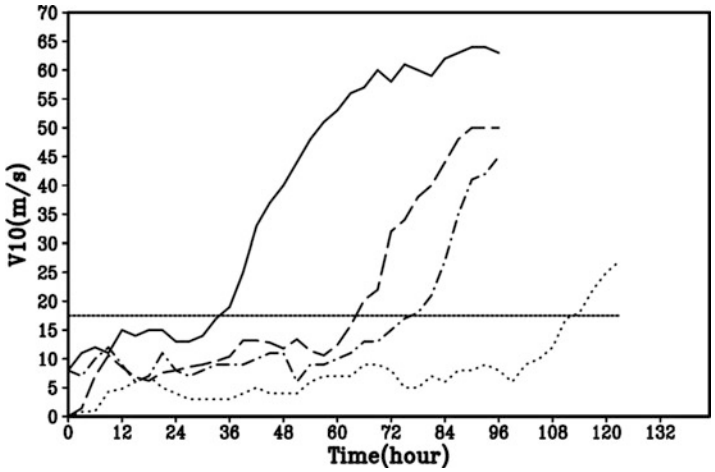

Fig. 4.10 Time evolution of the simulated maximum surface wind speed in BTM_VORTEX (*solid line*), MID_VORTEX (*dashed line*), SHAL_BTM (*dot-dashed line*), and SHAL_MID (*dotted line*). The horizontal *dotted line* in the *bottom panel* indicated the threshold of TC genesis when the wind speed reaches 17.5 ms^{-1} (From Ge et al. (2013). © Copyright 2013 Journal of Tropical Meteorology office)

SHAL_BTM (right panels of Fig. 4.11) bore many similarities to their counterparts with deeper vorticity profiles.

A common feature among the EBV and EMV experiments was the formation of a mid-level maximum vorticity prior to TC genesis irrespective where the initial vorticity maximum is located. A comparison of the BTM_VORTEX and MID_VORTEX experiments indicated that the former had greater genesis efficiency. A possible cause of this genesis efficiency difference was attributed to the initial column integrated absolute vorticity. Note that the former had greater column-integrated (from 1000 to 200 hPa) absolute vorticity than the latter. Physically, it was argued that vertically integrated absolute vorticity could affect vorticity segregation (Schecter and Dubin 1999). To examine additional factors that affected genesis efficiency, two shallow vortex cases (SHAL_BTM and SHAL_MID) were further considered, in which the vertically (1000–200 hPa) integrated absolute vorticity was almost same. The simulation results showed that the cyclogenesis time in SHAL_BTM occurred at hour 78, which was much faster than the genesis time (hour 114) in SHAL_MID. Thus the numerical model results indicated that given the same column integrated absolute vorticity, a bottom vortex was more efficient in cyclogenesis than a mid-level vortex. The difference was likely attributed to the effect of surface fluxes and PBL processes.

A common development characteristic among the four experiments was the occurrence of upscale cascade from randomly distributed cumulus-scale (~5 km) vertical hot towers (VHTs) to an organized meso-vortex-scale (~50–100 km) system (MVS). Sporadic cumulus-scale (~5 km) convective cells developed shortly after the integration started, due to the conditionally unstable environmental

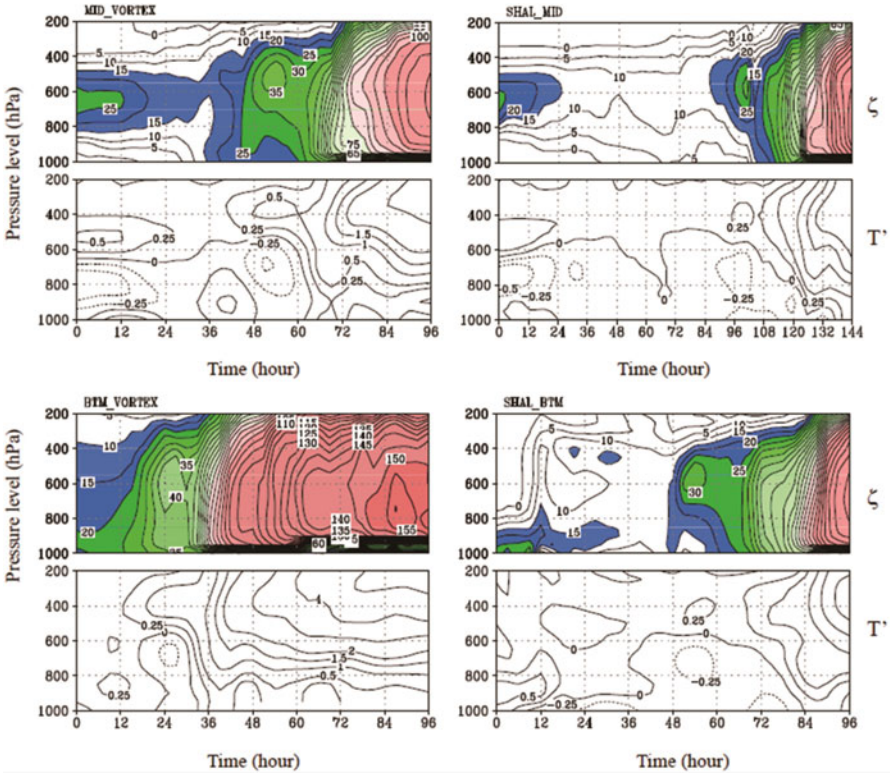

Fig. 4.11 Time-vertical (unit, hPa) cross section of relative vorticity (ζ, unit: 1×10^{-5} s^{-1}) and temperature anomaly (T′, unit: K) averaged over a 100 km × 100 km domain centered at the MSLP in MID_VORTEX (*top left*), BTM_VORTEX (*bottom left*), SHAL_MID (*top right*), and SHAL_BTM (*bottom right*) (From Ge et al. (2013). © Copyright 2013 Journal of Tropical Meteorology office)

condition and the surface evaporation over the ocean. While the cumulus-scale (~5 km) VHTs were randomly triggered initially, they were gradually organized and merged into a MVS through merging around the environmental vorticity center. This warm-core MVS differed from conventional mid-latitude mesoscale convective system that has a distinct cold-core structure. As shown in Fig. 4.12, in MID_VORTEX, several convective cells moved closer and merged into a larger vortex with the horizontal scale of about 50 km at 48 h. A similar evolution feature was seen in BTM_VORTEX, although cumulus-scale VHTs and a MVS developed earlier than in MID_VORTEX.

The vorticity segregation proposed by Schecter and Dubin (1999) is a possible mechanism for the VHTs merging. That is, cyclonic (anticyclonic) vorticity anomalies move up (down) the ambient vorticity gradient. As a result, cyclonic vorticity anomalies tend to move inward toward the vortex center, while anticyclonic anomalies tend to move outward away from the center. This vorticity segregation

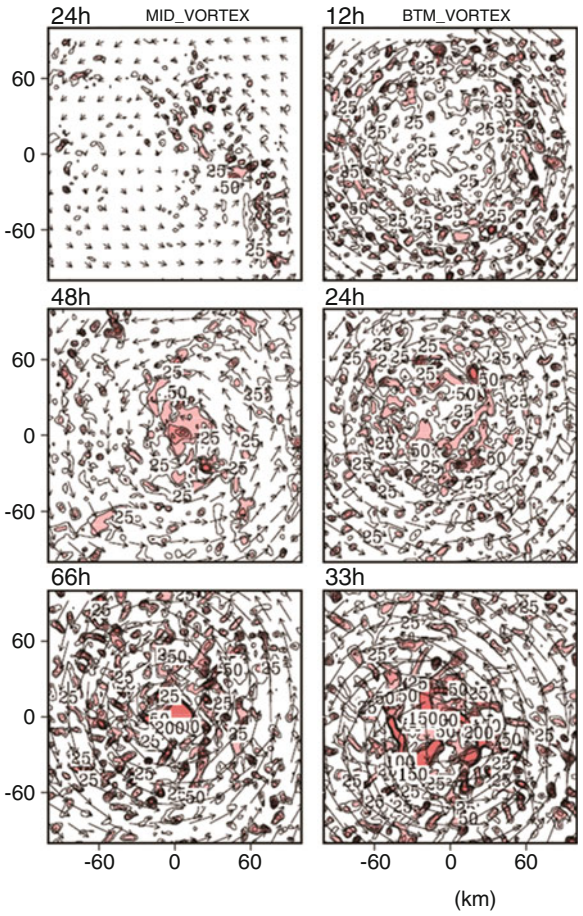

Fig. 4.12 Horizontal patterns of low-level (900 hPa) wind field (vector) and relative vorticity (greater than $3 \times 10^{-4}s^{-1}$ are *shaded*) in MID_VORTEX (*left*) and BTM_VORTEX (*right*) (From Ge et al. (2013). © Copyright 2013 Journal of Tropical Meteorology office)

as well as vortex merger or axisymmetrization (Hendricks et al. 2004; Montgomery et al. 2006; Tory et al. 2006) could cause upscale cascade from cumulus scale (~5 km) VHTs to a MVS. As seen from all experiments, the upscale cascade was the first key step toward cyclogenesis. Once the MVS system formed, the adjacent convective cells would be further absorbed or organized into outer spiral rain bands.

Another common development feature was the setup of a deep moist layer prior to cyclogenesis. For instance, in MID_VORTEX, there was a steady increase of the moist layer in the core region during hour 24–60. The 90% RH layer thickened from 900 hPa at hour 24 to about 500 hPa at hour 60. It was the establishment of this near-saturation air column that signified the next development stage: deepening of cyclonic vorticity and a rapid drop of minimum sea level pressure. Such a deepening of the moist layer appeared clearly in the other three experiments.

4.5 MJO and ENSO Impacts

In addition to an annual cycle, TC genesis frequency also experiences a significant intraseasonal variation (Gray 1979; Yamazaki and Murakami 1989; Hartmann et al. 1992; Liebmann et al. 1994; Maloney and Hartmann 2000). Several studies investigated how the atmospheric intraseasonal oscillation (ISO) modulates TC activity (Maloney and Hartmann 2001; Sobel and Maloney 2000; Maloney and Dickinson 2003). For example, Maloney and Dickinson (2003) suggested that the modulation is through enhancing or suppressing the tropical depression (TD)-type disturbances in lower troposphere. The enhancement of the TD-type disturbances is attributed to either Rossby wave accumulation caused by large-scale convergence (Holland 1995; Sobel and Bretherton 1999) or barotropic energy conversion during ISO westerly phases (Sobel and Maloney 2000; Maloney and Dickinson 2003).

The large-scale control of the ISO on the WNP cyclogenesis in 2000 and 2001 summers was examined by Fu et al. (2007). The pattern and the characteristics of the ISO were represented by the 20–70-day filtered OLR and 850 hPa zonal wind fields. Both the wind and OLR fields were widely used to represent ISO activity in many previous studies. Observational analyses showed that the ISO was characterized by enhanced (suppressed) convection and westerly (easterly) in 850 hPa zonal wind in its active (suppressed) phase. From a thermodynamic perspective, enhanced convection provided a greater large-scale low-level moisture convergence that favored the development of tropical depressions. From a dynamic perspective, the ISO westerly anomaly helped increase the cyclonic vorticity to the north and created favorable environment for tropical depression development. As a result, more TCs formed in the active phase of ISO.

The time series of area-averaged (5°N–25°N, 110°E–160°E) OLR perturbations are shown in the left panels of Fig. 4.13. There were two ISO events in the WNP each year. The active phase (negative OLR perturbations) occurred from 28 June to 15 July and from 6 August to 5 September in 2000 and from 16 June to 6 July and 8 August to 26 August for year 2001. Figure 4.13 also shows area-averaged OLR and zonal wind perturbations on the 34 cyclogenesis date in 2000 and 2001. It appears that most of TC geneses events in 2000 and 2001 were coincided with ISO active phases.

The relationship between the barotropic energy conversion and the TC genesis location during active and suppressed ISO phases are shown in Fig. 4.14. Positive conversion appeared in both the ISO active and suppressed phases, indicating that synoptic-scale disturbances always obtained kinetic energy from the total background mean (including ISO) flow (Hsu et al. 2011). Regions of enhanced barotropic conversion favored the development of synoptic seed disturbances, which could further grow into TCs. It was noted that TCs tended to form in the positive barotropic energy conversion regions. The amplitude and spatial pattern of the energy conversion varied with the ISO phase. During the ISO active phase, larger energy conversion occurred over the WNP south of 25°N (Fig. 4.14a). During the ISO suppressed phase, positive conversion with smaller amplitude

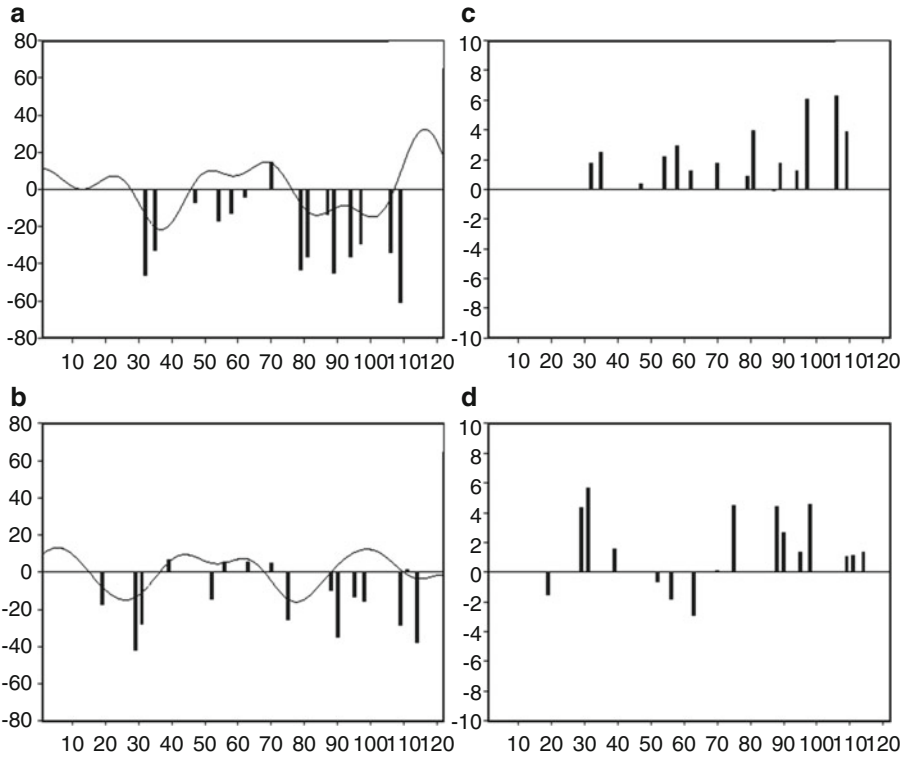

Fig. 4.13 The 20–70-day filtered OLR (unit, W/m^2) (*left panels*) and 850 mb zonal wind (unit, m/s) (*right panels*) in 2000 (*upper panels*) and 2001 (*lower panels*) as a function of time (From 1 June to 30 Sep, totally 122 days). Each bar represents the OLR or zonal wind perturbations at the location of TC genesis when TCs occur. The curves in the *left* panels are time series of 20–70-day filtered OLR averaged in the domain (5°N–25°N, 110°E–160°E) (From Fu et al. (2007). © Copyright 2007 American Meteorological Society (AMS))

appeared over the WNP (Fig. 4.14b). The TC genesis number in the WNP was approximately proportional to the barotropic energy conversion. For example, the TC genesis number during the ISO active phase was 43, 1.5 times greater than that during the ISO suppressed phase (27). A similar ratio appeared in the barotropic energy conversion amplitude.

What determines the interannual variation of TC genesis frequency in WNP? The simultaneous correlation between JJAS TC number and Nino3.4 index during 1979–2010 shows a positive value, but this correlation is statistically insignificant, from both Hadley and NOAA SST datasets (Table 4.1). Lagged correlations of JJAS TC number with the Nino3.4 index in the preceding winter (DJF 0) and in the succeeding winter (DJF +1), however, are both statistically significant at the 95% confidence level. The correlation with the Nino3.4 in the preceding winter is negative. This indicates that TC frequency decreased (increases) during El Niño (La Niña) decaying summer. The correlation with the Nino3.4 in the succeeding

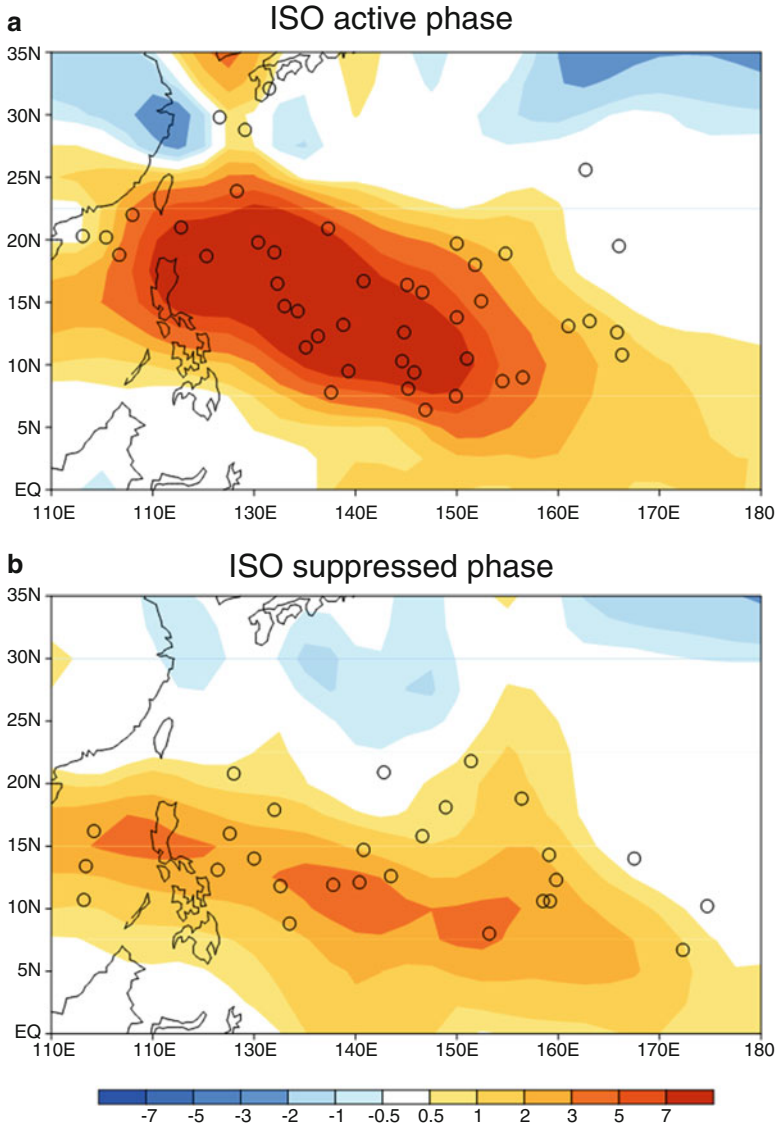

Fig. 4.14 Composites of 850-hPa barotropic energy conversion field (*shading*, unit: 10^{-5} m^2s^{-3}) and TC genesis location (*circle*) during the ISO (**a**) active and (**b**) suppressed phase (From Hsu et al. (2011). © Copyright 2011 American Meteorological Society (AMS))

winter is positive, indicating that TC frequency increased (decreased) during El Niño (La Niña) developing summer.

The observed TC number at each of El Niño developing and decaying summers is shown in Fig. 4.15. The average TC number during 1979–2010 was 15.75. Six out of eight El Niño developing summers had more than normal TC frequency, with

Table 4.1 Correlation coefficients between JJAS TC number in the WNP and Nino3.4 index at preceding winter (DJF 0), concurrent summer (JJAS), and succeeding winter (DJF+1) during 1979–2010. The first raw shows the correlation coefficients using raw SST data from the Hadley Center and NOAA. The second raw indicates the correlation coefficients using the linearly detrended SST fields from the same data sources. Bold numbers indicate correlation coefficients significant at the 0.05 level

		DJF 0	JJAS	DJF+1
Raw SST	Hadley	**−0.36**	0.25	**0.37**
	NOAA	**−0.37**	0.28	**0.35**
Detrended SST	Hadley	**−0.36**	0.26	**0.37**
	NOAA	**−0.35**	0.29	**0.36**

exceptional cases in 2006 and 2009. Six out of seven El Niño decaying summers (except in 1988) were characterized by less than normal TC frequency in the WNP. The ENSO-phase-dependent feature was quite consistent with Iizuka and Matsuura (2008), who analyzed the ENSO–TC relationship in a coupled atmosphere–ocean general circulation model.

What caused the ENSO-phase-dependent cyclogenesis feature? During the El Niño developing summer, equatorial westerly anomalies appeared in the central Pacific, which strengthened cyclonic shear and led to the southeastward shift of the monsoon trough. As seen from total and anomalous 850-hPa vorticity fields (Fig. 4.16), a maximum low-level vorticity belt extended southeastward. In the anomaly field, a large-scale positive vorticity anomaly occupied the WNP typhoon genesis region. The southeastward shift of the monsoon trough led to more frequent TC genesis in the southeast quadrant of the WNP (Wang and Chan 2002). During the El Niño decaying summer, a large-scale anomalous anticyclone appeared in the WNP (bottom panel of Fig. 4.16). This led to a weakening of the WNP monsoon trough. The ENSO-phase-dependent background flow condition caused distinctive behaviors in atmospheric ISO, with a stronger (weaker) ISO variability during the El Niño developing (decaying) summer. Thus the change of the large-scale background condition (including both the mean flow and ISO variability) was responsible for the opposite TC changes during ENSO developing and decaying summers.

Previous studies (e.g., Gray 1968; Emanuel and Nolan 2004) proposed universal TC genesis parameters for all TC basins. Given distinctive mean flow and disturbance characteristics between NATL and WNP, it is likely that factors controlling cyclogenesis differ. Peng et al. (2012) and Fu et al. (2012) investigated the differences of developing versus non-developing tropical disturbances using global daily analysis fields of the Navy Operational Atmospheric Prediction System (NOGAPS) from year 2003 to 2008. A box difference index (BDI) was introduced to quantitatively measure the differences between the developing and non-developing disturbances. The definition of the index is as below:

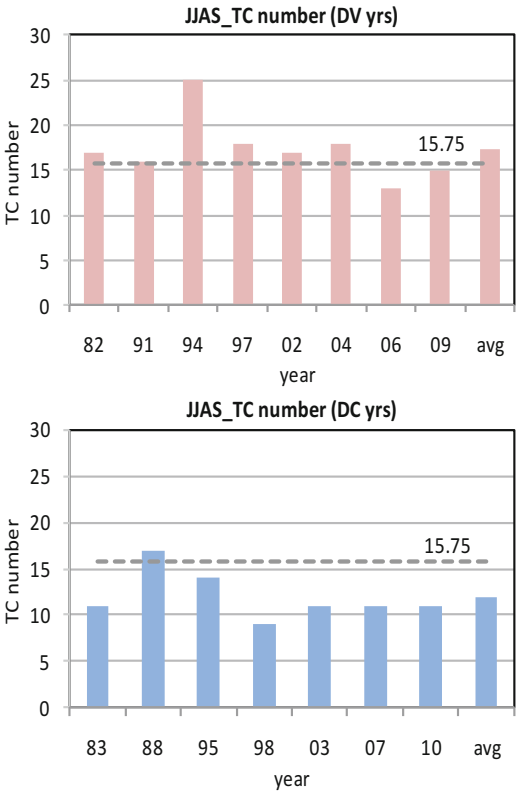

Fig. 4.15 JJAS tropical cyclone number in the WNP during the El Niño developing years (*upper panel*) and decaying years (*bottom panel*). The *dashed line* with number indicates the climatological TC number for 1979–2010

$$\mathrm{BDI} = \frac{M_{\mathrm{DEV}} - M_{\mathrm{NONDEV}}}{\sigma_{\mathrm{DEV}} + \sigma_{\mathrm{NONDEV}}},$$

where $M_{\mathrm{DEV}}$and σ_{DEV} (M_{NONDEV} and σ_{NONDEV}) represent the mean and standard deviation of a variable for the developing (non-developing) cases.

To illustrate what a BDI value means, one may take relative humidity as an example and consider a simple case that the standard deviations of the developing and non-developing groups are same. Figure 4.17 shows what it looks like in a box-and-whiskers figure when BDI is 0, 0.5, and 1. It is obvious that BDI = 0 implies that there is no difference between the two groups. BDI = 1 denotes a case in which the developing and non-developing groups are well separated, whereas BDI = 0.5 implies that the two groups are partially separated.

With the aid of the BDI, Peng et al. (2012) and Fu et al. (2012) objectively evaluated how important a genesis parameter was in distinguishing developing and non-developing disturbances at both the NATL and WNP basins. Larger BDI amplitude implies a greater possibility to differentiate the developing and non-developing groups. Using this objective method, they ranked key genesis parameters at the NATL and WNP basins.

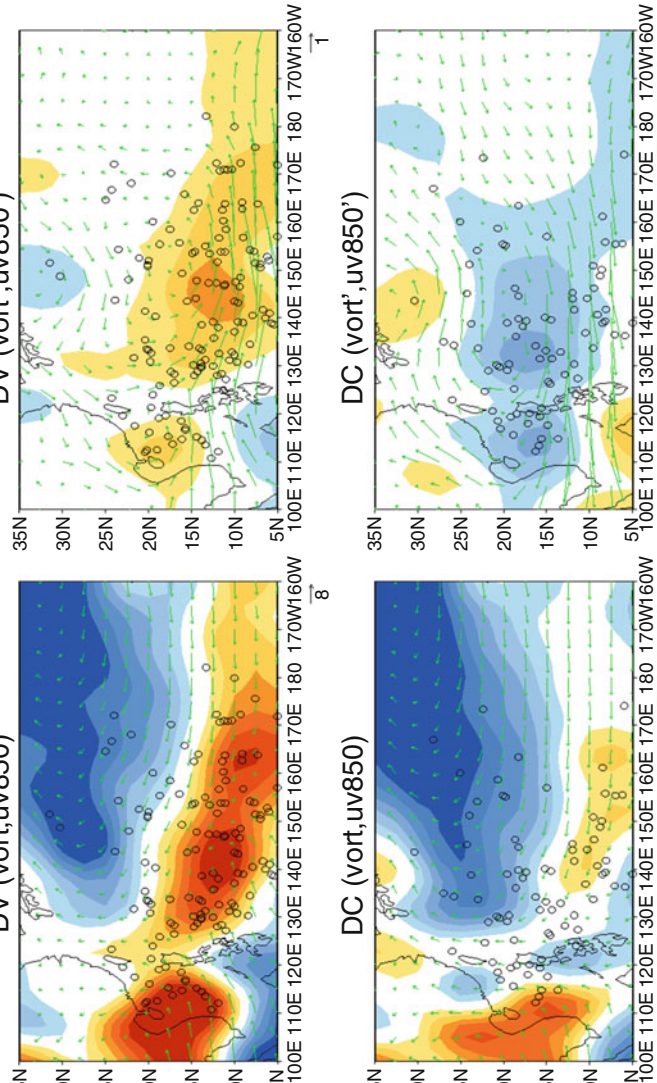

Fig. 4.16 *Left*: Composites of 850-hPa vorticity (*shading*, unit: 10^{-6} s^{-1}), wind field (*vector*, unit: m s^{-1}), and TC genesis location (*circle*) for the El Niño developing years (*upper*) and decaying years (*bottom*). *Right*: Same as *left panel* except that the shadings and vectors represent the anomalous vorticity and wind fields, respectively

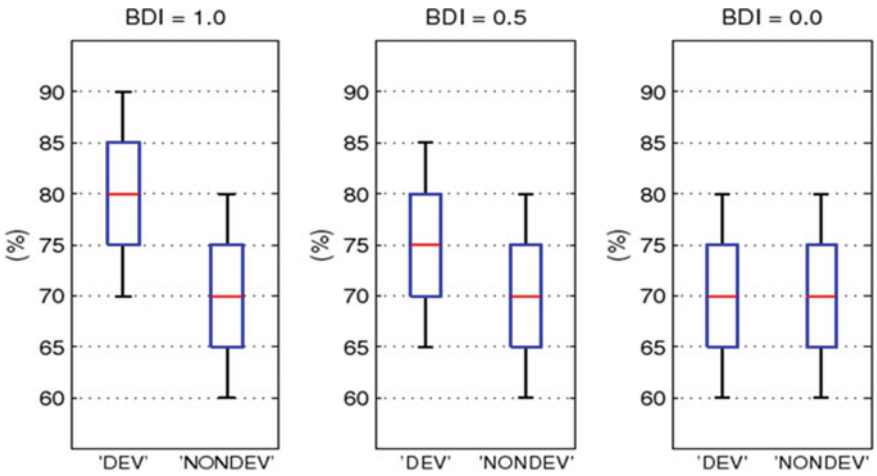

Fig. 4.17 Idealized box-and-whiskers figures for BDI = 1.0, 0.5, and 0. The *red* line denotes the mean value of a genesis parameter (say, relative humidity at 500 hPa), the *blue* box represents the standard deviation of the parameter within the developing (denoting as "DEV") and non-developing (denoting as "NONDEV") disturbance groups. Whiskers (*black line*) represent the minimum and maximum of the samples (From Peng et al. (2012). © Copyright 2012 American Meteorological Society (AMS))

Table 4.2 lists top-ranked genesis parameters in the NATL and the WNP based on the BDI calculations. It is interesting to note that the top three parameters in the NATL belong to the thermodynamic factor. For example, the vertically integrated specific humidity from 925 hPa to 400 hPa ranks the top of all the parameters, while the rain rate and SST follow as the second and the third most important parameters in NATL. In contrast, major genesis parameters in the WNP (except the rain rate) belong to the dynamic factors. Therefore, the BDI may provide a basis for selecting predictors for a statistical TC genesis forecast model at each basin.

4.6 Projection of Future TC Changes Under Global Warming

How global warming affects TC activity is a hotly debated topic (Webster et al. 2005; Emanuel 2005; Landsea et al. 2006). With the increase of the global SST and surface moisture, it was anticipated that more TCs would develop. However, many climate models simulated a global decreasing trend of TC frequency (Sugi et al. 2002; McDonald et al. 2005; Yoshimura et al. 2006; Oouchi et al. 2006; Bengtsson et al. 2007). One explanation of the decreasing trend was attributed to an increase of atmospheric static stability. This is because the global warming leads to a larger increase of air temperature in the upper troposphere than in the lower troposphere; as a result, the atmosphere becomes more stable, which suppresses the TC

Table 4.2 List of top four genesis parameters in the NATL and the WNP based on the BDI rank

Basin BDI rank	NATL	WNP
1	925–400-hPa water vapor content (**T**)	800-hPa maximum relative vorticity (**D**)
2	Rain rate (**T**)	Rain rate (**T**)
3	SST (**T**)	1000–400-hPa averaged $\partial u/\partial y$ (**D**)
4	700-hPa maximum relative vorticity (**D**)	1000–500-hPa averaged divergence (**D**)

From Peng et al. (2012). © Copyright 2012 American Meteorological Society (AMS)
"**T**" and "**D**" in the bracket denote the thermodynamic factor and the dynamic factor respectively

frequency (Sugi et al. 2002; Bengtsson et al. 2007). Does the same mechanism affect the regional TC change?

Li et al. (2010) investigated the cause of regional TC changes in the Pacific under global warming based on two high-resolution global AGCMs (Li et al. 2010). The first AGCM used was ECHAM5 (Roeckner et al. 2003) at a horizontal resolution of T319 (about 40-km grid). SST, the lower boundary condition of the model, was derived from a lower-resolution (T63) coupled version of the model (ECHAM5/MPI-OM) (Jungclaus et al. 2006), which participated in the fourth assessment report of intergovernmental panel for climate change (IPCC-AR4). Two different climate change scenarios (20C3M and A1B) were applied. In 20C3M scenario, increasing historical greenhouse gases in twentieth century were prescribed as a radiative forcing. In A1B scenario, carbon dioxide concentration was increased at a rate 1% per year till it reached 720 ppm and was then kept constant. A "time-slice" method (Bengtsson et al. 1996) was applied, in which the high-resolution AGCM was forced by SST during two 20-year periods (1980–1999 and 2080–2099). The two periods are hereafter referred to as 20C and 21C, respectively. The second model was the GFDL high-resolution (50-km) atmospheric model (HiRAM2.1). For detailed model description and its simulation of the annual, inter-annual and decadal variations of TC activity, readers are referred to Zhao et al. (2009). HiRAM2.1 was forced by an ensemble SST warming pattern in 21C derived from 18 IPCC AR4 models. It is worth mentioning that the two AGCMs have distinctive physical parameterization schemes in convection and radiation.

Figure 4.18 shows the difference of TC genesis frequency between the 20C and 21C simulations. In 20C, TCs form primarily over the western and eastern Pacific, similar to the distribution of the observed genesis locations. In 21C, however, more TCs shift their genesis locations to the Central Pacific. As seen from the difference map, there are two notable TC decrease and increase regions over the Pacific. One is over the WNP and the other the central North Pacific (CNP). In the ECHAM5 simulation, the numbers of TCs in 21C decreases by 31% over WNP but increases by 65% over CNP. Similarly, HiRAM2.1 projects a 30% decrease of TC genesis number in WNP but a 19% increase in CNP. Thus both the high-resolution AGCMs with distinctive model physics and different SST warming patterns simulate two opposite TC trends in WNP and CNP. Further HiRAM2.1 simulations with

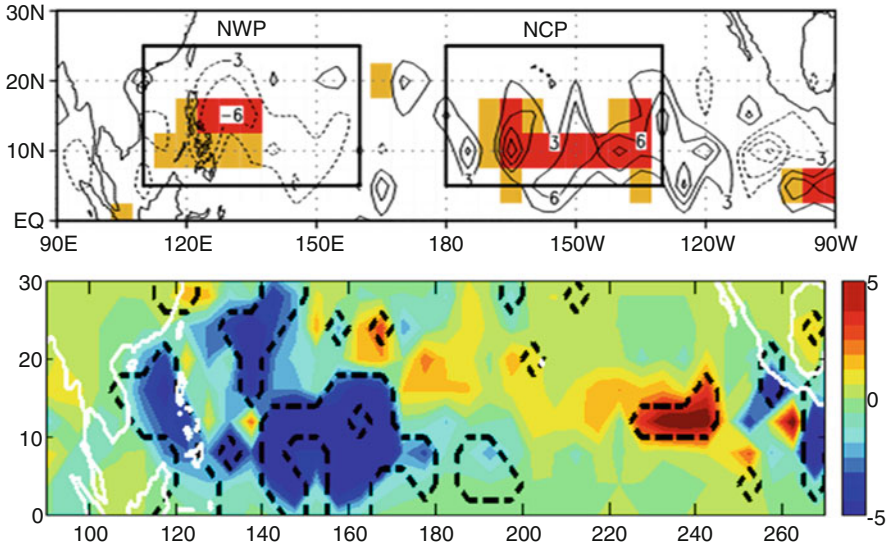

Fig. 4.18 Differences (21C minus 20C) of TC genesis number at each 2.5°× 2.5° box for a 20-year period derived from the ECHAM5 T319 (*top*) and HiRAM2.1 (*bottom*). In the *top* panel, *red* (*orange*) *shaded* areas indicate 95% (90%) confidence level. In the *bottom* panel, *dashed line* denotes the 95% confidence level (From Li et al. (2010). © Copyright 2010, American Geophysical Union (AGU))

different future SST warming patterns derived from GFDL CM2.0 and CM2.1, HADCM3, HADGEM1, ECHAM5, CCCMA, MRIGCM, and MIROCHI confirmed that the west–east shift of TC genesis location in the North Pacific is indeed a robust signal.

To understand the cause of this west–east shift, Li et al. (2010) diagnosed the dynamic and thermodynamic conditions in northern summer (July–October) over the WNP (5–25°N, 110°E–160°E) and CNP (5–25°N, 180–130°W) regions, respectively. The change of atmospheric stability parameter was examined. The result showed that the upper-level air temperature increased at a greater rate than that at lower levels in both the regions. As the static stability is measured by the vertical gradient of the potential temperature, the result implies that the atmosphere becomes more stable under the global warming in both the regions. Thus, the static stability change cannot explain the opposite trends of TC frequency between WNP and CNP.

A further analysis revealed that the fundamental cause of the opposite TC trends lies in the change of dynamic conditions. As we know, TCs originate from the tropical disturbances such as synoptic wave trains and easterly waves. The 21C simulation showed an increased variability of synoptic-scale disturbances over the NCP region but a decreased synoptic activity over the NWP region. Here the strength of the synoptic-scale disturbances was represented by the variance of the 850-hPa vorticity field filtered at a 2–8-day band using Lanczos digital filter

(Duchon 1979). Both the models showed a remarkable decrease of the synoptic-scale variance over WNP but an increase of the variance in CNP. Thus, it is likely that the decreasing trend in NWP is caused by the reduced synoptic-scale activity whereas the increasing trend in NCP is caused by the strengthening of synoptic disturbances.

The contrast of the synoptic-scale activity between WNP and CNP is likely a result of the change of the background vertical wind shear and low-level divergence (Fig. 4.19). Previous studies suggested that the easterly shear and low-level convergence of the background mean flow favored the development of tropical disturbances (Wang and Xie 1996; Li 2006; Sooraj et al. 2008). In the 20C simulation, the western Pacific and Indian monsoon regions have a prevailing easterly wind shear in association with large-scale convective heating. This easterly wind shear becomes weaker in the warming climate (Fig. 4.19a). The weakening of the easterly wind shear corresponds to a weakened western Pacific monsoon, as seen from Fig. 4.19b. The weakening of the easterly shear, along with low-level divergence to its east (Fig. 4.19c), further suppresses the development of tropical disturbances in WNP. In contrast, the easterly wind shear and low-level convergence in CNP are strengthened and so is the precipitation. They favor the development of TCs in CNP.

It was argued that the change of the background vertical shear and the low-level divergence is closely related to changes of the trade wind in the tropics (Fig. 4.19c). Many IPCC-AR4 and IPCC-AR5 models predicted an El Niño-like warming pattern in the Pacific under global warming (Solomon et al. 2007), that is, a greater SST warming would occur in the tropical eastern and central Pacific compared to that in the tropical western Pacific. As a result, the zonal SST gradient was reduced across the tropical Pacific. The reduced zonal SST gradient would decrease the trade wind (Lindzen and Nigam 1987) and weaken the Walker circulation. The weakening of the trades would lead to the decrease of the boundary–layer convergence in the western Pacific monsoon region and the increase of the boundary convergence in CNP (Fig. 4.19c). The former would suppress the monsoon convective heating and decrease the easterly shear in WNP, whereas the latter would strengthen the local boundary layer moisture convergence and convective heating and thus increase the easterly wind shear in CNP.

For the North Atlantic (NA), a number of studies addressed projected future changes in TC activity (Knutson et al. 2010). Although many modeling studies have explored future change in TC intensity or basin-total TC genesis frequency, few have considered projected future change in TC tracks. Murakami and Wang (2010) for the first time investigated future changes in TC tracks in NA using the 20-km mesh high-resolution Meteorological Research Institute (MRI)-atmospheric general circulation model version 3.1 (MRI-AGCM). Using the MRI-AGCM, a pair of simulations was performed: a present-day projection (PD, 1979–2003) with prescribed observed SST and a global-warming projection (GW, 2075–2099) with prescribed future SST based on an ensemble mean of 18 IPCC-AR4 models projected under the IPCC (Intergovernmental Panel for Climate Change Fourth

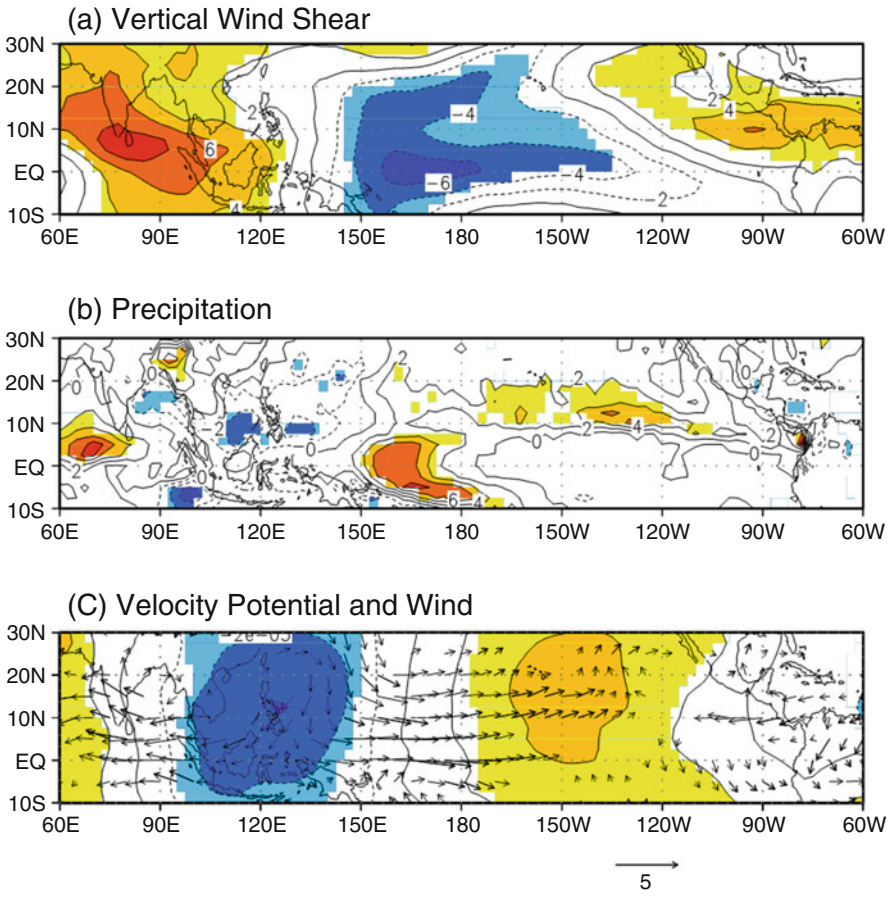

Fig. 4.19 Difference (21C–20C) fields of (**a**) the vertical shear of zonal wind (200 hPa minus 850 hPa, unit: m s^{-1}), (**b**) precipitation (unit, mm day^{-1}), and (**c**) velocity potential (unit, s^{-1}) and wind (unit, m s^{-1}) at 850 hPa during northern summer (July–October). Areas that exceed the 95% confidence level (Student's *t* test) are *shaded* (for contour) and *plotted* (for vector) (From Li et al. (2010). © Copyright 2010, American Geophysical Union (AGU))

Assessment Report, IPCC 2007) SRES (Special Report on Emission Scenarios) A1B scenario.

Figure 4.20a, b (Fig. 4.20c, d) show TC tracks (TC density) simulated in the PD and GW runs during July–October, respectively. The difference in TC density between the two runs is shown in Fig. 4.20e. Compared with the PD run, substantial changes are apparent in the GW run, including an increase in the TC density over the tropical eastern NA (ENA) and a decrease in the TC density over the tropical western NA (WNA). This result indicates an eastward shift in TC tracks that leads to a decrease in the frequency of TCs that affect the North American continent south of approximately 32°N and the West Indies.

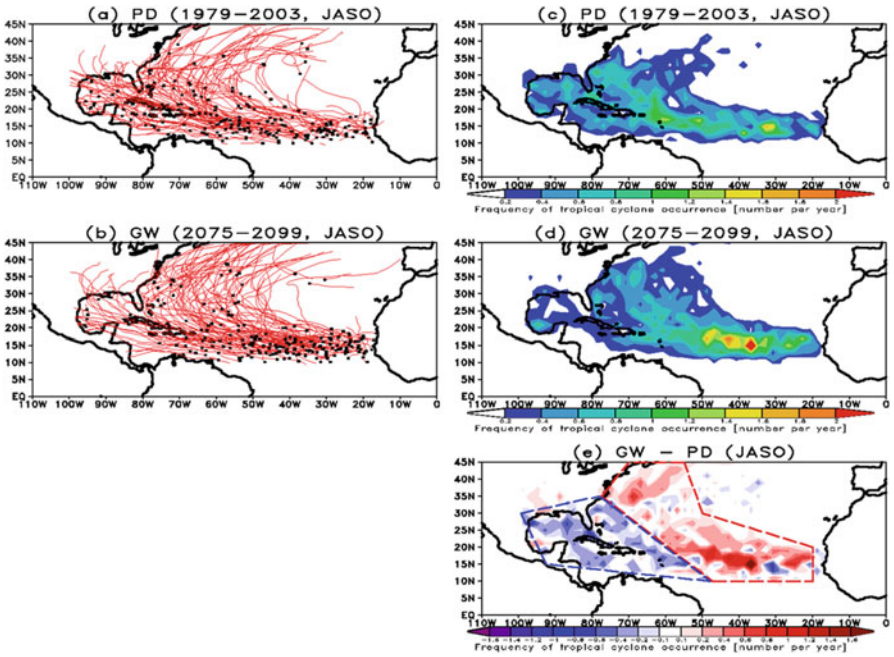

Fig. 4.20 Simulated tropical cyclone tracks (**a**)–(**b**) and TC density (**c**)–(**e**) during July–October in the North Atlantic. (**a**) and (**c**) are from the present-day (PD) simulation, whereas (**b**) and (**d**) are from the global-warming (GW) simulation. The difference in TC density between the PD and GW runs is shown in (**e**). *Black dots* in (**a**)–(**b**) show TC-genesis locations. The *dashed regions* in (**e**) highlight an east-west contrast in future change of TC density (From Murakami and Wang (2010). © Copyright 2010 American Meteorological Society (AMS))

The projected eastward shift in TC tracks is thought to result from changes in steering flows or genesis locations. However, the PD and GW runs showed only a small difference in steering flows, indicating that the primary reason for the changes is the changes in TC genesis locations. Figure 4.21a and b shows the frequency of TC genesis during July–October for the PD and GW runs, respectively. The future change is shown in Fig. 4.21c. It is clear that the genesis locations shift eastward from the PD to GW runs, resulting in a large increase in TC genesis in the ENA and a decrease in the WNA.

We investigate the reason for changes in genesis locations based on an analysis using the modified GPI. The formulation of the modified GPI is as follows:

$$\mathrm{GPI}' = \left|10^5\eta\right|^{\frac{3}{2}}\left(\frac{RH}{50}\right)^3\left(\frac{V_{\mathrm{pot}}}{70}\right)^3(1+0.1V_s)^{-2}\left(\frac{-\omega+0.1}{0.1}\right), \tag{4.1}$$

where η is the absolute vorticity (s^{-1}) at 850 hPa, RH is the relative humidity (%) at 700 hPa, Vpot is the maximum potential intensity (m s^{-1}), Vs is the magnitude of

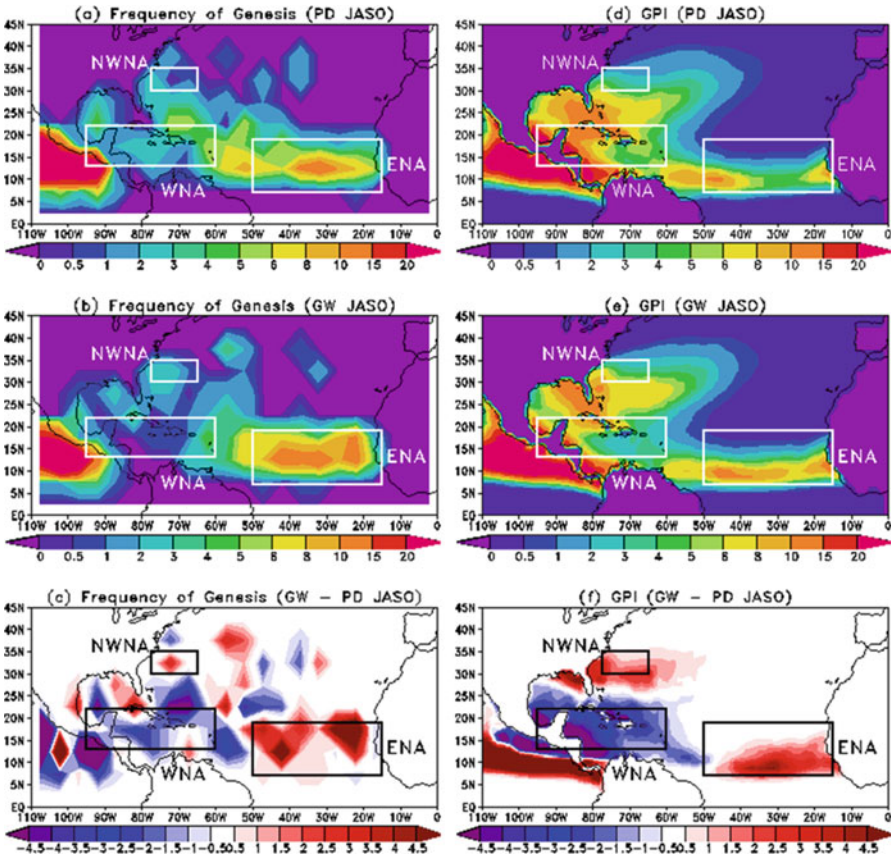

Fig. 4.21 Simulated frequency of tropical cyclone genesis for the peak cyclone season of July–October for (**a**) the present-day (PD) run, (**b**) the global warming (GW) run, and (**c**) the difference between the GW and PD runs. (**d–f**) are the same as (**a–c**), but for the Genesis Potential Index (GPI). Rectangles show regions (Eastern North Atlantic (ENA), Western North Atlantic (WNA), and Northwestern North Atlantic (NWNA)) with pronounced changes in TC genesis (From Murakami and Wang (2010). © Copyright 2010 American Meteorological Society (AMS))

the vertical wind shear (m s^{-1}) between 850 and 200 hPa, and ω is the vertical wind velocity (Pa s^{-1}).

Overall, the GPI (Fig. 4.21d, e) values computed from the large-scale parameters simulated by the experiments reproduce the distributions of detected TC genesis (Fig. 4.21a, b). When the projected changes in TC genesis frequency (Fig. 4.21c) is compared with those in GPI (Fig. 4.21f), GPI largely captures the changes in the detected TC genesis frequency. The GPI can be used to determine which of the factors contributes most to its future change. Here, we assign the future value to one of the five GPI elements in Eq. (4.1); the other elements are kept at present-day values, as used in the PD run. The "virtual" GPI value is then subtracted from the present-day GPI value. In the case of a large difference, the assigned GPI element is

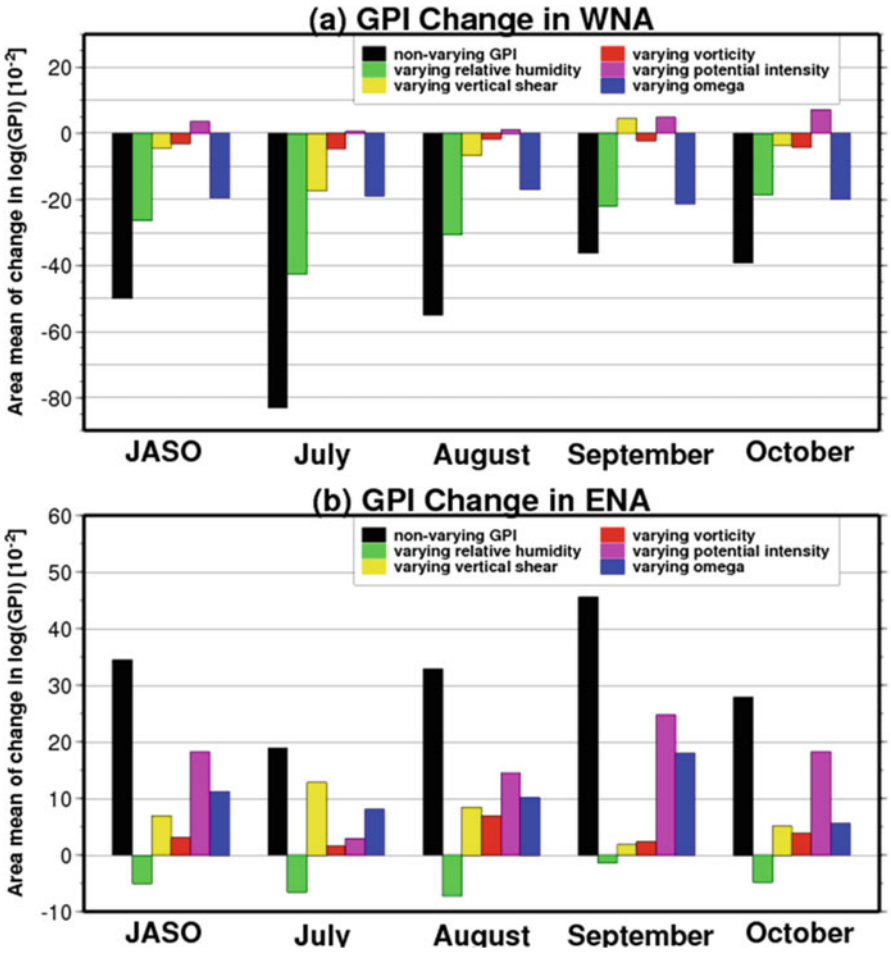

Fig. 4.22 Area mean of future change in the genesis potential index (GPI) during July–October and each month for (**a**) western North Atlantic (WNA) and (**b**) eastern North Atlantic (ENA). The non-varying GPI (*black*) is the difference in GPIs between the global warming (GW) and present-day (PD) runs. The varying GPIs (*colors*) are the virtual GPIs obtained by varying relative humidity (*green*), vertical shear (*yellow*), vorticity (*red*), maximum potential intensity (*pink*), and omega (*blue*), where in each case the other variables were those of the PD run (Adapted from Murakami and Wang (2010). © Copyright 2010 American Meteorological Society (AMS))

considered an influential factor in terms of GPI change. Figure 4.22 shows selected area means of future change in GPI and virtual GPIs for July–October and each month. It is notable that changes in the maximum potential intensity and omega terms make a dominant contribution to the increase in GPI within the ENA (Fig. 4.22b). The vertical shear term also contributes to the future increase in GPI to some degree, but the vorticity term makes only a minor contribution in the ENA (Fig. 4.22b). In contrast to the ENA, the relative humidity and omega terms make

the largest contribution to the decrease in GPI within the WNA (Fig. 4.22a). The dominant contributions of these terms are robust for the entire peak season (Fig. 4.22).

As shown above, the GPI change in the ENA is mainly due to change in large-scale vertical motion and maximum potential intensity, which appear to be related to enhanced convective activity in the intertropical convergence zone (ITCZ). In contrast to the findings for ENA, the WNA features a decrease in upward motion and reduced relative humidity associated with a subsidence anomaly. This finding indicates that the increase in vertical motion in the ENA region acts to enhance zonal circulation, which in turn results in the suppression of convective activity over the WNA. This local circulation change results in the active TCs over the ENA and inactive TCs over the WNP.

Consistent with the findings by Murakami et al. (2011), Colbert et al. (2013) also showed the eastward shift in TC tracks in their simulation using another dynamical model (figure not shown). Interestingly, Vecchi and Knutson (2008) reconstructed an observational TC dataset since the late 1800s and showed a similar trend with an east–west contrast in TC occurrence pattern. This consistency among different studies indicates the likelihood that a signal of climate change induced by global warming might have already appeared.

4.7 Concluding Remark

This chapter summarizes the synoptic and climatic aspects of tropical cyclogenesis in the WNP. Observational analyses identified three types of synoptic precursor perturbations at low levels in the WNP: TC energy dispersion induced Rossby wave train, northwest–southeast-oriented synoptic wave train, and Pacific easterly wave. This feature differs from that in the NATL where dominant precursor signal is African easterly wave. Besides the near surface precursor signals, some cyclogenesis events are associated with a mid-level vortex or TUTT.

A theoretical study suggested that the southeast–northwest-oriented synoptic wave train was originated from the instability of the summer mean flow in the presence of the convection–circulation–moisture feedback in the WNP. The dispersion characteristics of the Pacific easterly wave were examined through the diagnosis of observational data. A wave-activity diagnosis showed that the zonal scale contraction primarily contributes to the convergence of the wave activity, while the convergence of the mean flow contributes less to the wave-activity accumulation. An analysis of group velocity in the upper troposphere and in the vertical direction showed that there was downward propagation of wave activity from the upper levels and in the upper troposphere wave activity directed southward from the extratropics to the tropical central Pacific. The result indicates that the energy source of Pacific easterly waves is from mid-latitude Pacific jet.

The cyclogenesis associated with TCED was simulated in a 3D model. A new TC formed in the wake of a preexisting TC when a large-scale monsoon gyre was

present. Maximum vorticity generation appeared in the PBL, and the vorticity growth exhibited an oscillatory development. This oscillatory growth was also seen in the observed rainfall and cloud-top temperature fields. The diagnosis of the model output showed that the oscillatory development was attributed to the discharge and recharge of the PBL moisture and its interaction with convection and circulation. A cloud-resolving (2-km grid) model was used to investigate cyclogenesis efficiency in an environmental mid-level and bottom vortex. The results show that a bottom vortex is more efficient in cyclogenesis than a mid-level vortex, given the same column integrated absolute vorticity. Both the mid-level and bottom vortex experiments shared common development characteristics: (1) a transition from random cumulus-scale (~5 km) convective cells into an organized mesovortex-scale (~50 km) system through upscale cascade, (2) a setup of a nearly saturated air column prior to a rapid drop of the central minimum pressure, and (3) a convective-stratiform phase transition.

TC frequency in the WNP is strongly regulated by ISO activity. The number of TCs increases (decreases) during an active (suppressed) phase of ISO. Cyclogenesis activity is also El Niño-phase dependent. The TC genesis number increases (decreases) during El Niño developing (decaying) summer. A box difference index was used to differentiate the developing and non-developing disturbances and ranks major genesis parameters. It was found that whereas TC genesis in the NATL was more sensitive to the thermodynamic factors, dynamic factors played a major role in determining whether or not a tropical disturbance would develop in the WNP.

The future change of TC genesis in the North Pacific under global warming was investigated with the use of two global high-resolution models (ECHAM5 T319 and GFDL HiRAM2.1). A significant zonal shift was found in the location of TCs from the western to central North Pacific. The shift to more cyclones in the central Pacific and less in the western Pacific is not attributable to a change in atmospheric static stability but to a change in the variance of tropical synoptic-scale perturbations, which is caused by a change in the background vertical shear and boundary layer divergence.

A similar eastward shift of genesis frequency was found in North Atlantic. In addition to TC genesis frequency change, almost all models projected an increase (decrease) of number of intense (weak) TCs in future warmer climate at all TC basins. The physical cause of this change is likely attributed to the combined effect of increase of mean-state specific humidity and static stability in the troposphere.

Questions

1. What are precursory synoptic-scale perturbations for tropical cyclone genesis in western North Pacific? How do the precursory signals differ from TC genesis in the tropical Atlantic?
2. Assume initially we specify a gradient-wind-balanced vortex in a resting environment in a WRF model. What causes the breaking of the balance and the subsequent development of the initial vortex into a tropical cyclone?

3. Why do we observe the frequent development of synoptic-scale wave trains in the western North Pacific?
4. What are the horizontal and vertical structures of the Pacific easterly waves? What is the energy source of the waves?
5. To what extent does MJO influence TC genesis frequency in western North Pacific? Is such a relationship region dependent?
6. What is the relative role of MJO dynamic and thermodynamic fields in regulating TC development?
7. How do genesis frequency and location of western North Pacific TCs depend on the ENSO phases (e.g., El Niño versus La Niña, El Niño developing versus El Niño decaying summers?
8. What is the difference in environmental parameters that determine TC genesis between western North Pacific and North Atlantic?
9. What is the robust projection of TC activity change in the Pacific under global warming from global general circulation models? What causes such a change?
10. What is the robust projection of TC activity change in the North Atlantic under global warming? What is responsible for such a change?

References

Anthes R A, (1982) Tropical cyclone: their evolution, structure and effects. Meteorol Mongr No. 41, Amer Meteorol Soc, 208pp

Bengtsson L, Botzet M, Esch M (1996) Will greenhouse gas-induced warming over the next 50 years lead to higher frequency and greater intensity of hurricanes? Tellus 48A:57–73

Bengtsson L, Hodges KI, Esch M, Keenlyside N, Komblush L, Luo JJ, Yamagata T (2007) How many tropical cyclones change in a warmer climate. Tellus 59A:539–561

Briegel LM, Frank WM (1997) Large-scale influences on tropical cyclogenesis in the western North Pacific. Mon Weather Rev 125:1397–1413

Carr LE III and RL Elsberry (1994) Systematic and integrated approach to tropical cyclone track forecasting. Part I. Approach overview and description of meteorological basis. NPS Tech. Rep. NPS-MR-94-002, 273 pp

Carr LE III, Elsberry RL (1995) Monsoonal interactions leading to sudden tropical cyclone track changes. Mon Weather Rev 123:265–289

Colbert AJ, Soden B, Vecchi GA, Kirtman BP (2013) The impact of anthropogenic climate change on North Atlantic tropical cyclone tracks. J Clim 26:4088–4095

Colon JA, Nightingale WR (1963) Development of tropical cyclones in relation to circulation patterns at the 200 millibar level. Mon Weather Rev 91:329–336

Davidson NE, Hendon HH (1989) Downstream development in the southern hemisphere monsoon during FGGE/WMONEX. Mon Weather Rev 117:1458–1470

Dickinson M, Molinari J (2002) Mixed Rossby-gravity waves and western Pacific tropical cyclogenesis. Part I: synoptic evolution. J Atmos Sci 59:2183–2196

Duchon CE (1979) Lanczos filtering in one and two dimensions. J Appl Meteorol 18:1016–1022

Emanuel KA (2005) Increasing destructiveness of tropical cyclones over the past 30 years. Nature 436:686–688

Emanuel K A and D S Nolan (2004) Tropical cyclone activity and global climate, 26th conference on hurricanes and tropical meteorology, Am Meteorol Soc, Miami

Flierl GR (1984) Rossby wave radiation from a strongly nonlinear warm eddy. J Phys Oceanogr 14:47–58

Flierl GR, Haines K (1994) The decay of modons due to Rossby wave radiation. Phys Fluids 6:3487–3497

Flierl GR, Stern ME, Whitehead JA Jr (1983) The physical significance of modons: laboratory experiments and general integral constrains. Dyn Atmos Oceans 7:233–263

Frank WM (1982) Large-scale characteristics of tropical cyclones. Mon Weather Rev 110:572–586

Fu B, Li T, Peng M, Weng F (2007) Analysis of tropical cyclone genesis in the western North Pacific for 2000 and 2001. Weather Forecast 22:763–780

Fu B, Peng M, Li T, Stevens D (2012) Developing versus non-developing disturbances for tropical cyclone formation, Part II: western North Pacific. Mon Weather Rev 140:1067–1080

Ge X, Li T, Zhou X (2007) Tropical cyclone energy dispersion under vertical shears. Geophys Res Lett 34:L23807. doi:10.1029/2007GL031867

Ge X, Li T, Wang Y, Peng M (2008) Tropical cyclone energy dispersion in a three-dimensional primitive equation model: upper tropospheric influence. J Atmos Sci 65:2272–2289

Ge X, Li T, Peng M (2013) Tropical cyclone genesis efficiency: mid-level versus bottom vortex. J Trop Meteorol 19:197–213

Gray WM (1968) Global view of the origin of tropical disturbances and storms. Mon Weather Rev 96:669–700

Gray WM (1979) Hurricanes: their formation, structure, and likely role in the tropical circulation. Meteorology over the Tropical Oceans, D. B. Shaw, ED., Royal Meteorological Society, pp 155–218

Hartmann DL, Michelsen ML, Klein SA (1992) Seasonal variations of tropical intraseasonal oscillations: a 20–25 day oscillations in the western Pacific. J Atmos Sci 49:1277–1289

Held IM, Suarez MJ (1994) A proposal for the intercomparison of the dynamical cores of atmospheric general-circulation models. Bull Amer Meteor Soc 75:1825–1830

Hendricks EA, Montgomery MT, Davis CA (2004) The role of vortical hot towers in the formation of Tropical Cyclone Diana (1984). J Atmos Sci 61:1209–1232

Holland GJ (1995) Scale interaction in the western Pacific monsoon. Meteorol Atmos Phys 56:57–79

Holland GJ (1997) The maximum potential intensity of tropical cyclones. J Atmos Sci 54:2519–2541

Hsu P-C, Li T, Tsou C-H (2011) Interactions between boreal summer Intraseasonal oscillations and synoptic-scale disturbances over the western North Pacific. Part I: energetics diagnosis. J Clim 24:927–941

IPCC (2007) Climate change 2007: the physical science basis. Contribution of Working Group I to the Fourth Assessment Report of the Intergovernmental Panel on Climate Change. In: Solomon S, Qin D, Manning M, Chen Z, Marquis M, Averyt KB, Tignor M, and Miller HL, (eds) Cambridge University Press, Cambridge/New York, 996 pp

Iizuka S, Matsuura T (2008) ENSO and western north pacific tropical cyclone activity simulated in a CGCM. Clim Dyn 30:815–830

Jiang X, Li T (2005) Re-initiation of the boreal summer intraseasonal oscillation in the tropical Indian Ocean. J Clim 18:3777–3795

Jungclaus H, coauthors (2006) Ocean circulation and tropical variability in the coupled model ECHAM5/MPO-OM. J Clim 19:3952–3972

Kain JS, Fritsch JM (1990) A one-dimensional entraining/detraining plume model and its application in convective parameterization. J Atmos Sci 47:2784–2802

Knutson T, McBride JL, Chan J, Emanuel K, Holland G, Landsea C, Held I, Kossin JP, Srivastava AK, Sugi M (2010) Tropical cyclones and climate change. Nat Geosci 3:157–163

Landsea CW, Harper BA, Hoarau K, Knaff JA (2006) Can we detect trends in extreme tropical cyclones? Science 313:452–454
Lau K-H, Lau N-C (1990) Observed structure and propagation characteristics of tropical summertime synoptic-scale disturbances. Mon Weather Rev 118:1888–1913
Lau K-H, Lau N-C (1992) The energetics and propagation dynamics of tropical summertime synoptic-scale disturbances. Mon Weather Rev 120:2523–2539
Li T (2006) Origin of the summer time synoptic-scale wave train in the Western North Pacific. J Atmos Sci 63:1093–1102
Li T, Fu B (2006) Tropical cyclogenesis associated with Rossby wave energy dispersion of a preexisting Typhoon. Part I: satellite data analyses. J Atmos Sci 63:1377–1389
Li T, Fu B, Ge X, Wang B, Peng M (2003) Satellite data analysis and numerical simulation of tropical cyclone formation. Geophys Res Lett 30:2122–2126
Li T, Ge X, Wang B, Zhu T (2006) Tropical cyclogenesis associated with Rossby wave energy dispersion of a pre-existing Typhoon. Part II: numerical simulations. J Atmos Sci 63:1390–1409
Li T, Kwon M, Zhao M, Kug J-S, Luo J-J, Yu W (2010) Global warming shifts pacific tropical cyclone location. Geophys Res Lett 37:L21804. doi:10.1029/2010GL045124
Liebmann H, Hendon H, Glick JD (1994) The relationship between tropical cyclones of the western pacific and Indian Oceans and the Madden–Julian oscillation. J Meteor Soc Japan 72:401–411
Lin Y-L, Rarley RD, Orville HD (1983) Bulk parameterization of the snow field in a cloud model. J Appl Meteorol 22:1065–1092
Lindzen RS, Nigam S (1987) On the role of sea surface temperature gradients in forcing low level winds and convergence in the tropics. J Atmos Sci 44:2440–2458
Maloney ED, Dickinson MJ (2003) The intraseasonal oscillation and the energetics of summertime tropical western north pacific synoptic-scale disturbances. J Atmos Sci 60:2153–2168
Maloney ED, Hartmann DL (2000) Modulation of eastern north pacific hurricanes by the Madden-Julian oscillation. J Clim 13:1451–1460
Maloney ED, Hartmann DL (2001) The madden-julian oscillation, barotropic dynamics, and north pacific tropical cyclone formation. Part I: observations. J Atmos Sci 58:2545–2558
McDonald NR (1998) The decay of cyclonic eddies by Rossby wave radiation. J Fluid Mech 361:237–252
McDonald RE, coauthors (2005) Tropical storms: representation and diagnosis in climate models and the impacts of climate change. Clim Dyn 25:19–36
Montgomery MT, Nicholls ME, Cram TA, Saunders AB (2006) A vortical hot tower route to tropical cyclogenesis. J Atmos Sci 63:355–386
Murakami H, Wang B (2010) Future change of North Atlantic tropical cyclone tracks: projection by a 20-km-mesh global atmospheric model. J Clim 23:2699–2721
Murakami H, Wang B, Kitoh A (2011) Future change of western North Pacific typhoons: projections by a 20-kmmesh global atmospheric model. J Climate 24:1154–1169
Oouchi K, coauthors (2006) Tropical cyclone climatology in a global-warming climate as simulated in a 20km-mesh global atmospheric model: frequency and wind intensity analyses. J Meteorol Soc Japan 84:259–276
Peng M, Fu B, Li T, Stevens D (2012) Developing versus non-developing disturbances for tropical cyclone formation, Part I: north atlantic. Mon Weather Rev 140:1047–1066
Reed RJ, Recker EE (1971) Structure and properties of synoptic-scale wave disturbances in the equatorial western pacific. J Atmos Sci 28:1117–1133
Ritchie EA, Holland GJ (1997) Scale interactions during the formation of typhoon Irving. Mon Weather Rev 125:1377–1396
Ritchie EA, Holland GJ (1999) Large-scale patterns associated with tropical cyclogenesis in the western pacific. Mon Weather Rev 127:2027–2043
Roeckner E, coauthors (2003) The atmospheric general circulation model ECHAM5. Part I: model description, vol 349. Max Planck Institute for Meteorology Rep, Hamburg, 127 pp

Sadler JC (1976) A Role of the Tropical Upper Tropospheric Trough in Early Season Typhoon Development. Mon Weather Rev 104:1266–1278
Schecter DA, Dubin DH (1999) Vortex motion driven by a background vorticity gradient. Phys Rev Lett 83:2191–2194
Shapiro LJ, Ooyama KV (1990) Barotropic vortex evolution on a beta plane. J Atmos Sci 47:170–187
Simpson J, Ritchie E, Holland GJ, Halverson J, Stewart S (1997) Mesoscale interactions in tropical cyclone genesis. Mon Weather Rev 125:2643–2661
Sobel AH, Bretherton CS (1999) Development of synoptic-scale disturbances over the summertime tropical northwest pacific. J Atmos Sci 56:3106–3127
Sobel AH, Maloney ED (2000) Effect of ENSO and ISO on tropical depressions. Geophys Res Lett 27:1739–1742
Solomon S, coauthors (2007) Climate change 2007: the physical science basis. Press for the Intergovernmental Panel on Climate Change, Cambridge University
Sooraj KP, Kim D, Kug J-S, Yeh S-W, Jin F-F, Kang I-S (2008) Effects of the low frequency zonal wind variation on the high-frequency atmospheric variability over the tropics. Clim Dyn 33. doi:10.1007/s00382-008-0483-6 (CA)
Sugi M, Noda A, Sato N (2002) Influence of the global warming on tropical cyclone climatology: an experiment with the JMA global model. J Meteorol Soc Japan 80:249–272
Takaya K, Nakamura H (2001) A formulation of a phase-independent wave-activity flux for stationary and migratory quasigeostrophic eddies on a zonally varying basic flow. J Atmos Sci 58:608–627
Takayabu YN, Nitta T (1993) 3-5 day-period disturbances coupled with convection over the tropical pacific ocean. J Meteor Soc Japan 71:221–245
Tam C-Y, Li T (2006) The origin and dispersion characteristics of the observed summertime synoptic-scale waves over the western Pacific. Mon Weather Rev 134:1630–1646
Tory KJ, Montgomery MT, Davidson NE (2006) Prediction and diagnosis of tropical cyclone formation in an NWP system. Part I: the critical role of vortex enhancement in deep convection. J Atmos Sci 63:3077–3090
Vecchi GA, Knutson TR (2008) On estimates of historical north atlantic tropical cyclone activity. J Clim 21:3580–3600
Wang Y (2001) An explicit simulation of tropical cyclones with a triply nested movable mesh primitive equation model: TCM3. Part I: model description and control experiment. Mon Weather Rev 129:1370–1394
Wang B, Chan JCL (2002) How strong ENSO events affect tropical storm activity over the western north pacific. J Clim 15:1643–1658
Wang B, Xie X (1996) Low-frequency equatorial waves in sheared zonal flow. Part I: stable waves. J Atmos Sci 53:449–467
Wang B, Wu R, Li T (2003) Atmosphere-warm ocean interaction and its impact on Asian-Australian monsoon variation. J Clim 16:1195–1211
Webster PJ, Holland GJ, Curry JA, Chang H-R (2005) Changes in tropical cyclone number, duration, and intensity in a warming environment. Science 309:1844–1846
Yamazaki N, Murakami M (1989) An intraseasonal amplitude modulation of the short-term tropical disturbances over the western pacific. J Meteor Soc Japan 67:791–807
Yoshimura J, Sugi M, Noda A (2006) Influence of greenhouse warming on tropical cyclone frequency. J Meteorol Soc Japan 84:405–428
Yuter SE, Houze RA Jr (1995) Three-dimensional kinematic and microphysical evolution of Florida cumulonimbus. Part II: frequency distribution of vertical velocity, reflectivity, and differential reflectivity. Mon Weather Rev 123:1941–1963
Zhao M, Held IM, Lin S-J, Vecchi GA (2009) Simulations of global hurricane climatology, interannual variability, and response to global warming using a 50km resolution GCM. J Clim 22:6653–6678

Chapter 5
Dynamics of El Niño–Southern Oscillation

Abstract In this chapter, the observed characteristics of the El Niño – Southern Oscillation (ENSO) is described, followed by the discussion of the ENSO instability and oscillatory theories. Next, the mechanisms of its phase locking to the annual cycle are discussed. Through the oceanic mixed-layer budget analysis, physical mechanisms responsible for El Niño and La Niña amplitude asymmetry and El Niño and La Niña evolution asymmetry are investigated. How the interdecadal mean state modulates the El Niño behavior is further discussed. Finally, an air–sea interaction mode with a characterized zonal-dipole structure in the tropical Indian Ocean is described.

5.1 Observed Structure and Evolution

El Niño is characterized by unusual large-scale oceanic surface warming in the equatorial eastern Pacific (Rasmussen and Carpenter 1982; Philander 1990). It was originally a Spanish term (meaning "Christ Child") named by fishing men in Peru coast. Figure 5.1 shows the total SST field (left) and the SST anomaly field (right) along the equatorial Pacific from 1996 to 2004. Typically, the warm pool is confined in western Pacific, but during El Niño, in particular in 1997, the warm pool could well extend into the eastern Pacific, with a maximum anomalous SST exceeding 4 °C. Such a high abnormal SST is not found in other parts of world oceans.

Defining an eastern equatorial Pacific domain (5°S–5°N, 150°W–90°W) as a key El Niño developing region, one could examine how this area-averaged SSTA index varies with time (Fig. 5.2). It is clearly seen that the index oscillates irregularly on an interannual (2–7 years) period. Nowadays, a positive SSTA episode was called "El Niño," and a negative episode was referred to as "La Niña" (meaning a girl in Spanish).

While the oceanographic phenomenon El Niño was first discovered by Peru fishing men in the late nineteenth century, an atmospheric phenomenon named "Southern Oscillation" was discovered by Gilbert Walker in 1924. The Southern Oscillation describes a pressure seesaw between Darwin and Tahiti. When the surface pressure anomaly in Darwin is above normal, it is usually below normal in Tahiti (bottom panel of Fig. 5.3). While Walker (1924) revealed the pressure

T. Li, P.-c. Hsu, *Fundamentals of Tropical Climate Dynamics*,
Springer Atmospheric Sciences, DOI 10.1007/978-3-319-59597-9_5

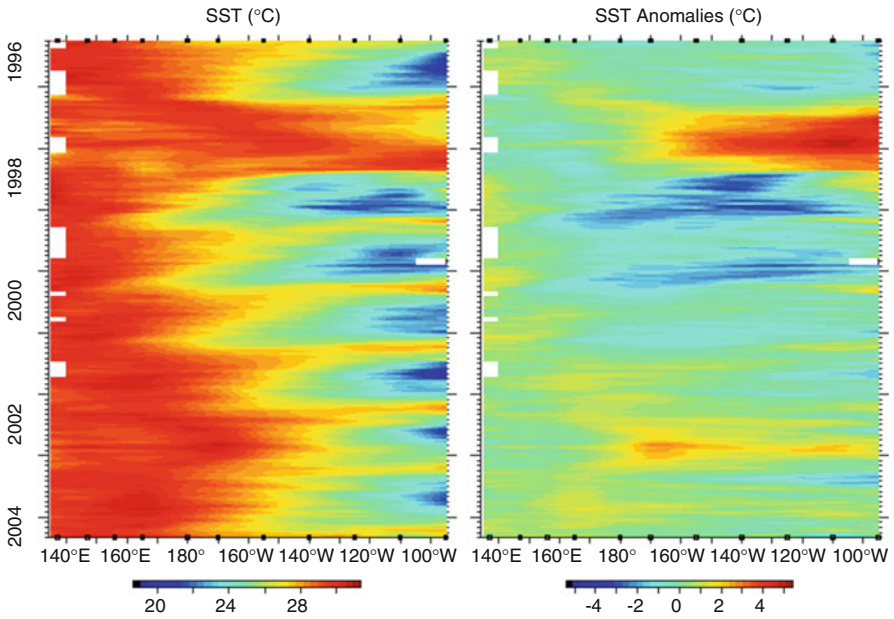

Fig. 5.1 Observed SST (°C) and SST anomaly (°C) along the equatorial Pacific from 1996 to 2004

fluctuation from two meteorological stations, later observational analyses revealed that the pressure seesaw has a large spatial scale, as shown in top panel of Fig. 5.3.

The meteorological investigation of the Southern Oscillation and the oceanographic investigation of El Niño proceeded separately until Bjerknes (1969) first suggested that they were two aspects of the same phenomenon. From an atmospheric point of view, the pressure fluctuation associated with the Southern Oscillation arises from the anomalous SST forcing in the equatorial Pacific. From an oceanic point of view, the SSTA pattern associated with El Niño results from the anomalous wind forcing associated with the pressure fluctuation. The circular argument implies that air–sea interaction holds a key.

Due to the air–sea interaction nature, this phenomenon in nowadays is named as "El Niño–Southern Oscillation" (ENSO, Philander 1990). Although its origin is in the tropics, ENSO exerts a great impact on climate around the globe, through its teleconnection patterns such as the Pacific–North America (PNA) pattern (Wallace and Gutzler 1981) in northern winter and Pacific–Japan (PJ) pattern (Nitta 1987) in northern summer. ENSO has become a major predictability source for seasonal prediction.

It is interesting to note from Fig. 5.2 that the mature phase of ENSO often occurs in northern winter (DJF). This implies that ENSO may be modulated by the climatological annual cycle. Recall in Chap. 2 that the SST in the eastern Pacific exhibits a remarkable annual cycle, and the annual cycle amplitude is comparable to that of ENSO. The horizontal pattern of SSTA difference between El Niño and

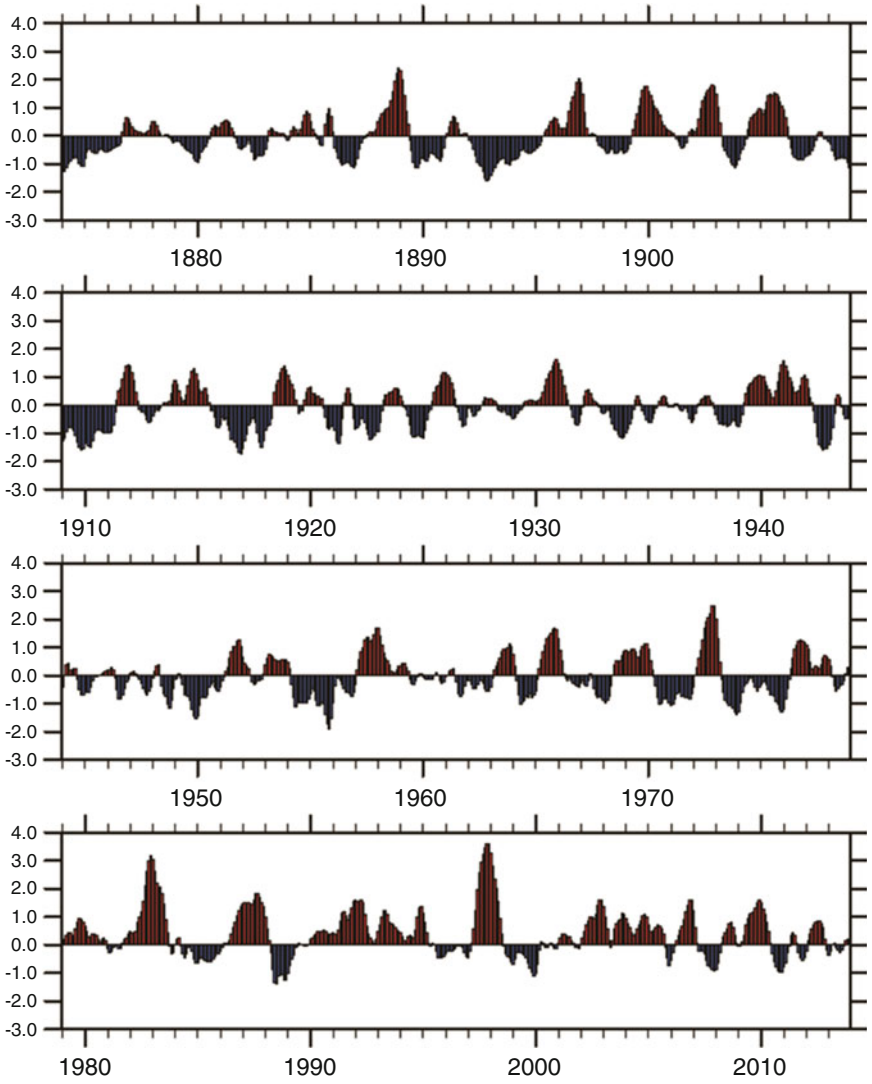

Fig. 5.2 Evolution of SST anomaly (°C) averaged at (150°W–90°W, 5°S–5°N) from 1874 to 2014 (Data source: ERSSTv3b)

La Niña also resembles the difference pattern of warm and cold phase of the annual cycle SST (i.e., March minus September SST pattern). Despite similar SST patterns, subsurface ocean temperature anomalies behavior differently between the interannual and annual timescales (Fig. 5.4). On the interannual timescale, the 20 °C isothermal depth (a proxy to represent the thermocline depth) exhibits a marked fluctuation. This implies that ocean thermocline variation and associated oceanic waves and subsurface temperature changes play an important role in

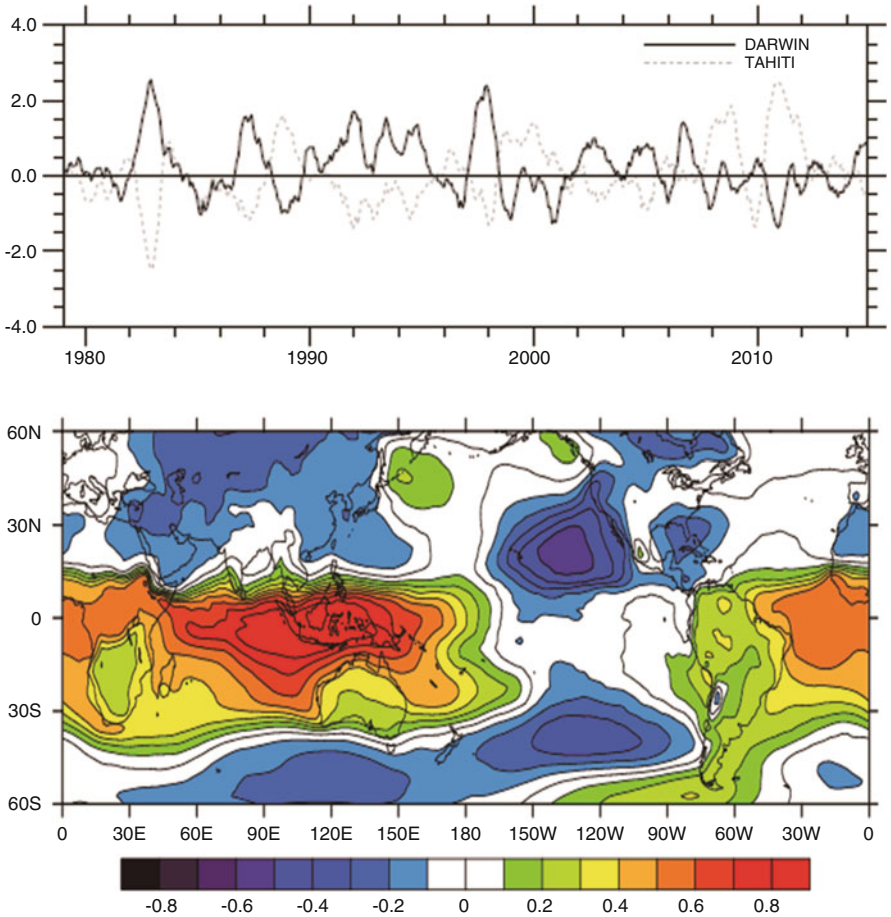

Fig. 5.3 (*Top*) Evolution of surface pressure anomalies in Darwin (*solid curve*) and Tahiti (*dashed curve*). (*Bottom*) Pattern of correlation coefficient between surface pressure field and a Southern Oscillation Index

regulating SST change on this timescale. On the annual timescale, the 20 °C isothermal depth does little change (Chang and Philander 1994). This implies that the SST change on the annual timescale is primarily controlled by oceanic mixed-layer dynamics, while thermocline depth fluctuation is of secondary importance.

The discussion above suggests that different mechanisms operate SST changes on the annual and interannual timescales. In the following, we will discuss fundamental science questions related to ENSO dynamics, namely, what causes its growth, what causes its oscillation, what is the mechanism responsible for the ENSO phase locking, what causes the El Niño and La Niña amplitude asymmetry, and what causes El Niño and La Niña evolution asymmetry?

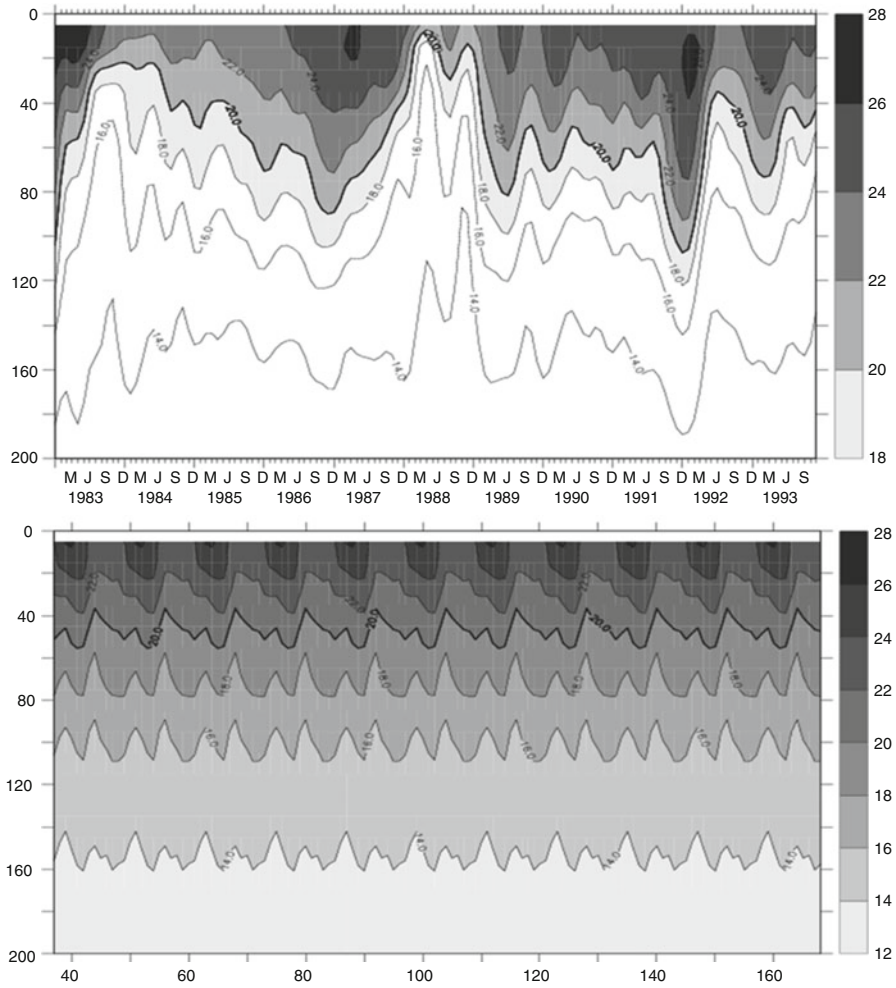

Fig. 5.4 Evolution of vertical profile of ocean temperature at (110°W, 0°N) from the surface to 200-m depth on interannual (*top*) and annual (*bottom*) timescales. Bold contour represents 20 °C isothermal

5.2 Instability Mechanisms

Various positive air–sea feedback processes may contribute to the growth of El Niño and La Niña perturbations (Philander et al. 1984; Hirst 1986, 1988). While heat flux terms in general tend to damp the SSTA, advection terms are responsible for its growth. Three major dynamic positive air–sea feedback processes are listed in the following SSTA tendency equation:

$$\frac{\partial T'}{\partial t} \approx -u'\bar{T}_x - w'\bar{T}_z - \bar{w}T'_z, \tag{5.1}$$

where the first term in the right-hand side of Eq. (5.1) represents zonal advective feedback, the second term represents Ekman pumping-induced anomalous upwelling feedback, and the third term represents Bjerknes thermocline feedback.

Figure 5.5 is a schematic diagram showing how these positive feedbacks work. Under a normal climate condition, trade winds at the equator push warmer upper-ocean water westward. This leads to titling of ocean thermocline deepening toward the west. As a material surface (i.e., no mass exchange between water above and below), the ocean thermocline represents a zone of maximum vertical temperature gradient, separating the upper-layer warmer water and lower-layer colder water. The equatorial easterly induces surface divergence of Ekman currents and ocean

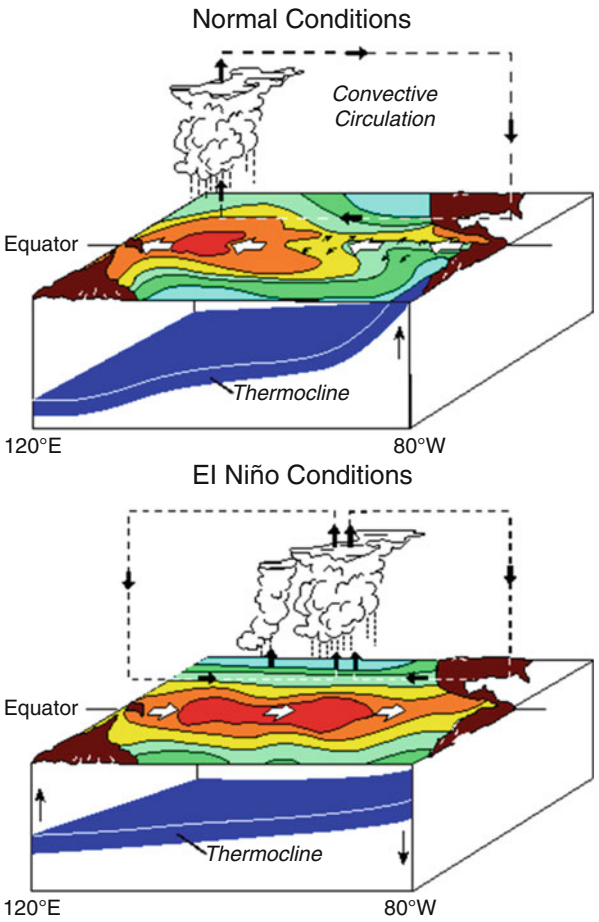

Fig. 5.5 Schematic diagram to illustrate atmospheric and oceanic circulation at the equatorial plane during the climatological mean condition and anomalous atmospheric and oceanic circulation during the El Niño (Images are from the NOAA website at http://www.pmel.noaa.gov/elnino/what-is-el-nino. Credit: NOAA)

upwelling, which brings colder water to the surface from below. As a result, a cold tongue forms in the eastern equatorial Pacific.

The zonal SST gradient further strengthens easterly winds at the equator. Surface winds converge over the warm water in the western Pacific warm pool, supporting large-scale convection in situ. Thus, a zonal vertical overturning circulation forms. This circulation is named as the "Walker circulation" by Bjerknes (1969).

Assume that initially a weak positive SSTA appears in the eastern equatorial Pacific. This anomalous positive SSTA may induce anomalous surface convergence and anomalous convection near the center of the positive SSTA. Anomalous westerlies to the west of the convection center may drive anomalous ocean zonal currents, which further advect high mean SST eastward, strengthening the initial warm SSTA. The increase of the positive SSTA can further enhance the westerly anomaly. The initial SSTA grows under this positive feedback loop. This process is termed as "zonal advective feedback."

The wind convergence into the initial positive SSTA also induces the convergence of ocean surface current at the equator and thus local anomalous downwelling at base of the ocean mixed layer. This weakens the climatological mean upwelling in the eastern equatorial Pacific, leading to a positive SSTA tendency there. This type of positive feedback is termed as "Ekman upwelling feedback."

The westerly wind anomaly in the central equatorial Pacific in response to the initial positive SSTA can weaken the east–west tilting of the climatological thermocline, leading to a deepening (shoaling) of the thermocline in the eastern (western) Pacific. The deepening of the ocean thermocline in eastern Pacific causes abnormal warm temperature in the subsurface below the ocean mixed layer. The mean upwelling currents thus advect warmer subsurface water upward, increasing the SSTA. This type of positive feedback is termed "Bjerknes thermocline feedback."

Ocean mixed-layer budget analyses with the use of ocean assimilation data reveal that Bjerknes thermocline feedback, zonal advective feedback, and Ekman upwelling feedback all contribute to the growth of El Niños and La Niñas during their developing phase. These positive dynamic air–sea feedbacks overwhelm negative thermodynamic feedbacks (e.g., cloud–SST feedback and evaporation–SST feedback), leading to the ENSO growth.

5.3 Oscillation Theories

Positive feedbacks mentioned above can explain rapid growth but cannot explain the ENSO phase transition (say, from a warm to a cold phase). The phase transition requires delayed negative feedbacks. What are these negative feedback processes? So far two theories are widely accepted. One is the delayed oscillator theory

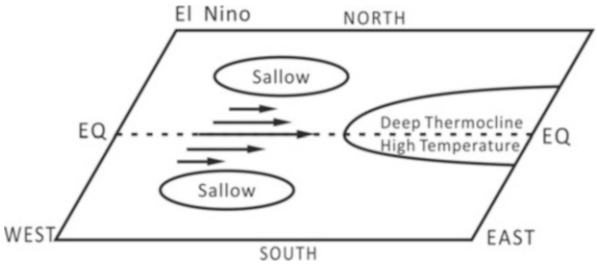

Fig. 5.6 Schematic diagram to show how the equatorial wind and off-equatorial Rossby waves respond to a positive SSTA in the eastern equatorial Pacific

(e.g., Sureaz and Schopf 1988; Battisiti and Hirst 1989). The main idea behind this theory is the delayed effect of equatorial ocean waves.

Figure 5.6 is a schematic diagram illustrating key processes related to this theory. A warm SSTA in the eastern equatorial Pacific induces westerly anomalies in the central equatorial Pacific. The zonal wind anomalies, on the one hand, deepen ocean thermocline in the eastern Pacific and enhance or maintain the warm SSTA and on the other hand excite off-equatorial Rossby waves with shallower thermocline anomalies (due to forcing by anomalous cyclonic wind stress curl). The anomalous shallower thermocline Rossby wave signals propagate westward, and part of the wave energy transfers, after reflected in the western boundary of the basin, into equatorial Kelvin waves that move eastward along the equator. The negative thermocline wave signals reach the eastern Pacific and promote a phase transition into a cold episode.

The second mechanism is the recharge oscillator theory. Key process behind this theory is the zonal mean thermocline variation (Jin 1997; Li 1997). Figure 5.7 is a schematic diagram illustrating how this mechanism works. The ocean thermocline anomaly associated with ENSO may be separated into two components, a zonal mean component and a zonal asymmetric component. While the zonal asymmetric component is temporally in phase with the SSTA in the eastern equatorial Pacific or the zonal wind anomaly in the central equatorial Pacific, the zonal mean component has a phase lag with the SSTA or the zonal wind anomaly. For example, in response to a warm SSTA in the eastern Pacific, the westerly anomaly appears in the central Pacific, and thermocline becomes anomalously deep (shallow) in eastern (western) Pacific (Fig. 5.7I). Meanwhile, the meridional curl of the surface wind anomaly leads to poleward upper-ocean mass transport. This leads to a shoaling of zonal mean thermocline at the equator (Fig. 5.7II). The shoaling of ocean thermocline eventually leads to the development of a negative SSTA in the eastern equatorial Pacific (Fig. 5.7III). The SSTA cooling causes the development of easterly anomalies in the central Pacific, which promote equatorward upper-ocean mass transport. As a result, zonal mean thermocline deepens at the equator. The deepened thermocline promotes a phase transition into a warm episode.

The aforementioned SSTA – zonal mean thermocline anomaly relationship – was supported by the observational ocean data analysis of Li (1997) and Meinen and McPhaden (2000). Figure 5.8 shows that while the zonal asymmetric component of the thermocline anomaly is approximately in phase with the eastern Pacific

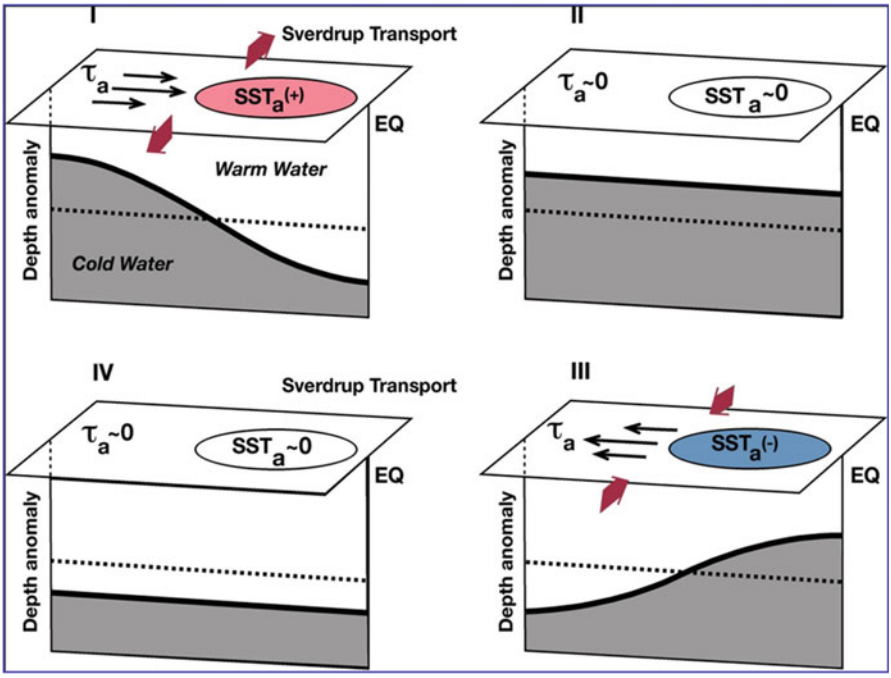

Fig. 5.7 Schematic diagram illustrating how the zonal mean thermocline depth anomaly has a delayed response to the SSTA-induced wind stress forcing, leading to a phase transition from a warm (cold) to a cold (warm) episode (From Meinen and McPhaden (2000). © Copyright 2000 American Meteorological Society (AMS))

SSTA and central Pacific zonal wind stress anomaly, the zonal mean component of the thermocline anomaly leads the SSTA by approximately 90° in phase. When the SSTA is normal, the zonal mean component reaches a maximum. When the SSTA is in a peak phase, the zonal mean thermocline anomaly is nearly zero.

It is worth mentioning that although ocean waves are not explicitly mentioned in the recharge oscillator theory, they can affect the zonal mean thermocline variation through an accumulated wave effect, as demonstrated by Li (1997) in an idealized shallow water model experiments with enlarged Pacific domain and strong damping in lateral boundary.

5.4 Phase Locking to the Annual Cycle

An interesting feature of ENSO evolution is its phase locking to the annual cycle. As seen from Fig. 5.2, most of El Niño peak phases appear in the northern winter (DJF). Two mechanisms might be responsible for the phase locking feature. The first one is season-dependent coupled instability. Following Li (1997), the simplest

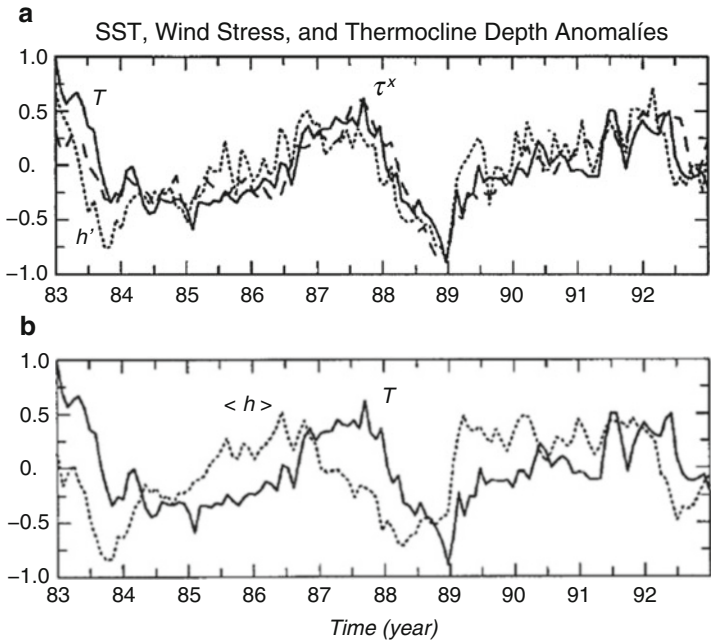

Fig. 5.8 (*Top*) Inphase evolutions of the eastern equatorial Pacific SSTA (*solid curve*), central equatorial Pacific zonal wind stress anomaly (*dashed curve*), and zonally asymmetric thermocline depth anomaly (*dotted curve*) from 1983 to 1992. (*Bottom*) Evolution of the eastern equatorial Pacific SSTA (*solid curve*) and the zonal mean thermocline depth anomaly (*dotted curve*) for the same period (From Li (1997). © Copyright 1997 American Meteorological Society (AMS))

set of equations describing ENSO dynamics includes an eastern Pacific SSTA tendency equation and a zonal mean thermocline anomaly tendency equation:

$$\frac{\partial T'}{\partial t} \approx \lambda T' + \sigma < h > \tag{5.2a}$$

$$\frac{d < h >}{d\,t} = -\Lambda T_E - \varepsilon < h > \tag{5.2b}$$

where parameter λ represents the sum of all positive air–sea feedback processes mentioned in Sect. 5.2 (such as Bjerknes thermocline feedback, zonal advective feedback, and Ekman upwelling feedback). λ is the function of background mean upwelling velocity in the eastern equatorial Pacific, background mean SST gradient, and background mean vertical temperature gradient, all of which vary with the season. For a given set of constant values of these background mean fields each month, one may calculate the growth rate and oscillation period of the above equation. Figure 5.9 shows that a maximum (minimum) growth rate occurs in September (March). The result implies that eastern Pacific SSTA grows rapidly

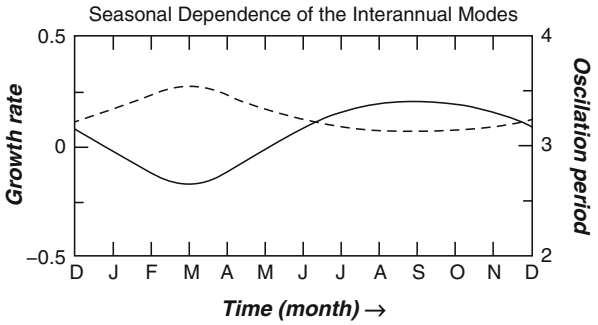

Fig. 5.9 Growth rate (*solid curve*) and frequency (*dashed curve*) of the ENSO mode calculated based on the simple coupled model (i.e., Eq. 5.2a and 5.2b) as a function of the specified climate mean state (from January through December) (From Li (1997). © Copyright 1997 American Meteorological Society (AMS))

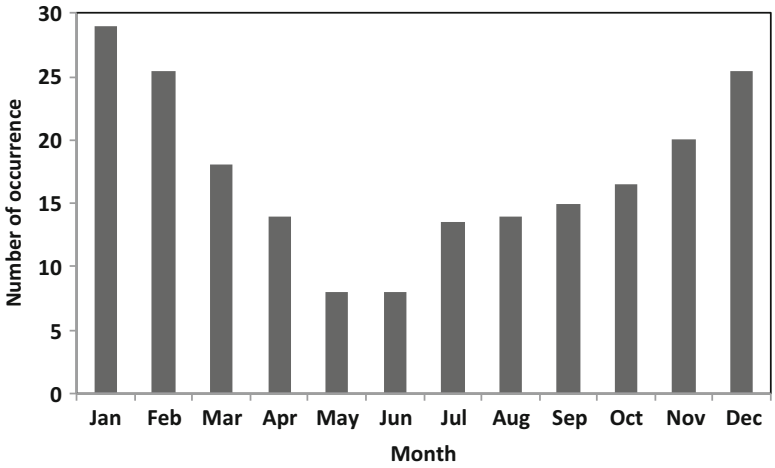

Fig. 5.10 Occurrence of the El Niño peak phases at each month when an observed background mean state (including mean upwelling velocity, mean zonal SST gradient, and mean ocean stratification) was specified in the model of Li (1997). The model was integrated for 1000 years

in northern fall and reaches a maximum value in northern winter. After that, the SSTA starts to decay.

The cause of the season-dependent coupled instability is primarily attributed to the annual cycle of background mean upwelling velocity and background mean SST gradient, both of which retain a maximum value in northern fall, when the cold tongue is strongest.

When an annual mean background state is specified, the model generates a regular oscillation with a period of 3.4 years. If one runs the model for a sufficiently long period (say, 1000 years), each month has an equal chance for the El Niño peak phase to occur. Figure 5.10 illustrates the number of occurrence of the peak El Niño

phase when a seasonally varying background state is specified. Note that in this case, the El Niño peak phase occurs more frequently in northern winter (DJF), consistent with the observation.

Another possible mechanism is attributed to anomalous easterly wind stress forcing associated with the Philippine Sea anomalous anticyclone (Wang et al. 2000), which often develops in northern fall of El Niño developing phase and matures in El Niño peak winter. Anomalous easterlies to the south of the anomalous anticyclone may force upwelling equatorial Kelvin waves (with a negative thermocline signal), which propagate eastward and induce surface cooling and ENSO phase transition in the eastern equatorial Pacific.

5.5 El Niño and La Niña Amplitude Asymmetry

It has been shown (e.g., Su et al. 2010) that the amplitude of El Niño is greater than that of La Niña. Figure 5.11 shows the skewness of SSTA in DJF in the tropical Pacific. The skewness is defined as

$$\text{Skewness} \equiv \frac{m_3}{(m_2)^{3/2}},$$

where m_k is the kth moment, $m_k = \sum_{i=1}^{N} \left((x_i - \bar{X})^k / N \right)$ and x_i are the ith observation, $\bar{X}$ is the long-term climatological mean, and N is the number of observations.

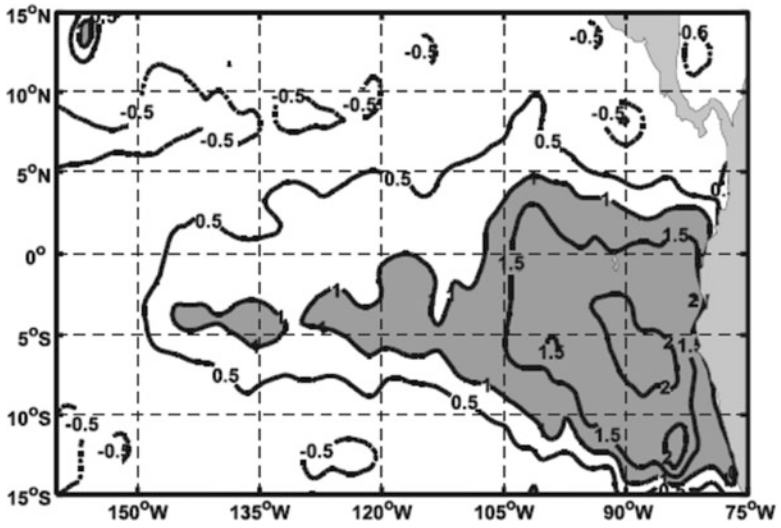

Fig. 5.11 Skewness of DJF mean SSTA calculated based on the period of 1979–2008. *Shaded area* indicates the region exceeding the 95% confidence level (From Su et al. (2010). © Copyright 2010 American Meteorological Society (AMS))

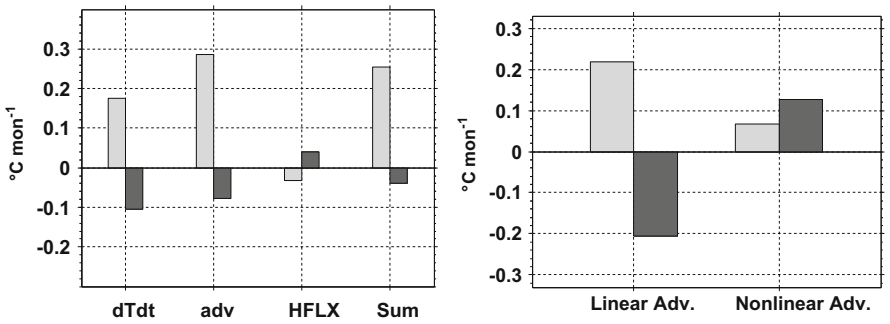

Fig. 5.12 (**Left**) The mixed-layer temperature tendency terms; from *left* to *right*, the observed temperature tendency, the 3D temperature advection, the surface flux heating, and the sum of the advection and the surface heat flux. The calculation is based on ensemble average of three oceanic reanalysis datasets (SODA 2.0.2, Soda1.4.2 and GODAS). *Gray* and *black bars* represent composite results for El Niño and La Niña events, respectively. All the terms are averaged over the far eastern equatorial Pacific (5°N–5°S, 110°W–80°W) for the developing phases. (**Right**) Same as in the left panel except for the linear and nonlinear temperature advection terms for El Niño and La Niña composites (From Su et al. (2010). © Copyright 2010 American Meteorological Society (AMS))

The skewness is often used to measure the extent of asymmetry between positive and negative anomalies. A positive skewness indicates that positive anomalies are much greater than negative anomalies, and vise versa. Figure 5.11 illustrates that a significant positive skewness appears over the far eastern equatorial Pacific (east of 110°W), meaning that the amplitude of the positive SSTA in this particular region is much greater than that of the negative SSTA.

The composite SSTA evolutions averaged over the box (shown in Fig. 5.11) illustrate that both El Niño and La Niña start to develop earlier of a calendar year and peak in DJF. Thus, the difference between SSTA amplitude at the peak phase is attributed to the difference of SSTA tendency during the developing phase.

Figure 5.12a shows the mixed-layer heat budget analysis results during the developing phase for both El Niño and La Niña. The greater mixed-layer temperature tendency in the El Niño composite than in the La Niña composite is attributed to anomalous 3D advection terms, not to the surface heat flux anomaly. A further separation of linear and nonlinear advection terms shows that the asymmetry is attributed to the nonlinear advection. The linear advection terms are positive (negative) for El Niño (La Niña) composite; thus, they contribute to the growth of both El Niño and La Niña (through various positive feedbacks). The nonlinear advection terms, on the other hand, are always positive, suggesting that they contribute to a greater (weaker) growth rate during El Niño (La Niña).

The separate contributions of zonal, meridional, and vertical components of the nonlinear advection term above are shown in Fig. 5.13. It is noted that nonlinear zonal and meridional advection terms are major contributions to the positive tendency and thus are responsible for greater El Niño than La Niña amplitude. Nonlinear vertical advection, on the other hand, plays an opposite role.

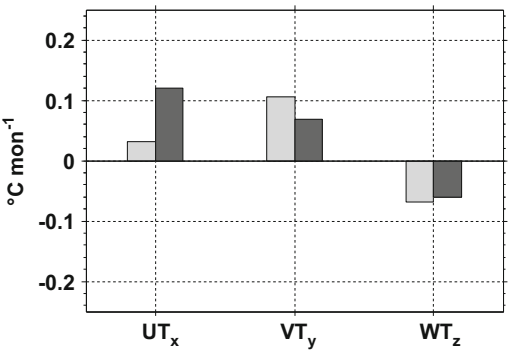

Fig. 5.13 Same as Fig. 5.12 except for zonal, meridional, and vertical components of the nonlinear advection term (From Su et al. (2010). © Copyright 2010 American Meteorological Society (AMS))

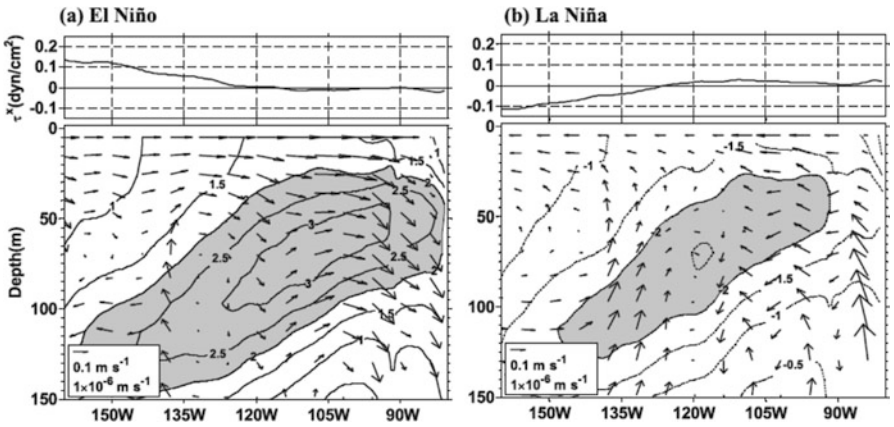

Fig. 5.14 Composite longitudinal profile of zonal wind stress anomaly and longitudinal-depth section of oceanic temperature and current anomalies averaged over 2°S–2°N during the developing phases for El Niño (*left panels*) and La Niña (*right panels*) (From Su et al. (2010). © Copyright 2010 American Meteorological Society (AMS))

To reveal how the nonlinear advection terms contribute to El Niño and La Niña amplitude asymmetry, one may examine the composite zonal–vertical structure of ocean temperature and current anomalies for El Niño and La Niña composite. Figure 5.14 shows that maximum temperature anomaly appears at subsurface along the climatological mean thermocline, where maximum vertical temperature gradient appears. Surface temperature anomaly has a maximum at 110°W for El Niño but a minimum at 120°W for La Niña. A worth noting feature is a westward zonal wind stress anomaly east of 120°W where surface ocean current anomaly is toward the east for El Niño composite (opposite is true for La Niña composite). The eastward anomalous current may advect the maximum positive SSTA eastward, leading to a positive nonlinear zonal advection. Similarly, during La Niña, westward current anomalies appear to the east of a maximum cold SSTA and are against

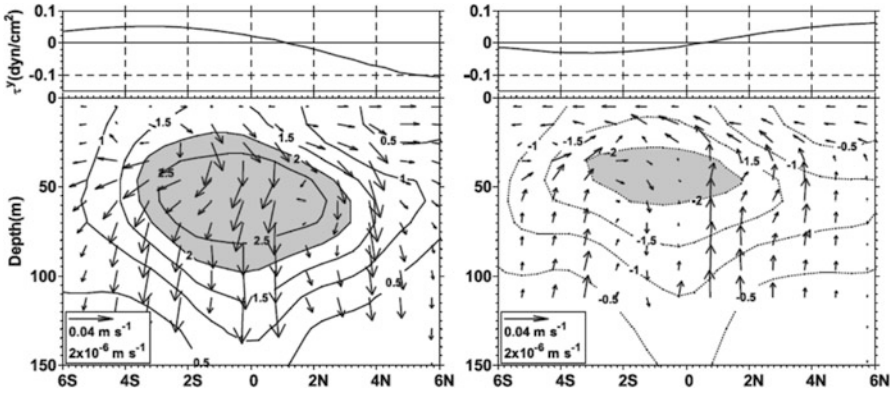

Fig. 5.15 Composite latitudinal profile of meridional wind stress anomaly and latitudinal-depth section of oceanic temperature and current anomalies averaged over the eastern Pacific (110°–80°W) 2°S – 2°N during the developing phases for El Niño (*left panels*) and La Niña (*right panels*) (From Su et al. (2010). © Copyright 2010 American Meteorological Society (AMS))

anomalous zonal wind stress forcing. As a result, a positive nonlinear zonal advection is resulted for La Niña composite too. A key question then becomes why the surface current anomaly in the far eastern Pacific is against the zonal wind stress anomaly.

By separating geostrophic and Ekman current components, Su et al. (2010) showed that the zonal surface current anomaly in the eastern equatorial Pacific is primarily controlled by the geostrophic current anomaly (determined by the thermocline depth anomaly), while the wind-induced Ekman current anomaly is negligible. This is very different from the surface meridional current anomaly in the tropical eastern Pacific, which is primarily determined by the Ekman current anomaly.

Figure 5.15 illustrates the composite meridional–vertical structure of ocean temperature and current anomalies averaged over the eastern Pacific sector for El Niño and La Niña composite. Note that a maximum (minimum) surface temperature anomaly center appears south of the equator for El Niño (La Niña) composite. Surface meridional wind anomalies, on the other hand, converge (with a zero velocity) north of the equator.

The mismatch between the SSTA center and the convergence center is attributed to the fact that the atmosphere only sees the total SST rather than the SSTA and that mean SST is much higher north of the equator. As a result, the total SST retains a maximum value north of the equator. This is in a way similar to the zonal SSTA precipitation anomaly phase relationship along the equator. Observations show that although the average SSTA center associated with El Niño is located at 110°W, the precipitation anomaly center in response to the SSTA appears in the central equatorial Pacific. This zonal phase shift results from the zonal gradient of the mean SST.

Because of the mismatch of the maximum SSTA center and the meridional wind convergence center in the eastern Pacific, northward cross-equatorial current anomalies in response to the northward cross-equatorial wind during El Niño and southward cross-equatorial current anomalies in response to the southward cross-equatorial wind during La Niña all result in a positive nonlinear meridional advection anomaly. Considering that the nonlinear zonal advection may be partially offset by the nonlinear vertical advection (the two current components are closely related due to mass continuity), one may conclude that nonlinear meridional advection is critical in determining the El Niño and La Niña amplitude asymmetry.

5.6 El Niño and La Niña Evolution Asymmetry

Examining the time series of observed SSTA averaged in the eastern equatorial Pacific (180°–80°W, 5°N–5°S) during 1980–2013, one may find that almost all El Niño events (except 1986–1987 El Niño) terminated rapidly after their peak phase in boreal winter, whereas almost all La Niña events (except 1988 and 2005 La Niña) redeveloped into another La Niña event in the subsequent boreal winter.

The temporal evolutions of the mixed-layer temperature anomalies (MLTAs) for both the El Niño and La Niña composites are displayed in Fig. 5.16. The El Niño and La Niña composites bear many similarities during the developing year (year 0). For the El Niño composite, a positive MLTA starts to develop in April and reaches its peak in December. For the La Niña composite, a negative MLTA starts to develop in June and reaches its peak in December too. The major evolution asymmetry happens in the second year (year +1). Following its peak phase, El Niño experiences a fast decay, and a negative MLTA occurs in July. In contrast, La Niña decays at a much slower rate, and by July of year +1, it still retains one third of the peak MLTA value. During the northern fall of year +1, the cold MLTA rapidly re-intensifies. As a result, a La Niña reemerges in the following winter.

To illustrate that the evolutions above reflect the common features of ENSO, the MLTA evolutions for all ENSO case composites were plotted (see green lines in Fig. 5.16). As one can see, the two time series bear a great similarity, indicating that the asymmetric evolution feature between El Niño and La Niña is quite robust.

As shown in Fig. 5.16, a key difference between El Niño and La Niña evolutions lies in the distinctive MLTA decaying rates during the earlier part of year +1, that is, El Niño decays much quickly than La Niña after their peak phase. Because of this difference, the positive MLTA associated with El Niño has changed its sign (becoming a cold anomaly) by July of the second year, while the MLTA associated with La Niña keeps the same sign.

Northern autumn is the season that attains the strongest coupled ENSO instability (Li 1997), because mean upwelling and mean zonal SST gradient along the equator reach a maximum in boreal fall at the season (Li and Philander 1996; Philander et al. 1996). As a result, the Bjerknes thermocline feedback ($-\bar{w}\partial T'/\partial z$) and the zonal advective feedback ($-u'\partial \bar{T}/\partial x$) are strongest in northern fall. Thus,

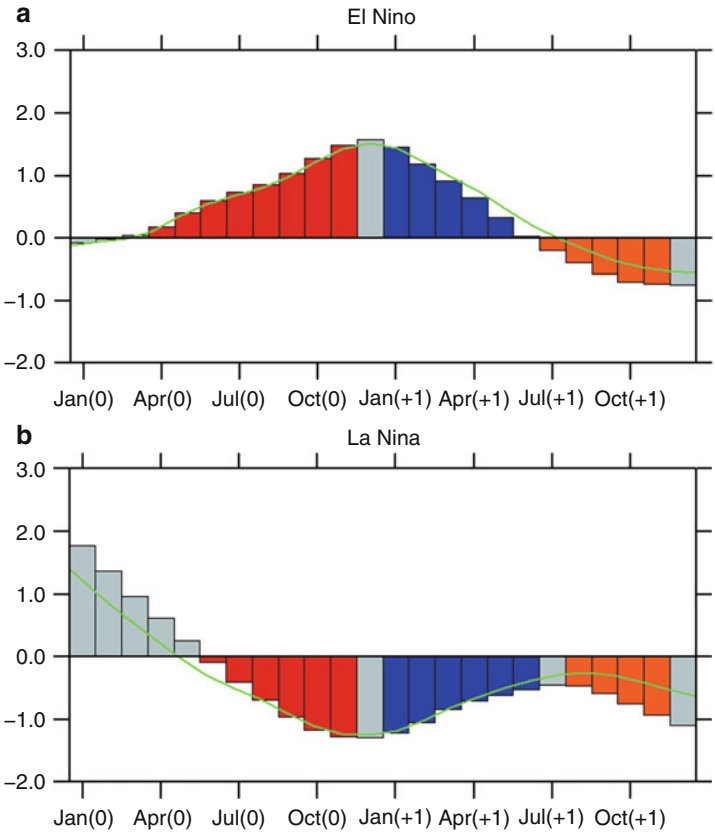

Fig. 5.16 Composite temporal evolutions of MLTAs (unit: °C) for selected (*bar*) and all (*green curve*) El Niño (**a**) and La Niña (**b**) events. *Red bars* represent El Niño (La Niña) developing phase, *blue bars* represent El Niño (La Niña) decaying phase, and *orange bars* represent El Niño transition (La Niña re-intensification) phase. Selected El Niño cases include 1982–1983, 1991–1992, 1994–1995, 1997–1998, 2002–2003, 2004–2005, 2006–2007, and 2009–2010 events, and selected La Niña cases include 1983–1984, 1995–1996, 1998–1999, 2007–2008, and 2010–2011 events (From Chen et al. (2016). © Copyright 2016 American Meteorological Society (AMS))

whether or not the sign of the SSTA would change by summer of year +1 is critical in determining the subsequent ENSO evolution. For the composite El Niño, a stronger damping in earlier year leads to a fast transition to a negative SSTA by July of year +1, which makes a "perfect" timing for further development of a cold episode. In contrast, a weaker damping during La Niña decaying phase retains a cold SSTA by summer of year +1, which starts to redevelop in northern fall and reaches a peak in the following winter. Thus, a key difference between El Niño and La Niña evolution asymmetry lies in the distinctive damping rates during the earlier part of year +1.

Table 5.1 Composite MLTA budget analysis (unit: °C/month) averaged in (5°N–5°S, 180°–80°W) during the decaying phase of El Niño and La Niña

	dT′/dt	Adv	Hflx	Sum	$-u'\partial\bar{T}/\partial x$	sw′	lh′
El Niño	**−0.28**	**−0.12**	**−0.20**	**−0.32**	−0.19	−0.07	−0.14
La Niña	**0.13**	**0.06**	**0.11**	**0.17**	0.10	0.04	0.06

From Chen et al. (2016). © Copyright 2016 American Meteorological Society (AMS)
"Adv" denotes advection terms, "Hflx" represents heat flux terms, "Sum" is the summation of "Adv" and "Hflx", "sw" denotes the anomalous shortwave radiation term, and "lh" is the anomalous latent heat flux term. The result is based on the ensemble average of two ocean reanalysis datasets (GODAS and SODA 2.1.6) and two surface heat flux products (NCEPv2 and OAFlux)

An oceanic mixed-layer heat budget analysis was conducted to reveal the dynamic and thermodynamic causes of the distinctive damping rates during the earlier part of year +1. Table 5.1 shows the composite MLTA budget analysis during the decaying phase of El Niño and La Niña. Note that the MLTA decaying rate during El Niño is about two times as large as that during La Niña. A further examination of the separate ocean advection and surface heat flux terms shows that both the dynamic and thermodynamic terms contribute equally to the El Niño and La Niña difference (Table 5.1). The dynamic term difference is primarily attributed to anomalous zonal advection ($-u'\partial\bar{T}/\partial x$), while the thermodynamic term difference is mainly due to anomalous surface shortwave radiation and latent heat flux effects.

The zonal current asymmetry between El Niño and La Niña arises from the asymmetry of atmospheric wind responses to ENSO forcing. The top panel of Fig. 5.17 shows the composite surface wind and wind stress curl anomalies during the El Niño and La Niña mature winter (DJF). Note that during El Niño, an anomalous off-equatorial anticyclone occurred over the western North Pacific (WNP). Easterly wind anomalies south of the anticyclone tend to stimulate oceanic upwelling Kelvin waves, lifting the equatorial thermocline. The negative thermocline anomalies induce westward geostrophic ocean surface currents, leading to a cold advection that damps the warm SSTA. In contrast, an anomalous cyclone occurs in the WNP during La Niña. However, this anomalous cyclone center shifts westward (Fig. 5.17b). As a result, an anomalous easterly, rather than an anomalous westerly, appears in the far western equatorial Pacific (135°E–150°E). This distinctive zonal wind asymmetry appears responsible for the anomalous zonal advection difference between El Niño and La Niña during their decaying phase.

Imagine if El Niño and La Niña circulation is perfectly symmetric, the sum of the two anomalous circulation fields should be vanished. Following Wu et al. (2010), the asymmetric (symmetric) component of anomalous wind field is defined as the sum of (difference between) the composite El Niño and La Niña wind fields. Figure 5.17c shows that the asymmetric wind field in the WNP is dominated by the El Niño composite pattern. The asymmetric circulation patterns between El Niño and La Niña in northern winter can be traced back to the local SSTA asymmetry in the preceding summer and fall (Wu et al. 2010).

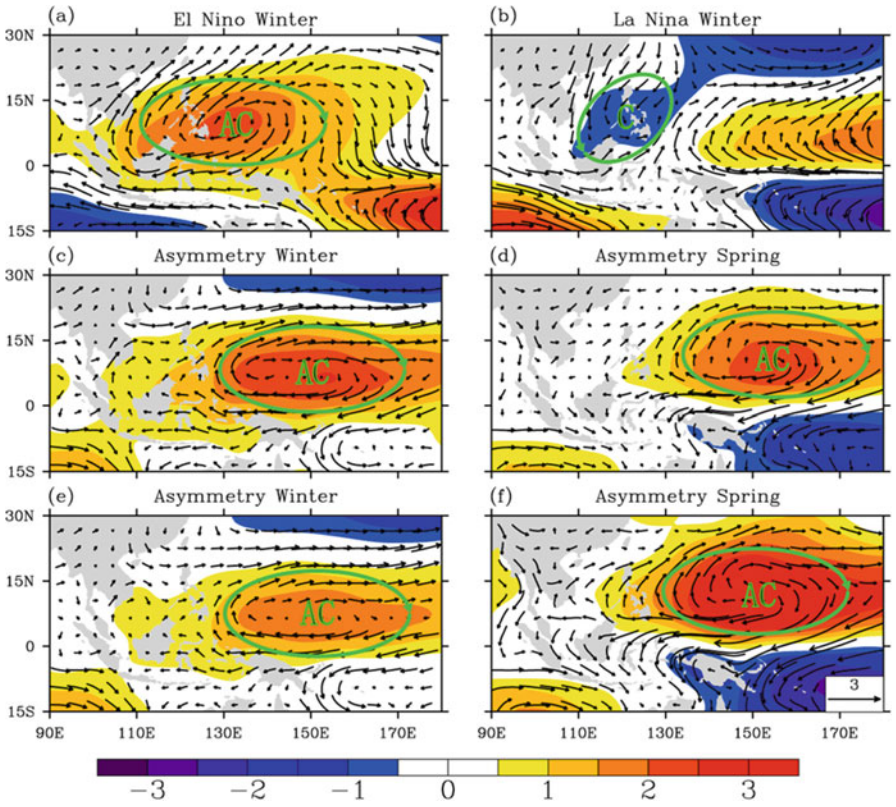

Fig. 5.17 Composite 925-hPa wind anomalies (vectors; m s^{-1}) and streamfunction anomalies (shading; 10^6 m^2 s^{-1}) during (a) El Niño and (b) La Niña mature winter (DJF) and asymmetric component estimated by the sum of them (c) during mature winter (DJF) and (d) following spring (MAM). (e), (f) The normalized asymmetric components are also shown (i.e., normalized according to the equatorial EP SSTA amplitude before calculating the asymmetric component). Areas marked with AC (C) denote anticyclonic (cyclonic) circulation. (From Chen et al. (2016).)

One possible cause of the above asymmetry in Fig. 5.17c is attributed to the asymmetry in the SSTA amplitude between El Niño and La Niña. To eliminate this factor, the anomalous wind fields are first divided by the amplitude of the SSTA in the eastern Pacific before computing the asymmetric component. The so-derived asymmetric wind fields are shown in Fig. 5.17e. As one can see, the asymmetry of the zonal wind fields between El Niño and La Niña is still clearly presented, indicating that the asymmetry arises mainly from the pattern asymmetry.

The asymmetry in the anomalous wind stress field exerts a great impact on thermocline evolutions between El Niño and La Niña in year +1 (Fig. 5.18). For El Niño composite, a stronger negative thermocline signal develops in the equatorial western Pacific in the earlier part of year +1 and penetrates into the eastern Pacific

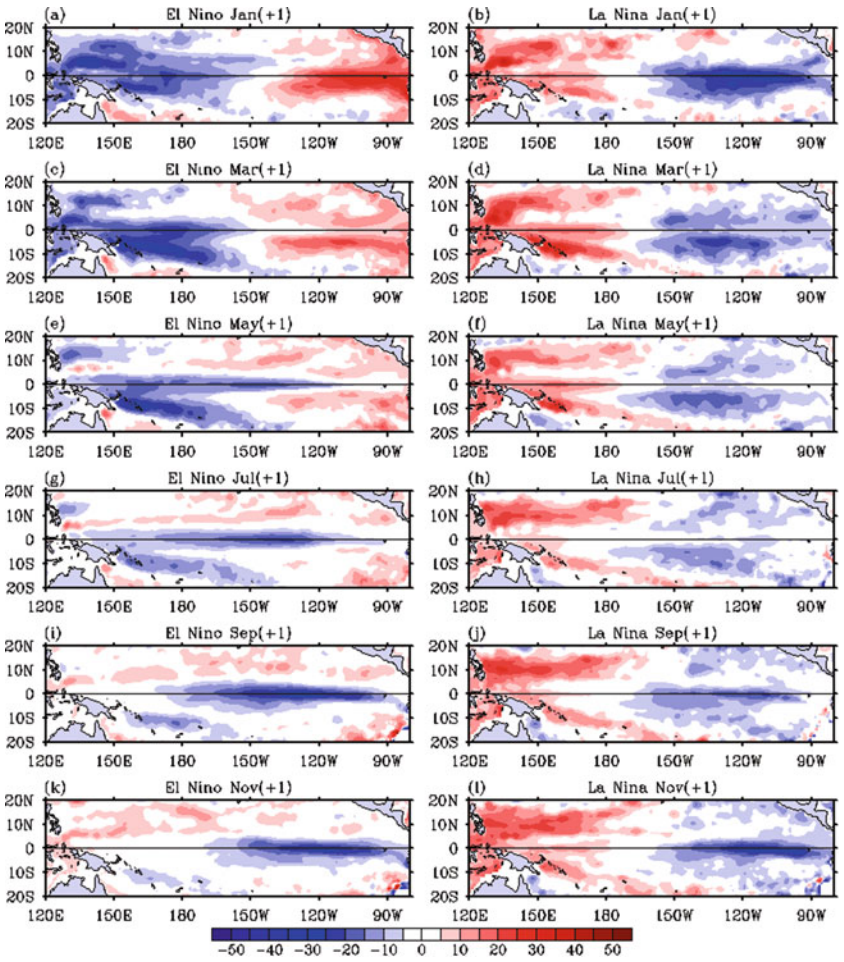

Fig. 5.18 Composite thermocline depth anomalies (*shading*; unit: m) for El Niño (*left panel*) and La Niña (*right panel*) episodes in year +1 (From Chen et al. (2016). © Copyright 2016 American Meteorological Society (AMS))

in May (+1) (left panel of Fig. 5.18). This negative thermocline anomaly continues strengthening as its center propagates to the east. This evolution feature is quite different from La Niña composite (right panel of Fig. 5.18), in which a positive thermocline anomaly signal is so weak that it cannot change the sign in the eastern equatorial Pacific. As a consequence of the weak wind forcing, an anomalous thermocline pattern with a minimum at the equator and two maximum centers off the equator emerges in May (Fig. 5.18f).

A much stronger equatorial thermocline response during El Niño may have the following two effects on the SSTA tendency. Firstly, shallower thermocline could induce greater westward geostrophic currents, which could lead to a cold advection

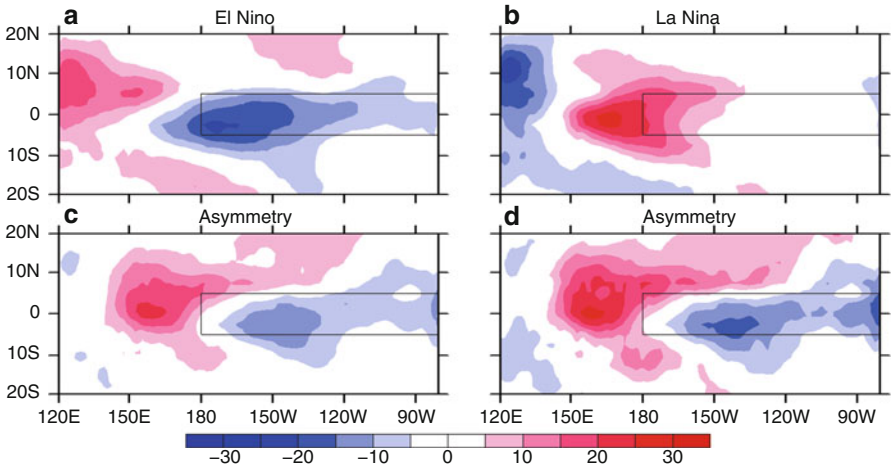

Fig. 5.19 Composite OLR anomaly patterns (shading; unit: W/m^2) during the decaying phase of (**a**) El Niño, (**b**) La Niña, (**c**) the asymmetric component between El Niño and La Niña, and (**d**) the normalized asymmetric component (From Chen et al. (2016). © Copyright 2016 American Meteorological Society (AMS))

anomaly ($-u'\partial\bar{T}/\partial x < 0$) to cool the SST. Secondly, a stronger negative thermocline depth anomaly could also induce a stronger negative subsurface temperature anomaly, which further cools the SST through anomalous vertical advection by mean upwelling. Both the effects favor a faster decaying of El Niño. In contrast, during March–May of the La Niña decaying phase, a weaker thermocline depth anomaly at the equator leads to a weaker eastward current anomaly, which causes a weaker MLTA tendency and thus a slower decaying rate during the La Niña decaying phase.

In addition to the aforementioned oceanic dynamic effect, the asymmetric thermodynamic feedback processes also contribute to the distinctive SSTA decaying rates between El Niño and La Niña (Table 5.1). Figure 5.19 shows the composite OLR anomaly patterns averaged during the decaying phase of El Niño and La Niña. A negative OLR anomaly, with a maximum center located in 160°W, occurs in the central and eastern Pacific during El Niño (Fig. 5.19a). In contrast, a positive OLR anomaly center during La Niña shifts westward by 40° in longitude (Fig. 5.19b). Given that SSTA centers are primarily located in the eastern equatorial Pacific, this anomalous OLR center shift implies a weaker negative cloud–radiation–SST feedback during La Niña. Figure 5.19c illustrates the asymmetric component of the OLR anomaly pattern between El Niño and La Niña. The result confirms the east–west asymmetry of cloud responses between El Niño and La Niña.

To examine whether or not the OLR asymmetry is attributed to SSTA amplitude difference between El Niño and La Niña, we also calculated the normalized OLR fields and their asymmetric component. Figure 5.19d shows the asymmetric OLR anomaly pattern per degree warming or cooling. One can see that even in the

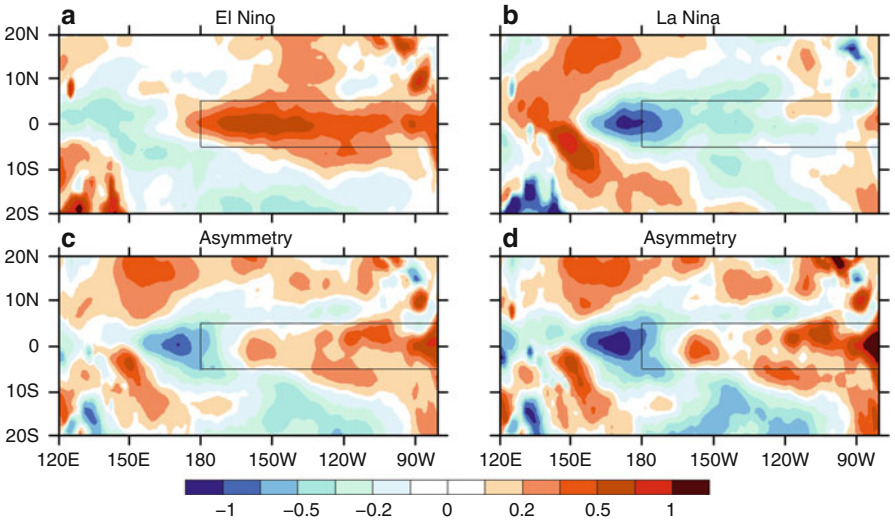

Fig. 5.20 Composite sea–air-specific humidity difference anomaly fields (shading; unit: k/kg) during the decaying phase of (**a**) El Niño, (**b**) La Niña, (**c**) the asymmetric component between El Niño and La Niña, and (**d**) the normalized asymmetric component (From Chen et al. (2016). © Copyright 2016 American Meteorological Society (AMS))

presence of same unit SSTA forcing, a stronger negative cloud–radiation–SST feedback is still presented during El Niño. Thus, the asymmetry is primarily caused by the OLR pattern asymmetry between El Niño and La Niña.

The asymmetry in the surface latent heat flux anomaly also contributes to the distinctive damping rates between El Niño and La Niña (Table 5.1). To examine whether the asymmetry is attributed to anomalous wind speed or anomalous sea–air-specific humidity difference, one may calculate their relative contributions. The diagnostic result shows that the major contribution arises from the anomalous sea–air-specific humidity difference field, whereas the anomalous wind contribution is relatively small.

Figure 5.20 shows the composite sea–air-specific humidity difference field during the decaying phase of El Niño and La Niña. In the El Niño decaying phase, a positive sea–air-specific humidity difference anomaly occurs in the eastern equatorial Pacific, with a maximum center located in 160°W (Fig. 5.20a). Comparing to El Niño, the negative sea–air-specific humidity difference anomaly center shifts westward during La Niña decaying phase (Fig. 5.20b). As a result, the specific humidity difference field shows a marked pattern asymmetry between El Niño and La Niña, characterized by a positive anomaly in the eastern equatorial Pacific and a negative anomaly to its west (Fig. 5.20c). This asymmetric pattern implies a weaker evaporative damping during La Niña than during El Niño. Figure 5.20d further indicates that this asymmetry does not depend on the amplitude of El Niño and La Niña. Therefore, the asymmetry of the evaporative damping between El Niño and

La Niña is primarily caused by the pattern asymmetry of sea–air-specific humidity difference field, in a way similar to that of the cloud–shortwave radiation–SST feedback.

To sum up, a mixed-layer heat budget analysis indicates that both the thermodynamic (heat flux) and dynamic (wind stress) processes contribute to the El Niño and La Niña evolution asymmetry. The former is related to asymmetric cloud–radiation–SST and evaporation–SST feedbacks, whereas the latter is associated with asymmetry of wind responses in western Pacific. A strong SSTA damping occurs during El Niño decaying phase, compared to a much weaker damping rate during La Niña decaying phase. Such a difference leads to a sign change of SSTA for El Niño but retaining of the same sign SSTA for La Niña by end of summer of year +1. A season-dependent coupled instability further kicks in during northern fall. This leads to the development of a La Niña by the end of the second year for El Niño composite but a reoccurrence of a La Niña episode by the end of the second year for La Niña composite. The heat budget analysis indicates that the thermodynamic process is as important as the dynamic process in causing the El Niño–La Niña evolution asymmetry.

5.7 Modulation of Interdecadal Mean State on El Niño Behavior

Canonical El Niño has a warming center in the eastern Pacific (EP), but since 1999, El Niño warming center tends to occur more frequently in the central Pacific (CP). Figure 5.21 shows dominant SSTA EOF patterns during two interdecadal periods of 1980–1998 and 1999–2010 (hereafter refer to as ID1 and ID2). The SSTA pattern during ID1 has a maximum center near South American coast and resembles a typical EP El Niño pattern. The SSTA pattern during ID2 has a maximum center near central equatorial Pacific and resembles a typical CP El Niño pattern. Both the patterns explain about 61% of total variance during their respective periods.

To understand the cause of the El Niño behavior change, one may first examine composite El Niño structure and evolution characteristics during ID1 and ID2. Based on the fact that the EP (CP) El Niño dominates over the first (second) epoch, one may use the two strong cases of 1982, 1997 as EP El Niño or EP warming (EPW), and 2002, 2004, and 2009 as CP El Niño or CP warming (CPW) to make the composite analysis (Fig. 5.22).

For EPW, deepened thermocline emerges in the equatorial western Pacific (WP) as a precursor of the El Niño, which then proceeds eastward steadily. Once the thermocline anomaly reaches the CP, it propagates eastward rapidly, ending up with a prominent warming in the equatorial eastern EP. Through Bjerknes feedback, the EP warming reinforces anomalous convection and surface westerly anomalies to the west, so that the convection and westerly anomalies migrate eastward accordingly and further feedback to the EP warming (Fig. 5.22a, b).

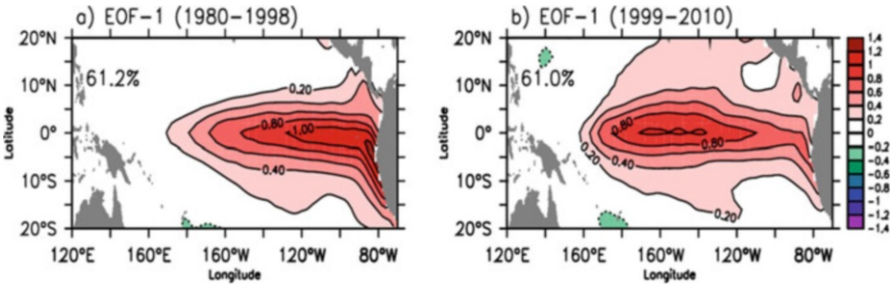

Fig. 5.21 The leading EOF mode pattern of monthly SSTA fields during ID1 (1980–1998) and ID2 (1999–2010) (From Xiang et al. (2013). Copyright © 2012, Springer-Verlag)

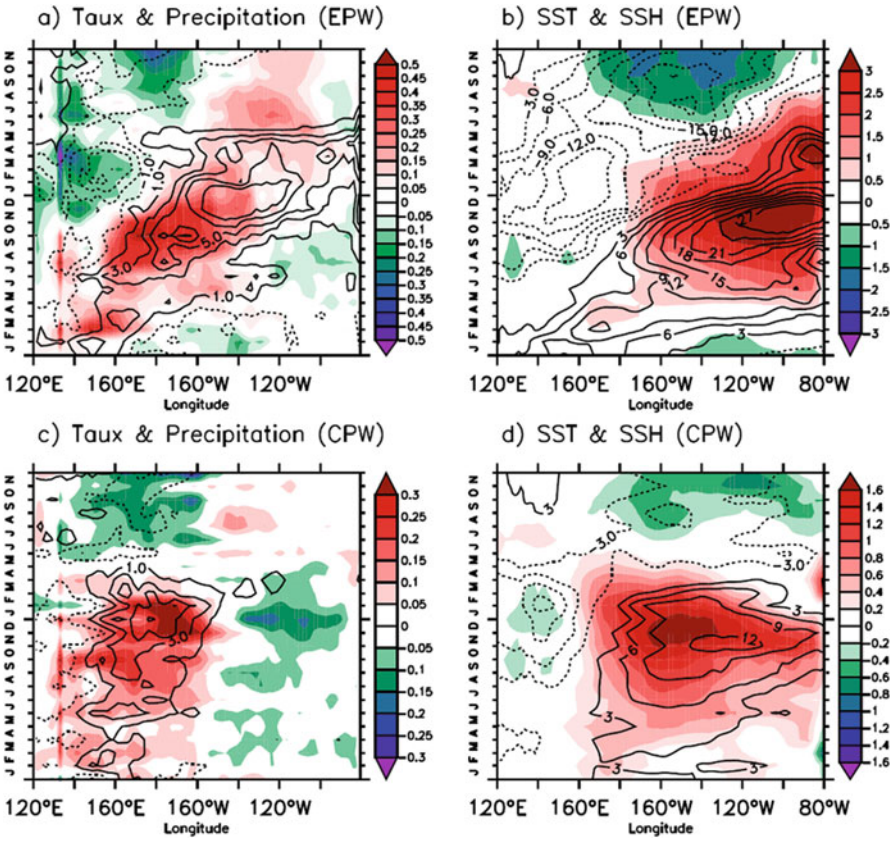

Fig. 5.22 Evolution of the composite EPW (1982, 1997, *upper panel*) and CPW (2002, 2004, 2009, *lower panel*) averaged between 2°S and 2°N. Panels (**a**) and (**c**) show the anomalous zonal wind stress (shaded in dyn/cm^2) and precipitation (contours in mm/day). Panels (**b**) and (**d**) display the SSTA (shaded in °C) and SSH anomaly (contours in cm). Note that zonal wind stress and SST anomalies use different color scale for EPW and CPW (From Xiang et al. (2013). Copyright © 2012, Springer-Verlag)

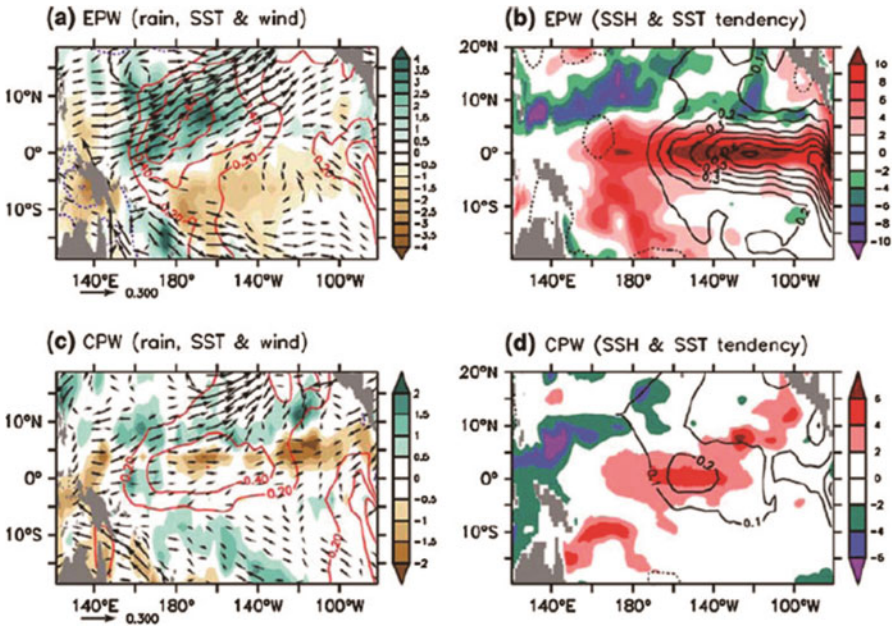

Fig. 5.23 Contrast of the spatial pattern of composite SSTA (contours in °C), zonal wind stress (shown only when its absolute value is greater than 0.05 dyn/cm^2), and precipitation anomaly (shading in mm/day) during the onset stage (April–May) of (**a**) EPW and (**b**) CPW. The *right panels* (**c**) and (**d**) are the corresponding SSH anomaly (shading in cm) and SSTA tendency (contour in °C/month) (From Xiang et al. (2013). Copyright © 2012, Springer-Verlag)

After boreal winter, the EP SST warming sustains for a longer period than the CP SST warming.

By contrast, for CPW, initiation of the deepening thermocline and SST warming occurs in the region near the dateline (160°E–160°W). Interestingly, the corresponding surface zonal wind stress is very weak during the onset stage. Although the maximum warming and the deepest thermocline anomaly areas expand toward the EP slowly, both of their maxima never reach the EP, indicating a standing feature. In accordance with the quasi-stationary oceanic anomalies, the enhanced convection and westerly anomalies are trapped in the region west of 160°W without clear eastward propagations.

The different behaviors of El Niño development during boreal spring have profound impacts on the following further development. As seen in Fig. 5.22b, d, after boreal spring, SSTA associated with CPW continues growing over the CP, while SSTA associated with EPW moves eastward. This implies that the SSTA tendencies are very different between CPW and EPW at that time. What causes such a tendency contrast while the warm SSTA in both the cases appears in the CP?

Let us compare the spatial patterns of the two types of El Niño in April–May (Fig. 5.23). Clearly, the EPW-related precipitation and wind anomalies are zonally

inphase with the underlying SSTA, whereas the CPW-related precipitation and zonal wind anomalies shift to the west of the maximum SSTA center (Fig. 5.23a, b). As a result, the CPW zonal wind stress anomaly exhibits a rather zonal symmetric structure with westerly anomalies in the WP and easterly anomalies in the EP (Fig. 5.23b), so that the maximum thermocline anomaly is confined in the CP (Fig. 5.23d). This is in contrast with the EPW case in which the zonally inphase wind stress anomaly leads to a response of maximum thermocline depth anomaly in EP (Fig. 5.23c). Such distinctive thermocline depth anomaly responses would lead to distinctive SSTA tendencies between the two types of El Niño.

A mixed-layer heat budget diagnosis using GODAS reanalysis data confirms the zonally asymmetric tendency distributions for EPW and CPW. Therefore, the occurrence of a maximum SSTA tendency east of the SSTA center favors the eastward migration in the EPW case. For the CPW, a maximum tendency is approximately in phase with the SSTA center, which explains why the CPW exhibits a nearly standing feature (with no clear eastward propagation). Therefore, unrevealing what causes the distinctive SST–precipitation–zonal wind phase relations during the period when both the SST anomalies are located in the central Pacific holds a key for understanding physical mechanisms behind the CPW and EPW.

It is hypothesized that ocean–atmosphere mean state change has a profound impact on ENSO behaviors. Figure 5.24 portrays the mean state differences between the two epochs (1999–2010 minus 1980–1998). The SST change exhibits a La Niña-like pattern characterized by SST cooling in the equatorial CP and subtropical EP and SST warming in other regions of the Pacific domain (Fig. 5.24a). The associated mean precipitation is severely suppressed in the equatorial Pacific particularly near the dateline, and the mean precipitation is reduced about 27% in the CP (5°S–5°N, 170°E–130°W). Consistently, enhanced trades and more east–west tilted thermocline appear in the second epoch (Fig. 5.24c).

Xiang et al. (2013) hypothesized that the enhanced background low-level divergence together with subsidence may inhibit the development of anomalous deep convection east of dateline, causing the nearly stationary convection and low-level wind anomalies confined to the WP. To test this hypothesis, ECHAM4.6 was used to conduct sensitivity experiments. To obtain realistic surface divergence fields for ID1 and ID2, a nudging term was added to the wind tendency equation from the 1000 hPa to 850 hPa. Given the two different background states in ID1 and ID2, an SSTA was then specified in the CP. The ECHAM sensitivity experiments show that the precipitation and 1000 hPa zonal wind response to the specified SSTA in CP tend to shift westward under the later decade (1999–2010) mean state, compared to that under the earlier decade (1980–1998) mean state (Fig. 5.25). The simulated precipitation and zonal wind phase shift are consistent with the observed, implying that the mean state difference is indeed responsible for the decadal change of the interannual SST–precipitation–zonal wind phase relation.

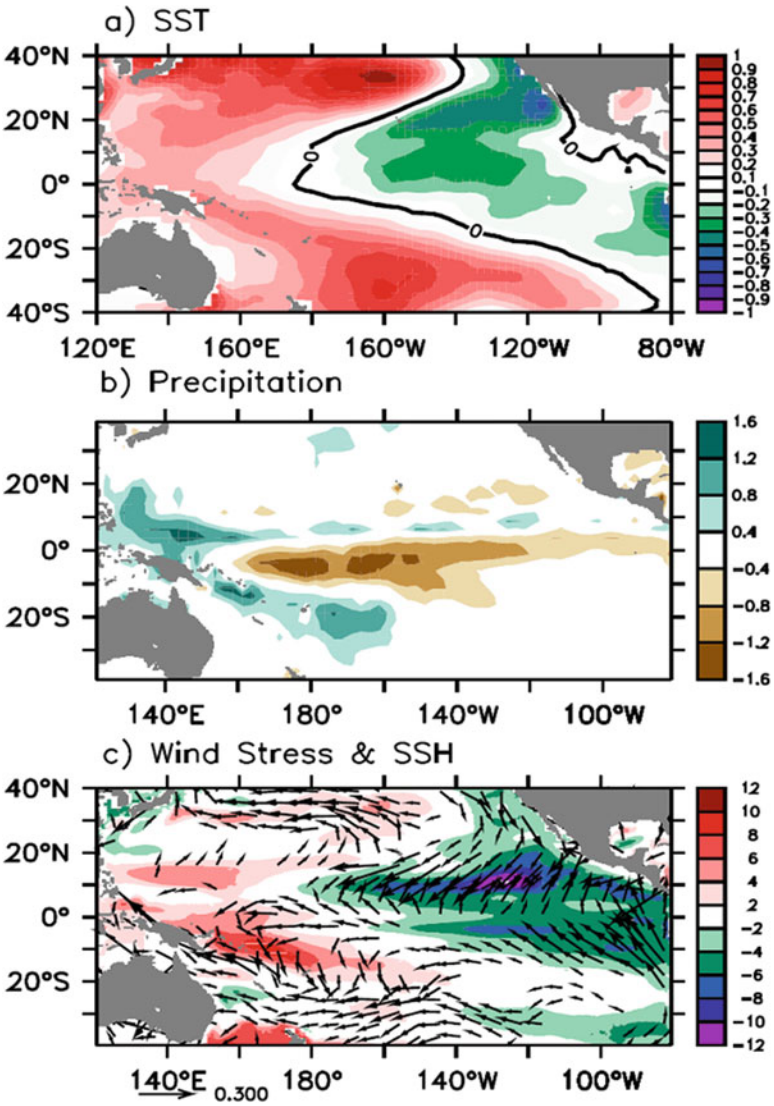

Fig. 5.24 Epochal difference (1999–2010 minus 1980–1998) of (**a**) SST (°C), (**b**) precipitation (mm/day), (**c**) SSH (shading in cm), and surface wind stress (shown only when its absolute value is greater than 0.05 dyn/cm^2) (From Xiang et al. (2013). Copyright © 2012, Springer-Verlag)

In addition to the low-level divergence impact, the background zonal SST gradient change may also contribute to the interdecadal change of the interannual SST–precipitation–zonal wind phase relation. Through idealized atmospheric and oceanic numerical experiments, Chung and Li (2013) showed that a greater background zonal SST gradient could cause a greater westward shift of convection and wind responses to the SSTA, which in turn could cause a greater SSTA tendency to

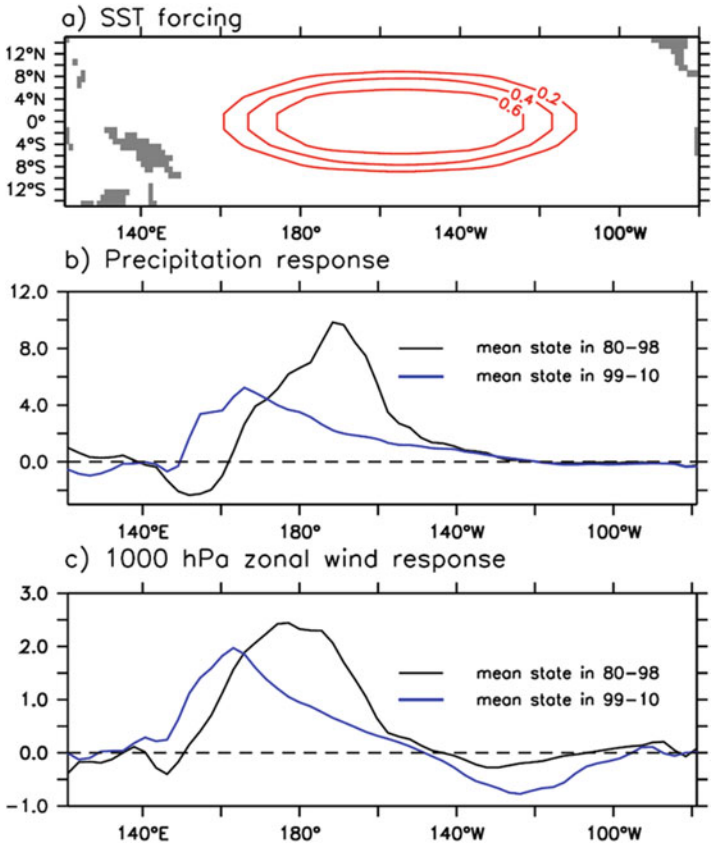

Fig. 5.25 (**a**) Prescribed SST warming in the ECHAM model, (**b**) equatorial (5°S–5°N) precipitation (mm/day) response to the prescribed SST warming for ID1 (*black*) and ID2 (*blue*), (**c**) same as (**b**) but for 1000 hPa zonal wind anomaly. Note that mean low-level converge was nudged toward the observed and mean SST during the two periods that were specified (From Xiang et al. (2013). Copyright © 2012, Springer-Verlag)

the west of an arbitrarily specified SSTA. As a consequence, the coupled system favors the development of CP-type El Niño. Under a weaker background zonal SST gradient, the coupled system favors the development of EP-type El Niño.

To sum up, a weaker mean SST gradient and relatively stronger low-level convergence in CP during ID1 favor the anomalous SST–precipitation–zonal wind inphase relations and thus the eastward-propagating SSTA mode, which eventually leads to the EPW episode. A greater mean SST gradient and stronger low-level mean divergence in CP during ID2, on the other hand, promote a westward phase shift of the anomalous convection and wind, which eventually leads to the development of a standing CP El Niño.

5.8 Indian Ocean Dipole

An air–sea interaction phenomenon similar to El Niño occurs in the tropical Indian Ocean (IO). This coupled air–sea mode is characterized by east–west SSTA contrast along the equatorial IO and is referred to as the Indian Ocean dipole (IOD) (Saji et al. 1999; Webster et al. 1999). Although such dipole events with weaker amplitudes have been noticed previously, the 1997 IOD event attracted great attention when it reached the highest magnitude in the past century and was associated with severe floods in East Africa and droughts over Indonesia. It has been suggested that the unusual Indian monsoon–ENSO relationship in 1997 may result from this abnormal SST condition in the IO.

An important scientific question about IOD is whether or not it is a self-sustained mode like the ENSO. Great similarity in the anomalous surface zonal wind–SST relationship has prompted some investigators to hypothesize that the similar mechanism as ENSO may operate in the IO. On the other hand, it is noted that the tropical Pacific and IO exhibit a remarkable difference in basic-state wind and SST fields. By physical reasoning, Li et al. (2003) argued that there are four fundamental differences of air–sea interaction processes between the tropical Pacific and IO.

The first difference is a zonal phase relationship between anomalous convection and SST. By examining observed SST and net surface shortwave radiation fields obtained from the El Niño and IOD composites, one may find that a remarkable difference between the two composites is that the SST and shortwave radiation (or cloud) anomalies have significant zonal phase differences in the eastern Pacific, but they are in phase in the IO. The differences arise from the distinctive atmospheric responses to an SSTA in the warm pool and the cold tongue. In general, atmospheric deep convection is triggered in the region where SST is above 27 °C. This is why anomalous convection associated with El Niño is often observed in the central equatorial Pacific even though the maximum SSTA appears in the eastern Pacific. Because of this phase difference, the reduction of the downward shortwave radiation due to the deep convection cannot efficiently damp the El Niño. In warm oceans, on the other hand, a modest SSTA may induce deep convection in situ, so that the anomalous SST and clouds are generally in phase. The increased clouds tend to reduce the downward shortwave radiation and thus decrease the SST, leading to a negative feedback between the atmosphere and ocean.

The strength of the negative cloud–radiation–SST feedback in the warm ocean may be estimated based on a linear Newtonian damping formula. According to the observed SST–shortwave radiation relationship, a reversed damping timescale of 100 days is obtained for a mixed-layer depth of 50 m. Such a strong thermodynamic damping implies that SST variability in the tropical IO is in general small except in regions where there exists a strong positive feedback or under a strong, persistent external forcing.

The second difference is attributed to the great contrast of the basic-state zonal wind and the effect of ocean waves. Whereas the tropical Pacific is dominated by easterly trades, the winds in the tropical IO are characterized by cross-equatorial

monsoonal circulation. At the equator, the annual mean wind is strong easterly in the Pacific but weaker westerly in the IO. Such a difference results in opposite thermocline gradients across the two ocean basins.

The reversal of the basic-state wind and zonal thermocline gradient in the IO implies that the effect of equatorial ocean waves might differ from the Pacific counterpart. In the Pacific, an El Niño-like warming leads to westerly anomalies in the central equatorial Pacific that further induce oceanic Rossby waves with negative thermocline depth anomalies. After reflected in the western boundary, the Rossby waves become an upwelling Kelvin waves that propagate eastward, reversing the sign of the SSTA later. Thus, in the El Niño scenario, ocean waves act as a negative feedback agent and are responsible for the phase reversal.

Unlike the Pacific whose thermocline is tilted to the east, the thermocline in the equatorial IO is shallower toward the west. As a result, except a few hundred kilometers off the coast of Sumatra, the SST is more sensitive to the wave-induced thermocline change in the west than in the east. In the IOD scenario, oceanic Rossby waves generated by the curl of anomalous wind stress in response to a positive IOD carry deeper thermocline signals and propagate westward, enhancing the warm SSTA in the western IO where the mean thermocline is relatively shallow. As a result, the ocean waves have a positive effect on the IOD during the initial development stage. The reflected Kelvin waves also have a negative effect on the SSTA in the eastern IO, but this negative effect was realized only in the late development stage when it contributed to a conversion from a dipole mode to a basin mode. The signals of the Rossby wave propagation and associated ocean warming were clearly detected by satellite observations (e.g., Webster et al. 1999) and well simulated by oceanic models.

The third difference lies in the existence of the South Asian monsoon and its interaction with adjacent oceans. A warm SSTA in the IO may enhance the Indian monsoon through increased moisture fluxes (Meehl 1997). To investigate the possible impact of the IOD on the Indian monsoon, atmospheric general circulation model (AGCM) experiments with ECHAM4 were conducted. The model was forced by observed monthly SST fields in 1997 in the tropical IO (30°S–30°N, 40°E–110°E) and climatological SST fields elsewhere. The atmospheric response to the IOD was obtained by subtracting ten ensemble mean simulations from that in a control experiment in which climatological monthly SST was specified in global oceans. The AGCM ensemble simulations indicate that a positive phase of the IOD tends to enhance the Indian monsoon rainfall.

How does a strengthened monsoon further feedback to the IOD? It is argued that a stronger Indian monsoon enhances northward cross-equatorial wind along the coast of Africa and westerly in the northern IO, leading to a cold SSTA in the western IO (through enhanced surface evaporation, ocean mixing, and coastal upwelling). Meanwhile, the strengthened monsoon may enhance the large-scale east–west circulation and leads to a positive SSTA in the western Pacific/maritime continent (Chang and Li 2000). As a result, the local Walker cell over IO is enhanced. The enhanced Walker cell favors a warm (cold) SSTA in the eastern (western) IO through anomalous thermocline change. Both the remote and local

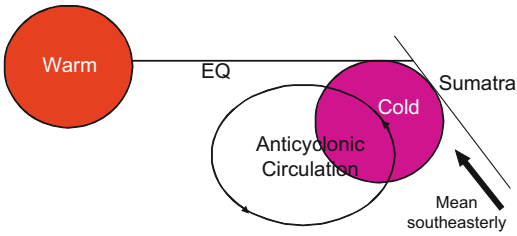

Fig. 5.26 Schematic diagram for a positive air–sea feedback in southeast IO in boreal summer (From Li et al. (2003). © Copyright 2003 American Meteorological Society (AMS))

processes tend to damp the original IOD. Therefore, the monsoon feedback may induce a negative feedback on the IOD.

The fourth difference is that different from eastern Pacific where steady trade wind appears, the seasonal reversal of prevailing wind off Sumatra causes a season-dependent air–sea feedback in the southeast IO. During northern summer (winter), a positive (negative) air–sea feedback exists off Sumatra. Figure 5.26 is a schematic diagram illustrating how a positive air–sea feedback occurs in boreal summer. Compared to the southeast coasts of the tropical Pacific characterized by cold SST tongue and low stratus cloud, the southeast IO (off Sumatra) is a region with persistent high mean SST and deep convection. Assume initially that a modest cold SSTA appears off Sumatra in boreal summer. Since the southeast IO is a region of intense convection, the cold SSTA implies the decrease of atmospheric convective heating or an atmospheric heat sink. According to Gill's (1980) solution, the heat sink will induce a descending Rossby wave response to its west, resulting in an anomalous low-level anticyclonic flow. The local mean flow in northern summer is southeasterly. Thus, the anomalous wind enhances the total wind speed and lowers the SST further through enhanced surface evaporation, vertical mixing, and coastal upwelling. Through this positive air–sea feedback, the cold SSTA and the anomalous anticyclone grow.

The positive feedback is only effective in boreal summer when the mean southeasterly flow is pronounced. With the seasonal reversal of the background flow in boreal winter, the same anomalous wind tends to reduce the total wind speed and thus damp the original cold SSTA. Thus, air–sea coupling supports a negative feedback in northern winter. This season-dependent air–sea feedback mechanism explains why IOD that grows rapidly in northern summer reaches a peak phase in northern fall and decays in northern winter.

A simple analytical coupled air–sea model was built to understand the origin of IOD. The model contains five boxes, representing western tropical IO region, eastern tropical IO region, South Asian monsoon region, western Pacific/maritime continent region, and eastern equatorial Pacific region. For details of this model configuration and the derivation of the model equations, readers are referred to Li et al. (2003). Various positive and negative air–sea feedback processes are considered, including the cloud–radiation–SST feedback, the wind–evaporation–SST feedback, the Bjerknes thermocline feedback, the season-dependent air–sea feedback over southeast IO, and the monsoon–ocean interaction.

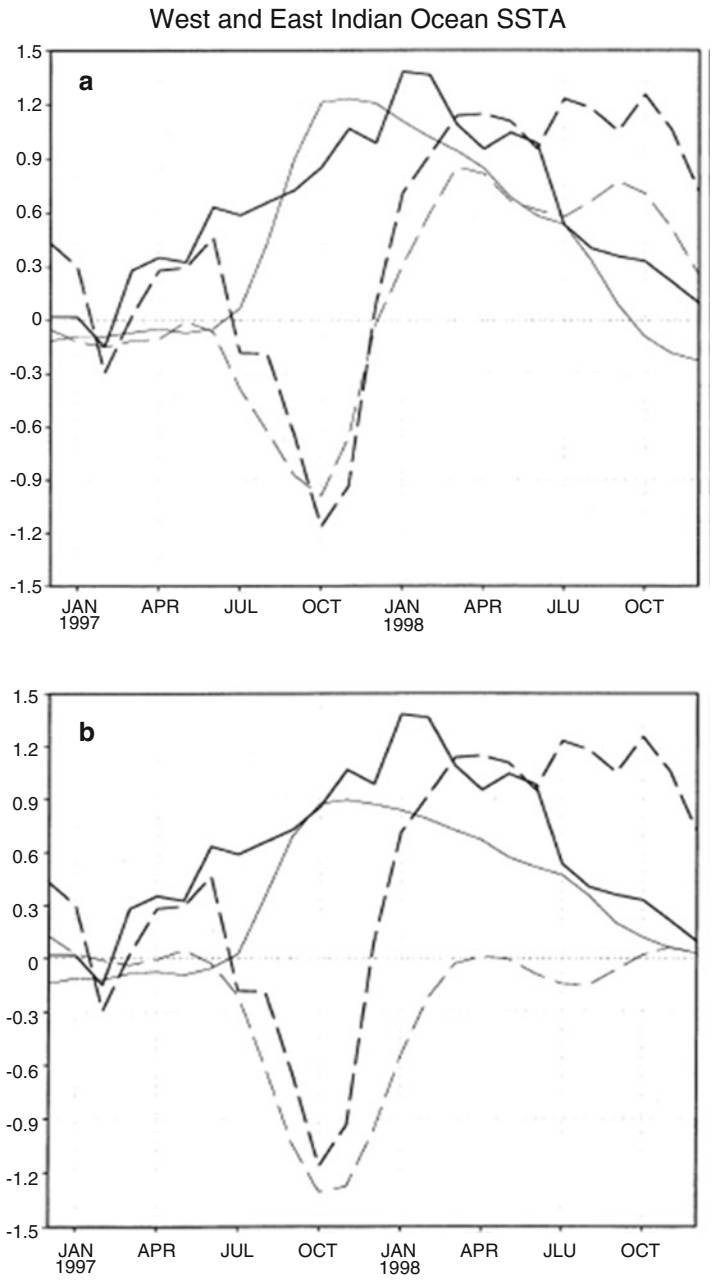

Fig. 5.27 Evolution of observed (*thick curve*) and simulated (*thin curve*) SSTA in the east pole (*dashed*) and west pole (*solid*) during 1997–1998 in the presence (*top*) and absence (*bottom*) of the ocean wave effect (From Li et al. (2003). © Copyright 2003 American Meteorological Society (AMS))

In the absence of external ISO and ENSO forcing, the model generates a weakly damped mode, suggesting that unlike ENSO, IOD cannot be self-sustained. On the other hand, due to its strong instability in boreal summer, this mode can be readily triggered during northern summer by any persistent external forcing such as ENSO. A weak irregular oscillation is generated with high-frequency ISO forcing.

In the presence of realistic ISO and ENSO forcing, the model reproduces, to a great extent, the observed SSTA variability over western and eastern IO. Figure 5.27 shows the temporal evolution of observed and simulated SSTA in the west and east pole during 1997–1998. In the east pole, the cold SSTA reached the peak phase in October 1997 and then decayed rapidly. After January 1998, the ocean surface warmed rapidly. Such a SSTA transition appeared in both the observation and the simulation. As a result, a basin-wide warming appeared in the tropical IO after December 1997.

A sensitivity experiment with the ocean wave effect being removed indicates the warming in the east pole is primarily caused by positive thermocline anomalies associated with delayed ocean wave effect. The initial rapid damping of the cold anomaly in the east pole from October to December 1997 was primarily attributed to a positive shortwave radiation anomaly induced by El Niño-induced downward motion as well as the season-dependent evaporation–wind–SST feedback. A further transition from a normal condition in the east pole to abnormal warming is mainly attributed to the ocean wave effect, as demonstrated by the sensitivity experiment.

Questions

1. What is the observed atmosphere–ocean structure in the Pacific associated with a typical El Niño?
2. What is the major teleconnection pattern during El Niño peak in winter?
3. Why does strong El Niño variability occur only in the eastern equatorial Pacific? What types of positive air–sea feedback processes are involved during ENSO development?
4. What is the relative role of these positive air–sea feedback processes? What is the effect of surface heat fluxes during ENSO development?
5. What theories have been proposed to explain the ENSO phase transition from a warm (cold) to a cold (warm) anomaly?
6. Describe a possible mechanism responsible for the peak phase of ENSO in northern winter.
7. Describe physical processes responsible for peak phase of the Indian Ocean dipole in northern fall.
8. What causes the amplitude asymmetry between El Niño and La Niña?
9. What causes the evolution asymmetry between El Niño and La Niña?
10. How does the interdecadal mean state change in tropical Pacific modulate El Niño behavior during 1980–2012?

References

Battisti DS, Hirst AC (1989) Interannual variability in a tropical atmosphere–ocean model: influence of the basic state, ocean geometry and nonlinearity. J Atmos Sci 46:1687–1712

Bjerknes J (1969) Atmospheric teleconnections from the equatorial Pacific. Mon Weather Rev 97:163–172

Chang C-P, Li T (2000) A theory for the tropical tropospheric biennial oscillation. J Atmos Sci 57:2209–2224

Chang P, Philander SGH (1994) A coupled ocean–atmosphere instability of relevance to the seasonal cycle. J Atmos Sci 51:3627–3648

Chen M, Li T, Shen X, Wu B (2016) Relative roles of dynamic and thermodynamic processes in causing evolution asymmetry between El Niño and La Niña. J Clim 29:2201–2220

Chung P-H, Li T (2013) Interdecadal relationship between the mean state and El Niño types. J Clim 26:361–379

Gill AE (1980) Some simple solutions for heat-induced tropical circulation. Quart J Roy Meteorol Soc 106:447–462

Hirst AC (1986) Unstable and damped equatorial modes in simple coupled ocean–atmosphere models. J Atmos Sci 43:606–632

Hirst AC (1988) Slow instabilities in tropical ocean basin-global atmosphere models. J Atmos Sci 45:830–852

Jin F-F (1997) An equatorial ocean recharge paradigm for ENSO. Part I: Conceptual mode. J Atmos Sci 54:811–829

Li T, Philander SGH (1996) On the annual cycle of the equatorial eastern Pacific. J Climate 9:2986–2998

Li T (1997) Phase transition of the El Niño-Southern oscillation: a stationary SST mode. J Atmos Sci 54:2872–2887

Li T, Wang B, Chang C-P, Zhang Y (2003) A theory for the Indian Ocean dipole-zonal mode. J Atmos Sci 60:2119–2135

Meehl GA (1997) The south Asian monsoon and the tropospheric biennial oscillation. J Clim 10:1921–1943

Meinen CS, McPhaden MJ (2000) Observations of warm water volume changes in the equatorial Pacific and their relationship to El Niño and La Niña. J Clim 13:3551–3559

Nitta T (1987) Convective activities in the tropical western Pacific and their impact on the northern hemisphere summer circulation. J Meteorol Soc Jpn 65:373–390

Philander SGH (1990) El Niño, La Niña, and the Southern oscillation. Academic Press, London, 289 pp

Philander SGH, Yamagada T, Pacanowski RC (1984) Unstable air-sea interactions in the tropics. J Atmos Sci 41:604–613

Philander SGH, Gu D, Halpern D, Lambert G, Lau NC, Li T, Pacanowski R (1996) Why the ITCZ is mostly north of the equator. J Climate 9:2958–2972

Rasmusson EM, Carpenter TH (1982) Variations in tropical sea surface temperature and surface wind fields associated with the Southern oscillation/El Niño. Mon Weather Rev 110:354–384

Saji NH, Goswami BN, Vinayachandran PN, Yamagata T (1999) A dipole mode in the tropical Indian Ocean. Nature 401:360–363

Su J, Zhang R, Li T, Rong X, Kug J, Hong C-C (2010) Amplitude asymmetry of El Niño and La Niña in the eastern equatorial Pacific. J Clim 23:605–617

Suarez MJ, Schopf PS (1988) A delayed action oscillator for ENSO. J Atmos Sci 45:3283–3287

Wallace JM, Gutzler DS (1981) Teleconnections in the geopotential height field during the northern hemisphere winter. Mon Weather Rev 109:784–812

Walker GT (1924) Correlation in seasonal variations of weather, IX: A further study of world weather. Memoires of the Indian Meteorological Department, Calcutta 24:275–332

Wang B, Wu R, Fu X (2000) Pacific–East Asian teleconnection: how does ENSO affect East Asian climate? J Clim 13:1517–1536

Webster PJ, Moore AM, Loschnigg JP, Leben RR (1999) Coupled ocean–atmosphere dynamics in the Indian Ocean during 1997–98. Nature 401:356–360

Wu B, Li T, Zhou T (2010) Asymmetry of atmospheric circulation anomalies over the western North Pacific between El Niño and La Niña. J Clim 23:4807–4822

Xiang B, Wang B, Li T (2013) A new paradigm for the predominance of standing Central Pacific warming after the late 1990s. Clim Dyn 41:327–340

Chapter 6
Monsoon Dynamics and Its Interactions with Ocean

Abstract In this chapter, the basic concept of the monsoon is introduced, followed by the discussion of monsoon variability on the quasi-biennial and lower-frequency timescales. The mechanisms responsible for the tropospheric biennial oscillation (TBO) and the monsoon – warm ocean interaction – are discussed. Next, how the ENSO affects the monsoon variability over East Asia and South Asia and how the remote and local SST anomalies affect western Pacific circulation anomalies are discussed. Finally, the physical mechanisms responsible for the in-phase and out-of-phase relationships among the Indian monsoon, western North Pacific monsoon, and Australian monsoon are discussed.

6.1 Introduction

The original meaning of the monsoon was derived from an Arabic word for season. The monsoon is characterized by the seasonal reversal of prevailing wind direction. Figure 6.1 shows large-scale surface wind and pressure patterns in northern winter and summer. In northern winter, the southern hemisphere surface receives more shortwave radiation. As a result, high pressure controls the Eurasian continent, and there is an anticyclonic flow around the continent due to the rotation of Earth. Southward cross-equatorial flows converge onto the ITCZ south of the equator over the Indian Ocean and the Australian monsoon region. In northern summer, the surface pressure and wind in general reverse sign, with low-pressure center and cyclonic flow located over the Eurasian continent and northward cross-equatorial wind over the Indo-western Pacific sector. Thus, the seasonal change of land–ocean thermal contrast in response to solar forcing is a major driver for the generation of the monsoon. Because Eurasia contains the largest land mass and the highest mountains in the world, Asian monsoon becomes the most powerful monsoon system in the Earth.

The classic definition of the monsoon was based on the reversal of the seasonal wind, but such a definition may include high-latitude regions. Thus, it is proper to consider the seasonal change of rainfall. In addition to land–ocean thermal contrast, the monsoon can be also driven by hemispheric asymmetric SST gradient. In this regard, a concept of oceanic monsoon is introduced, to differentiate it from the classic "continent monsoon." Furthermore, due to the thermal forcing of the

T. Li, P.-c. Hsu, *Fundamentals of Tropical Climate Dynamics*,
Springer Atmospheric Sciences, DOI 10.1007/978-3-319-59597-9_6

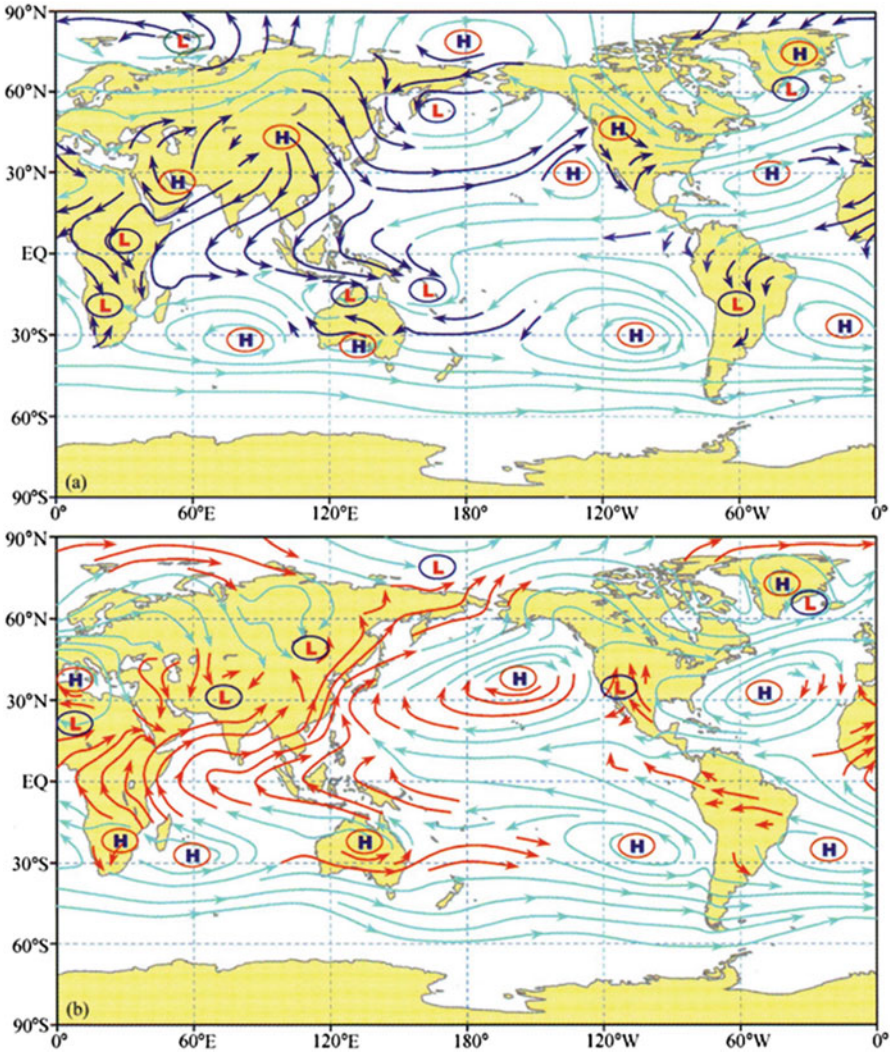

Fig. 6.1 Schematic of global surface pressure and wind patterns in northern winter (DJF) and northern summer season (JJA)

Tibetan Plateau, the monsoonal flow can penetrate into mid-latitudes. In this regard, a new concept of subtropical monsoon is introduced.

Base on the above consideration, the Asian monsoon system is further separated into three subcomponents, namely, Indian monsoon (IM), East Asian monsoon (EAM), and western North Pacific monsoon (WNPM). Figure 6.2a shows the domain of the three sub-monsoon systems (Wang et al. 2003a, b) based on the characteristics of summer–winter precipitation and low-level wind difference fields. As seen from this figure, IM is characterized by lower-level westerlies and

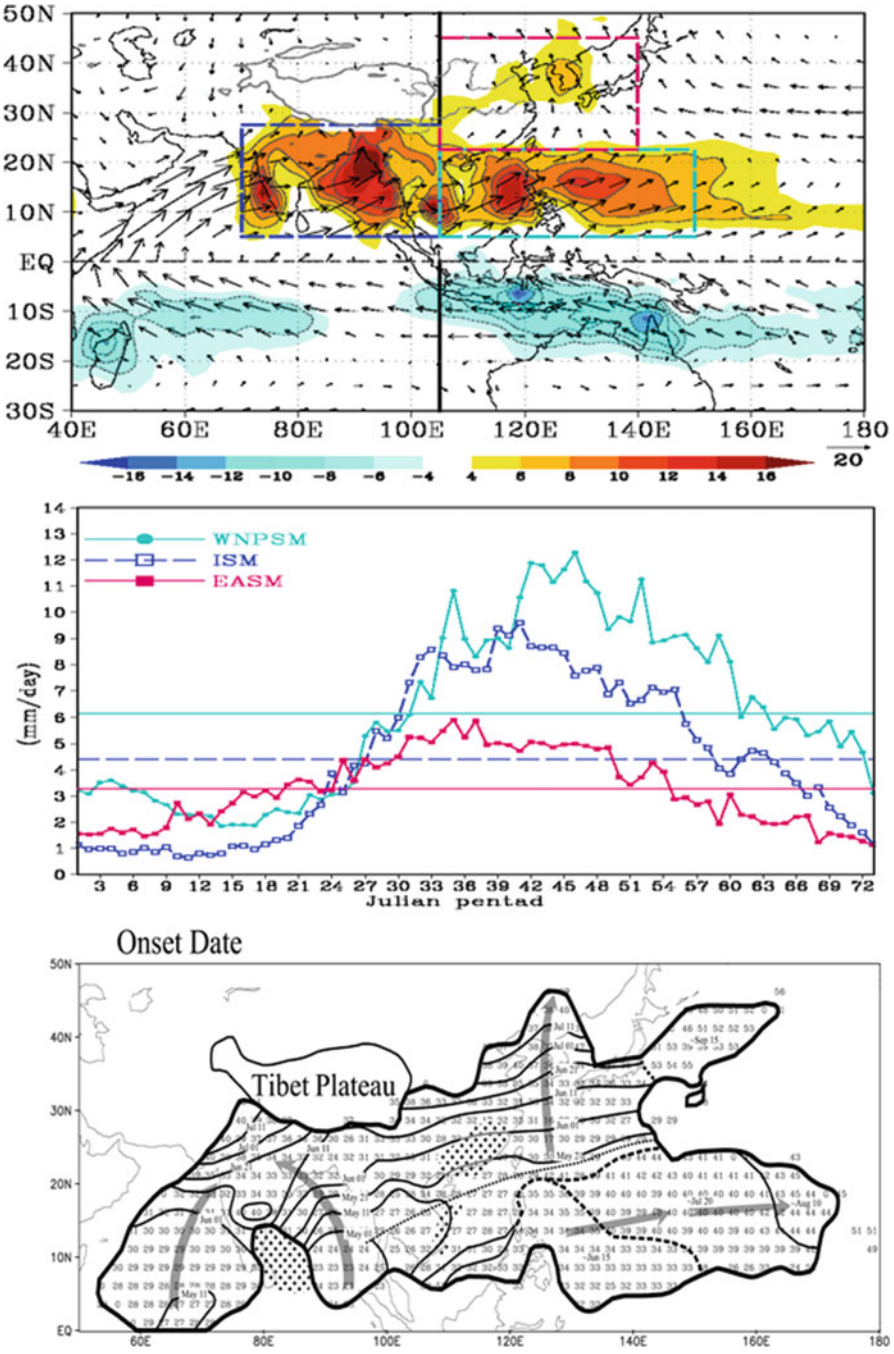

Fig. 6.2 The domain of IM, WNPM, and EAM and rainfall (shading) and 850-hPa wind (vector) difference fields between July–August and January–February (*top panel*, from Wang et al. 2003a), the climatological pended rainfall evolution averaged over the IM, WNPM, and EAM boxes (*middle panel*, from Wang et al. 2003a) (Copyright © 2003 Elsevier B. V. All rights reserved). (*Bottom*) climatological onset date for the Asian monsoon region (From Wang and LinHo (2002). © Copyright 2002 American Meteorological Society (AMS))

upper-level easterlies, being in a thermal wind relation with a north–south thermal contrast between the heated Asian land and cool Indian Ocean, while EAM has pronounced lower-level southerlies in association with the east–west thermal contrast between the Asian continent and mid-latitude Pacific Ocean. Whereas IM and EAM are typical continental monsoons driven by land–ocean thermal contrast, WNPM is an oceanic monsoon driven primarily by hemispheric asymmetric SST gradients.

Figure 6.2b shows climatological annual rainfall evolution averaged over the three equal-area boxes. The strength of the three sub-monsoon systems is distinctive, with greatest (least) total rainfall amounts occurring in the WNPM (EAM) region. The time evolution of the Asian monsoon has distinctive regional characteristics (Fig. 6.2c). The convection first develops over the Bay of Bengal (BOB) in late April. After that, the monsoon is triggered over the South China Sea (SCS) and then moves northward to East Asia. EAM is normally referred to as a subtropical monsoon encompassing eastern China, Japan, Korea, and adjacent marginal seas and monsoon oceans, i.e., the area between 20° and 45°N and from 100° to 140°E. The major rain-producing system is the monsoon subtropical front, which is also known as Meiyu or Baiu front during early summer when it is located along the Yangtze River valley extending to southern Japan. The Meiyu is preceded by the onset of the SCS summer monsoon, which, on average, occurs in mid-May when heavy convective rainfall suddenly develops over the northern SCS and westerly flows control the central SCS (e.g., Wang and Wu 1997; Xie et al. 1998; Lau and Wu 2001). The SCS onset is first followed by an establishment of a rainband over the northwest flank of the WNP subtropical high extending from the southern coast of China, to Taiwan, to east of Okinawa. Around June 10, the EAM front and associated rainband move rapidly northward to the Yangtze River valley and southern Japan, where continuous rain and cloudiness last for about a month. In mid-July the rain belt further advances northward to northern and northeast China. In late August, the EASM begins to withdraw southward in northern China. The sub-seasonal stepwise progression of the EAM rainband is one of the features distinctive from IM. During the IM period, the convective rainband gradually moves northward from BOB and Arabian Sea from early May to July. WNPM, on the other hand, is characterized by the eastward propagation of convective rainbands from middle May to August.

In addition to a remarkable annual cycle, the Asian monsoon also exhibits a strong intraseasonal oscillation (ISO) in both rainfall and circulation fields. ISO was first detected by Madden and Julian (1971), who found a significant period of 40–50 days in the zonal wind field over the Canton Island. Later they further found that this oscillation is of global scale and is characterized primarily by equatorial eastward propagation with a zonal wave number-one structure (Madden and Julian 1972). While the eastward propagating ISO mode is primarily observed in boreal winter, ISO in boreal summer is dominated by northward propagation in the Asian monsoon region. In Chap. 3 we discuss the physical mechanisms responsible for the northward propagation. The northward propagation is primarily found

over northern Indian Ocean and South China Sea regions, while the westward propagation of ISO is found in the off-equatorial tropical western North Pacific.

Observations show that the intraseasonal variation of the rainfall over the South Asian monsoon region is closely linked to the northward propagation of BSISO. Figure 6.3 illustrates the total variance of the boreal summer ISO (BSISO) over a 20-year period and area-averaged rainfall evolution over Indian subcontinent in 2004. It is worth noting that the amplitude of the intraseasonal rainfall variation over the Indian monsoon region is comparable to that of the annual cycle. This indicates that even within the monsoon season, rainfall change can be quite large. From May to October 2004, Indian rainfall experienced six major active phases, and each phase or peak corresponds well to a northward-propagating ISO. Given such a close relationship, forecasting the active and break phase of the Indian monsoon becomes possible, as long as that the model is able to capture the northward-propagation of ISO.

Besides the strong intraseasonal variability, the Asian monsoon also experiences a significant year-to-year change. Among many factors, El Niño–Southern Oscillation (ENSO) has been considered as a major forcing factor that regulates the interannual monsoon rainfall variability. Walker (1923, 1924) first recognized the effect of the Southern Oscillation on IM. Since then, a number of studies have been conducted to elucidate the monsoon–ENSO relationship (e.g., Yasunari 1990; Webster and Yang 1992; Ju and Slingo 1995; Lau and Yang 1996; see Webster et al. 1998 for a review). IM tends to have a simultaneous negative correlation with the eastern Pacific SST. The physical process through which ENSO impacts the IM is through the modulation of convective heating over the Maritime Continent (MC), which further induces low-level anticyclonic circulation to its northwest as a Rossby wave response (Gill 1982). The summer mean flow (e.g., easterly vertical shear) further modulates this anomalous Rossby wave response (Wang et al. 2003a, b). In addition to the external forcing from ENSO, monsoon–ocean interaction itself in the warm pool may support a natural quasi-biennial mode, and this mode is named as the tropospheric biennial oscillation (TBO). In the subsequent sections, we will first introduce TBO, followed by the monsoon–ENSO interaction.

6.2 Theories on Tropospheric Biennial Oscillation (TBO)

Observed all-Indian rainfall time series (climatological mean removed) shows a clear quasi-biennial signal (Fig. 6.4a). Surprisingly, such a rainfall fluctuation is highly correlated to ocean subsurface temperature change thousands of miles away in the equatorial western Pacific. This observed relationship implies that active ocean–atmosphere interactions that happen in the vast are of the warm pool on the quasi-biennial timescale. Figure 6.4b illustrates the power spectrum of the all-Indian rainfall index during 1949–1998. Note that different from the Niño 3 index that has a maximum power-spectrum peak at 3–4 years, the monsoon

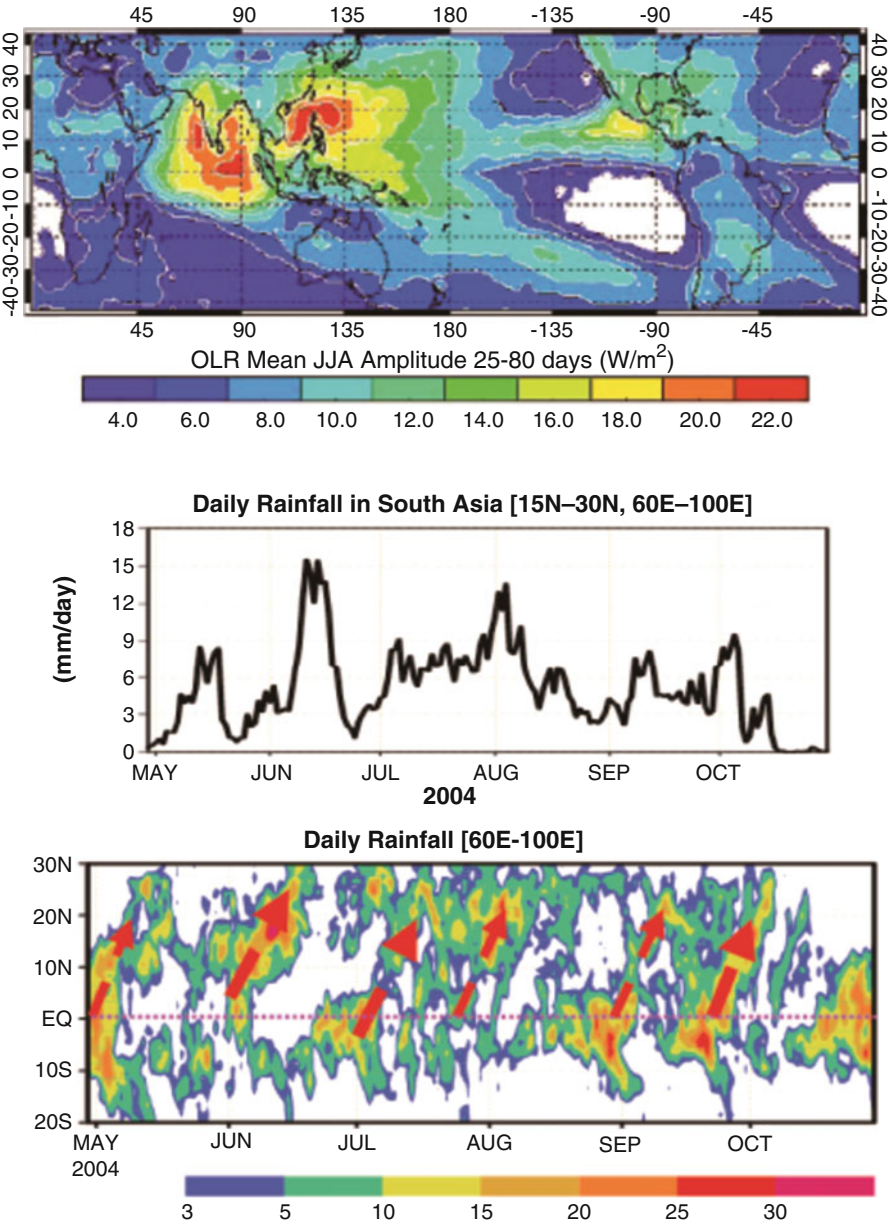

Fig. 6.3 Standard deviation of 25–80-day filtered OLR fields for the period of 1981–2002 (*top panel*), time evolution of 2004 daily rainfall averaged over South Asia (15°–30°N, 60°–100°E) (*middle panel*), and the latitude-time section of the 2004 daily rainfall along 60°–100°E (*bottom panel*)

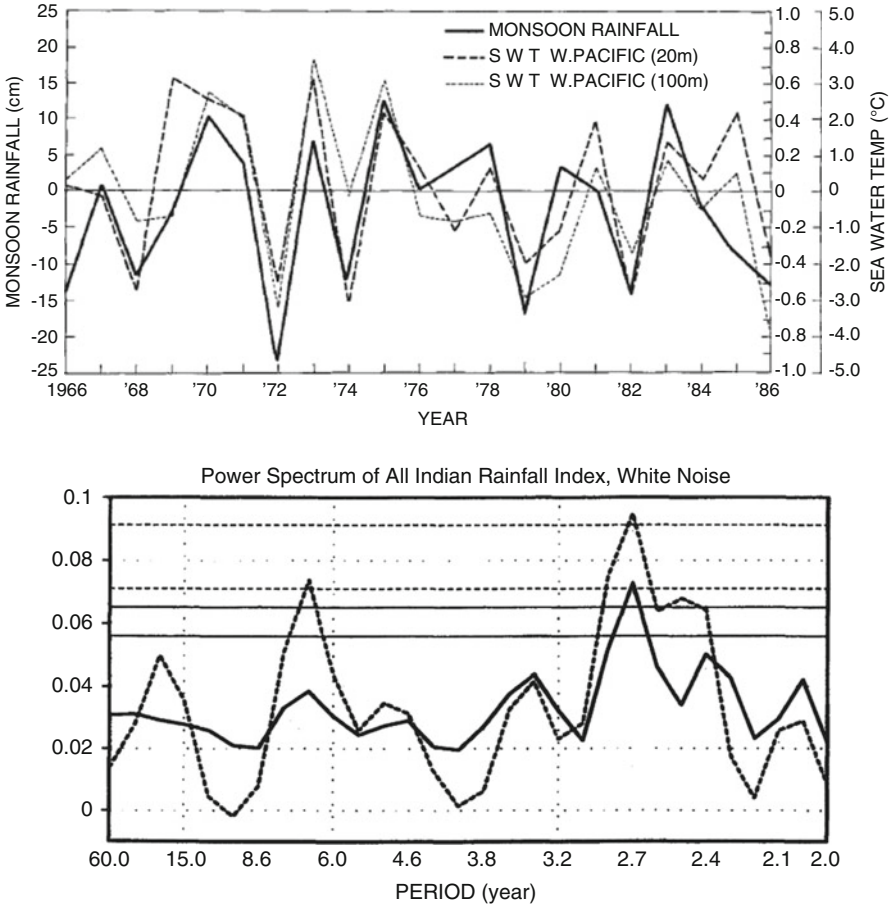

Fig. 6.4 (*Top*) Time series of anomalous all-Indian rainfall and ocean temperature anomalies at 20-m and 100-m depth over equatorial western Pacific (From Yasunari 1990). (*Bottom*) Power spectrum of all-Indian rainfall index during 1949–1998 (From Li et al. 2001. © Copyright 2001 American Meteorological Society (AMS))

exhibits a strongest peak at the quasi-biennial (2–3 years) period. The observational facts above indicate the quasi-biennial nature of the monsoon.

The tendency of the rainfall anomaly to "flip-flop" in successive years is referred to as the tropospheric biennial oscillation (TBO, Meehl 1994, 1997). Observations show that TBO is manifested over various monsoon regions such as Indonesia/Northern Australia (Nicholls 1978; Yasunari and Suppiah 1988), East Asia/WNP (Lau and Sheu 1988; Tian and Yasunari 1992; Shen and Lau 1995; Chang et al. 2000a, b; Wang and Li 2004; Li and Wang 2005), and India (Mooley and Parthasarathy 1984; Meehl 1987; Rasmusson et al. 1990; Yasunari 1990, 1991).

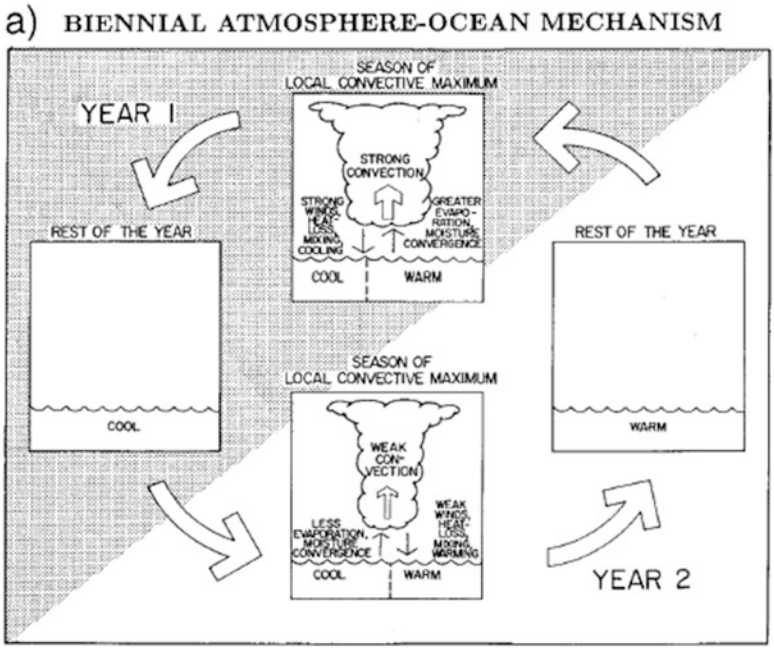

Fig. 6.5 A schematic diagram illustrating a local atmosphere–ocean interaction mechanism for generating a biennial oscillation (From Meehl (1993). © Copyright 1993 American Meteorological Society (AMS))

Why does the monsoon favor the quasi-biennial variability? So far three theories have been put forward in an attempt to understand the origin of the TBO. The first theory emphasizes local air–sea interaction (Nicholls 1978; Meehl 1987). Figure 6.5 is a schematic diagram illustrating essential processes responsible for the TBO. Because of circular argument, one may start from any time point. Suppose we start from a strong monsoon season. Due to strengthened monsoon, surface wind and convective clouds are both enhanced. This leads to enhanced surface evaporation and reduced shortwave radiation into the ocean. Thus, the ocean surface cools. Assume the cooling of the ocean can last for three seasons till the onset of the next monsoon due to long ocean memory. The cooler ocean next summer would lead to a weaker monsoon. The weakened monsoon leads to weakened surface wind and less clouds, which can warm the ocean through reduced surface evaporation and enhanced downward shortwave radiation. The warming may last three inactive seasons to impact the monsoon intensity in the following year. Through this local air–sea feedback process, a biennial oscillation is generated.

The second theory involves inter-basin teleconnection between tropical Indian Ocean and western Pacific and Indian and Australian monsoon interaction with surrounding oceans (Chang and Li 2000; Li et al. 2006). A simple five-box model was constructed, to understand the observed Indian monsoon – Australian monsoon in-phase relationship (Fig. 6.6). A warm SSTA over tropical Indian Ocean favors a

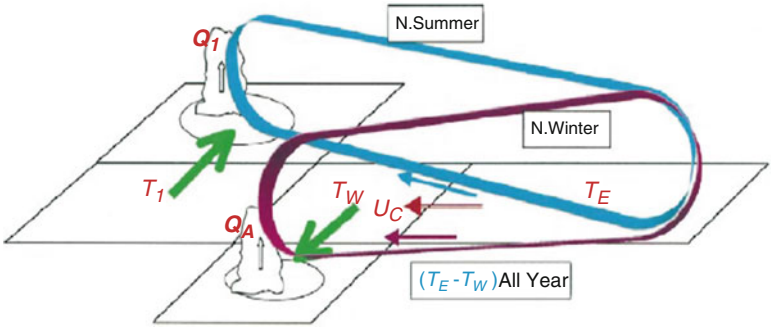

Fig. 6.6 Schematic diagram from a five-box model with T_I and $\mathbf{T_W}$ denoting SST over tropical Indian Ocean and Maritime Continent/western Pacific, Q_I and Q_A denoting heating over Indian monsoon and Australian monsoon regions, the eastern box denoting tropical eastern Pacific (From Chang and Li (2000). © Copyright 2000 American Meteorological Society (AMS))

strengthening of the Indian monsoon through enhanced moisture transport. The strengthened monsoon induces a large-scale east–west circulation and thus an easterly anomaly over the Maritime Continent, the latter of which further warms the SST in the region in the subsequent season as the anomalous wind is against the mean westerly. The SST warming over the Maritime Continent north of Australia further strengthens the Australian monsoon. The strengthened Australian monsoon induces westerly anomalies over the equatorial Indian Ocean, which may cool the ocean through both the increase of the surface evaporation (because mean wind is westerly) and cold zonal advection. The cooling of the tropical Indian Ocean would lead to the weakening of the Indian monsoon in the subsequent summer. Through this inter-basin teleconnection, a biennial oscillation is generated for both the Indian and Australian monsoon, and an enhanced Australian monsoon always follows an enhanced Indian monsoon.

To test the hypothesis that the ocean–atmosphere interactions in the monsoon/warm ocean region may lead to the TBO, Li et al. (2006) conducted idealized numerical experiments of a hybrid coupled atmosphere–ocean GCM. The atmospheric component of this hybrid coupled model is the ECHAM4 T30L19 version. The ECHAM4 has been coupled to an intermediate ocean model (Wang et al. 1995) without a heat flux correction (e.g., Fu et al. 2002, 2003). The intermediate ocean model consists of two active layers of the upper ocean, a mixed layer with variable depth, and a thermocline layer overlying an inert deep ocean (Wang et al. 1995). The latest version of the model combines the upper-ocean dynamics described in McCreary and Yu (1992) and the mixed-layer physics (Gaspar 1988). The model has a self-contained parameterization scheme for entrained water temperature that considers influences on entrained water temperature from both the thermocline displacement and the mixed-layer temperature (Wang et al. 1995). The effects of shear production, wind stirring, and buoyancy forcing are included in the vertical entrainment velocity calculation. The model has the capability of simulating

realistic annual cycle and interannual variations of SST, thermocline depth, and mixed-layer depth (Fu and Wang 2001).

To explore the role of the atmosphere–warm ocean interaction, Li et al. (2006) designed an idealized hybrid coupled GCM experiment in which the atmosphere and ocean are coupled only in the tropical IO and western Pacific (30°S–30°N, 40°E–180°E), while the climatological monthly mean SST is specified elsewhere. By doing so, we exclude the effect of the remote El Niño forcing.

After initial 10-year spin-up, the coupled model was integrated for 50 years. The long-term simulation shows that the coupled model is capable of simulating realistic annual cycle and ENSO-like interannual variability in the equatorial Pacific. The seasonal mean SST errors are in general smaller than 1 °C in the most of the ocean domain except near the coast of North Africa in boreal summer and the coast of west Australia and SCS in boreal winter.

The diagnosis of standard deviation of the total interannual (1–8-year) variability of the model SST and the relative strength of the quasi-biennial (QB, 1.5–2.5-year) component reveals that the greatest interannual SST variabilities appear in the BOB, southeast Indian Ocean (SEIO), WNP, and SPCZ, where the biennial component is also largest. The averaged ratio of the biennial SST variability in the four regions exceeds 60%, about a factor of two larger than the observed, indicating that in this model configuration without the eastern tropical Pacific, the TBO is a dominant signal. Strong TBO signals also appear in the middle-tropospheric (500 mb) vertical motion and low-level (850 mb) zonal and meridional wind components. The power spectrums of the time series of the model SST and 500 mb vertical velocity show that the TBO peaks, ranged from the period of 20–28 m, clearly appear in these spectrums, and they exceed a 95% significance level. The results suggest that the monsoon–warm ocean interaction favors a pronounced biennial variability.

To illustrate the spatial pattern and evolution characteristics of TBO in the Indo-Pacific warm ocean region, a season-sequence EOF analysis is performed for both the model and the NCEP reanalysis. Figure 6.7 illustrates the seasonal evolution of 850mb wind and 500mb vertical p-velocity fields in the model. Here, the vertical velocity has been multiplied by −1 so that a positive value in Fig. 6.7 represents an enhanced rainfall anomaly. It is noted that the model in general captures the gross structure and evolution patterns of the observed TBO in the region. For instance, in JJA(0), the circulation anomaly in the SEIO is characterized by downward motion (or suppressed convection) and anticyclonic low-level flows, while in the WNP, it is characterized by cyclonic flows and upward motion. The SEIO anticyclone is pronounced in northern fall and decays in subsequent seasons. Subsidence motion and anticyclonic flows develop over the Philippines and SCS in SON(0), and they shift slightly eastward in subsequent seasons and persist until JJA(1). The circulation anomalies in JJA(1) have an opposite polarity relative to those in the previous summer.

Since the model does not contain the ENSO mode, the model TBO arises solely from air–sea interactions in the Indo-Pacific warm ocean region. What are specific processes that give rise to the TBO variability in this region? Figure 6.8 illustrates

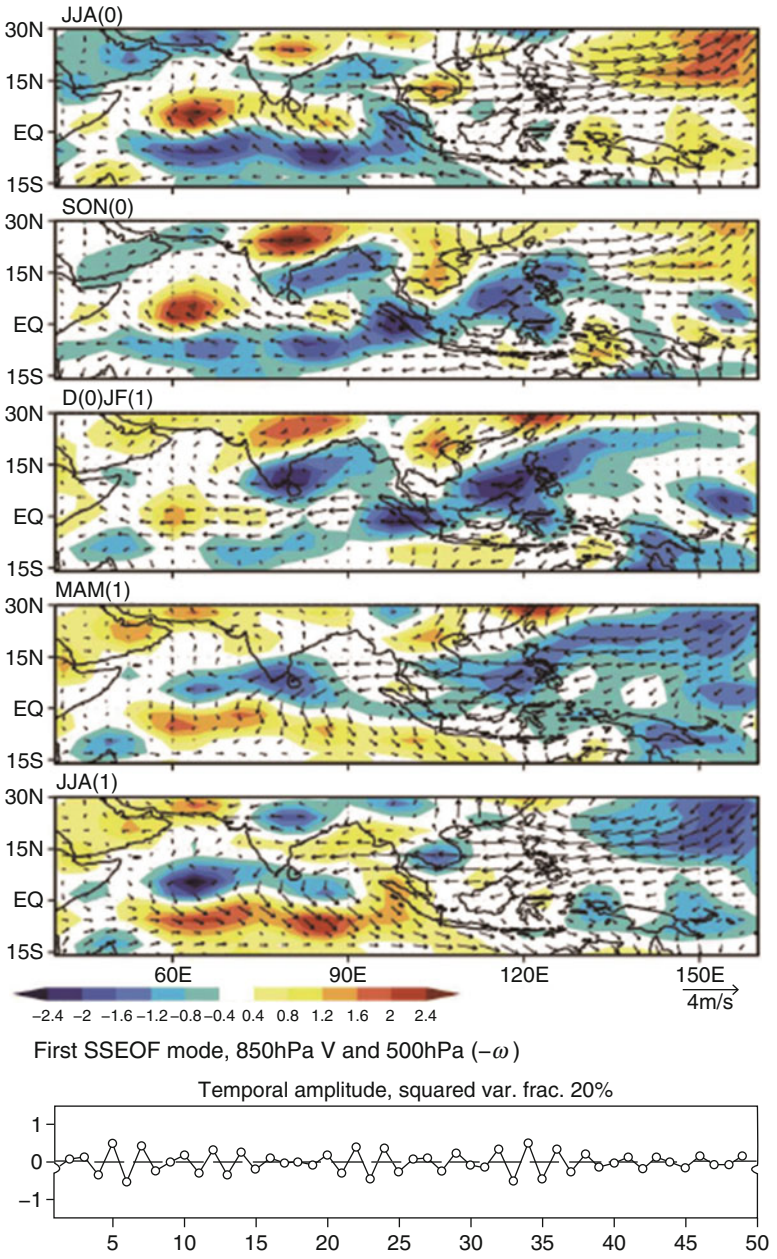

Fig. 6.7 Seasonal evolution of 500 hPa vertical p-velocity (*color shaded*; units, Pa/s) and 850 hPa wind anomaly (vector) associated with the TBO obtained from a season-sequence EOF analysis of 50-year. output of the hybrid coupled GCM (Li et al. 2006). The time coefficient of the SSEOF mode is shown in the *bottom panel*. The vertical velocity has been multiplied by −1 so that positive contours represent enhanced convection anomalies (From Li et al. (2006). © Copyright 2006 American Meteorological Society (AMS))

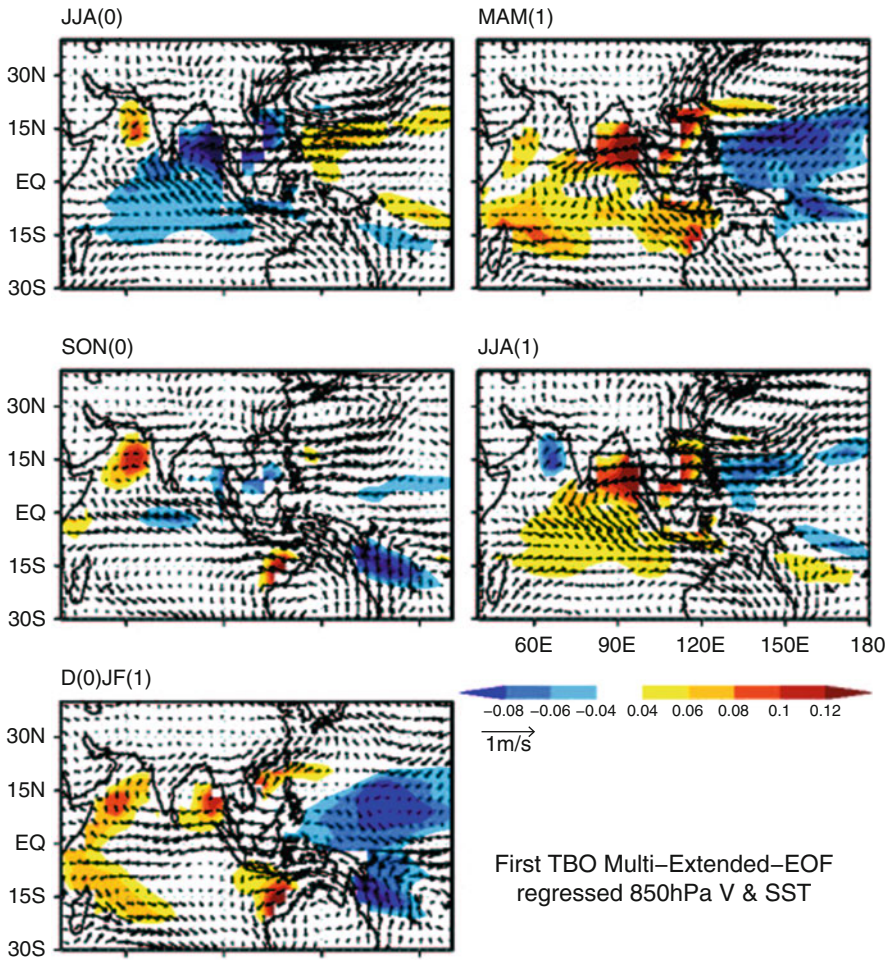

Fig. 6.8 Same as Fig. 6.7 except for the regressed SST (*shading*; unit, K) field from the hybrid coupled GCM (Form Li et al. (2006). © Copyright 2006 American Meteorological Society (AMS))

the seasonal evolution pattern of the SSTA, which is regressed based on the time coefficient of the first SS-EOF mode. A significant surface cooling occurs in JJA (0) in the eastern IO and off the Asian coast, with maximum cold SSTA appearing in BOB and SCS. While the cold SSTA decays in subsequent seasons, new cold SST anomalies develop in the western Pacific in SON(0) and DJF(1). In particular, the cold SSTA in the WNP reaches a peak in DJF(1) and persists for 2–3 seasons till the following summer, JJA(1), when the SSTA in the eastern IO and SCS has completely reversed sign from a cold to a warm anomaly.

The diagnosis of the model SST budget reveals that the cooling in the IO in JJA (0) is primarily attributed to the surface evaporation and vertical ocean mixing due to enhanced surface wind speeds, whereas the cooling in the western Pacific in SON

(0) and DJF(1) is mainly attributed to the ocean dynamic processes in response to anomalous wind stress curl (see discussions below). Based on the model circulation and SST evolution, a hypothesis is put forth to explain the TBO in the model. Assume we start from a strong WNP monsoon in JJA(0). In response to enhanced WNP monsoon heating, northward low-level cross-equatorial winds are generated. The anomalous winds enhance the seasonal mean winds, leading to increased surface evaporation and ocean vertical mixing and thus negative SSTA in the eastern IO and off the Asian coast. It is seen from Fig. 6.8 that the strongest SST cooling appears in the BOB, SCS, and MC. This SST cooling has a significant impact on the strength of the annual convective maximum that migrates to Southeast Asia in SON and MC in DJF (Meehl 1987). The so-induced suppressed convection in SCS and MC may further induce anomalous westerlies over the equatorial western Pacific through anomalous Walker circulation.

The curl of the zonal wind stress anomaly near the equator may exert a dynamic impact on SST by exciting upwelling oceanic Rossby waves and by lifting the ocean thermocline. As a result, the ocean surface cools. The diagnosis of the mixed-layer heat budget in the ocean model confirmed that the negative SST tendency in the western Pacific in SON(0) and DJF(1) is indeed attributed to the ocean dynamics terms (i.e., 3D ocean temperature advection), while the net heat flux effect is modest, particularly in DJF(1).

The cold SSTA over the WNP, once initiated by the ocean dynamics, may persist from northern winter to the following summer through the positive thermodynamic air–sea (TAS) feedback proposed by Wang et al. (2000). The persisted cold SSTA eventually leads to suppressed convection and thus a weaker WNP monsoon in JJA (1), thus completing a TBO transition from a local cyclonic circulation in JJA(0) to an anticyclone in JJA(1). The weakened WNP monsoon induces southward cross-equatorial flows, leading to anomalous ocean surface warming in the eastern IO and SCS, and thus the second half of the TBO cycle begins in this region.

Figure 6.9 is a flow chart that illustrates key physical processes that causes the TBO in the hybrid coupled GCM. Starting from a strong WNP monsoon in boreal summer, the strong convection in the WNP causes strong northward cross-equatorial flows. The anomalous winds induce cold SSTA in the SCS, MC, and SEIO off Sumatra, leading to suppressed convection in the MC through either a local SSTA impact on the seasonal convective maximum or its effect in surface wind divergence/moisture and local Walker circulation over the IO. The suppressed convection in the MC induces anomalous westerlies in the western Pacific, which further lead to a cold SSTA in the WNP through either a direct ocean dynamic effect (via ocean Rossby waves and thermocline changes) or an indirect atmospheric effect (through the central-eastern equatorial Pacific heating and associated atmospheric Rossby wave response). The so-induced cold SSTA in the WNP persists through the TAS feedback and leads to the weakening of the WNP monsoon in the following summer. Thus, the second half cycle of the TBO begins. This confirms earlier hypotheses that the biennial component of ENSO is a part of TBO, resulting from teleconnections between the tropical Pacific and Indian Oceans.

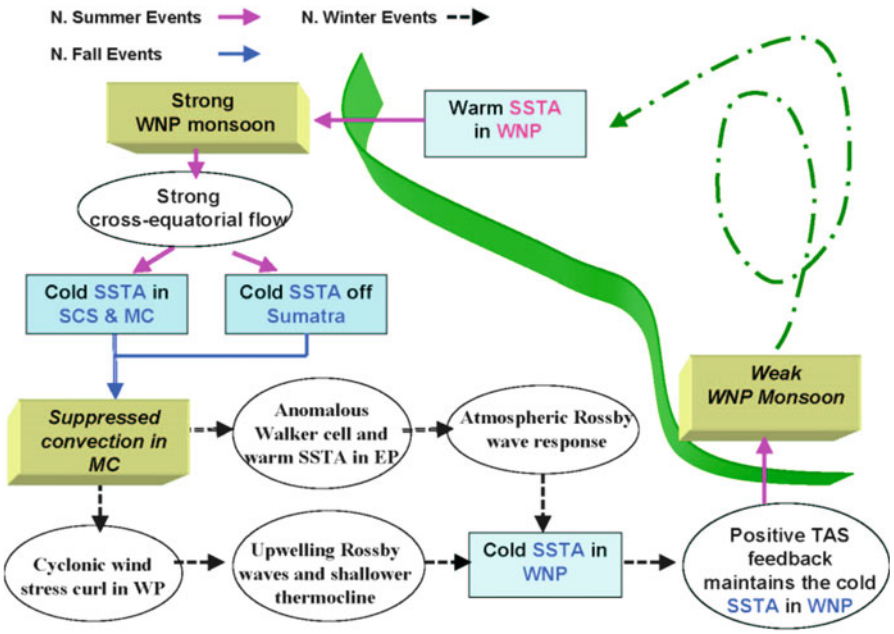

Fig. 6.9 A schematic diagram illustrating essential processes that lead to the TBO in the tropical Pacific and Indian Oceans. The *left* part of a *green ribbon* consists of a half of the TBO cycle, which starts from a strong WNP summer monsoon at year 0 and ends to a weak monsoon at year 1. The *red*, *blue*, and *black arrows* indicate, respectively, northern summer, fall, and winter events (From Li et al. (2006). © Copyright 2006 American Meteorological Society (AMS))

The third theory involves a tropical–mid-latitude interaction (Meehl 1997). Based on a model diagnosis, Meehl (1997) suggested tropical heating anomalies associated with strengthened monsoon may exert a remote forcing in mid-latitude circulation in such a way that it reduces land–ocean thermal contrast over the Asian Continent–Indian Ocean sector and promotes a weakened monsoon in the following summer. However, given the chaotic nature of mid-latitude circulation, how teleconnection patterns associated with tropical forcing can persist through a few seasons is a key issue that needs to be resolved.

6.3 Quasi-Biennial and Lower-Frequency Variability of the Monsoon

The power spectrum of the time series of the domain-averaged India rainfall reveals that on interannual timescales, there are two distinctive peaks (bottom panel of Fig. 6.4), with the quasi-biennial (QB) component [2–3 years, hereafter referred to as the monsoon QB mode or tropospheric biennial oscillation (TBO) mode] being

much greater than the lower-frequency (LF) component [3–7 years, hereafter referred to as the monsoon LF mode]. The similar two power-spectrum peaks also appeared in the first EOF mode of the global precipitation field (Lau and Sheu 1988) and in the meridional wind over the South China Sea and sea-level pressure difference between the Asian continent and Northwestern Pacific (Tomita and Yasunari 1996). Webster et al. (1998) investigated the temporal characteristics of the Indian monsoon rainfall variability by the use of a wavelet analysis and found the intermittent recurrence of the two power-spectrum peaks. The Niño 3 SST anomaly (SSTA) also has two significant spectrum peaks, but its LF component is much greater than its QB component. Natural questions that need be addressed are why the Indian monsoon has a more pronounced QB spectrum peak and what physical mechanisms are responsible for the monsoon variability on both the timescales.

In this section we discuss the physical mechanisms responsible for the QB and LF variability of the Indian monsoon rainfall by revealing the spatial and temporal structures of atmospheric circulation and SST associated with the two modes. Our strategy is first to apply a time-filtering technique to separate rainfall data into 2–3-year and 3–7-year bands, respectively. Then, by analyzing the spatial and temporal patterns of atmospheric circulation associated with the two bands, we intend to investigate physical processes responsible for the rainfall variability on the two timescales. To compare with results from the time-filtering analysis, we will also conduct a composite analysis using the original unfiltered data.

The primary data used in this study are the domain-averaged Indian rainfall; NCAR/NCEP reanalysis that includes wind, moisture, temperature, and geopotential height fields; and the Reynolds SST (Reynolds and Smith 1994) for a period of 1949–1998. The Indian rainfall is represented by an area-averaged precipitation from 26 stations reasonably distributed over the Indian subcontinent. These gauge stations are picked up from the NOAA climatological baseline station data over land, documented at NCDC, and updated from CAC global CEAS summary of day/month observations. This area-averaged rainfall has a correlation coefficient of 0.86 with the all-Indian rainfall index (Mooley and Parthasarathy 1984).

A band-pass filter (Murakami 1979) is used to separate the data into approximately 2–3-year and 3–7-year windows, respectively. These two bands represent the two significant power-spectrum peaks in the area-averaged Indian rainfall field. A lagged correlation analysis is then performed for each dataset. A composite analysis using the original unfiltered data is also carried out to crosscheck the lagged correlation analysis results obtained from the time-filtered data.

Figure 6.10 shows the lagged correlation between the Indian summer rainfall and domain-averaged SSTs in the Indian Ocean (IO, 60°–95°E and 0°–15°N), western Pacific (WP, 130°–150°E and 10°–20°N), and eastern Pacific (EP, 170°–120°W and 5°S–5°N). In the 2–3-year band (top panel), a significant positive correlation between the IO SSTA and the monsoon rainfall appears in the preceding winter and spring, with a maximum correlation coefficient exceeding 0.6, far above the 95% significance level. (The 95% level corresponds to a correlation coefficient

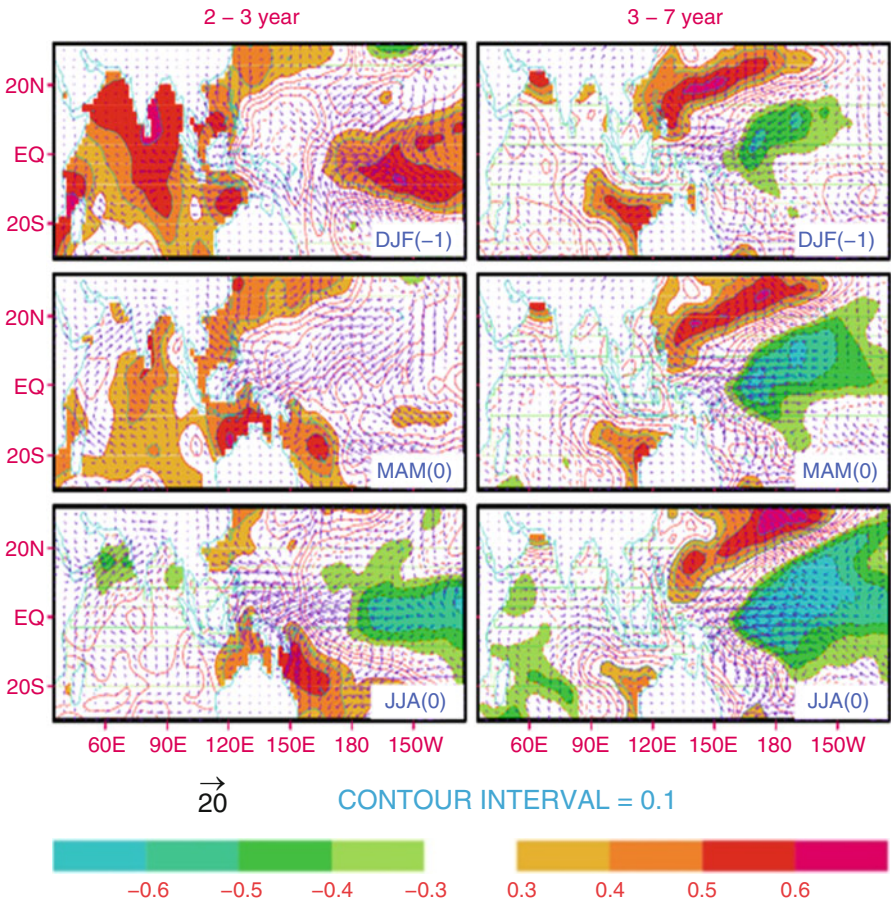

Fig. 6.10 Lagged correlation of the SSTA (*shading*) and lagged regression of 850-hPa wind with the all-Indian monsoon rainfall from the preceding winter to the concurrent summer for the 2–3-year (*left panel*) and 3–7-year (*right panel*) bands. The correlation above 0.4 corresponds to the 95% significance level or above (From Li et al. (2001). © Copyright 2001, American Geophysical Union (AGU))

of about 0.4 when taking into account the decrease of degrees of freedom due to the time filtering.) The fact that a warm IO SSTA leads to a wet monsoon implies that the IO SSTA may play an active role in affecting the Indian monsoon.

A warm SSTA in the IO in the preceding winter may result from the decrease of the prevailing northerly associated with a weak Asian winter monsoon. It is seen from Fig. 6.10 that the meridional wind at the surface is positively, lagged correlated (with a maximum correlation coefficient greater than 0.4) with the summer monsoon. This implies that a southerly wind anomaly appears over the northern IO in the preceding winter. The southerly wind anomaly can contribute to the ocean warming through (1) reduced surface evaporation (because the mean wind is

northerly in northern winter) and (2) anomalous meridional temperature advection that brings warmer water from the south. Thus, on the TBO timescale, a strong Indian summer monsoon is preceded by a weak winter Asian monsoon that is characterized by anomalous southerly over the northern IO.

Another notable feature associated with the monsoon TBO mode is the phase reversal of the EP SSTA in spring. The SST correlation coefficient changes its sign from a positive value in the preceding winter to a negative value in summer. Associated with this SSTA phase transition, the surface wind anomaly switches from westerly to easterly in the central equatorial Pacific.

In contrast to their high lagged correlation, the simultaneous correlation between the Indian monsoon and the IO SSTA is very low. This is because a strong Indian monsoon generates strong surface winds that further cool the ocean through enhanced surface evaporation and ocean mixing. As a result, the SSTA weakens rapidly in summer in the northern IO, especially along the eastern coast of Africa and in the Arabian Sea.

For the monsoon LF mode, the most significant SST correlation appears in the Pacific. While the WP SSTA has a positive, lagged correlation (+0.4) with the monsoon in the preceding winter, the EP SSTA has a simultaneous negative correlation (−0.5). The correlation with the IO SSTA is weak for all seasons prior to the monsoon onset, whereas a negative correlation appears after the monsoon onset, indicating a strong monsoon impact on the IO SSTA.

A common feature in both the 2–3-year and 3–7-year bands is that there is a strong simultaneous, negative correlation between the Indian monsoon and the EP SSTA. This points out an interactive nature of the monsoon–ENSO system. On one hand, a positive (negative) SSTA may have a remote impact on the monsoon through large-scale vertical overturning (Meehl 1987). On the other hand, anomalous monsoon heating may alter the EP SST through the change of winds over the central and western Pacific (Chang and Li 2001).

To examine the effect of anomalous moisture transport, we composite the 1000 hPa moisture flux convergence field based on the NCEP/NCAR reanalysis data. Ten wettest and ten driest years are selected based on the filtered monsoon rainfall data for both bands. From wet-minus-dry composites, one can see that in the 2–3-year band, there is significant low-level moisture convergence over the Indian subcontinent in the preceding winter and spring. In the 3–7-year band, the anomalous moisture flux convergence is quite different – no significant moisture convergence appears in the Indian subcontinent.

The Walker circulation is regarded as an important agent that links the Pacific Ocean to the Asian monsoon. Since the vertical motion in the mid-troposphere is related to upper and lower tropospheric divergent flows, we use the velocity potential difference (VPD) between 850 and 200 hPa to represent the vertical overturning cell of the Walker circulation. A positive (negative) VPD center corresponds to a strong ascending (descending) motion. Figure 6.11 illustrates the composite VPD field for the 3–7 year bands. A similar feature in both bands is that in summer (JJA), the Walker circulation is characterized by a strong ascending (descending) branch over the monsoon (EP) region. However, the evolution of the

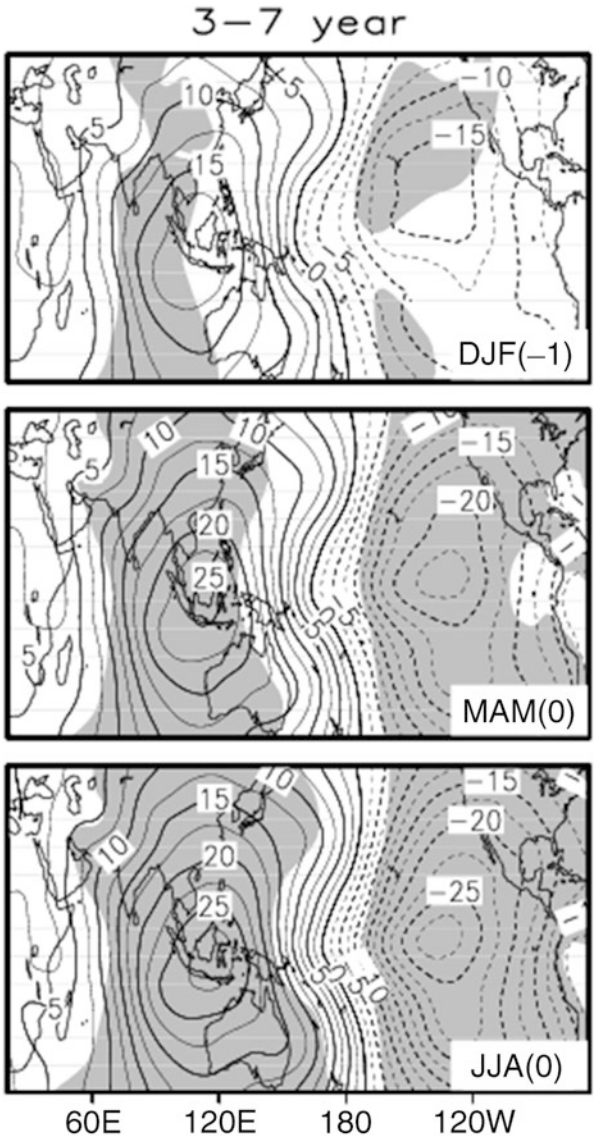

Fig. 6.11 Wet-minus-dry composites of the velocity potential difference (850 hPa minus 200 hPa) field in DJF (−1), MAM (0), and JJA (0) for the 3–7-year bands. The shaded regions represent the statistical significance of 95% and above

Walker cell in the two bands is quite different. For the LF mode, the ascending and descending branches are almost stationary, whereas for the QB mode, there is slow eastward propagation of the ascending and descending branches. This temporal evolution feature is somewhat similar to that found by Barnett (1991). Another feature in the 2–3 year band is that even though there is a remote SSTA forcing in the EP in winter, an ascending branch appears in the equatorial IO. This ascending motion results from the direct impact of the warm SSTA in the IO, which

compensates the effect of the El Niño in the EP. Thus, in addition to its moisture effect, the IO SSTA may have a dynamic impact on the vertical overturning of the Walker cell.

The land–ocean thermal contrast between the Asian continent and Indian Ocean was regarded as a good indication of the monsoon strength (e.g., Li and Yanai 1996; Yang et al. 1996). To examine the role of the land–ocean thermal contrast on the monsoon variability, we calculated the lagged correlation between the monsoon rainfall and the mean (between 200 and 500 hPa) tropospheric temperature. Figure 6.12 shows the lagged correlation maps. At the 2–3-year window (left panel), the increase of the tropospheric mean temperature is concurrent with the warming of the SST in the IO in the preceding winter and spring, while no significant temperature changes are found over the Eurasian continent. At the 3–7-year window (right panel of Fig. 6.12), a significant warming of the tropospheric mean temperature appears over the subtropical Eurasian continent in the preceding winter, with the correlation coefficient greater than 0.7. Meanwhile, a negative correlation center is located over the western equatorial IO. This north–south thermal contrast is even enhanced in northern spring and is significantly correlated with the summer monsoon rainfall. The physical processes that give rise to such a land–ocean thermal contrast are not clear, although several investigators (e.g., Meehl 1997; Yang and Lau 1998) have hypothesized that it might result from remote SST forcing in the tropics. The establishment of the meridional temperature gradient in the preceding season may help to set up the monsoon southwesterly earlier and stronger.

The time-filtering analysis above shows that the monsoon QB and LF modes have distinctive spatial and temporal structures. For the QB mode, a positive SSTA in the IO leads to a wet monsoon and the SSTA in the EP changes its phase in spring, whereas for the LF mode, a cold SSTA in the EP persists from winter to summer and is associated with a wet monsoon.

The time-filtering analysis indicates that the Indian monsoon rainfall is significantly correlated with the IO SSTA in the preceding winter and spring on the TBO timescale. A natural question is through what process the IO SSTA in the preceding seasons influences the monsoon. The IO SSTA may influence the Indian monsoon via both dynamic and thermodynamic effects. The dynamic impact is through induced upward motion in the monsoon sector that may compensate the effect of El Niño forcing from the EP. The thermodynamic impact is through the moisture effect. We argue that a warm SSTA can increase local moisture over the ocean through enhanced surface evaporation. The overall increase of specific humidity over the Indian Ocean is a good precondition for a strong monsoon, because after the monsoon onset, the southwesterly flows would transport these excess moistures into the monsoon region. A strong monsoon enhances surface winds that cool the ocean through surface evaporation and ocean mixing, resulting in a colder than normal IO SSTA that further reduces the moisture accumulation and leads to a weak monsoon next year.

In addition to the IO SST, the low-level moisture convergence in the preceding spring is significantly correlated with the monsoon on the TBO timescale. We argue

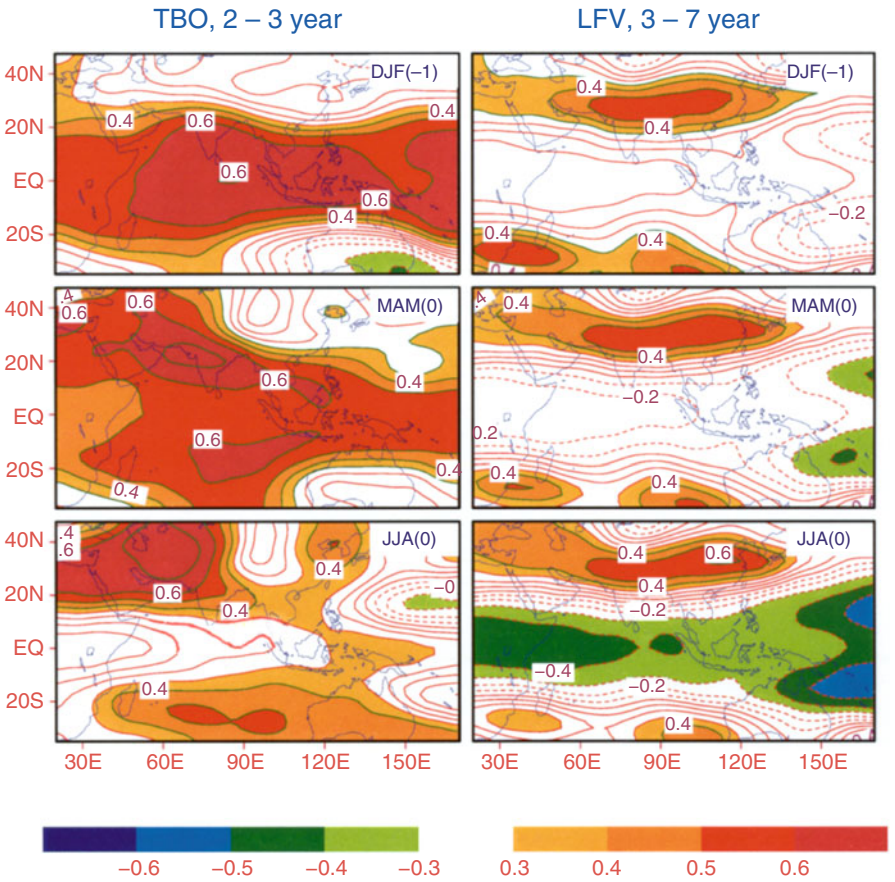

Fig. 6.12 Lagged correlation maps between the all-Indian monsoon rainfall and the mean tropospheric (200–500 hPa) temperature in DJF(−1), MAM(0), and JJA(0) for the 2–3-year and 3–7-year bands (contour interval, 0.1). The regions where the positive (negative) correlation exceeds 0.3 are heavily (lightly) shaded. The statistical significance exceeds the 95% level when the correlation is above 0.4 (From Li et al. (2001). © Copyright 2001, American Geophysical Union (AGU))

that the anomalous moisture convergence may influence the monsoon through the accumulation of local moisture. As we know, during the dry seasons, the local atmosphere over India is in a convectively stable regime. Because of that, the convergent water vapor prior to the monsoon onset can be used only for moistening the local air. The increase of local humidity may initially help strengthen the monsoon intensity, which may further induce anomalous southwesterly flows during the monsoon season and help to bring more moistures from the tropical ocean. Note that this anomalous moisture convergence mechanism differs from the effect of the IO SSTA. The former is associated with the moisture flux by

anomalous winds, whereas the latter is related to anomalous moisture advection by the mean monsoon flow.

While the monsoon TBO is primarily controlled by local processes, the monsoon LF variability might be due to the remote forcing of the SSTA in the Pacific. We argue that three possible processes may contribute to the rainfall anomaly on the lower-frequency timescale. The first is the direct impact of the EP SSTA through the vertical overturning of the large-scale east–west circulation (e.g., Meehl 1987). This mechanism can be readily seen from the wet-minus-dry composites of the velocity potential difference field (Fig. 6.11). The second is the effect of the anomalous SST in the WP. Associated with a cold SSTA in the equatorial EP, a positive SSTA appears in the WP. This warm SSTA may further affect local convective activity and induce anomalous lower tropospheric circulation off the Philippines (Tomita and Yasunari 1993). It is speculated that the enhanced convective activity in the WP may increase the frequency or intensity of the northwestward-propagating synoptic-scale disturbances and thus enhances the monsoon trough from the equatorial WP to the Indian subcontinent. The third process is attributed to the impact of the remote tropical SSTA forcing on the mid-latitude atmospheric circulation. The wet-minus-dry mean tropospheric temperature composite shows that 3–6 months prior to a wet monsoon, a north–south thermal contrast has already been established across South Asia and the IO, with the warm core centered over the Tibetan Plateau. The location of this warm core is consistent with the hypotheses that Tibetan heating and/or Eurasian snow cover prior to the monsoon onset play an important role in the strength of the monsoon (e.g., Mooley and Shukla 1987; Yanai et al. 1992). This differs markedly from the monsoon TBO mode, in which the Indian subcontinent and the IO are both covered by an elongated warm anomaly belt in the preceding winter and spring. Thus, an enhanced (reduced) land–ocean thermal contrast precedes a strong (weak) monsoon on the lower-frequency timescale but not on the TBO timescale.

6.4 Pacific–East Asia Teleconnection

Observational analyses indicate that while IM is primarily influenced by ENSO during its developing phase, the interannual variability of EAM is highly correlated with ENSO during its decaying phase. In the summer after an El Niño, the Meiyu/Baiu rainfall tends to be abundant (Huang and Wu 1989, Wang and Li 1990, Zhang et al. 1996; Lau and Yang 1996; Soman and Slingo 1997; Kawamura 1998), even though during that season, SST in the eastern equatorial Pacific is nearly normal (Fig. 6.13). Why does the ENSO have a delayed impact on the EAM?

To address this question, one must first reveal dominant seasonal evolving circulation patterns in the monsoon sector in association with the developing and decaying phases of ENSO. A season-sequence singular vector decomposition (SS-SVD) analysis method is applied, following Wang et al. (2003a, b). Figure 6.14 displays the evolution of anomalous 850 hPa winds and vertical p-velocity

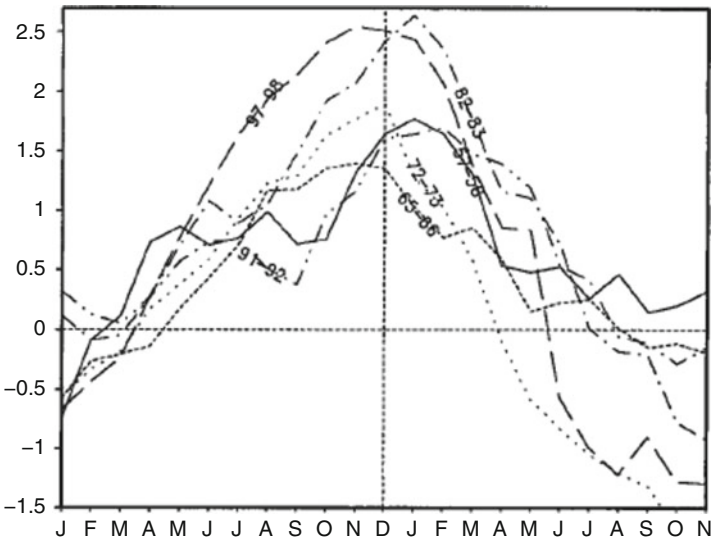

Fig. 6.13 Time evolution of Niño 3.4 SSTA for individual El Niño events during 1956–2000 (From Wang et al. (2000). © Copyright 2000 American Meteorological Society (AMS))

associated with ENSO turnabout revealed by the first SS-SVD mode. This mode describes 91% of the total covariance between the SST anomalies in the tropical Pacific and Indian Oceans (40°E–90°W, 20°S–20°N) and five seasonal mean 850 hPa wind anomalies.

During the summer when the El Niño develops, the low-level circulation anomalies are dominated by an elongated anticyclonic ridge extending from the Maritime Continent to the southern tip of the India. Associated with this anticyclonic ridge is a tilted belt of pronounced anomalous westerlies extending from the Bay of Bengal to the WNP, suppressed convection over the Maritime Continent, and enhanced convection over the Philippine Sea (Fig. 6.14a). The enhanced WNP monsoon trough greatly increases the number of tropical storm formation in the southeast quadrant of the tropical WNP (5°–17°N, 140°–170°E) (Chen et al. 1998; Wang and Chan 2002). On the other hand, the weak anticyclonic anomalies over India imply a moderately deficient ISM.

During the fall of El Niño developing year, the southern Indian Ocean (SIO) anticyclone grows explosively, leading to a giant anticyclonic ridge dominating the Indian Ocean with the anticyclone center at 10°S, 90°E, a tilted ridge extending from western Australia all the way to the Arabian Sea (Fig. 6.14b). Note that a new anomalous low-level anticyclone starts to form in the vicinity of Philippines.

In the mature phase of El Niño, D(0)/JF(1), the low-level circulation anomalies are dominated by two subtropical anticyclonic systems located in the SIO and the WNP, respectively (Fig. 6.14c). The former is a result of the weakening and eastward retreat of the SIO anticyclone from boreal fall, while the latter results

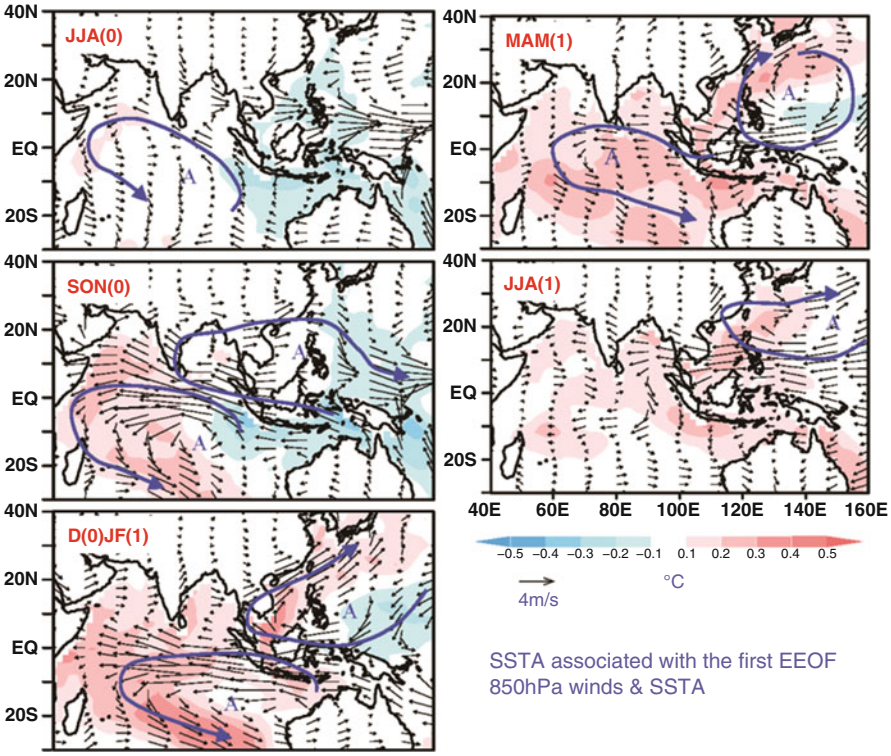

Fig. 6.14 Seasonal evolving patterns of 850-hPa wind (vector) and SST (*shading*) anomalies associated with El Niño turnabout from the developing summer, JJA(0), to the decaying summer, JJA(1), calculated based on the SS-SVD analysis (From Wang et al. (2003b). © Copyright 2003 American Meteorological Society (AMS))

from the amplification and eastward migration of the Philippine anticyclone. The most suppressed convection centered east of Philippine.

MAM(1) and JJA(1) have similar anomaly patterns, which are characterized by the pronounced WNP anomalous anticyclone (Fig. 6.14d and e). The intensity of the WNP anticyclone, however, decreases toward JJA(1). By summer JJA(1), subsidence controls the Philippine Sea and Southeast Asia, signifying weakening of the summer monsoon over the WNP and South Asia. The anomaly pattern exhibits nearly opposing polarities with that in the summer of the previous year, indicating a strong biennial tendency associated with the El Niño turnabout.

The most interesting feature of the seasonal evolving monsoon patterns in Fig. 6.14 is the persistence of the anomalous anticyclone in WNP from the El Niño peak winter to the subsequent summer. It is the anomalous anticyclone in JJA (1) that leads to enhanced rainfall in the Meiyu region through enhanced pressure gradients and moisture transport (Chang et al. 2000a, b). As the atmosphere itself does not hold a long memory, the persistence of the anomalous Philippine Sea

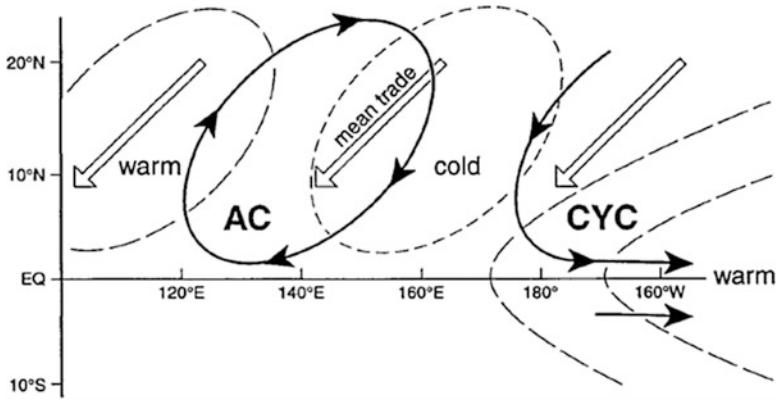

Fig. 6.15 A schematic diagram illustrating the effect of a positive air–sea feedback between the PSAC and cold SSTA in WNP. The *double arrow* denotes the background mean trade wind, and heavy lines with *black arrows* represent the anomalous wind. The long (short) *dashed lines* represent a positive (negative) SSTA (From Wang et al. (2000). © Copyright 2000 American Meteorological Society (AMS))

anticyclone (PSAC) from the boreal winter to summer calls for a dynamic explanation.

The process through which ENSO has a delayed impact on the EAM was illustrated by Wang et al. (2000) (see a schematic diagram in Fig. 6.15). The essential part of the proposed mechanism lies in a local positive air–sea feedback between atmospheric descending Rossby waves and the underlying cold SST anomaly in WNP that maintains the anomalous PSAC from the mature El Niño to the ensuing summer. This positive feedback, operated in the presence of background northeasterly trade winds, may be described as follows: to the east of the anomalous PSAC, the increased total wind speed cools the ocean surface where it induces excessive evaporation and entrainment. The cooling, in turn, suppresses convection and reduces latent heating in the atmosphere, which excites descending atmospheric Rossby waves that reinforce the PSAC in their decaying journey to the west. The initial triggering of the cold SSTA may be attributed to the atmospheric Rossby wave responses to the central equatorial Pacific heating during the El Niño peak winter – the so-induced anomalous flows coincide with the background mean wind and lead to enhanced evaporation and thus the cooling of the local ocean surface. The initial triggering of an anomalous PSAC may arise from the cold surge intrusion from the Asian continent (Wang and Zhang 2002) or the eastward propagation of a low-level anticyclone from the tropical Indian Ocean (Chen et al. 2007).

In contrast to its weakening in the El Niño decaying summer, the WNPM tends to strengthen in the El Niño developing summer (Fig. 6.14). The possible cause of this enhancement during the El Niño developing phase is as follows: First, it is attributed to the increases of low-level cyclonic vorticity associated with equatorial westerly anomalies. Secondly, in response to El Niño forcing, convection over the

Maritime Continent is suppressed. The suppressed convection leads to an equatorial-asymmetric atmospheric Rossby wave response in the presence of the asymmetry of easterly shear of the summer mean zonal flow (Wang et al. 2003b). Thus, a strong anticyclonic cell appears north of the equator, with an anomalous ridge tilted northwestward toward the Indian subcontinent. This leads dry monsoon over India. Meanwhile, the anomalous anticyclonic flow enhances low-level westerlies and thus convective activities over the WNP. This explains the observed negative correlation between the interannual anomalies of the IM and WNPM.

6.5 Effects of Indian Ocean and WNP SSTA on Circulation in WNP

6.5.1 Season-Dependent Indian Ocean SSTA Forcing Effect

Figure 6.16 shows the composite anomalous atmospheric circulation and SST fields associated with El Niño composite from El Niño mature winter (DJF) to the subsequent summer (JJA) during 1950–2006. Note that an anomalous anticyclone persists in the tropical WNP from El Niño mature winter to the subsequent summer. It is this anomalous anticyclone that causes devastating rainfall in central China during the El Niño decaying summer.

What maintains the anomalous anticyclone from the winter to summer? The positive thermodynamic air–sea interaction mechanism illustrated by Fig. 6.15 may

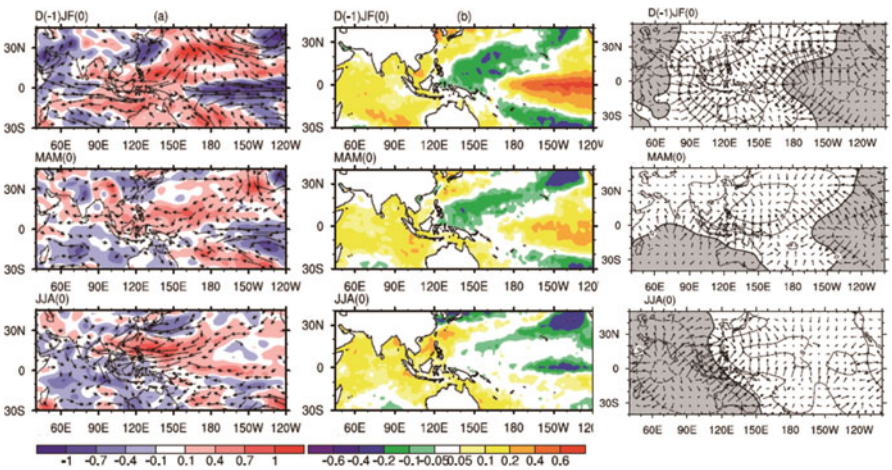

Fig. 6.16 Seasonal evolution patterns of (*left*) anomalous 850 hPa wind (vector) and 500 hPa vertical p-velocity, (*middle*) SST and (*right*) 200 hPa velocity potential fields derived from 12 El Niño composite from El Niño mature winter to the subsequent summer during 1950–2006 (From Wu et al. (2009). © Copyright 2009 American Meteorological Society (AMS))

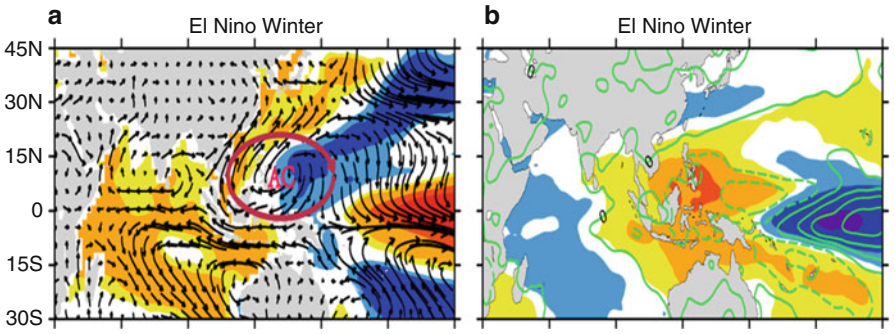

Fig. 6.17 Composite patterns of 925 hPa wind (vectors; unit, m/s) and SSTA (*shading*; unit, °C) fields (*left*) and OLR (*shading*; unit, W/m^2) and precipitation (contours; unit, mm) fields (*right*) during El Niño mature phase (DJF). Composite is based on 1980–2013 (From Chen et al. (2016). © Copyright 2016 American Meteorological Society (AMS))

explain its maintenance from northern winter to spring, as the mean flow is northeasterly during this period, but in the summer after the mean flow switches its direction, it becomes a negative feedback. Meanwhile, in association with El Niño decaying, an Indian Ocean basin-wide warming is observed, and this basin-wide warming persists from El Niño mature winter to the subsequent summer. Does the Indian Ocean SSTA play a role in affecting WNP anomalous circulation?

A study by Wu et al. (2009) argued that the Indian Ocean basin-wide warming can only have an impact on the WNP anomalous anticyclone in El Niño decaying summer, not in El Niño mature winter and following spring. The following is the physical reasoning.

Although the basin-wide SSTA pattern occurs in IO, rainfall and OLR anomalies show a clear east–west dipole structure, with enhanced (suppressed) convection over the western (eastern) IO. Prior to this season, the SSTA in IO is dominated by a zonal dipole, with strong cooling in the eastern pole. The rapid warming in eastern IO from northern fall to winter is attributed to both strengthened shortwave radiation forcing and ocean wave effect (Li et al. 2003; Hong et al. 2010).

The observed IO rainfall–SST relationship (Fig. 6.17) in El Niño mature winter implies a distinctive role the SSTA plays in affecting local convection and circulation. While the local warming in the eastern IO plays a passive role (i.e., it is local atmosphere that influences the ocean), the SSTA in the western IO plays an active role in strengthening atmospheric convection (i.e., it is the ocean that primarily influences the atmosphere) (Wu et al. 2009, 2012).

Given such a complex relationship, one needs to be cautious when designing numerical model experiments. Forced SSTA experiments may lead to a basin-wide precipitation anomaly over IO, which according to Gill's (1980) solution, would lead to a response of low-level easterlies in the western equatorial Pacific. Rainfall anomalies simulated by this forced experiment, however, were against the observed rainfall pattern.

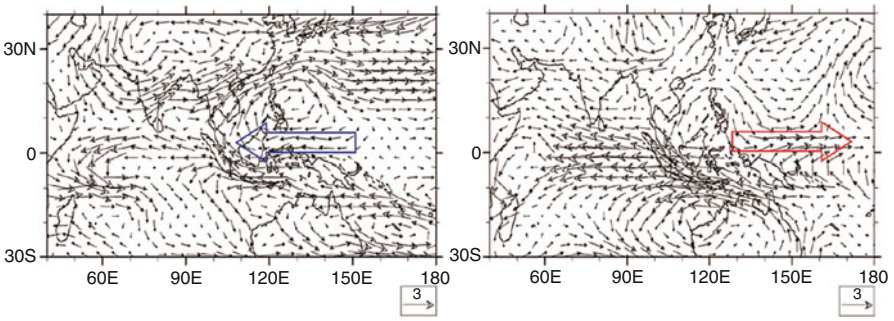

Fig. 6.18 The 850 hPa wind anomaly fields (vectors; unit, m/s) simulated from ECHAM4 in response to a specified SSTA forcing in tropical Indian Ocean (IO; *left*) and in response to a specified diabatic heating anomaly in the tropical IO (*right*). The *blue* vector denotes anomalous easterly wind, and red vector denotes anomalous westerly wind (From Chen et al. (2016).)

To demonstrate how a specified SSTA experiment in IO might "screw up" the atmospheric response in WP, we conducted a control experiment (in which the climatologic monthly SST is specified everywhere in the ocean) and two sensitivity experiments using ECHAM4. In the first sensitivity experiment, the observed SSTA in IO (same as that shown in Fig. 6.17a) is superposed onto the climatologic SST field. In the second sensitivity experiment, a dipole heating pattern that has the same horizontal pattern as the precipitation anomaly shown in Fig. 6.17b and an idealized vertical profile that has a maximum at middle troposphere is specified. Figure 6.18 shows the model simulation result from the two experiments. As expected, a basin-wide precipitation anomaly occurs in the specified SSTA experiment; as a result the low-level wind anomaly in equatorial WP is dominated by easterlies. In contrast, a westerly anomaly appears in the equatorial WP in the specified heating experiment because anomalous descending (ascending) motion in eastern (western) IO favors a reversed Walker circulation in both the tropical IO and Pacific.

The numerical experiments above indicate that a caution is needed in designing idealized atmospheric model experiments with specified SSTA forcing. It is important to compare observed and simulated rainfall anomalies in the specified SSTA region, to make sure that the local heating anomaly pattern is realistic.

While the anomalous vertical motion or precipitation field in the IO has a dominant east–west dipole pattern in El Niño mature winter, it becomes a north–south dipole in the subsequent spring, with anomalous ascending motion south of the equator (Fig. 6.16). Only in the summer following a peak El Niño, when SSTA in the eastern equatorial Pacific has dissipated, a basin-wide anomalous ascending motion and precipitation was observed. Such a basin-wide feature was also seen in the 200 hPa velocity potential field (Fig. 6.16). This points out that only in this season the basin-wide SSTA in IO can induce a basin-wide large-scale convective heating, which can further impact the circulation remotely in the Pacific.

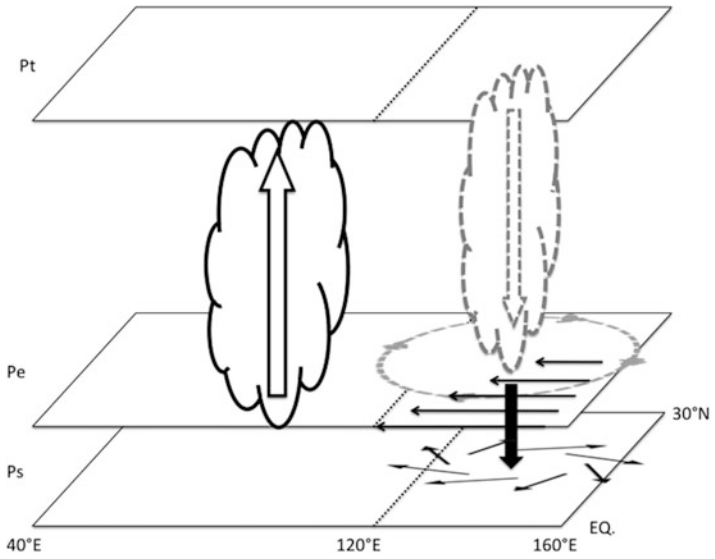

Fig. 6.19 Schematic diagram illustrating the impact of IO basin-wide heating on WNP anomalous anticyclone during El Niño decaying summer (From Wu et al. (2009). © Copyright 2009 American Meteorological Society (AMS))

Schematic diagram Fig. 6.19 describes how the basin-wide convection in IO can impact the anomalous anticyclone in the WNP. In response to basin-wide equatorial convective heating in IO, a Kelvin wave response with easterly anomalies appears in the western Pacific (Gill 1982). This Kelvin wave response has maximum amplitude at the equator, decreasing with increased latitudes. Anomalous anticyclonic shear north of the equator associated with this Kelvin wave response causes anomalous divergence and descending motion in the PBL, leading to the reduction of PBL specific humidity. The reduced moisture suppresses the monsoon heating, which can further induce low-level anomalous anticyclone in the WNP. Through this remote forcing mechanism, IO impacts the WNP circulation during El Niño decaying summer. This mechanism was called as IO capacity effect by Xie et al. (2009).

6.5.2 Relative Role of Indian Ocean and WNP SSTA Forcing

As discussed in the previous section, the maintenance of the WNPAC from the El Niño mature winter to the subsequent spring is attributed to a positive thermodynamic air–sea feedback. A cold SSTA in the WNP suppresses local convection, which stimulates low-level atmospheric anticyclone anomaly to its west. The northeasterly anomalies to the eastern flank of the WNPAC enhance the mean

trade wind and cool the SST in situ through enhanced surface latent heat flux (Wang et al. 2000).

With the onset of the WNP summer monsoon, the mean southwesterly monsoon circulation replaces the northeasterly trade wind. As a result, a negative evaporation–wind–SST feedback appears in the region. The negative air–sea feedback weakens the negative SSTA in the WNP throughout the El Niño decaying summer. In contrast to the weakening of the local negative SSTA, the WNPAC is strengthened from the preceding spring to the summer (Fig. 6.16).

A possible cause of strengthening of the WNPAC during the El Niño decaying summer is attributed to the remote SSTA forcing from the tropical Indian Ocean (TIO) (Wu et al. 2009; Xie et al. 2009). An Indian Ocean basin mode (IOBM) establishes after the ENSO mature winter. The basin-wide warming in the TIO is possibly caused by anomalous surface heat flux associated with the descending branch of the anomalous Walker circulation (Klein et al. 1999; Lau and Nath 2003) or the change of tropical tropospheric temperature (Chiang and Sobel 2002). In addition, ocean dynamic processes also play a role (Li et al. 2003). The IOBM may strengthen the WNPAC in boreal summer through the following two processes. Firstly, through enhanced convection over the TIO, the IOBM may stimulate a Kelvin wave-type easterly response in the western Pacific. The anticyclonic shear vorticity associated with the easterly anomalies may weaken the WNP summer monsoon through Ekman pumping divergences (Wu et al. 2009). Secondly, the IOBM may increase the surface moisture and thus enhance the low-level moisture transport and convection over the Maritime Continent, the latter of which may further induce the subsidence over the WNP through anomalous Hadley circulation (Chang and Li 2000; Li et al. 2001; Sui et al. 2007).

It appears that both the local forcing of the negative SSTA in the WNP and the remote SSTA forcing from the TIO may impact the WNPAC during the El Niño decaying summer. However, their relative contributions are still not clear.

Idealized numerical model experiments were designed to reveal the relative contribution from the TIO and western Pacific (WP) SSTA forcing. In a control run (CTRL), ECHAM4 was integrated for 20 years, forced by monthly climatological SST. In three sets of sensitivity experiments, the composite SSTA pattern in the global ocean (hereafter GB run), the TIO only (hereafter IND run), or the WP only (hereafter WP run) was added to the climatological SST as the model's lower boundary condition. Note that in the IND (WP) run, the SST climatology was prescribed in the regions outside of the TIO (WP). Each experiment was integrated from April to August, with 20 ensemble members. The ensemble mean results of June, July, and August are analyzed.

The difference between the GB and CTRL runs provides an evaluation on the performance of the model in reproducing the WNPAC. The difference between the IND and CTRL runs examines the sole contribution of the remote IOBM forcing to the WNPAC, and the difference between the WP and CTRL runs examines the sole contribution of the local WP SSTA forcing.

The above numerical sensitivity experiments demonstrate that both the remote IOBM forcing and the local WP SSTA forcing contribute to the maintenance of the

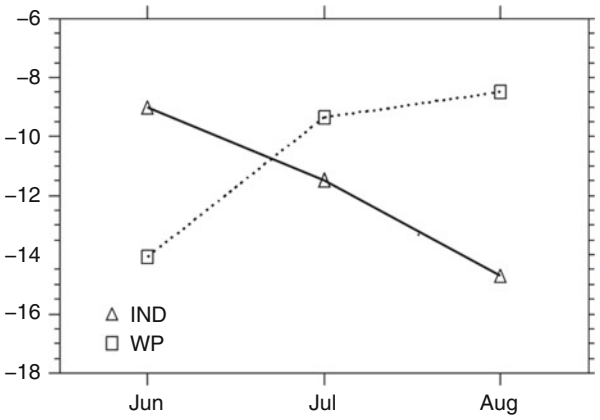

Fig. 6.20 Temporal evolutions of area-averaged vorticity anomalies (units, 10^{-6} m^2 s^{-1}) over the region of 10–35°N, 115–160°E for the WP (*dashed line*) and IND (*solid lines*) runs (From Wu et al. (2010). © Copyright 2010 American Meteorological Society (AMS))

WNPAC during the El Niño decaying summer. Figure 6.20 shows area-averaged vorticity anomaly over the WNP region (10°–35°N, 115°–160°E) from June to August derived from the WP and IND runs. The amplitude of JJA mean vorticity anomalies from the two runs are comparable, indicating that both the local WP SSTA forcing and remote TIO SSTA forcing are equally important in maintaining the WNPAC during El Niño decaying summer. A further examination of sub-seasonal evolutions of the two runs reveals an interesting difference. The local WP SSTA forcing leads to the strongest WNPAC response in June, and such a response weakens quickly in July and August. The remote TIO forcing, on the other hand, is relatively weak in early summer and strengthens greatly toward the end of the summer. What causes such a difference?

In the WP run, the WNPAC is primarily forced by the local negative SSTA. A significant large negative SSTA appears in the WNP prior to the El Niño decaying summer due to a positive thermodynamic air–sea feedback, as discussed in the previous section. As the summer comes, the reversal of the mean wind leads to a negative air–sea feedback. Despite of this negative feedback, the cold SSTA in the WNP is still quite large in June and July (Fig. 6.16) and affecting the local circulation anomaly in situ. The decay of the local SSTA forcing due to a negative feedback leads to the continuous weakening of the simulated WNPAC from June to August.

Different from the WP run, the evolution of the WNPAC in the IND run is associated with the sub-seasonal change of the background mean flow. The WNP monsoon trough becomes fully developed only in the later summer (after July 15). Although the amplitude of the IOBM weakens slightly from June to August, the simulated WNPAC intensifies with time and expands eastward. The intensification and expansion are consistent with the establishment of the climatological WNP monsoon trough in late summer. As a Kelvin wave response to positive heating anomalies in the tropical Indian Ocean, easterly anomalies in the western Pacific cause an anticyclonic shear and thus a boundary layer divergence over the WNP through Ekman pumping (Wu et al. 2009). The boundary layer divergence leads to

a greater negative precipitation anomaly response in late summer, when the monsoon trough is fully established. This explains why the remote Indian Ocean forcing effect is strengthened from June to August even though the IOBM weakens.

In summary, the WNPAC during the El Niño decaying summer is attributed to both the remote TIO and local WNP SSTA forcing. In early summer, the WNPAC is primarily influenced by the local negative SSTA, whereas in late summer, the IOBM plays a more important role in maintaining the WNPAC.

6.6 Modulation of the Monsoon Mean Flow on El Niño Response

Figure 6.21 shows the pattern of composite precipitation and low-level circulation anomalies during El Niño developing summer. Note that during the El Niño forcing, large-scale negative rainfall anomalies appear over the Maritime Continent. Two Rossby wave gyres occur to the west of the large-scale negative heating anomaly over the Maritime Continent. It is interesting to note that the two gyres, one at south of the equator and another at north of the equator, are not symmetric about the equator. The northern gyre is much greater.

Why is the circulation response asymmetric to a symmetric El Niño forcing? It is hypothesized that the asymmetric response is primarily attributed to the equatorial asymmetry of the summer mean flow, in particular the mean vertical shear. Figure 6.22a shows that background vertical shear in boreal summer is asymmetric about the equator. Over the Indian monsoon region, there are pronounced low-level westerlies and upper-level easterlies. As a result, there is strong background

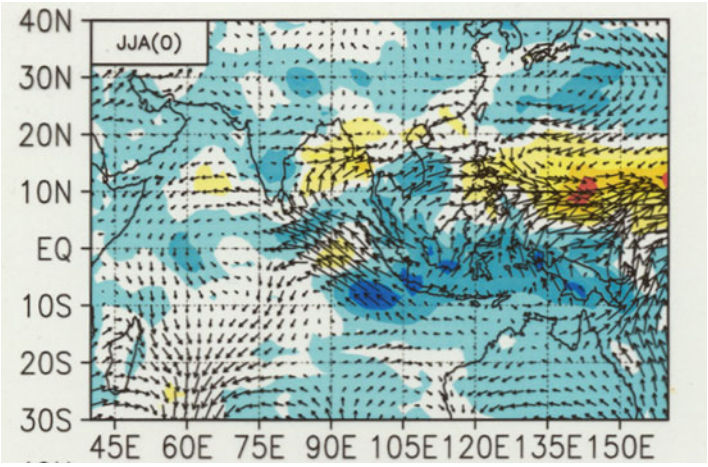

Fig. 6.21 Pattern of composite precipitation and 925 hPa wind anomalies during El Niño developing summer. The composite is based on all El Niño cases during 1950–2006

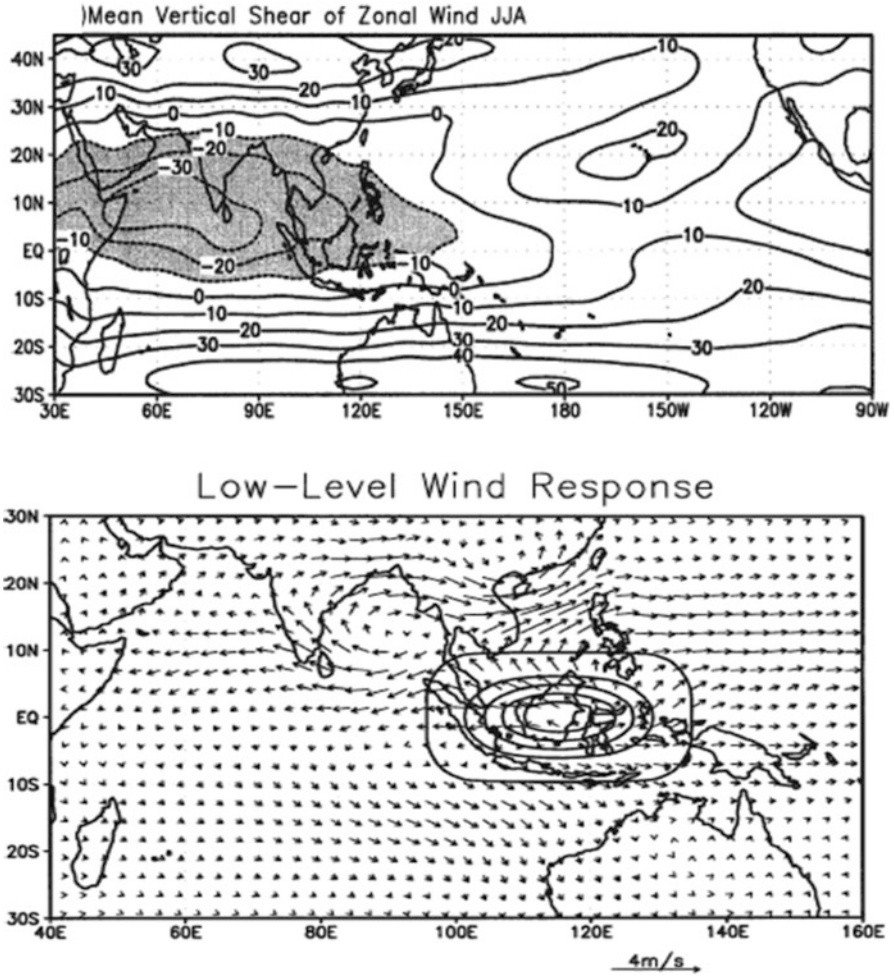

Fig. 6.22 (*Top*) The pattern of vertical shear of climatological zonal wind between 200 and 850 hPa averaged in JJA. (*Bottom*) Low-level wind response to a specified negative heating anomaly over the Maritime Continent simulated by an anomalous AGCM in which observed summer mean flow is specified as a background state (From Wang et al. (2003a, b). © Copyright 2003 American Meteorological Society (AMS))

easterly vertical shear in the northern Indian Ocean, while the shear is much weaker in the southern Indian Ocean. A theoretical study by Wang and Xie (1996) showed that background easterly (westerly) shear favors the growth of tropical Rossby wave type perturbations in the lower (upper) troposphere. Because energy source in the tropics is primarily latent heat, a stronger lower-tropospheric vorticity would favor a stronger PBL moisture convergence and a thus a stronger convective feedback (Li 2006).

To examine how the background mean flow modulates the anomalous circulation response in the Indo-western Pacific region, we conducted an anomaly GCM experiment, in which the summer mean flow is specified, and an equatorially symmetric negative heating anomaly is specified in the Maritime Continent (to mimic the direct El Niño forcing effect). The bottom in Fig. 6.22 illustrates the low-level circulation anomaly response to this prescribed symmetric heating. Similar to the observed, a greater Rossby wave gyre response appears in the northern hemisphere. Thus, the modeling study confirms the effect of the asymmetric summer mean flow in regulating the El Niño teleconnection pattern in South Asia/TIO.

6.7 Inter-monsoon Relationships

Meehl (1987) pointed out an in-phase relationship between the Indian summer monsoon (IM) and Australian summer monsoon (AM), based on limited data. Is this relationship steady? How is this relationship comparable to phase relations between WNP summer monsoon (WNPM) and IM/AM?

Gu et al. (2010) examined the relationship among three tropical monsoons, IM, WNPM, and AM, using different reanalysis datasets. Table 6.1 shows the correlations among the time series of the WNPM, AM, and IM intensity indices from 1979 to 2005. The correlation coefficient between WNPM and the preceding AM is 0.37, passing the 90% significance level. This implies that a strong (weak) AM might be associated with a succeeding strong (weak) WNPM. This in-phase relation appears in 19 out of the total 27 years. By checking winter (DJF) Niño3.4 index for each WNPM-AM in-phase years, we found that the eastern Pacific SSTA is all positive (negative) for the negative (positive) strong in-phase events, implying that ENSO is a major controlling factor for the AM-WNPM in-phase relationship.

The correlation coefficient between WNPM and the succeeding AM is −0.41, exceeding the 95% significance level. This points out an out-of-phase relation between the two sub-monsoon systems, that is, a strong (weak) WNPM often

Table 6.1 Lagged correlation coefficients among WNPM, IM, and AM for 1979–2005 using NCEP-DOE and CMAP

From	IM	AM	***WNPM***	***AM***	***WNPM***
	JJA(0)	DJF(0)	***JJA(0)***	***DJF(0)***	***JJA(0)***
To	AM	IM	***AM***	***WNPM***	***IM***
	DJF(1)	JJA(0)	***DJF(1)***	***JJA(0)***	***JJA(0)***
Correlation coefficient	0.29	−0.28	***−0.41***	***0.37***	***−0.64***
Number of events	17	17	***17***	***19***	***17***

From Gu et al. (2010). © Copyright 2010 American Meteorological Society (AMS)
Note: The 90% (95%) significance level corresponds to a correlation coefficient of 0.32 (0.38). Number of events indicates the number of years during which the relationship between two monsoons is consistent with the correlation coefficient

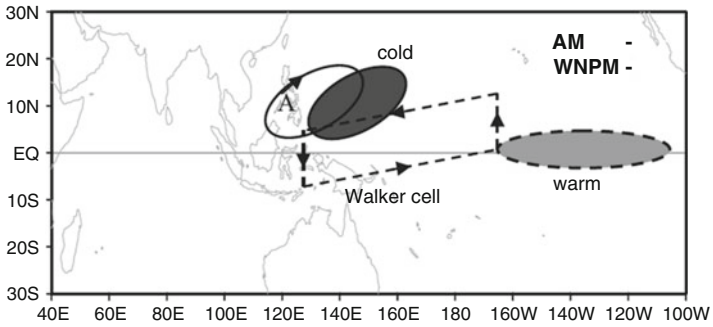

Fig. 6.23 Schematic diagram showing DJF (*dashed line*) and JJA (*solid line*) processes responsible for in-phase relation from AM to the succeeding WNPM (From Gu et al. (2010). © Copyright 2010 American Meteorological Society (AMS))

leads a weak (strong) AM. A further examination shows that about two thirds of all events reflect the out-of-phase relationship.

The most significant correlation appears in the simultaneous correlation between WNPM and IM, which is −0.64, passing the 99% significance level. This simultaneous out-of-phase relation appears in 17 summers during 1979–2005.

As seen from Table 6.1, compared with the correlations between the WNPM and AM/IM, the correlation coefficients between IM and AM are relatively weak and not statistically significant. Different from the many previous studies that made composites based on El Niño and La Niña conditions, the composite here is based on the anomalous monsoon intensity. In the following we will particularly focus on the phase relations of WNPM with other two sub-monsoon systems, as they are most significant relationships. The strategy is to examine the circulation and SST evolution characteristics to find the common features and similar physical mechanisms that control these relationships.

Figures 6.23, 6.24, and 6.25 are schematic diagrams illustrating the essential physical processes that may contribute to each of the sub-monsoon phase relations. The in-phase relationship from AM to the succeeding WNPM occurs primarily during the ENSO decaying phase (Fig. 6.23). On the one hand, the warm SSTA in the eastern Pacific induces a reversed anomalous Walker cell and causes a weak AM during the El Niño mature winter. On the other hand, an anomalous anticyclone is induced in WNP through either the Pacific–East Asia teleconnection (Wang et al. 2000; Wang and Zhang 2002) or the eastward propagation of a low-level anticyclone anomaly in the tropical Indian Ocean (Chen et al. 2007). The WNP anomalous anticyclone is maintained through a positive local thermodynamic air–sea feedback between the anticyclone and a cold SSTA (Wang et al. 2003a, b) from the boreal winter to late spring in the presence of the mean northeasterly. The local cold SSTA leads to a weak WNPM in boreal summer.

The out-of-phase relation from WNPM to the succeeding AM includes two different scenarios (Fig. 6.24). Scenario 1 describes the El Niño early onset or the La Niña persistence events. Scenario 2 consists of El Niño decaying/La Niña

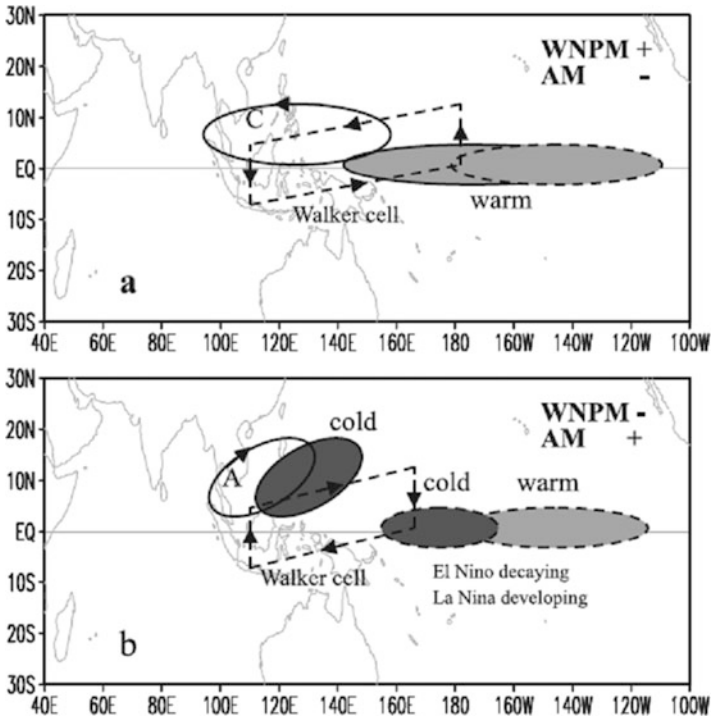

Fig. 6.24 Schematic diagrams showing the JJA (*solid line*) and DJF (*dashed line*) processes responsible for (**a**) out-of-phase relation from a strong WNPM to a weak AM and (**b**) out-of-phase relation from a weak WNPM to a strong AM (From Gu et al. (2010). © Copyright 2010 American Meteorological Society (AMS))

developing or La Niña decaying/El Niño Modoki developing events. For the first scenario, the remote forcing of the eastern Pacific SSTA holds a key. For example, a warm SSTA forces a Rossby wave response and low-level cyclonic shear over WNP (Gill 1980), which further enhances WNPM through the Ekman-pumping induced boundary layer convergence. As the SSTA continues to develop toward the boreal winter, the same sign of the SSTA weakens the AM through the anomalous Walker circulation in boreal winter. For the second scenario, the persistence of an anomalous anticyclone during the El Niño decaying phase holds a key in inducing a weak WNPM. As the decay of an El Niño is often accompanied with the onset of La Niña in the late year, the cold SSTA in the eastern Pacific may enhance AM in boreal winter through anomalous Walker circulation. Thus, the connection of WNPM and AM in the second scenario depends on both the persistence of the anomalous WNP anticyclone and the phase transition of the eastern Pacific SSTA (Fig. 6.24b).

The negative simultaneous correlation between WNPM and IM is mainly caused by the following two scenarios. The first scenario consists of the El Niño earlier onset (or La Niña persistence) events. The SSTA in the eastern Pacific, through

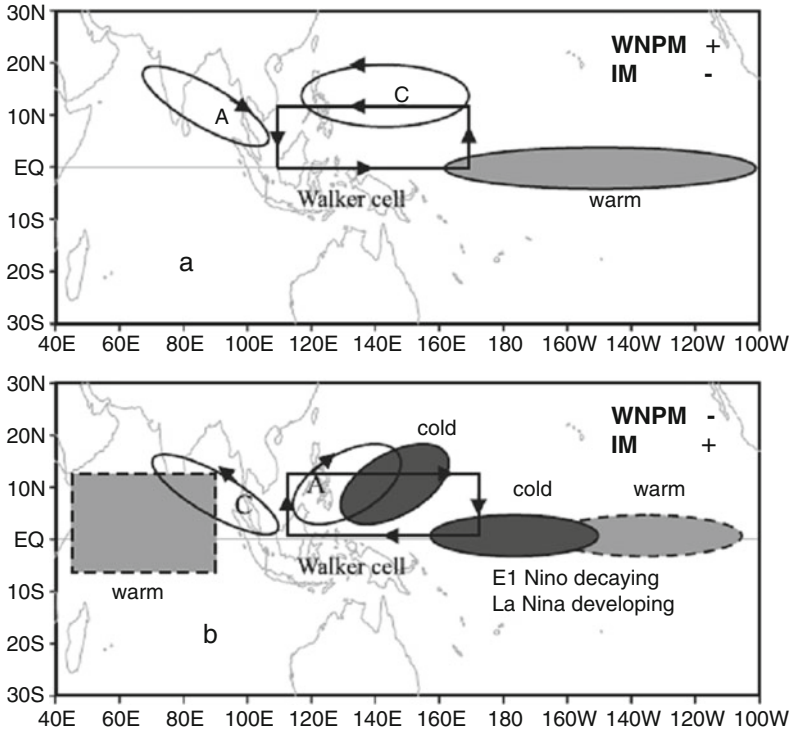

Fig. 6.25 Schematic diagrams showing the JJA (*solid line*) and DJF (*dashed line*) processes responsible for (**a**) simultaneous negative correlation between a strong WNPM and a weak IM and (**b**) simultaneous negative correlation between a weak WNPM and a strong IM (From Gu et al. (2010). © Copyright 2010 American Meteorological Society (AMS))

anomalous central equatorial heating, leads to the cyclonic wind shear in WNP and subsidence over the Maritime Continent. The former enhances the WNPM while the latter suppresses the IM (Fig. 6.25a). The second scenario consists of the El Niño decaying/La Niña developing (or La Niña decaying/El Niño developing) events. While a dry (wet) WNPM is attributed to the anomalous low-level anticyclone (cyclone) over WNP that persists from boreal winter to summer, a wet (dry) IM is caused by the eastern Pacific SSTA that has transitioned from a positive (negative) to a negative (positive) episode in JJA or by a basin-wide Indian Ocean warming (cooling) (Fig. 6.25b) that persists from El Niño (La Niña) mature winter to the subsequent summer. The basin-wide Indian Ocean warming may enhance (weaken) IM through increased (decreased) moisture transport (Chang and Li 2000; Li et al. 2001; Li and Zhang 2002).

Previous observational studies (e.g., Lau and Yang 1996; Li et al. 2001; Li and Zhang 2002) revealed that a warm SST anomaly in the tropical Indian Ocean leads a strong Indian monsoon. Chang and Li (2000) argued that the warm SSTA in Indian Ocean has both positive and negative effects on the Indian monsoon rainfall.

Table 6.2 Lagged correlation coefficients among WNPM, IM, and AM for 1979–2005 using GPCP2 and JRA data

From	***IM***	AM	***WNPM***	***AM***	***WNPM***
	JJA(0)	DJF(0)	***JJA(0)***	***DJF(0)***	***JJA(0)***
To	***AM***	IM	***AM***	***WNPM***	***IM***
	DJF(1)	JJA(0)	***DJF(1)***	***JJA(0)***	***JJA(0)***
Correlation coefficient	***0.35***	−0.26	***−0.32***	***0.32***	***−0.70***
Number of events	***17***	14	***14***	***18***	***15***

From Gu et al. (2010). © Copyright 2010 American Meteorological Society (AMS)
Note: The 90% (95%) significance level corresponds to a correlation coefficient of 0.32 (0.38). Number of events indicates the number of years during which the relationship between two monsoons is consistent with the correlation coefficient

A positive SST anomaly, on the one hand, increases the local surface humidity. The increased moisture may be further transported by the mean monsoon circulation, leading to a strong monsoon. On the other hand, the positive SSTA reduces the land–sea thermal contrast and thus decreases the monsoon rainfall. Both the scale analysis (Chang and Li 2000) and model simulations (e.g., Meehl and Arblaster 2002) showed that the positive effect is greater.

In analyzing the simultaneous IM-WNPM negative correlation, we notice a special case in summer 2001 that does not belong to both the scenarios above. As an anomalous cyclone persisted over SCS/WNP from winter to summer 2001 in association with the decay of a La Niña episode, no significant basin-wide SST anomalies appeared prior to the monsoon season in the tropical Indian Ocean, and by summer 2001, the tropical eastern Pacific SST became normal. Nevertheless, the IM was significantly weakened. The cause of the weak IM is possibly attributed to the atmospheric Rossby wave response to suppressed convection over the Maritime Continent, which, in turn, is caused by enhanced convective heating over the WNPM through the anomalous local Hadley cell (Kajikawa and Yasunari 2003). This implies that there might be a possible self-regulating process between the two sub-monsoon systems.

The composite analysis results above are based on the CMAP and NCEP Reanalysis 2 data. To examine the sensitivity of the aforementioned phase relationships to different data products, we conduct the same analysis procedure for two independent datasets. The first dataset includes GPCP2 rainfall and JRA reanalysis for the same period. The second dataset includes the PREC rainfall and NCEP/NCAR reanalysis for a longer period (1948–2006). Table 6.2 shows the lagged correlations among the three sub-monsoon systems using the GPCP/JRA dataset. It is found that the correlation coefficient between WNPM and the succeeding AM is −0.32, and the correlation coefficient between WNPM and the preceding AM is 0.32, both of which just pass the 90% significance level. The simultaneous correlation coefficient between WNPM and IM is −0.70, exceeding the 99% significant level.

The calculation of the longer record (1948–2006) dataset of NCEP/NCAR and PREC products (see Table 6.3) shows that the correlation coefficient between

Table 6.3 Lagged correlation coefficients among WNPM, IM, and AM for 1948–2006 using NECP/NCAR and PREC data

From	IM	AM	***WNPM***	AM	***WNPM***
	JJA(0)	DJF(0)	***JJA(0)***	DJF(0)	***JJA(0)***
To	AM	IM	***AM***	WNPM	***IM***
	DJF(1)	JJA(0)	***DJF(1)***	JJA(0)	***JJA(0)***
Correlation coefficient	0.21	−0.06	***−0.39***	0.07	***−0.29***
Number of events	36	36	***36***	34	***33***

From Gu et al. (2010). © Copyright 2010 American Meteorological Society (AMS)
Note: The 90% (95%) significance level corresponds to a correlation coefficient of 0.22 (0.26). Number of events indicates the number of years during which the relationship between two monsoons is consistent with the correlation coefficient

WNPM and the succeeding AM is −0.39, exceeding the 99% significance level. The simultaneous correlation coefficient between WNPM and IM is −0.29, exceeding the 95% significance level. The lagged correlation between AM and the succeeding WNPM, however, becomes insignificant. Thus, the three datasets point out in general a robust simultaneous IM-WNPM relation and a robust lagged phase relation between WNPM and the subsequent AM but a weak phase relation between AM and the subsequent WNPM. Thus, a caution is needed when a seasonal forecast is conducted based on the weak phase relationship.

A further analysis of the longer-record data reveals that the inter-monsoon relations are not stationary and they exhibit a marked interdecadal variation. For example, the significant negative correlation between WNPM and the succeeding AM appears at the beginning of 1960s, the mid-1970s, and after 1985. The significant negative simultaneous correlation between IM and WNPM occurs after 1975. The significant positive correlation between WNPM and the preceding AM appears from the end of 1960s to the beginning of 1970s. During other periods, the positive correlation is weak.

It is worth mentioning that the mechanisms discussed above are primarily based on the SSTA forcing. As we know, in addition to the lower boundary forcing, the monsoons are also influenced by internal atmospheric modes, such as synoptic and intraseasonal timescale motions.

6.8 Effect of Aerosol on Monsoon

Because of agriculture burning and burning fossil fuel, aerosol concentration in the troposphere increases rather steadily in the twentieth century (IPCC 2007). Anthropogenic aerosols absorb and scatter solar radiation and thus impose a negative radiative forcing to the earth surface ("dimming effect") (Meywerk and Ramanathan 1999; Ramanathan et al. 2005). Aerosols can also serve as cloud condensation nuclei and affect cloud formation, through which aerosols can also affect climate indirectly (Rosenfeld 2000; Rosenfeld et al. 2014). It has been

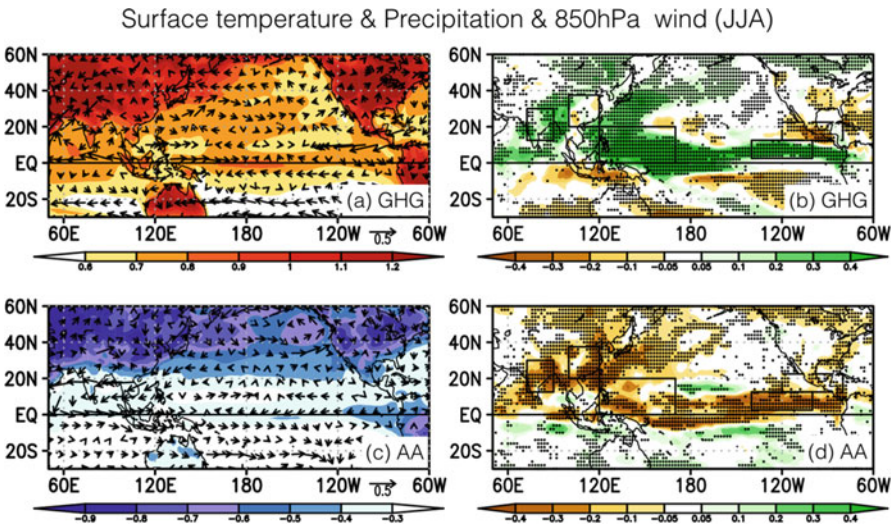

Fig. 6.26 Trends of surface temperature (shading, K century^{-1}) and 850 hPa winds (vector, m/s century^{-1}) during boreal summer over the period 1850–2005 are shown in left column and precipitation trends (shading, mm day^{-1} century^{-1}) in right column. (**a**) and (**b**) for results from greenhouse gas only experiments, (**c**) and (**d**) for the aerosol only experiments. Stippling denotes the regions where precipitation trends in at least 7 (out of 9) models agree with the sign of multi-model mean precipitation trends (From Zhang and Li (2016a). © Copyright 2016, American Geophysical Union (AGU))

reported that the radiative forcing of anthropogenic aerosols can be as large as that of anthropogenic greenhouse gases but with opposite sign, despite larger uncertainty (IPCC 2007).

However, unlike the anthropogenic greenhouse gases, the lifetime of anthropogenic aerosols is relatively short (Ramanathan et al. 2005). Consequently, aerosols concentrate and are thus more influential over the land area in the northern hemisphere (Li et al. 2015; Zhang and Li 2016a). As a result, the anthropogenic aerosols can significantly affect land–ocean thermal contrast, which is the main driver of the monsoon system (Guo et al. 2015; Salzmann et al. 2014). Indeed, it has been found that the East Asian summer monsoon rainfall has been weakening due to the substantial land cooling associated with the anthropogenic aerosols (Song et al. 2014). A prominent drying trend has also been found over the Indian summer monsoon region, which has been related to the anthropogenic aerosol effect as well (Bollasina et al. 2011; Li et al. 2015). Furthermore, the weakening of the Indian summer monsoon circulation has been attributed to the anthropogenic aerosol-induced interhemispheric cooling contrast, i.e., greater cooling in northern hemisphere (Bollasina et al. 2011).

Figure 6.26 shows single-forcing experiments from the Coupled Model Intercomparison Project Phase 5 (CMIP5) climate models that separate the effects of anthropogenic aerosols and greenhouse gases. It is clear that the anthropogenic aerosols induce prominent surface cooling anomalies over the northern hemisphere

during boreal summer, which consequently results in reduced land–ocean thermal contrast and weakened summer monsoon circulations. For instance, low-level easterly and northerly anomalies prevail over the Indian summer monsoon region, opposing the mean state southwesterlies (Fig. 6.26c). Similarly, the East Asian summer monsoon circulation is weakened due to the anthropogenic aerosol effect. The decreased moisture transport associated with these circulation changes induces drying anomalies over the Asian summer monsoon region (Fig. 6.26d). The inter-tropical convergence zone (ITCZ) over eastern tropical Pacific is also weakened associated with the anthropogenic aerosol-induced surface cooling anomalies. In addition to the dynamic effect, anthropogenic aerosol-induced cooling anomalies can also reduce the water vapor content and thus affect rainfall thermodynamically. This effect is important for driving the negative rainfall anomalies over the western North Pacific summer monsoon region.

In contrast to the anthropogenic aerosols, anthropogenic greenhouse gases tend to enhance rainfall by raising temperature and thus increasing moisture. As a result, both the Asian summer monsoon region and the ITCZ receive more rainfall due to the anthropogenic greenhouse gases (Fig. 6.26a). Note also that the land warming associated with anthropogenic greenhouse gases is apparently greater than that over the ocean surface, despite its relatively uniform distribution in the troposphere. This land–ocean warming contrast is a well-known feature that can be found in both observations and climate model simulations (Zhang and Li 2016b). As a result, the land–ocean thermal contrast is enhanced over the Asian summer monsoon region, which induces enhanced monsoon circulation over India that brings about more precipitation (Fig. 6.26a, b).

It is interesting to note that the East Asian summer monsoon circulation is not enhanced by the anthropogenic greenhouse gas effect, despite the greater land surface warming. This is in contrast to the weakened southwesterlies over East Asia when the land–ocean thermal contrast is reduced due to the aerosol effect (Fig. 6.26c). When forced with anthropogenic greenhouse gases, there is substantial positive rainfall anomaly over the western North Pacific summer monsoon region, which in turn drives low-level convergence anomaly that further enhances rainfall in situ ("richest-get-richer", Hsu and Li 2012). Since the East Asia and western North Pacific summer monsoon are dynamically connected, the circulation change over the western North Pacific will induce anomalous divergence over East Asia that reduces moisture transport and favors a drying anomaly. The combined dynamic and thermodynamic effect of the anthropogenic greenhouse gases leaves a small rainfall change over the East Asian summer monsoon region (Fig. 6.26b).

Hence, the two primary anthropogenic forcings act against each other over most regions. Note that the linear addition of the two single-forcing experiments reasonably reproduces the anomalies from the experiments in which the two forcing exist simultaneously (Fig. 6.27). Hence, these two forcing act mostly in a linear way. However, the relative importance of the two anthropogenic forcing is different over different regions. Overall, the thermodynamic effect of greenhouse gases is greater than that of aerosols due to the greater radiative forcing. Consequently, the rainfall changes over the western North Pacific summer monsoon region and the ITCZ over

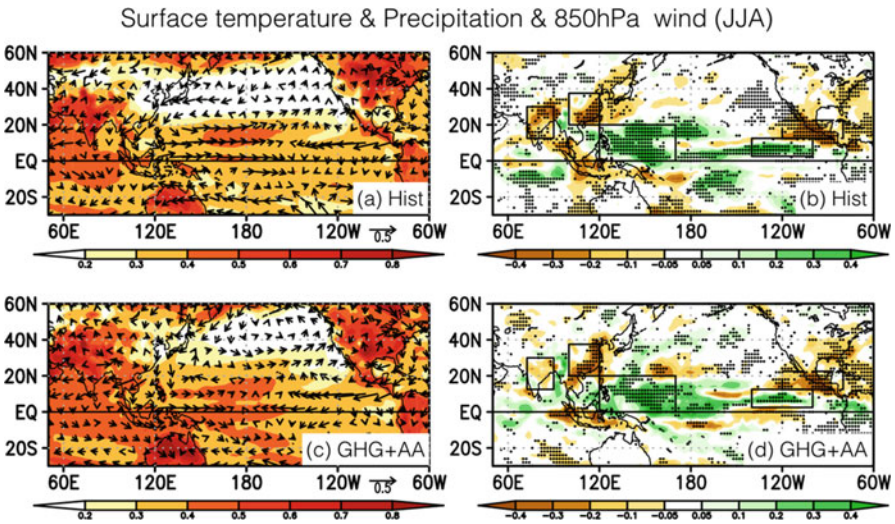

Fig. 6.27 Same as Fig. 6.1 but for results from total forcing experiments in (**a**) and (**b**), and the linear addition of results from greenhouse gas only and aerosol only experiments in (**c**) and (**d**) (Adapted from Zhang and Li (2016a). © Copyright 2016, American Geophysical Union (AGU))

eastern tropical Pacific are dominated by the greenhouse gas effect and thus positive. Over the land monsoon region, such as the Indian and East Asian summer monsoon region, the rainfall anomalies are negative, which is primarily associated with weakening of the monsoon circulation caused by reduced land–ocean thermal contrast associated with the aerosol effect (Fig. 6.27).

Questions

1. Through what physical processes does the El Niño exert a remote impact on the Indian summer monsoon?
2. Through what physical processes does the El Niño exert a remote impact on the East Asian summer monsoon? What is the key circulation system that connects El Niño and East Asian summer monsoon?
3. Through what processes does the anomalous anticyclone in WNP affect the Meiyu rainfall in East Asia?
4. What triggers and maintains the WNP anomalous anticyclone during El Niño developing and mature phases?
5. Through what processes does the tropical Indian Ocean SST anomaly influence the WNP circulation anomaly?
6. Why does the Indian Ocean basin warming become effective in influencing the WNP circulation anomaly only during El Niño decaying summer?
7. What is the relative role of tropical Indian Ocean basin warming and local cold SSTA in maintaining the anomalous anticyclone in WNP during El Niño decaying summer?

8. What is the phase relationship between the WNP monsoon and the Indian monsoon?
9. What is the tropospheric biennial oscillation (TBO)? What theories have been proposed to explain the TBO?
10. What causes the quasi-biennial and lower-frequency variability of the Indian summer monsoon precipitation?

References

Barnett TP (1991) The interaction of multiple time scales in the tropical climate system. J Clim 4:269–285

Bollasina MA, Ming Y, Ramaswamy V (2011) Anthropogenic aerosols and the weakening of the South Asian summer monsoon. Science 334:502–505. doi:10.1126/science.1204994

Chang C-P, Li T (2000) A theory for the tropical tropospheric biennial oscillation. J Atmos Sci 57:2209–2224

Chang C-P, Li T (2001) Nonlinear interactions between the TBO and ENSO. In: Chang CP et al (eds) East Asian and western Pacific meteorology and climate, World Scientific Series on Meteorology East Asia, vol 1. World Science, Singapore, pp 167–179

Chang C-P, Zhang Y, Li T (2000a) Interannual and interdecadal variations of the East Asian summer monsoon and tropical Pacific SSTs. Part I: Roles of the subtropical ridge. J Clim 13:4310–4325

Chang C-P, Zhang Y, Li T (2000b) Interannual and interdecadal variations of the East Asian summer monsoon and tropical Pacific SSTs. Part II: Meridional structure of the monsoon. J Clim 13:4326–4340

Chen TC, Weng SP, Yamazaki N, Kiehne S (1998) Interannual variation in the tropical cyclone formation over the western North Pacific. Mon Weather Rev 126:1080–1090

Chen J-M, Li T, Shih J (2007) Fall persistence barrier of SST in the South China Sea associated with ENSO. J Clim 20:158–172

Chen M, Li T, Shen X, Wu B (2016) Relative roles of dynamic and thermodynamic processes in causing evolution asymmetry between El Niño and La Niña. J Clim 29:2201–2220

Chiang JCH, Sobel AH (2002) Tropical tropospheric temperature variations caused by ENSO and their influence on the remote tropical climate. J Clim 15:2616–2631

Fu X, Wang B (2001) A coupled modeling study of the annual cycle of Pacific cold tongue. Part I: Simulation and sensitivity experiments. J Clim 14:765–779

Fu X, Wang B, Li T (2002) Impacts of air-sea coupling on the simulation of the mean Asian summer monsoon in the ECHAM4 model. Mon Weather Rev 130:2889–2904

Fu X, Wang B, Li T, McCreary J (2003) Coupling between northward propagating ISO and SST in the Indian Ocean. J Atmos Sci 60:1733–1753

Gaspar P (1988) Modeling the seasonal cycle of the upper ocean. J Phys Oceanogr 18:161–180

Gill AE (1980) Some simple solutions for heat-induced tropical circulation. Q J R Meterol Soc 106:447–462

Gill AE (1982) Atmosphere and ocean dynamics. Academic, New York

Gu D, Li T, Ji Z, Zheng B (2010) On the Western North Pacific Monsoon, Indian Monsoon and Australian Monsoon Phase Relations. J Clim 23:5572–5589

Guo L, Turner AG, Highwood EJ (2015) Impacts of 20th century aerosol emissions on the South Asian monsoon in the CMIP5 models. Atmos Chem Phys 15:6367–6378. doi:10.5194/acp-15-6367-2015

Hong C-C, Li T, Lin H, Chen Y-C (2010) Asymmetry of the Indian Ocean basin-wide SST anomalies: roles of ENSO and IOD. J Clim 23:3563–3576

Hsu P-C, Li T (2012) Is "rich-get-richer" valid for Indian Ocean and Atlantic ITCZ? Geophys Res Lett 39:L13705. doi:10.1029/2012gl052399
Huang R, Wu Y (1989) The influence of ENSO on the summer climate change in China and its mechanism. Adv Atmos Sci 6:21–32
IPCC, Climate Change (2007) The physical science basis. In: Solomon S et al (eds) Contribution of Working Group I to the fourth assessment report of the Intergovernmental Panel on Climate Change. Cambridge University Press, Cambridge/New York, 996 pp
Ju J, Slingo JM (1995) The Asian summer monsoon and ENSO. Q J R Meteorol Soc 121:1133–1168
Kajikawa Y, Yasunari T (2003) The role of the local Hadley circulation over the western Pacific on the zonally asymmetric anomalies over the Indian Ocean. J Meteorol Soc Jpn 81:259–276
Kawamura R (1998) A possible mechanism of the Asian summer monsoon-ENSO coupling. J Meteorol Soc Jpn 76:1009–1027
Klein SA, Soden BJ, Lau NC (1999) Remote sea surface temperature variations during ENSO: evidence for a tropical atmospheric bridge. J Clim 12:917–932
Lau N-C, Nath MJ (2003) Atmosphere–ocean variations in the Indo-Pacific sector during ENSO episodes. J Clim 16:3–20
Lau K-M, Sheu PJ (1988) Annual cycle, quasi-biennial oscillation, and southern oscillation in global precipitation. J Geophys Res 93:10975–10988
Lau K-M, Wu HT (2001) Principal modes of rainfall–SST variability of the Asian summer monsoon: a reassessment of the monsoon–ENSO relationship. J Clim 14:2880–2895
Lau K-M, Yang S (1996) The Asian monsoon and predictability of the tropical ocean-atmosphere system. Q J R Meteorol Soc 122:945–957
Li T (2006) Origin of the summertime synoptic-scale wave train in the western North Pacific. J Atmos Sci 63:1093–1102
Li T, Wang B (2005) A review on the western North Pacific monsoon: synoptic-to-interannual variabilities. Terr Atmos Ocean Sci 16:285–314
Li C, Yanai M (1996) The onset and interannual variability of the Asian summer monsoon in relation to land-sea thermal contrast. J Clim 9:358–375
Li T, Zhang Y (2002) Processes that determine the quasibiennial and lower-frequency variability of the South Asian monsoon. J Meteorol Soc Jpn 80:1149–1163
Li T, Zhang YS, Chang CP, Wang B (2001) On the relationship between Indian Ocean SST and Asian summer monsoon. Geophys Res Lett 28:2843–2846
Li T, Wang B, Chang CP, Zhang YS (2003) A theory for the Indian Ocean dipole-zonal mode. J Atmos Sci 60:2119–2135
Li T, Liu P, Fu X, Wang B, Meehl GA (2006) Spatiotemporal structures and mechanisms of the tropospheric biennial oscillation in the Indo-Pacific warm ocean regions. J Clim 19:3070–3087
Li X, Ting M, Li C, Henderson N (2015) Mechanisms of Asian summer monsoon changes in response to anthropogenic forcing in CMIP5 models. J Clim 28:4107–4125. doi:10.1175/JCLI-D-14-00559.1
Madden RA, Julian PR (1971) Detection of a 40–50 day oscillation in the zonal wind in the tropical Pacific. J Atmos Sci 28:702–708
Madden RA, Julian PR (1972) Description of global-scale circulation cells in the tropics with a 40–50 day period. J Atmos Sci 29:1109–1123
McCreary JP, Yu ZJ (1992) Equatorial dynamics in a 2.5-layer model. Prog Oceanogr 29:61–132
Meehl GA (1987) The annual cycle and interannual variability in the tropical Pacific and Indian Ocean regions. Mon Weather Rev 115:27–50
Meehl GA (1993) A coupled air-sea biennial mechanism in the tropical Indian and Pacific regions: role of the ocean. J Clim 6:31–41
Meehl GA (1994) Coupled land-ocean-atmosphere processes and south Asian monsoon variability. Science 266:263–267
Meehl GA (1997) The South Asian monsoon and the tropospheric biennial oscillation. J Clim 10:1921–1943

Meehl GA, Arblaster JM (2002) GCM sensitivity experiments for the Indian monsoon and tropospheric biennial oscillation transition conditions. J Clim 15:923–944
Meywerk J, Ramanathan V (1999) Observations of the spectral clear-sky aerosol forcing over the tropical Indian Ocean. J Geophys Res 104:24359–24370. doi:10.1029/1999JD900502
Mooley DA, Parthasarathy B (1984) Fluctuations in all- India summer monsoon rainfall during 1871–1978. Clim Chang 6:287–301
Mooley DA, Shukla J (1987) Variability and forecasting of the summer monsoon rainfall over India. In: Chang C-P, Krishnamurti TN (eds) Monsoon meteorology. Oxford University Press, New York, pp 26–59
Murakami M (1979) Large-scale aspects of deep convective activity over the GATE data. Mon Weather Rev 107:994–1013
Nicholls N (1978) Air-sea interaction and the quasi-biennial oscillation. Mon Weather Rev 106:1505–1508
Ramanathan V et al (2005) Atmospheric brown clouds: impacts on South Asian climate and hydrological cycle. Proc Natl Acad Sci **102**:5326–5333. doi:10.1073/pnas.0500656102
Rasmusson EM, Wang X-L, Ropelewski CF (1990) The biennial component of ENSO variability. J Mar Syst 1:71–96
Reynolds RW, Smith TM (1994) Improved global sea surface temperature analyses using optimum interpolation. J Clim 7:929–948
Rosenfeld D (2000) Suppression of rain and snow by urban and industrial air pollution. Science 287:1793–1796. doi:10.1126/science.287.5459.1793
Rosenfeld D, Sherwood S, Wood R, Donner L (2014) Climate effects of aerosol-cloud interactions. Science 343:379–380. doi:10.1126/science.1247490
Salzmann M, Weser H, Cherian R (2014) Robust response of Asian summer monsoon to anthropogenic aerosols in CMIP5 models. J Geophys Res Atmos 119, 11, 321–11, 337. doi:10.1002/2014JD021783
Shen S, Lau K-M (1995) Biennial oscillation associated with the East Asian summer monsoon and tropical Pacific sea surface temperatures. J Meteorol Soc Jpn 73:105–124
Soman MK, Slingo JM (1997) Sensitivity of the Asian summer monsoon-aspects of sea-surface-temperature anomalies in the tropical Pacific Ocean. Q J R Meteorol Soc 123:309–336
Song F, Zhou T, Qian Y (2014) Responses of East Asian summer monsoon to natural and anthropogenic forcings in the 17 latest CMIP5 models. Geophys Res Lett 41:596–603. doi:10.1002/2013GL058705
Sui C-H, Chung P-H, Li T (2007) Interannual and interdecadal variability of the summertime western North Pacific subtropical high. Geophys Res Lett 34:L11701
Tian SF, Yasunari T (1992) Time and space structure of interannual variations in summer rainfall over China. J Meteorol Soc Jpn 70:585–596
Tomita T, Yasunari T (1993) The two types of ENSO. J Meteorol Soc Jpn 71:273–284
Tomita T, Yasunari T (1996) Role of the northeast winter monsoon on the biennial oscillation of the ENSO/monsoon system. J Meteorol Soc Jpn 74:399–413
Walker GT (1923) Correlations in seasonal variations of weather. VIII, A further study of world weather. Mem Indian Meteorol Dept 24:75–131
Walker GT (1924) Correlations in seasonal variations of weather. VIII, A further study of world weather. Mem Indian Meteorol Dept 24:275–332
Wang B, Chan JC-L (2002) How strong ENSO regulates tropical storm activity over the western North Pacific. J Clim 15:1643–1658
Wang WC, Li K (1990) Precipitation fluctuation over semiarid region in northern China and the relationship with El Niño/southern oscillation. J Clim 3:769–783
Wang B, Li T (2004) East Asian monsoon-ENSO interactions. In: Chang CP et al (eds) East Asian and Western Pacific meteorology and climate, World Scientific Series Meteorology East Asia, vol 2. World Science, Singapore, pp 177–212
Wang B, LinHo (2002) Rainy seasons of the Asian-Pacific monsoon. J Clim 15:386–398

Wang B, Wu R (1997) Peculiar temporal structure of the South China Sea summer monsoon. Adv Atmos Sci 14:177–194
Wang B, Xie X (1996) Low-Frequency equatorial waves in vertically shear flow. Part I: Stable waves. J Atmos Sci 53:449–467
Wang B, Zhang Q (2002) Pacific–East Asian teleconnection, Part II: How the Philippine Sea anticyclone is established during El Niþo development. J Clim 15:3252–3265
Wang B, Li T, Chang P (1995) An intermediate model of the tropical Pacific ocean. J Phys Oceanogr 25:1599–1616
Wang B, Wu R, Fu X (2000) Pacific–East Asian teleconnection: How does ENSO affect East Asian climate? J Clim 13:1517–1536
Wang B, Clemons SC, Liu P (2003a) Contrasting the Indian and East Asian monsoons: implications on geologic timescales. Mar Geol 201:5–21
Wang B, Wu R, Li T (2003b) Atmosphere-warm ocean interaction and its impact on Asian-Australian Monsoon variation. J Clim 16:1195–1211
Webster PJ, Yang S (1992) Monsoon and ENSO: selectively interactive systems. Q J R Meteorol Soc 118:877–926
Webster PJ, Magana VO, Palmer TN, Shukla J, Tomas RA, Yanai M, Yasunari T (1998) Monsoons: processes, predictability, and the prospects for prediction. J Geophys Res 103:14451–14510
Wu B, Zhou T, Li T (2009) Seasonally evolving dominant interannual variability modes of East Asian climate. J Clim 22:2992–3005
Wu B, Li T, Zhou T (2010) Relative contributions of the Indian Ocean and local SST anomalies to the maintenance of the western North Pacific anomalous anticyclone during El Niño decaying summer. J Clim 23:2974–2986
Wu B, Zhou T, Li T (2012) Two distinct modes of tropical Indian Ocean precipitation in boreal winter and their impacts on equatorial western Pacific. J Clim 25:921–938
Xie A, Chung Y-S, Liu X, Ye Q (1998) The interannual variations of the summer monsoon onset over the South China Sea. Theor Appl Climatol 59:201–213
Xie S-P, Hu K, Hafner J, Tokinaga H, Du Y, Huang G, Sampe T (2009) Indian Ocean capacitor effect on Indo–western Pacific climate during the summer following El Niño. J Clim 22:730–747
Yanai M, Li C, Song Z (1992) Seasonal heating of the Tibetan Plateau and its effects on the evolution of the Asian summer monsoon. J Meteorol Soc Jpn 70:319–351
Yang S, Lau K-M (1998) Influences of sea surface temperature and ground wetness on Asian summer monsoon. J Clim 11:3230–3246
Yang S, Lau K-M, Sankar-Rao M (1996) Precursory signals associated with the interannual variability of the Asian summer monsoon. J Clim 9:949–964
Yasunari T (1990) Impact of the Indian monsoon on the coupled atmosphere/ocean system in the tropical Pacific. Meteorog Atmos Phys 44:29–41
Yasunari T (1991) The monsoon year—a new concept of the climatic year in the tropics. Bull Am Meteorol Soc 72:1331–1338
Yasunari T, Suppiah R (1988) Some problems on the interannual variability of Indonesian monsoon rainfall. In: Theon JS, Fugono N (eds) Tropical rainfall measurements. A. Deepak, Hampton, pp 113–122
Zhang L, Li T (2016a) Relative roles of anthropogenic aerosols and greenhouse gases in land and oceanic monsoon changes during past 156 years in CMIP5 models. Geophys Res Lett 43:5295–5301. doi:10.1002/2016GL069282
Zhang L, Li T (2016b) Relative roles of differential SST warming, uniform SST warming and land surface warming in determining the Walker circulation changes under global warming. Clim Dyn:1–11. doi:10.1007/s00382-016-3123-6
Zhang R, Sumi A, Kimoto M (1996) Impact of El Niño on the East Asian monsoon: a diagnostic study of the 86/87 and 91/92 events. J Meteorol Soc Jpn 74:49–62